Phase Transitions and Quench Dynamics in Driven-Dissipative Condensates

Paolo Comaron

Thesis submitted for the degree of
Doctor of Philosophy

School of Mathematics, Statistics & Physics
Newcastle University
Newcastle upon Tyne
United Kingdom

June 2018

To nonna Angelina

Acknowledgements

First, I would like to thank my supervisor Dr. Nick Proukakis for the support which he has constantly given me, the interesting discussions, the passion for research and his guidance throughout my PhD. I am grateful to Luca Salasnich, as without him I would not have started this project. I also thank EPSRC and the School of Mathematics, Statistics & Physics for providing financial support of this project. I want to extend my gratitude to Galbadrakh Dagvadorj, Alex Zamora, Marzena Szymańska and Iacopo Carusotto for stimulating discussions on the work included in this thesis.

Further to this, I would like to thank Luca Galantucci and Kean Loon Lee for sharing their technical knowledge, scientific advice and support. I want to extend my gratitude to those who contributed on the proofreading of this theses: Tom Bland, André Cidrim, Lewis Clark, Philipp Edelmann, Horacio Guerra and Sophie Harbisher. I would like to thank my former and present office-mates: Azhana Ahmad, Marios Bounakis, Svetlana Cherlin, Francesca Fedele, Kavita Gangal, Aida Gjoca, Katie Marshall, Siddiqua Mazhar, Rute Velosa, Joe Reid, A'yunin Sofro, Batuush Undrakh for the many hours of fun and litres of coffee drunk.

I would like to thank those who made of my PhD an enjoyable experience: Clarissa Barratt, Dimitrios Chiotis, David Cushing, Ilke Canakci, Quentin Clairon, Liam Dobson, Matthew Edmonds, Can Evirgen, Donatello Gallucci, Natalia Gomez Perez, Chris Hales, Alex Hindle, James Hollins, Ste Johnson, Sarah Jowett, Evgenios Kakariadis, Fabrizio Larcher, Christian Lawson-Perfect, Gary Liu, Nick Loughlin, Anne Malchow, Quentin Marolleau, Joe Matthews, Mariam Garba, David McGeene, Hayley Moore, Keith Newman, Sirio Orozco-Fuentes, Rob Pattinson, David Pescod, Rathish Ratnasingam, Jason Reneuve, Em Rickinson, David Robertson, Matthew Robinson, Luis Santiago Rodrigues, Tim-O. Sauer, Amit Seta, George Stagg, David Stuart, Matina Trachana, Klejdja Xhani, Laura Wadkin, James Walton, Gavin Whitaker for the enjoyable times, general chats, entertaining coffee times and nights out.

I would also like to thank Michael Beaty, Chris Graham and John Nicholson for technical support and computer advice.

Last but not the least, I would like to thank my family: my parents Mariangela and Bruno, my brothers Francesco and Lorenzo for supporting me in my life in general. A special thank goes to Sara, for her eternal patience, constant support and love.

Abstract

Exciton-polaritons are composite quasi-particles, thought of as being half-matter and half-light: they have a low effective mass, enabling them to form a Bose-Einstein condensate at room temperature, but are inherently unstable quasi-particles, with the observed coherence arising as a result of the interplay between driving and decay. An important open question tackled in this thesis, is the extent to which the driven-dissipative nature of these "fluids of light" makes them different to the usual "equilibrium" condensates. Exciton-polariton condensates are of particular interest both for fundamental studies and for potential applications in quantum technologies. In this thesis, we focus on the investigation of static and dynamic properties of such systems, specifically addressing the nature of the phase transition and the dynamics during and after a quench. After confirming the validity of our model (a stochastic nonlinear equation for the lower-polariton branch) for experimentally-relevant parameters, we perform a detailed characterisation of the steady-state system, obtaining results in broad agreement with the Berezinskii-Kosterlitz-Thouless phase transition characterising the transition from a disordered to an ordered state in two-dimensional equilibrium systems. Our analysis enables us to identify the critical external pumping rate at which the phase transition occurs, critical for our next study. Firstly, by instantaneously quenching the system across the transition, we discuss dynamical scaling of defects and characteristic length of the system: this enables us to evaluate the dynamical critical exponent characterising the growth of long-range order. Our results reveal that universal critical properties of driven-dissipative polariton systems are consistent with those expected for the equilibrium Berezinskii-Kosterlitz Thouless transition, ruling out other proposed scenarios ("conservative superfluid", "Kardar-Parisi-Zhang" predictions). Finally, analysing finite-duration quench dynamics across the phase transition, we explicitly verify universal behaviour in the form of the Kibble-Zurek mechanism, a universal scaling law relating the number of spontaneously-generated defects (vortices) to the quench duration.

Contents

Part I

Introduction, theoretical and numerical analysis

Chapter 1

Introduction

A phase transition, which describes the transformation process between different equilibrium configurations of a system, is a phenomenon which can be experienced and observed in everyday life. A state, or phase, of a thermodynamic system is commonly described as a domain of a many-body system within which all relevant physical properties are uniform (Fermi, 1956); as an example, among the most familiar states of matter which surround us, we identify liquid, gas and solid. Although their features are routinely visible in the macroscopic world, the profound source of such macroscopic phenomena have been understood to lie in the microscopic world. For instance, when viewed macroscopically, it is well known that the properties of a microscopic phenomena such as magnetisation can be inferred from the arrangement of microscopic components called spins (Huang, 2000).

The branch of physics which describes these complex systems, often referred to as "theory of phase transitions", proposes many diverse statistical-physics models. It is not surprising that these same models are also used to describe complex systems in different fields, such as economics (Dragulescu and Yakovenko, 2000), biology (Stanley, 1999), sociology (Castellano *et al.*, 2009) and psychology (Spivey *et al.*, 2009). All these phenomena share the property that the nature of the state changes under the variation of a well defined parameter. The notation of order is fundamental to any phase transition; this is often, but not always, related to the more subtle concept of change of symmetry, or spontaneous symmetry breaking. Statistical theories of complex systems aim to describe how these transition processes happen, through the formulation of descriptive theories which rely on only a few thermodynamic variables.

In 1933 Paul Ehrenfest introduced a classification for phase transitions (Sauer, 2017): a phase transition is of the n-th order if the n-th derivative of the free energy of the system

is discontinuous at the critical point. The modern classification of phase transitions improved Ehrenfest's picture (Jaeger, 1998). First order phase transitions involve the presence of latent heat, as the transition between solid and liquid phases. Second order phase transitions are instead continuous and involve i) a divergent susceptibility and ii) an algebraic growth of the correlation length near the critical point. An example of such a transition is the ferromagnetic transition. Infinite order phase transitions are continuous; however, spontaneous symmetry breaking does not strictly apply as we cannot talk of a "fully" ordered state. An example of infinite phase transition is the Berezinskii-Kosterlitz-Thouless transition in the two-dimensional ($2d$) XY model (Huang, 2000), which describes the change, at some threshold, from proliferation of free vortices at high temperatures to bound vortex-antivortex pairs at low temperatures.

In nature, there exist many examples of phase transitions, with some describing transformations between exotic phases. The low-temperature world is indeed a fascinating environment where phase transitions are affected by the quantum nature of particles. It is well known that below certain temperatures, particles no longer behave as discrete entities with definite positions, but instead they acquire wave-like properties. This uncertainty is governed by the Heisenberg uncertainty principle (Heisenberg, 1927). The wave-particle duality concept was suggested for the first time by de Broglie (de Broglie, 1925), who proposed the original idea of a matter wave. In the case of an ideal (non-interacting) gas of free massive particles, the thermal de Broglie wavelength, which corresponds to the spatial width of a particle with mass m and temperature T, is defined as

$$\lambda_{\mathrm{dB}} = \frac{\hbar}{\sqrt{2\pi m k_{\mathrm{B}} T}}, \tag{1.1}$$

where k_B is the Boltzmann constant and $\hbar$ is the Planck constant.

Among the most exotic low-temperature phases known to date, we find the Bose-Einstein condensate (BEC). This phenomenon has been proposed for the first time by the Indian physicist Bose (Bose, 1924), and subsequently expanded by Einstein who, fascinated by Bose's work, decided to first translate it, before generalising it for a non-interacting gas of massive particles (Einstein, 1924). Bose-Einstein condensation is a phase transition of the second order. It takes place at some critical threshold below which a macroscopic fraction of Bose particles occupies the lowest energy state possible. This is related to the statistical property of bosons, particles with integer spin, which can occupy the energy level ϵ_{i} of the i-th state with particle number n_{i} (Pethick and Smith, 2008),

according to:

$$\langle n_{\rm i}(\epsilon_{\rm i})\rangle = \frac{1}{e^{\frac{\epsilon_{\rm i}-\mu}{k_{\rm B}T}}-1}, \tag{1.2}$$

for $\epsilon_{\rm i} > \mu$, where μ is the chemical potential. A distinct scenario pertains to fermionic particle: in such a system, the Pauli exclusion principle (Pauli, 1925) does not allow two particles with same spin to occupy the same quantum level. For a d-dimensional uniform Bose gas, condensation is the result of the competition between the average particles distance $\ell = n^{-1/d}$ (where d is the system dimension) and the de Broglie wavelength, $\lambda_{\rm dB}$, defined in Eq. (1.1). For typical (high) temperature values and mass, $\lambda_{\rm dB}$ is negligible when compared with the average distance between particles ℓ, implying that a quantum object is described as particle rather than a wave. In the opposite low-temperature limit, the wave-packet size increases, and a wave-like description becomes predominant. For the case of an ideal gas of particles, with mass m, the critical temperature reads

$$T_{\rm c} = \frac{2\pi\hbar^2}{mk_{\rm B}T}\left(\frac{n}{\zeta(3/2)}\right)^{2/3}, \tag{1.3}$$

from which we derive the condition for condensation of a free gas of non-interacting particles, namely $n\lambda_{\rm dB}^3 \geq \zeta(3/2) \approx 2.612$.

For a homogeneous $2d$ gas of bosons, the scenario is drastically modified (Petrov and Shlyapnikov, 2001). Condensation only occurs at $T = 0K$, thus macroscopic occupation at non-zero temperatures is forbidden. The absence of BEC in $2d$ uniform and infinitely large system at $T \neq 0$ is a direct consequence of the infrared diverging behaviour of the distribution of particles outside the condensate. The number of particles in the excited states is given by (Pethick and Smith, 2008; Hadzibabic and Dalibard, 2011):

$$N_{\rm ex} = \frac{mL^2}{2\pi\hbar^2}\int_0^\infty d\epsilon \frac{1}{e^{\frac{\epsilon-\mu}{k_{\rm B}T}}-1}, \tag{1.4}$$

where the prefactor $mL^2/2\pi\hbar^2$ is the $2d$ smoothed density of states for a homogeneous $2d$ gas, with L^2 the surface area and $\mu \leq 0$. To estimate the number of excited particles $N_{\rm ex}$, one can introduce an infrared cut-off at the energy of the single-particle ground state $\epsilon = \epsilon_{\rm min}$. From the relation obtained for $N_{\rm ex}$, one can then infer that the "new" $2d$ critical temperature would scale with the density of particles over the logarithm of the total number of particles (Pethick and Smith, 2008). At the thermodynamic limit, we conclude that $T_{\rm c}$ tends to zero, i.e. BEC does not occur in the ideal infinite uniform $2d$ Bose gas. As we will discuss in more detail in the next section, for a $2d$ system at non-zero temperature the destruction of "full" order is however only marginal. Although BEC is forbidden, the system is still able to exhibit a "quasi-ordered" phase, without precluding

the possibility of a phase transitions in $2d$ systems.

1.1 Physical systems exhibiting Bose-Einstein condensation

In the years 1928-1932, W.H. Keesom *et al.* realised that, below a critical threshold known as the λ-point ($T \sim 2.2$K), ^{4}He could exhibit a phase transition to a state with non-classical properties (Keesom, 1942). At this critical temperature, they also measured a peak of the specific heat. A few years later, in 1938, Kapitza (Kapitza, 1938) and Allen and Misener (Allen and Misener, 1938) published the experimental evidence that below the λ-point, a strong-interacting liquid, ^{4}He, could exhibit a lack of viscosity, with flow rates independent of pressure drops. The result was striking, as it was the first observation of superfluidity. In the same year, this phenomena was suggested to be related to Bose-Einstein condensation by Fritz London (London, 1938), although the strongly interacting nature of ^{4}He differed from the theoretical prediction for dilute non-interacting particles (London also proposed that superconductivity, observed for the first time in 1911 by Heike Kamerlingh Onnes (Onnes, 1911), could be interpreted as superfluidity of the electron gas in a metal). The effect of such strong interactions is the reduction of the condensate fraction, so that less than 10% of the system is condensed even at the lowest achievable temperatures where the system is purely superfluid. Shortly afterwards, Tisza (Tisza, 1938) assumed that superfluidity could be explained by a simple two-fluid model, where the total atom density is subdivided into a superfluid part, n_s, and a normal part, n_n, such that $n = n_\mathrm{s} + n_\mathrm{n}$. In 1941, Landau improved this model without considering BEC but through a consideration of the energy states of the liquid, instead of individual atoms. His main works on superfluidity (Landau, 1941) led to the Nobel Prize in Physics in 1962.

A real turning point in the study of BEC physics has been the first "pure" realisation of a BEC in the lab in a system of trapped weakly-interacting bosonic atoms. Historically, the first ideal candidate for BEC of atoms was spin-polarised hydrogen, suggested by Hecht in 1959 (Hecht, 1959) and Stwalley and Nosanow in 1976 (Stwalley and Nosanow, 1976). Condensation of ^{87}Rb atoms in a harmonic trap was instead accomplished in 1995 by Cornell and Wieman for the first time (Anderson *et al.*, 1995), an achievement which eventually led to their award of the 2001 Nobel prize, jointly with Ketterle (Davis *et al.*, 1995). This discovery was made thanks to advanced-at-the-time techniques such as laser cooling and magnetic evaporative cooling and trapping (1997 Nobel prize to Phillips, Cohen-Tannoudji and Chu). Demonstration of gaseous BEC has been achieved in other species, including ^{7}Li (Bradley *et al.*, 1995, 1997), ^{23}Na (Davis *et al.*, 1995), ^{85}Rb (Cornish *et al.*, 2000), ^{41}K (Modugno *et al.*, 2001), metastable ^{4}He (Robert *et al.*, 2001), ^{174}Yb (Takasu *et al.*, 2003), ^{133}Cs (Weber *et al.*, 2003), ^{52}Cr (Griesmaier *et al.*, 2005), ^{84}Sr (Stellmer *et al.*,

2009), ^{86}Sr (Stellmer *et al.*, 2010), ^{88}Sr (Mickelson *et al.*, 2010), ^{40}Ca (Kraft *et al.*, 2009), ^{164}Dy (Lu *et al.*, 2011). .

In the years following these pioneering discoveries, BEC properties have been observed in other physical systems. In such systems scientists have focused on reaching quantum effects at higher temperatures by working with lower-mass quasiparticles, resulting in a higher condensation temperature. Quasi-particles in semiconductors, collective excitations of materials which behave as a particle, became promising candidates for this role. In 1961, Böer *et al.* proposed condensation of excitons (Blatt *et al.*, 1962), a bosonic quasi-particle formed by electron-holes pairs in semiconductors bounded by Coulomb interaction, but their realisation has not been as straightforward as thought initially: many noteworthy advances followed (Butov *et al.*, 2002; High *et al.*, 2012), but the issue of whether condensation has been observed remains controversial, even today. Similar issues have arisen when probing macroscopic coherence in other systems. In 2006, Demokritov *et al.* demonstrated the achievement of condensation of magnons (Demokritov *et al.*, 2006) in magnetic materials. This was followed by the observation of condensation of triplons in antiferromagnets (Aczel *et al.*, 2009).

Exciting outcomes have been obtained for quasiparticles of light. This is made possible by the strong coupling between excitons and the cavity mode, when placed inside a high quality factor cavity, resulting in a new quasiparticle called exciton-polariton, often simply referred to as polariton. Normally, free photons are non-interacting, massless and short lifetime particles (photons have been predicted to interact in a vacuum, but the probability of the creation of a stable system is extremely small (Berestetskii *et al.*, 1982)), whereas excitons are massive and strongly interacting (Combescot *et al.*, 2017). The strong coupling regime represents an efficient mechanism to provide interactions of photons, and indeed becomes an essential condition for the onset of polariton condensation. The effect of strong coupling is to lower the effective mass of the exciton, or equivalently, to provide the cavity photon a mass through the effect of stronger interactions.

Photons can also be condensed in a cavity filled with a solution of dye molecules, which facilitates their interactions. This approach has been used for reaching condensation of (weakly interacting) photons in 2010 by Weitz's group in Bonn (Klaers *et al.*, 2010).

1.1.1 Bose-Einstein condensation of exciton-polaritons

In the previous section we introduced exciton-polaritons as quasiparticles which are the result of the superposition of light and an electronic excitation in a solid (Littlewood and Edelman, 2017). Excitons are electronic excitations in a semiconductor. They are created

by inducing an external stimulation, typically energetically proportional to the material band gap, in order to promote an electron from the valence band to the conduction band. As a consequence, a hole in the valence band, with opposite electron charge, is formed. A hydrogen-like particle, the so-called "exciton", is then formed by virtue of the Coulomb force exerted between electron and hole. The exciton frequency dispersion reads $\omega_{\mathrm{x}}(k_{\shortparallel}) = \omega_{\mathrm{x}}^{0} + \hbar k_{\shortparallel}^{2}/2m_{\mathrm{x}}$, with m_{x} the exciton mass, which is typically one order lower than the electronic mass m_{e}, and $k_{\shortparallel}$ is the in-plane $2d$ wavevector.

The strong coupling has the important effect to dress the cavity photon and give it an effective mass. Experimentally, this is engineered by introducing a spatial confinement and embedding the polaritons inside a mirror (Weisbuch *et al.*, 1992). The frequency dispersion of the photon, which is obtained by fixing the transverse (quantised) wavevector $k_{\mathrm{z}} = N\pi/L$, reads $\omega_{\mathrm{c}}(k_{\shortparallel}) = (c/n)\sqrt{(N\pi/L)^2 + k_{\shortparallel}^2}$, where c is the speed of light, n is the cavity refractive index, N is the cavity mode index, L is the distance between the mirrors, and $k_{\shortparallel}$ is the in-plane wavevector. The quadratic dependence on $k_{\shortparallel}$ when $k_{\shortparallel} \to 0$ corresponds to a photonic effective mass $m_{\mathrm{c}} = \pi\hbar N n/Lc$. The exciton dispersion, much weaker than the photonic one, can thus be approximated by a constant $\omega_{\mathrm{x}}(k_{\shortparallel}) = \omega_{\mathrm{x}}$.

Strong coupling has been successfully achieved in several media, such as that of semiconductors (Reithmaier *et al.*, 2004), high quality-factor cavities (Benyoucef *et al.*, 2011) and ultracold atoms (Hattermann *et al.*, 2017). The energy of the exciton and photons under the strong coupling regime presents two new dispersion relations, one for the upper (high energy) polariton and another for the lower (low energy) polariton branches. The Rabi splitting Ω_{R}, which quantifies the strong coupling between the two, depends on the product of the amplitude of the cavity photon electric field and the electric dipole of the quantum well exciton transition. Its energy is on the order of ≈ 10 meV (Keeling *et al.*, 2007), and its requirement is to be larger than the other energy scales such as temperature, binding energy and interactions. The resulting two branches read:

$$E_{\mathrm{k}}^{\mathrm{LP,UP}} = \frac{1}{2}\left[\left(\delta + \frac{k_{\shortparallel}^2}{2m_{\mathrm{x}}} + \frac{k_{\shortparallel}^2}{2m_{\mathrm{c}}}\right) \mp \sqrt{\delta + \frac{k_{\shortparallel}^2}{2m_{\mathrm{x}}} - \frac{k_{\shortparallel}^2}{2m_{\mathrm{c}}} + \Omega_{\mathrm{R}}^2}\right], \tag{1.5}$$

where $\delta = \hbar\omega_0 - \epsilon_0$ is the detuning between the bottom of the photon and exciton bands. A sketch of the system and exciton-polariton dispersion relation is shown in Fig. 1.1.

Polariton condensation presents few distinct characteristics. First, due to the presence of driving and dissipation, polaritons are classified as non-conservative systems. The requirement of a pump which continuously replenishes carriers (with coherent or inco-

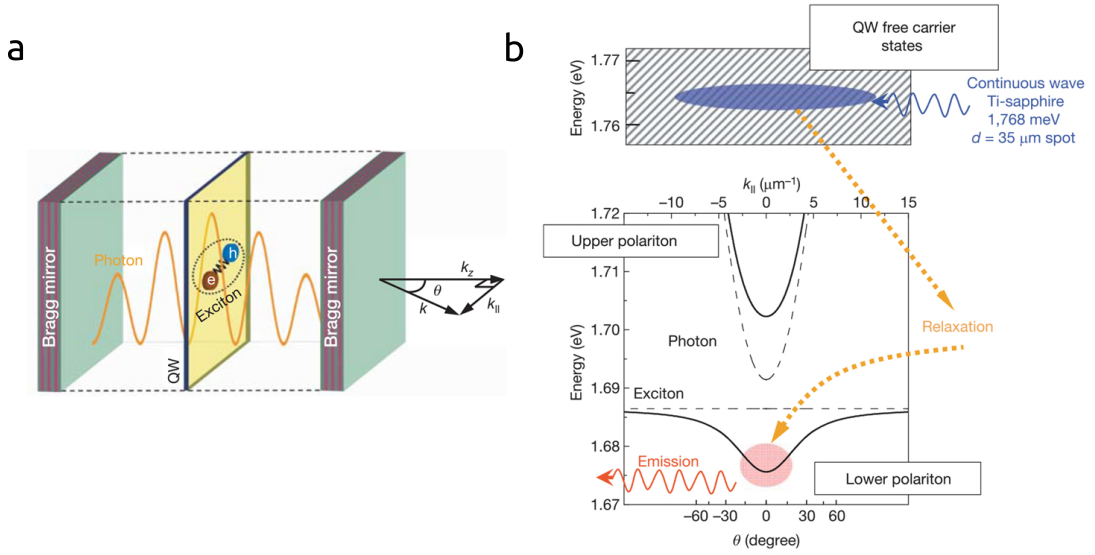

Figure 1.1: **Microcavity system and energy dispersion.** (a) Simplified representation of an optical microcavity where a planar quantum well (QW) is embedded in between of two Bragg mirrors. An incident laser shed at an angle θ excites a microcavity mode with a wavevector $k_{\parallel}$, while the wavevector in the z direction is quantised. The QW exciton with frequency ω_X, is confined and free to move in a $2d$ geometry. When the cavity mode is tuned to be in resonance with the exciton frequency, strong coupling takes place. From the emitted light, information about the dispersion relation, shown in (b), can be extracted. In a typical experimental setup, high-energy QW excitons relax down to the minimum of the dispersion relations, an effect of the strong light-matter coupling. Detailed explanation of such a relaxation process is given in Sec. 2.2.4. Both figures are adapted from (Kasprzak *et al.*, 2006).

herent nature, depending on the pumping mechanism selected) is due to the presence of cavity losses, which induce decoherence through emission. The study of the extent of nonequilibrium features on BEC and superfluidity has become an important subject, still debated nowadays (Carusotto and Ciuti, 2013; Sieberer *et al.*, 2016a; Proukakis *et al.*, 2017). Secondly, polaritons live in an almost pure planar geometry: this property makes the polariton system a perfect laboratory for studies of $2d$ nonequilibrium physics.

Similarly to polariton BEC, laser devices emit coherent light. Both mechanisms are also implemented in a medium where photons and electronic transitions play a major role (Snoke, 2012). It is not surprising that for a long time the scientific community argued whether the coherence measured outside the cavity was actually either of spontaneous nature or due to lasing processes (Byrnes *et al.*, 2014). The critical difference lies in the presence of the particle interaction and in the equilibrium nature of the system. More precisely, as discussed at the beginning of this section, polariton BEC is favoured when light-matter coupling is strong. This is essential to enhance a process called stimu-

lated scattering (eventually leading to condensation), which would not exist without the presence of interactions. Moreover, spontaneous coherence has been measured in both equilibrium (Kasprzak *et al.*, 2006) and nonequilibrium (Sun *et al.*, 2017) configurations. On the other hand, the process of lasing occurs within a weakly interacting environment of light and matter, due to the intense activity of emission and absorption processes. Also, lasing cannot exist in thermal equilibrium, as the medium needs to be highly excited in order to favour the inversion process.

Intense research activity focussed on addressing whether a coherent steady state in a dissipative system is achievable, and to investigate the theoretical differences between a nonequilibrium coherent steady state, an equilibrium BEC and a laser. A field-theoretical approach, based on the laser Hamiltonian (Haken, 1970), has been studied in (Eastham and Littlewood, 2000; Keeling *et al.*, 2004; Szymańska *et al.*, 2006). Differences with lasing have been examined by (Haken, 1970). A clear distinction between laser and nonequilibrium condensation processes is summarised in (Szymańska *et al.*, 2006). Simultaneously, similar results have been theoretically achieved with different approaches (Wouters and Carusotto, 2007a,b) and experimental setups (Porras *et al.*, 2002).

Historically, the investigation of coherence phenomena of microcavity polaritons has deep roots in the strong interest by the scientific community to achieve Bose-Einstein condensation of excitons. The partial "failure" (see Sec. 1.1 for a historical review) of such a phenomenon cleared the way for the investigation of lighter particles, namely polaritons. The very first observation of temporal and spatial long-range coherence in a microcavity occurs by means of a particular configuration for the coherent pump shone in the cavity, namely the Optical Parametric Oscillator (OPO) regime (Baumberg *et al.*, 2000; Stevenson *et al.*, 2000). It consists in a coherent beam tuned to a specific wavevector $\mathbf{k}_p$, close to the bottleneck region of the lower polariton branch. The repeated injection of carriers enhance the collisions between polaritons which are eventually scattered into two other modes, the signal $\mathbf{k}_s$ and the idler $\mathbf{k}_i$. The fixed pump wavevector is chosen such that the process occurs with conservation of energy and momentum. The nonlinearity of the medium $\chi^{(3)}$, resulting from the interaction between polaritons, mediates the scattering process of polaritons in the two modes. We refer to Ch. 2 for further discussion of the condensation mechanism under parametric pumping.

This experiment showed that, for a value of the pumping higher than a specific threshold, a parametric oscillation process would eventually macroscopically populate the lowest modes of the polariton branch (signal) and a second mode (idler), accordingly

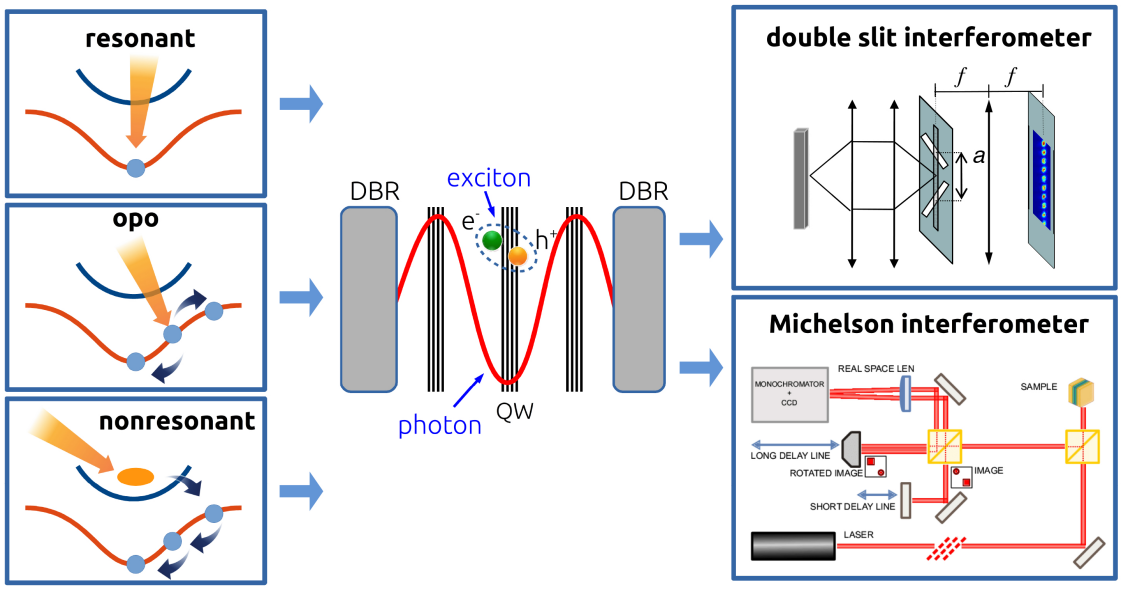

Figure 1.2: **Typical experimental setup.** The strong coupling between light and matter in a quantum microcavity can be reproduced in several ways. A first method consists of shining a laser in resonance of the minimum of the dispersion relation (top left). Although the flexible procedure produces clean measurements, the coherence is trivial since inherited directly from the pump properties. A second approach consist in parametrically pumping in the vicinity of the bottleneck region (middle left), resulting in spontaneous coherence. However, in this case the condensate is very sensitive to the laser parameters. A third approach consists of pumping incoherently high-energy excitons which eventually relax down and condense in the system ground state (bottom left). The double slit interferometer (top right) is able to measure the spatial coherence properties of the condensate. The interference fringes measured by the spectrometer with a lens of focal length f is the result of the phase shift introduced by splitting the coherent signal in two paths. Alternatively, the Michelson interferometer (bottom right) produces interference pattern by splitting the light beam so that one beam strikes a fixed mirror and the other a movable mirror. Figures adapted from (Wertz *et al.*, 2010) and (Caputo *et al.*, 2017), respectively.

to a spontaneous break of the $U(1)$ symmetry. The final emission exhibits coherence due to this phase transition rather than due to the coherent properties of the pump. Such a phase transition within the OPO mechanism has been theoretically described in 2005 by (Carusotto and Ciuti, 2005), with earlier works on the theory of the polariton amplifier process conducted by (Ciuti *et al.*, 2000) and (Whittaker, 2001).

In order to achieve condensation of polaritons under an incoherent pump, scientists had to wait until 2006, when (Kasprzak *et al.*, 2006) observed *"massive occupation of the ground state developing from a polariton gas at thermal equilibrium at* 19*K, an increase of temporal coherence, and the build-up of long-range spatial coherence and linear polarisation, all of which indicate the spontaneous onset of a macroscopic quantum phase"*. Previous experimental studies attempted to reach the same outcome, even if they could not achieve full thermalisation. They did however provide encouraging preliminary results as described by (Dang *et al.*,

1998) and (Richard *et al.*, 2005). In Fig. 1.2 we show a typical experimental setup employed for probing coherence properties of a polariton condensate.

The incoherent pumping process differs fundamentally from the coherent one: firstly, it is not very sensitive to laser parameters, as occurs for the OPO scheme; more importantly, the polariton cloud does not inherit any coherence properties from the incident beam, which is of course essential in order to study the spontaneous formation of coherence. On the other hand, the nature of the incoherent pumping relaxation process, through which any coherence features are gradually lost, is so complex, that a precise description is still missing. A tentative investigation on the microscopic features of such a mechanism has been performed by (Porras *et al.*, 2002), and a study accounting for coupling to multiple baths describing pumping and decay has been proposed in (Szymańska *et al.*, 2006). A phenomenological model consisting of two coupled equations, one for the reservoir and one for the lower-polariton branch, has been developed for the first time in (Wouters and Carusotto, 2007b). A model solely for the lower polariton branch has been considered in (Keeling and Berloff, 2008). To account for stronger scattering into the condensate, a frequency dependent amplification term has been subsequently included as in (Wouters and Carusotto, 2010). Thermal and quantum fluctuations have been introduced by models based on the Truncated Wigner Approximation (TWA) as in (Wouters and Savona, 2009) or via a Keldysh diagram approach (Szymańska *et al.*, 2006). We refer to section 2.2.2 and 2.3 for a more detailed analysis of the models mentioned above.

Spatial condensation has also been observed in a trap by (Balili *et al.*, 2007), for which similarities can be drawn with harmonically trapped atomic condensates. Coherence phenomena such as spectral and spatial narrowing and spontaneous linear polarisation of the light emission are measured by means of the drifting of polaritons, initially created 50 μm away from the potential minimum, into the trap. The vast majority of the preliminary research has been historically conducted in semiconductor cavities; however BEC of polaritons has been demonstrated to be achievable in organic materials as well. The first realisation under a nonresonant pumping has been done by (Kéna-Cohen and Forrest, 2010), with subsequent studies by (Daskalakis *et al.*, 2014) and (Lerario *et al.*, 2017).

Since the first approaches to the study of BEC of polaritons, scientists realised that the first concrete experimental challenge consisted in the understanding of the important rule of the driving and dissipation of the system. The nonequilibrium nature is directly linked to the presence of a continuous leakage of particles from the system. A “nonequilibrium" steady state is thus measurable only if the pump overcome the system losses. For describing a “nonequilibrium" systems, usual equilibrium thermodynamic approaches fails, and

new techniques are required. The emerging question then was: is polariton condensation *intrinsically* a nonequilibrium effect? The essence of the problem lies in the competition between the lifetime, τ_{pol}, of the unstable polariton quasiparticle and the thermalisation time, τ_{therm}.

The polariton lifetime (τ_{pol}) is usually proportional to the inverse of the Q factor of the cavity mode, which quantifies the goodness of the reflectivity properties of the cavity. Thermalisation times, instead, depend on the nature of the quasiparticle. Many theoretical works also debate about the "nonequilibrium" nature of polariton condensation such as (Byrnes *et al.*, 2014) and (Sanvitto and Kéna-Cohen, 2016). Theoretically, a quantitative criterion for assessing the equilibrium nature of a specific condensation process is presented in (Chiocchetta *et al.*, 2017), based on the study of the behaviour of the fluctuation-dissipation theorem in different models.

From the experimental point of view, early realisations of polariton BEC exhibit a "partial" (Deng *et al.*, 2006; Kasprzak *et al.*, 2006) rather than "full" thermalisation. In the early experimental observations of coherence from the cavity, polariton lifetimes are of the order of ps: for instance $\tau_{\text{pol}} = 2 - 4$ps in (Roumpos *et al.*, 2012) and $\tau_{\text{pol}} = 30$ps for better quality cavity (Wertz *et al.*, 2010), and Q factors are of the order of $Q_{\text{cav}} \approx 3000$ (Nitsche *et al.*, 2014). Thermalisation times, meaning the typical times needed by the system to reach a steady state configuration, depends on the nature of the quasiparticle; $\tau_{\text{therm}} \approx 40$ps: for exciton-like massive particles as in (Deng *et al.*, 2006), and can be even longer for lighter more weakly-interacting particles. Nowadays new technology has been able to improve the numbers above, by means of new cavities characterised by higher quality factors ($Q \approx 100000$) thus leading to much longer lifetimes ($\tau_{\text{pol}} \approx 100ps$), (Sun *et al.*, 2017), (Ballarini *et al.*, 2017) and (Caputo *et al.*, 2017).

1.2 Condensation, superfluidity and phase coherence for an equilibrium system

Stimulated by the experimental observation of macroscopic population of the ground state in ultracold dilute atomic gases (Anderson *et al.*, 1995; Davis *et al.*, 1995), intense effort has been made by the scientific community to understand the subtle details underlying this phenomena. In this section, the main differences between condensation, superfluidity and phase coherence for an equilibrium Bose gas are briefly reviewed.

For a $3d$ dilute and ultracold atomic gas in thermal equilibrium, Bose Einstein conden-

sation is a second order phase transition whose phase diagram describes the transformation from a (disordered) non-condensed phase to an (ordered) condensed phase. In the case of an equilibrium system, as reported in textbooks (Pitaevskii and Stringari, 2003), the appearance of BEC in the ordered phase is associated with the onset of off-diagonal long-range order (ODLRO). It is defined by means of specific conditions for the one-body density matrix, namely

$$\langle \psi^\dagger(\mathbf{r})\psi(\mathbf{r}')\rangle \neq 0 \quad , \quad |\mathbf{r}-\mathbf{r}'| \to \infty, \tag{1.6}$$

for the condensate wavefunction ψ at a position $\mathbf{r}$. Physically, this means that the condensate phase is correlated at large distances, and the first order correlation function, Eq. (1.6), decay to a non-zero value. Information about density coherence is instead given by the second-order correlation function, see (Pitaevskii and Stringari, 2003).

Emergence of ODLRO also corresponds to a spontaneous breaking of the $U(1)$ symmetry of the system Hamiltonian, consisting in an arbitrary but fixed choice for the value of the condensate phase. Experimentally, it is possible to access information on the phase through interferometric measurements.

Three-dimensional ($3d$) systems also exhibit superfluid phenomena. Early observations of superfluid properties in liquid Helium verified that, below a certain critical temperature, the fluid was flowed without viscosity. Even though the flowing of a condensate takes place without losing energy, the presence of excitations can potentially give rise to energy dissipation. This behaviour is easily described by Landau's "criterion of superfluidity" (Landau, 1941), which specifies the maximum velocity that an obstacle immersed in the fluid can travel without establishing dissipation. The picture is relatively simple: an impurity plunged into a fluid might create an excitation of energy $\hbar\omega(\mathbf{k})$ and momentum $\hbar\mathbf{k}$. In order to describe this excitation, we consider the Bogoliubov equations for small excitations around the stationary state. If the impurity velocity v is lower than a critical velocity v_c, defined in terms if the Bogoliubov dispersion as

$$v_c = \min_k \left[\frac{\omega(\mathbf{k})}{k}\right], \tag{1.7}$$

with $k = |\mathbf{k}|$, no excitations can be generated by the object, because it would violate energy and momentum conservation. The result is indeed surprising: if $v < v_c$, the object moves within the fluid without dissipating, i.e. no energy exchange, behaving like a superfluid. On the other hand, for speeds $v > v_c$, excitations are created and the fluid behaves normally.

In the previous section we mentioned that BEC is forbidden for uniform large $2d$ systems. This is consistent with the Mermin-Wagner-Hohenberg theorem, which es-

sentially asserts that in lower dimensions, Bose-Einstein condensation is destroyed by long-wavelength (small momentum) excitations. Nevertheless, this prediction is strictly valid in the thermodynamic limit, when the number of particles N and volume V diverge while the ratio N/V is kept constant. Below the critical point, however, an equilibrium uniform $2d$ gas at non-zero temperature is still able to exhibit a "quasi-ordered" state, which is superfluid and characterised by a power-law decay of the first order correlation function

$$\langle \psi^\dagger(\mathbf{r})\psi(\mathbf{r}')\rangle = |\mathbf{r}-\mathbf{r}'|^{-\alpha}, \qquad \alpha = \frac{1}{n_\mathrm{s}\lambda_\mathrm{dB}^2}, \tag{1.8}$$

where λ_dB is the thermal de Broglie length and n_s is the superfluid density, which eventually vanishes algebraically at large distances. This particular form of the spatial coherence bears the name of *quasi-long-range order*. In Sec. 4.1, we will discuss in more detail the Berezinskii-Kosterlitz-Thouless (BKT) theory, which describes the transition, across a critical temperature T_BKT, from a $2d$ normal state populated of free vortices to a superfluid one, where vortices are bound in pairs. The exponent α is found to be smaller than or equal to $1/4$ in the superfluid state (Hadzibabic and Dalibard, 2011), as predicted by simple calculations for superfluid density n_s at the transition temperature T_BKT (Nelson and Kosterlitz, 1977). Thus superfluidity in a finite system are not exactly equivalent to BEC.

We have seen that the dimensionality of the system is crucial for characterizing condensation, coherence and superfluid properties. However, the geometry and the interaction nature of a system can actually also be used as a "knob" for studying the emergence of condensation. In fact, a finite-size $2d$ ideal gas confined in a trap undergoes condensation even at non-zero temperatures, with a threshold similar to the one of a three-dimensional Bose gas in a confinement of the same type (Holzmann *et al.*, 2007) and (Berman *et al.*, 2008). We can thus refer to equilibrium BEC in $2d$ and $3d$ finite trapped systems using the same formulation.

1.3 Nonequilibrium phenomena

In the previous sections we introduced the general concepts of ODLRO, superfluidity and phase coherence. The focus of this section, and partially of this thesis, is to study the application to driven-dissipative condensates, and the differences with their equilibrium counterparts.

The first clear difference between equilibrium and driven-dissipative condensates

manifests in the Bogoliubov excitation spectrum. On the one hand, it is well-known that the Bogoliubov excitation spectrum of an equilibrium condensate, obtained by the GPE equation, presents a sonic (free-particle) behaviour at low (high) momentum (Pitaevskii and Stringari, 2003). On the other hand, solutions for the driven-dissipative GPE within the coherent pumping mechanism (Carusotto and Ciuti, 2013) show a completely different scenario, due to the presence of dumping of long wavelengths, i.e. diffusive behaviour at low momenta. It originates from the presence of a non-zero branch of the imaginary part of the Bogoliubov excitations spectrum. We refer to Sec. 2.2.5 for further discussion of this phenomenon.

1.3.1 Quantum fluids of light

After the first observation of polariton BEC (reviewed in section 1.1.1), and the consequent investigation of its condensation features, the interest of the scientific community moved to the study of superfluidity in driven-dissipative systems. As discussed in the previous section, superfluidity in an equilibrium system can be defined by means of Landau's criterion. In the case of polariton systems, their intrinsic driven-dissipative nature complicates the problem. At first glance, a naive application of the Landau criterion to the excitation spectrum of driven-dissipative condensates, would suggest that the diffusive behaviour at low momenta would not allow the presence of a superfluid part. This is because the critical velocity for a diffusive fluid is set to $v_s = 0$, preventing the establishment of superfluidity.

However, absence of superfluidity in nonequilibrium condensates is inconsistent with observations of almost perfect superfluid-like phenomena under coherent pumping (Amo *et al.*, 2009a). In this specific case, a superfluid pocket of polaritons is seen to reverts back to its original shape after hitting an obstacle. A study by (Wouters and Carusotto, 2010) on superfluid phenomena in incoherently-pumped driven-dissipative condensate has been subsequently proposed to solve this apparent contradiction. It involves the direct measurement of the drag force F_{drag} experienced by the object as a function of the defect velocity v. Let us consider the static drag force on the $2d$ defect, which is given by

$$F_{\text{drag}} \propto \int d^2\mathbf{r}\, |\psi(\mathbf{r})|^2 \nabla V_{\text{def}}(\mathbf{r}), \tag{1.9}$$

with $V_{\text{def}}(\mathbf{r})$ the defect potential, also used for calculations of the motion of a heavy impurity through a Bose-Einstein condensate (Astrakharchik and Pitaevskii, 2004). While equilibrium models, able to describe a perfect superfluid, would predict $F_{\text{drag}} = 0$ for $v < v_c$, nonequilibrium counterparts estimates a non-vanishing value of F_{drag} at

all v, directly connected to the diffusive features exhibited at low momenta and the (apparent) absence of superfluidity. However, in this case a crossover for F_{drag}, with a clear threshold at $v = v_c$ still exists, suggesting the existence of an (imperfect but measurable) superfluid phase. The weaker the cavity losses, the sharper the threshold. Up to now, experimentalists have measured many examples of superfluid-like behaviours in polariton systems (Amo *et al.*, 2009a,b), but a precise measurement of superfluid density has not been achieved.

1.3.2 Phase transitions in driven-dissipative condensates

After the achievement of condensation and the study of the onset of a nonequilibrium steady state and polariton superfluid properties, the interest of the scientific community has shifted to the investigation of the properties of the polariton phase transition.

There are several theoretical papers which tentatively approach the characterisation of the nonequilibrium BKT phase transition. A suitable tool able to address phase coherence, is the first order correlation function, as discussed in Section 1.2. The long-distance decay of the spatial correlations is in fact the best approach to address the steady state properties, whether characterised by either ODLRO or superfluidity. A first study, by means of the Bogoliubov theory, has been conducted by (Chiocchetta and Carusotto, 2013), which found that in $2d$ the correlation function at long distances exhibits algebraic order.

Altman *et al.* discussed further the possibilities of equilibrium coherence in driven-dissipative systems. By mapping the polariton phenomenological models into a more general nonlinear stochastic partial differential equation for the phase of the order parameter (which is nonlinear in the phase), they concluded that geometrical isotropy plays a crucial role in the behaviour of correlations at large distances (Altman *et al.*, 2015). In simple terms, for isotropic systems, algebraic order survives only below a definite length-scale, after which a faster stretched-exponential decay of correlations appears. On the other side, algebraic order is still a feature for systems with strong anisotropic geometries (Altman *et al.*, 2015). Deviation from standard scaling have been also encountered in $1d$ driven-dissipative quantum systems (Gladilin *et al.*, 2014).

Explicit numerical studies of the nonequilibrium phase transition have been reported by (Dagvadorj *et al.*, 2015), in the case of a parametrically driven polariton condensate. By studying the behaviour of topological defects and correlation functions in the vicinity of the threshold, they could confirm another peculiarity of the nonequilibrium BKT transition, namely the possibility of the exponent α to exceed the "equilibrium" limit of 1/4. This feature had previously been recorded experimentally in (Roumpos *et al.*,

2012). Recent numerical and experimental studies (Nitsche *et al.*, 2014; Caputo *et al.*, 2017) suggest that equilibrium BKT can be achieved in driven-dissipative condensates. We give a detailed theoretical and numerical analysis of the BKT phase transition for an incoherently-pumped polariton condensate in Ch. 4 of this thesis.

1.3.3 Quench dynamics across the phase transition

While the steady state properties of polariton BECs have been extensively investigated analytically, numerically and experimentally (Carusotto and Ciuti, 2013), a lot is still unknown about the out of equilibrium dynamics of a driven-dissipative system after a quench across the transition. In many physical fields, from liquid crystals and ferromagnets, to the cosmos, there is a large interest in the behaviour of the macroscopic characteristic quantities of the system when approaching the transition threshold. Characterisation of such critical behaviour, in fact, allows one to categorise systems of very different nature in classes with same universal behaviour (Domb, 2000).

The theory of critical phenomena predicts that for a continuous phase transition, macroscopic quantities show universal features in the vicinity of a critical point (Zinn-Justin, 2002). This scaling behaviour is characterised by well-defined critical exponents, which depend only on few general properties of the system, such as dimensionality, symmetry of the order parameter and range of interactions. Universality classes distinguish phase transitions according to the critical exponents exhibited by the physical system analysed.

A BEC is a phase transition of the second order in $3d$ (Pitaevskii and Stringari, 2003) and of infinite order in $2d$ (Hadzibabic and Dalibard, 2011). The scaling of both correlations and relaxation time are determined by a set of critical exponents, which are independent of the microscopic configurations of the system. As an example, we can take a $3d$ homogeneous interacting Bose gas: when the order parameter is approaching the critical point, static and dynamical quantities diverge with the same set of exponents as those of the classical $3d$ XY model, which describes magnetic systems with planar spin Hamiltonians (Gottlob and Hasenbusch, 1993).

Specifically, the XY model admit the existence of topological defects, vortices, and a clear separation in near and far zones for a system of vortex lines such as in ^{4}He (Kleinert, 1989). Peculiarly interesting is the $2d$ XY model, which shows a particular phase transition, the so called Kosterlitz Thouless (KT) transition. This has been observed experimentally in liquid crystals, films of superconductors, thin films of liquid helium. Indeed, above a certain critical temperature it admits the existence of a superfluid fraction, where vortices

are bound in vortex anti-vortex pairs. The same model also describes the superfluid phase transition in ^{3}He.

Generally, critical exponents can be extracted for each physical quantity which is diverging at the critical point (Huang, 2000). However, the most commonly-encountered critical exponents are the ones which describe the static and dynamical universal properties of a system. The *static exponent* ν describes the temperature variation of the characteristic length L. The *dynamical exponent* z describes the growth of the equilibration time τ of the system, or the growth of the characteristic length L in time.

By quenching infinitely rapidly across the critical region, physicists have been able to study the late time dynamics of the ordered structure of the system, prior to reaching a specific steady state. This process is named *phase ordering*. Such a process is based on the *scaling hypothesis*, which consists of the ability of the ordered structures in the system to exhibit universal (dynamical) scaling relations. From this scaling, a dynamical exponent z can be measured (Bray, 2002). A detailed study of such physics for driven-dissipative system is given in Ch. 5 of this thesis.

Equilibrium theory of criticality is particularly useful for the investigation of corresponding universal dynamical phenomena, characterising the nonequilibrium dynamics of the transition across the critical point. The Kibble-Zurek Mechanism (KZM) states that for a second-order phase transition, the distribution of defects in the broken symmetry phase is set by the average size of domains at the time the system departs from equilibrium, which obeys a power-law in the quench rate (del Campo and Zurek, 2014). Historically, this model has been proposed for the description of early stages of the universe by Kibble (Kibble, 1976) and later applied to the superfluid phase transition in condensed matter physics by Zurek (Zurek, 1985).

The investigation of criticality, phase ordering and the KZM in polariton condensates are of great interest to the polariton scientific community. Preliminary work for phase ordering kinetic has been presented by (Kulczykowski and Matuszewski, 2017) but many open questions remain. Regarding the study of KZM, preliminary results have been proposed by (Liew *et al.*, 2015) for 2d systems and (Matuszewski and Witkowska, 2014a) for 1d systems. However, an exhaustive and complete picture concerning this mechanism under different pumping mechanisms is still missing. The detailed study of both these issues forms the main part of this thesis.

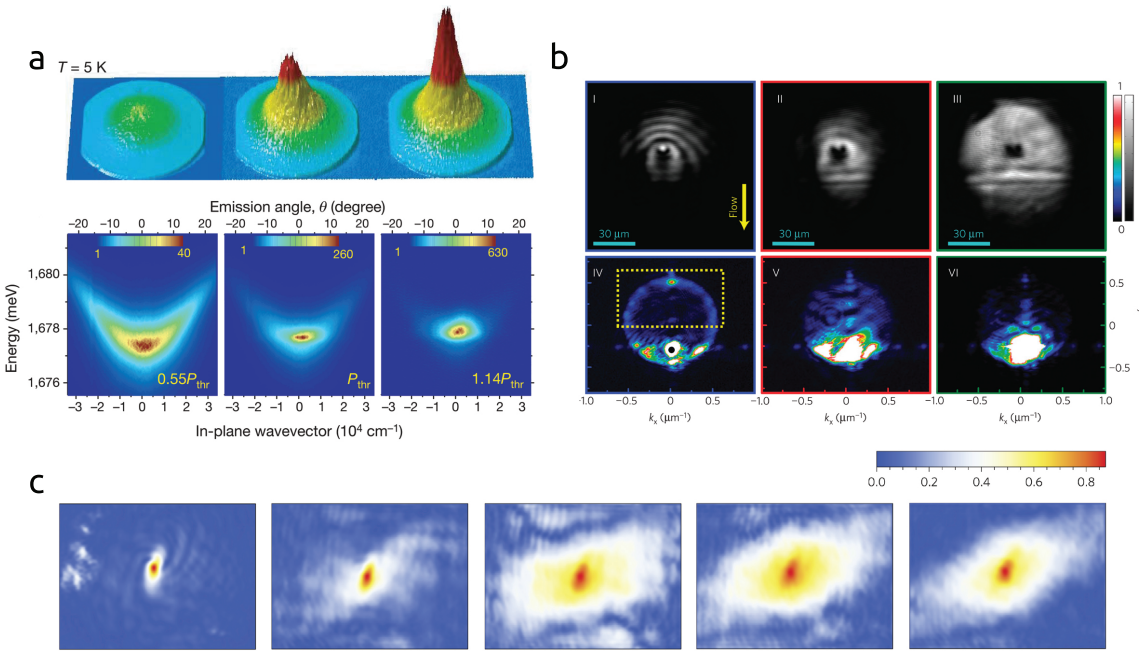

Figure 1.3: **Key experimental results.** (a) Experimental observation of polariton Bose-Einstein condensation obtained by increasing the intensity of the incoherent pumping mechanism. Adapted from (Kasprzak *et al.*, 2006). (b) Experimental images of the real-space (top row) and momentum-space (bottom row) space polariton density for increasing values of the pump (left to right). Superfluidity is verified as the fringes (Rayleigh scattering ring) disappear (appears) from the real (momentum) space figures. Adapted from (Amo *et al.*, 2009a). (c) $2d$ spatial coherence corresponding to increasing densities of the polariton field (from left to right). Adapted from (Caputo *et al.*, 2017).

1.4 Experimental studies with polariton condensates.

The first experimental evidence of superfluid features under the OPO mechanism in fluids of light has been provided by (Amo *et al.*, 2009a), where a polariton spot has been observed to pass through a defect. A Čerenkov-like wake pattern has been observed by (Amo *et al.*, 2009b) when the flow velocity exceeds the speed of sound. Bogoliubov-like phonon excitations have been measured in incoherently-pumped trapped polariton condensates (Utsunomiya *et al.*, 2008). Hydrodynamic excitations such as solitons have been observed by (Amo *et al.*, 2011). Quantised vortices have been measured in (Lagoudakis *et al.*, 2008) and (Sanvitto *et al.*, 2010a), whereas bound vortex-antivortex pairs have been clearly observed by (Roumpos *et al.*, 2010).

Experiments on incoherently-pumped polariton condensates carried by Yamamoto's group (Nitsche *et al.*, 2014) have on the one hand measured algebraic decay of correlations, which correspond to a signature of a steady state showing BKT physics, but simultane-

ously they found such algebraic decay to be characterised by values of the power-law exponent $\alpha > 1/4$ (Roumpos *et al.*, 2012). Correlations have been extracted by interferometric measurement of fringes, by means of a Michelson interferometer [Fig. 1.2 (bottom right)]. The concept of equilibrium versus nonequilibrium BKT transition is discussed in (Caputo *et al.*, 2017). Here the driven-dissipative nature of the system has been linked to the relation between spatial and temporal correlation exponents. In Section 1.3.2 we introduced how quasi-long range order is forbidden at large scales, under isotropic confinement.

The success of the measurement of a "pure" power-low decay of correlation functions in the superfluid phase for the experiments discussed above, is mainly due to two aspects. First, the experimental setup always introduces a degree of anisotropy: in (Roumpos *et al.*, 2012) it was caused by the interplay between polarisation pinning to the crystal structure, and the splitting of the two transverse electric and magnetic cavity modes (Keeling *et al.*, 2017). Secondly, in the case of weak (or even no) anisotropy, quasi long-range order is forbidden after a characteristic lengthscale introduced in (Altman *et al.*, 2015), but which results in an "astronomical" system size compared to any reasonable system size, accessible either experimentally or computationally. Nevertheless, as previously mentioned, experimental observation of quasi-long-range order in driven-dissipative condensates has shown that at the critical point, the system is able to exhibit a power-law decay with the exponent exceeding the equilibrium limit of 1/4.

Below we give a general outlook of the thesis and a brief explanation of the chapters.

1.5 Thesis overview and collaborations

This thesis is divided in two parts.

- Part I gives an introduction to the physical system, the model we use to simulate the physics of phase transitions and quench dynamics and a numerical analysis and discussion of the main tools used.
- Part II gives explicit physical results which provide insight into the equilibrium and dynamical properties of polariton condensates.

Part I - Introduction, theoretical and numerical analysis

Chapter 2 describes the theoretical tools and mean-field methodology that allows us to accurately model a polariton condensate. We describe the Gross-Pitaevskii equation

(GPE), steady state and Bogoliubov theory for equilibrium systems at zero temperature. Subsequently, we focus on the mean-field approach of nonequilibrium systems, explaining the different pumping mechanisms. We highlight the differences between the physical outcomes of equilibrium and nonequilibrium models. We discuss details of the incoherently-pumped polariton model which includes quantum and thermal fluctuations.

Chapter 3 describes the implementation of various numerical procedures we use to generate the simulations and results presented. We show a typical dynamical growth of the system, a numerical analysis of the model and discuss our parameter choice for the main results obtained in Part II.

Part II - Steady state and quench dynamics of a driven-dissipative polariton condensate

Part II includes a selection of the numerical simulations we have performed, and the arising interpretations of the results for phase transition and quench dynamics of polariton condensates, which form the novel aspect of this work.

Chapter 4 extends recent studies on the BKT phase transition of a nonequilibrium condensate and discusses the main differences of its equilibrium counterpart. We undertake a detailed numerical study of the steady state properties of an incoherently-pumped exciton polariton condensate, and demonstrate the crossover from the disordered to the ordered phase by means of spatial correlations and topological defects. We investigate the nature of the phase transition, focussing on the behaviour of the system in the vicinity of the critical region.

In Ch. 5 we describe numerical studies of the critical dynamics of driven-dissipative condensates under different pumping mechanisms. By instantaneously quenching the system across the nonequilibrium BKT transition, we investigate the dynamical scaling of defects and the characteristic length of the system at late times. The dynamical critical exponents extracted from the growth of long-range order reveal that universal critical properties of driven-dissipative polariton systems are consistent with those expected for the equilibrium BKT transition, being consistent with prediction of the $2d$ XY model.

In Ch. 6 we investigate critical behaviour of nonequilibrium systems in the vicinity of the phase transition. We discuss preliminary results on the critical slowing down of the equilibrium correlation length and relaxation time. The numerical results extracted are then employed in the study of finite-duration quench dynamics across the critical region. We undertake a detailed study on the scaling of the freeze-out time as a function of the quench duration.

This thesis includes studies and results which have been developed through the scientific support of external collaborators. We highlight the role of the collaborators into subsequent chapters. The results of Ch. 5 are presented in a work accepted for publication to Phys. Rev. Lett., written in collaboration with Galbadrakh Dagvadorj (Department of Physics and Astronomy, University College London, United Kingdom), Alex Zamora (Department of Physics and Astronomy, University College London, United Kingdom), Marzena Szymańska (Department of Physics and Astronomy, University College London, United Kingdom), Iacopo Carusotto (INO-CNR BEC Center and Universitá di Trento, Italy) and my supervisor within the School of Mathematics, Statistics and Physics at Newcastle University, Nick Proukakis. In particular, all numerical results in that chapter concerning the OPO mechanism has been conducted by Galbadrakh Dagvadorj and Alex Zamora, under the supervision of Marzena Szymańska.

Part of this thesis is presented in the following publications:

- *Dynamical critical exponents in driven-dissipative quantum systems*

  P. Comaron, G. Dagvadorj, A. Zamora, I. Carusotto, N. P. Proukakis and M. H. Szymańska

  arXiv:1708.09199 (2017)

  accepted for publication in Physics Review Letters

- *Quench dynamics in driven-dissipative quantum systems*

  A. Zamora, G. Dagvadorj, P. Comaron, N. P. Proukakis, M. H. Szymanska and I. Carusotto

  in preparation

Chapter 2

Theoretical background

For the study of critical phenomena and phase transitions, fluctuations are a key ingredient for determining the physical properties of a specific state. Statistical models which are generalisations of mean-field equations which include phase and density fluctuations, are suitable tools for the study of the physics around the critical region. In this chapter we discuss the theoretical concepts and methods concerning the modelling of equilibrium and nonequilibrium condensates, and thus motivate the use of the numerical methods subsequently implemented in part II of this thesis.

2.1 Modelling of equilibrium condensates

2.1.1 The Gross-Pitaevskii equation (GPE)

Firstly, we revisit the formalism leading to the theoretical description of many-body quantum systems at equilibrium. The Hamiltonian for a many-body system of ultracold and dilute Bose particles, written in the occupation number representation, reads (Proukakis and Jackson, 2008)

$$\hat{H} = \int d\mathbf{r}\hat{\Psi}^\dagger(\mathbf{r},t)\hat{h}_0(\mathbf{r})\hat{\Psi}^\dagger(\mathbf{r},t) + \frac{1}{2}\iint d\mathbf{r}d\mathbf{r}'\ \hat{\Psi}^\dagger(\mathbf{r},t)\hat{\Psi}^\dagger(\mathbf{r}',t)V_{\text{int}}(\mathbf{r}-\mathbf{r}')\hat{\Psi}(\mathbf{r}',t)\hat{\Psi}(\mathbf{r},t), \tag{2.1}$$

where $\hat{\Psi}^\dagger(\mathbf{r},t)$ $\left(\hat{\Psi}(\mathbf{r},t)\right)$ is a Bose field operator which creates (annihilates) a particle at position $\mathbf{r}$ and time t. The operator for the single particle in a confined environment $V^{\text{ext}}(\mathbf{r},t)$ is defined by $\hat{h}_0(\mathbf{r}) = -\hbar^2\nabla^2/2m + V^{\text{ext}}(\mathbf{r},t)$. In the case of an atomic system at very low temperatures, standard scattering theory states that high energy scattering channels can be discarded and thus the interaction can be modelled by a single parameter, the boson-boson scattering length a_s.

Under the assumption that the gas is in the strongly dilute regime, namely the inter-

atomic distance $\ell = n^{-1/3} \gg a_s$, the interaction two-body potential $V_{\rm int}(\mathbf{r} - \mathbf{r}')$ can be replaced by a contact interaction potential

$$V_{\rm int}(\mathbf{r} - \mathbf{r}') = g_{3d}\delta(\mathbf{r} - \mathbf{r}'), \tag{2.2}$$

where $g_{3d} = 4\pi\hbar^2 a_s/m$ is the effective interaction strength.

The evolution of the system can then be extracted by considering the Heisenberg equation of motion for the Bose field operator, namely

$$i\hbar\frac{\partial\hat{\Psi}(\mathbf{r},t)}{\partial t} = [\hat{\Psi}(\mathbf{r},t), \hat{H}]. \tag{2.3}$$

The commutator can then be expanded by means of the commutation relations

$$\left[\hat{\Psi}(\mathbf{r},t), \hat{\Psi}^\dagger(\mathbf{r}',t)\right] = \delta(\mathbf{r} - \mathbf{r}'), \tag{2.4}$$

$$\left[\hat{\Psi}(\mathbf{r},t), \hat{\Psi}(\mathbf{r}',t)\right] = \left[\hat{\Psi}^\dagger(\mathbf{r},t), \hat{\Psi}^\dagger(\mathbf{r}',t)\right] = 0. \tag{2.5}$$

The resulting equation of motion for the Bose field operator reads:

$$i\hbar\frac{\partial\hat{\Psi}(\mathbf{r},t)}{\partial t} = \hat{h}_0\hat{\Psi}(\mathbf{r},t) + g_{3d}\hat{\Psi}^\dagger(\mathbf{r},t)\hat{\Psi}(\mathbf{r},t)\hat{\Psi}(\mathbf{r},t). \tag{2.6}$$

In general, Bose condensed systems can be described by a condensate (characterised by the macroscopic occupation of the lower energy state) plus a thermal gas of particles which occupies the excited states on top of the condensate. We can thus split the Bose field operator in two parts:

$$\hat{\Psi}(\mathbf{r},t) = \hat{\psi}(\mathbf{r},t) + \hat{\delta}(\mathbf{r},t), \tag{2.7}$$

a condensate component $\hat{\psi}(\mathbf{r},t)$ and a component $\hat{\delta}(\mathbf{r},t)$ describing quantum and thermal fluctuations (Fetter, 1972). A further approximation consists of replacing the condensate field $\hat{\psi}(\mathbf{r},t)$ with a classical mean-field, namely

$$\hat{\psi}(\mathbf{r},t) \to \psi(\mathbf{r},t). \tag{2.8}$$

This is the so-called Bogoliubov replacement (Bogoliubov, 1947), and technically implies fixing the condensate phase, a phenomenon which is directly connected to the symmetry-breaking of the order parameter. In the limit of $T = 0$ then, Eq. (2.6) takes the form of the so-called Gross-Pitaevskii equation (GPE) (Gross, 1957; Ginzburg and Pitaevskii, 1958),

which reads

$$i\hbar\frac{\partial\psi(\mathbf{r},t)}{\partial t}=\left[-\frac{\hbar^2\nabla^2}{2m}+V_{\mathrm{ext}}(\mathbf{r},t)+g_{3\mathrm{d}}|\psi_0(\mathbf{r},t)|^2\right]\psi(\mathbf{r},t), \tag{2.9}$$

and is valid for any dilute weakly-interacting ultracold Bose gas at near-zero temperatures.

2.1.2 Steady state of an equilibrium condensate

A static condensate ψ_0 can be obtained by looking at the stationary solution of Eq. (2.9). By considering the condensate field in the form $\psi(\mathbf{r},t)=\psi_0 e^{-i\mu t/\hbar}$, we obtain the time-independent GPE (Pitaevskii and Stringari, 2003):

$$\left[-\frac{\hbar^2\nabla^2}{2m}+V_{\mathrm{ext}}(\mathbf{r})+g_{3\mathrm{d}}|\psi(\mathbf{r})|^2\right]\psi_0(\mathbf{r})=\mu\psi_0(\mathbf{r}), \tag{2.10}$$

for the lowest eigenvalue μ, which gives the chemical potential of the system. Thermodynamically, μ represents the energetic cost of including (removing) a particle in (from) the condensate. In a trapped system the condensate corresponds to the lowest eigenstate of the confining potential. In free space, when $V_{\mathrm{ext}}=0$, the condensate consists of the $\mathbf{k}=0$ plane wave. In the latter case, the chemical potential reads

$$\mu=g_{3\mathrm{d}}|\psi_0|^2. \tag{2.11}$$

2.1.3 Bogoliubov dispersion of elementary excitations

In order to study the excitations on top of the condensate, one can probe the response of the system to small perturbations (Pitaevskii and Stringari, 2003). The ordinary approach consists of considering the following ansatz for the condensate wavefunction

$$\psi(\mathbf{r},t)=\left[\psi_0(\mathbf{r},t)+\delta\phi(\mathbf{r},t)\right]e^{-i\mu t}, \tag{2.12}$$

where ψ_0 denotes the stationary ground state and fluctuations are considered within the term $\delta\phi(\mathbf{r},t)$. By substituting Eq. (2.12) in the timedependent GPE, Eq. (2.9), and considering the regime of small perturbations, namely $|\delta\phi(\mathbf{r},t)|\ll|\psi_0(\mathbf{r},t)|$, one obtains a linearised equation for the excitations. One can then decompose the excitation field in a sum of different components which oscillate at frequencies ω_{i}, namely

$$\delta\phi(\mathbf{r},t)=\sum_{\mathrm{i}}\left(u_{\mathrm{i}}(\mathbf{r})e^{i\omega_{\mathrm{i}}t}+v_{\mathrm{i}}^*(\mathbf{r})e^{-i\omega_{\mathrm{i}}t}\right), \tag{2.13}$$

with $u_{\mathrm{i}}(\mathbf{r})$ and $v_{\mathrm{i}}(\mathbf{r})^*$ describing complex amplitudes of the i-mode. Inserting this ansatz into the linearised equation leads to two coupled equations:

$$\begin{pmatrix} L(\mathbf{r}) & M(\mathbf{r}) \\ -M^*(\mathbf{r}) & -L^*(\mathbf{r}) \end{pmatrix} \begin{pmatrix} u_\mathrm{i}(\mathbf{r}) \\ v_\mathrm{i}(\mathbf{r}) \end{pmatrix} = \hbar\omega_\mathrm{i} \begin{pmatrix} u_\mathrm{i} \\ v_\mathrm{i} \end{pmatrix}, \tag{2.14}$$

with

$$\hat{L}(\mathbf{r}) = -\frac{\hbar^2\nabla^2}{2m} + V_\mathrm{ext}(\mathbf{r},t) + 2g_\mathrm{3d}|\psi_0(\mathbf{r},t)|^2 - \mu, \tag{2.15}$$

$$\hat{M}(\mathbf{r}) = g_\mathrm{3d}|\psi_0(\mathbf{r},t)|^2. \tag{2.16}$$

For a spatially homogeneous condensate, the solutions of the Bogoliubov equations are plane waves of the form $u(\mathbf{r}) = ue^{i\mathbf{k}\cdot\mathbf{r}}$ and $v(\mathbf{r}) = ve^{i\mathbf{k}\cdot\mathbf{r}}$, and the chemical potential reads . By solving the system of coupled equations, we obtain the zero-temperature Bogoliubov excitation spectrum,

$$\hbar\omega_\mathrm{bog} = \pm\sqrt{\frac{\hbar^2k^2}{2m}\left(\frac{\hbar^2k^2}{2m} + 2\mu\right)}. \tag{2.17}$$

We can distinguish two different regimes: for small $k = |\mathbf{k}|$, the dispersion show a sonic behaviour with $\omega = c_\mathrm{s}k$ and $c_\mathrm{s} = \sqrt{\mu/m}$; at large momenta k the free-particle dispersion prevails. The changeover is set to the excitation momenta $k = 1/\xi$ relative to the system healing length, defined in a uniform system as

$$\xi = \frac{\hbar}{\sqrt{mg_\mathrm{3d}|\psi_0|^2}}. \tag{2.18}$$

2.2 Modelling of nonequilibrium condensates

Spontaneous polariton coherence can be observed under different pumping mechanisms. In the present section we introduce the theoretical models which are commonly employed to simulate the condensate dynamics of the polariton condensate under the mean field approximation.

2.2.1 A dissipative model: the complex Ginzburg-Landau equation

One of the most studied (and used) nonlinear equations for describing a large class of phenomena in spatially-extended systems, such as nonlinear waves, second-order phase transitions, superconductivity, superfluidity and Bose-Einstein condensation, is the complex Ginzburg-Landau equation (cGLE) (van Saarloos and Hohenberg, 1992; Aranson and Kramer, 2002):

$$\frac{\partial\chi}{\partial t} = \epsilon\chi + (1+ib)\nabla^2\chi - (1+ic)|\chi|^2\chi. \tag{2.19}$$

where $\chi = \chi(\mathbf{r}, t)$ is a complex function of space and time, often referred to as the order parameter (in the sense that it is the observable which quantifies order across a phase transition), ϵ, b and c real parameters which describe linear and nonlinear dispersion, respectively.

Moreover, it may also be written as a dissipative extension of the *conservative* nonlinear Schrödinger Equation, which eventually takes the form (Bobrovska and Matuszewski, 2015)

$$i\hbar \frac{\partial \chi}{\partial t} = \left[A - B\nabla^2 + C|\chi|^2 + i(D - E|\chi|^2)\right]\chi. \tag{2.20}$$

in cases where the terms B, C, D and E are positive, Eq. (2.20) admits a stable non-trivial solution of the form $\chi(\mathbf{r}, t) = \chi_0 e^{-i\mu t}$ with $\chi_0 = \sqrt{D/E}$ and $\mu = A + C|\chi_0|^2$. We note that this formulation resembles closely the GPE, Eq. (2.9), apart from dissipative terms proportional to D and E. The equation acquires now the characteristics of describing an open system, where a nonequilibrium steady state arises as the consequence of the competition between gain and losses.

A modified GPE (2.9), which closely resembles Eq. (2.20), was proposed for describing nonequilibrium systems (Carusotto and Ciuti, 2013). Such an equation reads

$$i\hbar\frac{\partial \psi_{\mathrm{LP}}(\mathbf{r}, t)}{\partial t} = \hbar\omega^0_{\mathrm{LP}}\psi_{\mathrm{LP}} + \left[-\frac{\hbar^2\nabla^2}{2m_{\mathrm{LP}}} + V_{\mathrm{ext}}(\mathbf{r}, t) + g_{\mathrm{LP}}|\psi_{\mathrm{LP}}(\mathbf{r}, t)|^2\right]\psi_{\mathrm{LP}}(\mathbf{r}, t) + i\hbar D^{\mathrm{pump}}(\mathbf{r}) - i\hbar D^{\mathrm{loss}}\psi_{\mathrm{LP}}, \tag{2.21}$$

where $\hbar\omega^0_{\mathrm{LP}}$ is the energy of the bottom of the lower-polariton branch. Driving and losses rates of the system are included by means of the real terms D^{pump} and D^{loss}, respectively. Such description is formulated —for both resonant, OPO and incoherent pumping mechanisms— under the assumption that the dynamics take place on the lower-polariton branch only (so that ψ_{LP} describes the lower-polariton wavefunction), and that the excitonic part does not contribute to the dynamics of the system. All three main pumping schemes, namely resonant pumping, parametric oscillation regime and incoherent (nonresonant) pumping (Wouters and Carusotto, 2007c), can be modelled using this formalism.

2.2.2 A mean-field approach: the Gross-Pitaevskii equation (GPE) for polaritons

In Section 1.1.1 we have introduced the basic experimental phenomena for the creation of exciton-polaritons in semiconductor microcavities. The mean-field models that have been developed for the different experimental configurations will be presented here.

A generic microscopic quantum mechanical model written in a second quantised formalism has been reviewed in (Carusotto and Ciuti, 2013). The formulation consists of coupling Hamiltonians describing the dynamics of excitons and photons for the quantum fields, $\hat{\Psi}_X$ and $\hat{\Psi}_C$, respectively. Interaction and external-potential contributions are also taken into consideration. The mean-field approximation is a powerful method which is based on replacing the ensemble average of the bosonic field operator with a classical field. In the exciton-polariton case, the classical fields are then defined as $\psi_X = \langle\hat{\Psi}_X\rangle$ and $\psi_C = \langle\hat{\Psi}_C\rangle$.

We focus on the pumping schemes which have been extensively used for probing properties of polariton condensates. In the following sections, we introduce a mean-field model used to simulate OPO experiments, where the photon field $\hat{\Psi}_C$ and exciton field $\hat{\Psi}_X$ are treated independently. Thus, polariton dynamics are implemented through a system of two coupled equations, one for the photonic, and one for the excitonic component.

2.2.3 The Optical Parametric Oscillator (OPO) regime

We revisit the properties and models of the historically first studied experimental pumping mechanism, which is the optical parametric oscillator regime (OPO) (Savvidis *et al.*, 2000). A review of this physical process can be found in (Ciuti *et al.*, 2003).

A sketch of the OPO process is illustrated in Fig. 2.1 (a). It consists of a coherent beam tuned to a specific wavevector $\mathbf{k}_p$, close to the bottle neck region of the lower polariton branch. The repeated injection of carriers enhances the collisions between polaritons which are eventually scattered into two other modes, the signal $\mathbf{k}_s$ and the idler $\mathbf{k}_i$. This process takes the name of *parametric scattering* and the fixed pump wavevector is chosen such that the process occurs with conservation of energy and momentum. The nonlinearity of the medium $\chi^{(3)}$, resulting from the interaction between polaritons, mediates the scattering process of polaritons in the two modes. The idea behind this mechanism is similar to a mechanical driven harmonic oscillator in which the oscillations are driven by varying some parameter of the system at some frequency, typically different from the natural frequency of the oscillator. Under a low intensity optical stimulation, the system would also behave as a *parametric amplifier* for an additional incident beam shone close to the signal wavevector (Ciuti *et al.*, 2000).

Within this picture, the scattering process between polaritons is the one responsible for populating the final states, which eventually would stimulate the scattering process back. In case the pump is strong enough to overcome the losses of the optical cavity, the

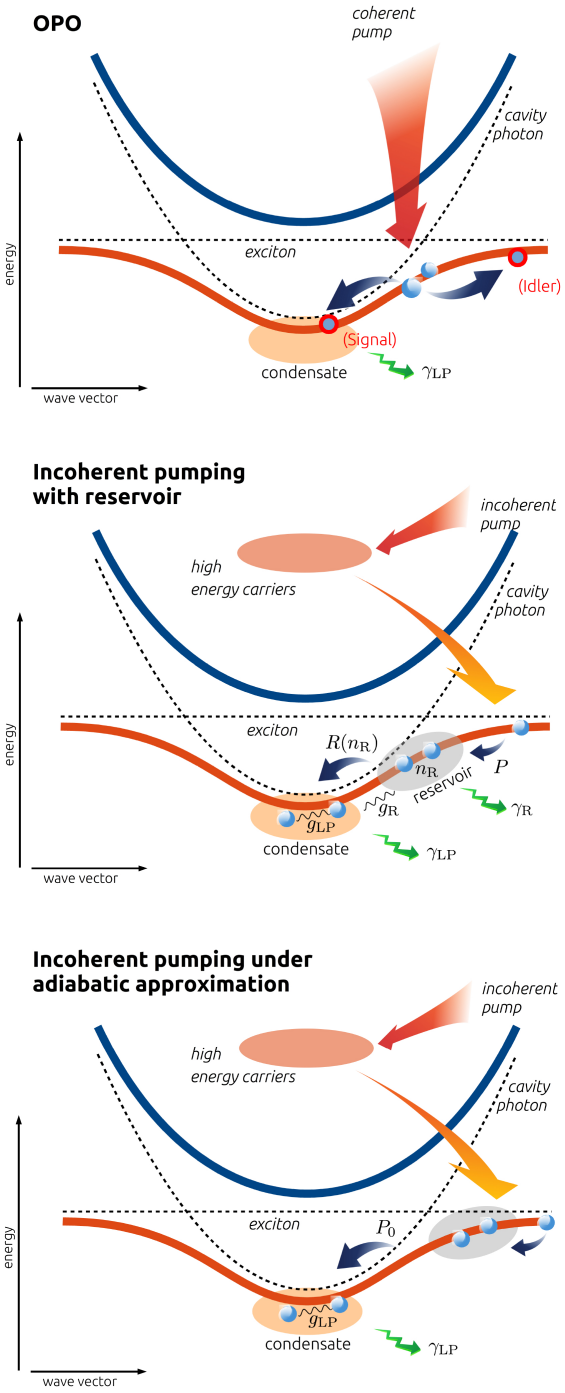

Figure 2.1: **Schematic of the polariton system under different pumping schemes.** Representation of the polaritonic spectrum in the OPO regime (top) shows the parametric scattering from the coherent pump state to the signal and idler modes. Middle/bottom plots show corresponding schematics of the incoherently pumped polariton condensate with reservoir and under adiabatic approximation are displayed.

system can be dynamically driven to a macroscopic and coherent state of polaritons in the signal (and idler) wavevector. Because of the presence of driven-dissipative effects, the phase transition this system undergoes when the pump power is driven from below to above a certain threshold value belongs to the class of non-equilibrium physics problems. Similarly to an equilibrium condensate, above a certain threshold value, the $U(1)$ symmetry is broken and the system has to rotate by an arbitrary, but fixed, value for the phase, corresponding to a rotation θ of the global signal and idler phases: $S \rightarrow Se^{i\theta}$ and $I \rightarrow Ie^{-i\theta}$.

To describe the dynamics of polaritons in the OPO regime, one can make use of *ab initio* models where microscopic details of the system are considered. More specifically, one can treat the exciton field $\hat{\Psi}_{\mathrm{X}}$ and the cavity-photon fields $\hat{\Psi}_{\mathrm{C}}$ as two distinct objects (Ciuti *et al.*, 2003), but which are coupled in the system Hamiltonian (using here the commonly-adopted simplified notation $\hbar = 1$):

$$\hat{H}_{\mathrm{S}} = \int d\mathbf{r} \left(\hat{\Psi}_{\mathrm{X}}^{\dagger} \hat{\Psi}_{\mathrm{C}}^{\dagger}\right) \begin{pmatrix} -\frac{\nabla^2}{2m_{\mathrm{X}}} + \frac{g_{\mathrm{X}}}{2}|\Psi_{\mathrm{X}}|^2 & \frac{\Omega_{\mathrm{R}}}{2} \\ \frac{\Omega_{\mathrm{R}}}{2} & -\frac{\nabla^2}{2m_{\mathrm{C}}} \end{pmatrix} \begin{pmatrix} \hat{\Psi}_{\mathrm{X}} \\ \hat{\Psi}_{\mathrm{C}} \end{pmatrix}. \tag{2.22}$$

Here m_{X} and m_{C} correspond to the exciton and cavity-photon masses respectively. The exciton-photon Rabi-splitting is given by Ω_{R}, the exciton-exciton interaction strength by g_{X}. External driving and dissipation effects are then introduced by means of a system-bath Hamiltonian, where the coherent beam is modelled by the term

$$F(\mathbf{r}, t) = f_{\mathrm{p}} e^{i(\mathbf{k}_{\mathrm{p}}\mathbf{r} - \omega_{\mathrm{p}} t)}. \tag{2.23}$$

Its function is to continuously insert carriers with specific momentum $\mathbf{k}_{\mathrm{p}}$ and frequency ω_{p}.

The description of the optical parametric oscillation process can be simplified writing down a master equation where external degrees of freedom are eliminated by standard optical methods (Szymańska *et al.*, 2007). Within the mean-field approximation, the quantum field $\hat{\Psi}_{X,C}$ is replaced by the classical field $\psi_{X,C}$. Under this assumption, the mean-field Hamiltonian reads:

$$i\frac{\partial}{\partial t}\begin{pmatrix} \psi_{\mathrm{X}} \\ \psi_{\mathrm{C}} \end{pmatrix} = \begin{pmatrix} \frac{-\nabla^2}{2m_{\mathrm{X}}} + \frac{g_{\mathrm{X}}}{2}|\psi_{\mathrm{X}}|^2 - i\kappa_{\mathrm{X}} & \frac{\Omega_{\mathrm{R}}}{2} \\ \frac{\Omega_{\mathrm{R}}}{2} & \frac{-\nabla^2}{2m_{\mathrm{C}}} - i\kappa_{\mathrm{C}} \end{pmatrix} \begin{pmatrix} \psi_{\mathrm{X}} \\ \psi_{\mathrm{C}} \end{pmatrix} + \begin{pmatrix} 0 \\ F(\mathbf{r}, t) \end{pmatrix}. \tag{2.24}$$

Mean-field properties in the OPO have been studied extensively, both analytically and numerically (Wouters and Carusotto, 2007d). In particular, excitation on top of the OPO condensate for the $1d$ case have been calculated by means of Bogoliubov theory in (Wouters and Carusotto, 2006) and (Wouters and Carusotto, 2007e). We refer to Sec. 2.2.5 for a

detailed discussion regarding the OPO excitation spectrum.

2.2.4 Incoherent saturable driving models

In the previous section we discussed the OPO mechanism, in which a coherent pump is shone inside the cavity. Many experiments, including the first observation of spontaneous coherence of a polariton condensate (Kasprzak *et al.*, 2006), were performed under a different incoherent pumping mechanism, in which excitons are created with energy above the band gap. In this section we review the phenomenological model which describes the physics of incoherently pumped polariton condensates.

An illustration of the relaxation process is given in Fig. 2.1 (b). Due to the injection of carriers at high energies, the relaxation process to the bottom of the low-polariton branch turns out to be more complicated than the coherent or parametric pumping schemes, where the microscopic parameters of the system are controlled by the incident beam. Initially, a number of high energy excitons is created above the exciton dispersion. Then, due to scattering with the lattice phonons, the thermal cloud relaxes down to the top of the lower-polariton branch. At this stage, a continuous replenishment of energetic excitons is already needed, since the relaxation towards the polariton band is slowed down by the decreased density of the low-energy states. For strong enough pumping the newly formed highly energetic polaritons would start populating a zone in the bottleneck region, in the vicinity of the inflection point, called *reservoir*, where they would start to accumulate. As a consequence, the reservoir density increases and two-body interactions start to play a role.

For high-enough reservoir density, a different relaxation process, called *stimulated scattering* takes place: when two particles collide and exchange momentum, one scatters at the bottom of the polariton dispersion, the other above the reservoir, which would eventually restart its relaxation process. When the stimulated scattering process overcomes the losses of the cavity, due to the bosonic nature of the polaritons, a macroscopic population will appear around the $\mathbf{k} = 0$ mode. Modelling of incoherently pumped polaritons has been proposed in many works (Wouters and Carusotto, 2007b),(Keeling and Berloff, 2008) and (Szymańska *et al.*, 2006), which we describe separately below.

Incoherent pumping with reservoir

A phenomenological model describing the dynamics of an uniform system of lower-polaritons under incoherent pumping was introduced by M. Wouters and I. Carusotto (Wouters and Carusotto, 2007b), through a mean-field approach in terms of a generalised

2*d* Gross-Pitaevskii Equation. The equation reads

$$i\hbar\frac{\partial\psi(\mathbf{r},t)}{\partial t} = \left[-\frac{\hbar^2\nabla^2}{2m_{\mathrm{LP}}} + \frac{i\hbar}{2}\left[R(n_{\mathrm{R}}) - \gamma_{\mathrm{LP}}\right] + g_{\mathrm{LP}}|\psi|^2 + 2g_{\mathrm{R}}n_{\mathrm{R}}\right]\psi(\mathbf{r},t), \tag{2.25}$$

where $\psi(\mathbf{r})$ corresponds to the condensate wavefunction and m_{LP} to the particle mass. The injection of polaritons from the reservoir into the condensate is here accounted by the term proportional to $R(n_{\mathrm{R}})$, which is a function of the density of the polariton reservoir $n_R(\mathbf{r})$ in the bottleneck region. The term R quantifies the amplification process of stimulated scattering of polaritons from the reservoir to the condensate. The interaction strength between lower-branch and reservoir polaritons is modelled by the parameter g_{R}, whereas interactions within the condensate are modelled by the term g_{LP}.

In order to account for the dynamics close to the bottleneck region, the lower-polariton equation (2.25) is coupled with a second equation for the reservoir density n_{R}. The latter equation describes the evolution of particles contained in the reservoir following the injection of high-energy polaritons pumped at a rate P and decaying at a rate γ_{R}. The rate equation takes the form (Wouters and Carusotto, 2007b)

$$\frac{\partial n_{\mathrm{R}}}{\partial t} = P - \gamma_{\mathrm{R}}n_{\mathrm{R}} - R(n_{\mathrm{R}})|\psi_{\mathrm{LP}}(\mathbf{r})|^2, \tag{2.26}$$

where the term $R(n_{\mathrm{R}})|\psi_{\mathrm{LP}}(\mathbf{r})|^2$ accounts for the scattering of reservoir polaritons into the condensate. Such a model has been successfully employed for simulating a plethora of experiments, e.g. (Kasprzak *et al.*, 2006; Lagoudakis *et al.*, 2008). Compared to the case of a compressible inviscid fluid, the non-conservative nature of the model discussed above affects the form of the continuity equation and Euler equation, which now present additive terms proportional to the pump and losses strengths (Ballarini *et al.*, 2017; Franchetti, 2013).

Incoherent pumping under adiabatic approximation

An approximation we can apply to the model (2.25)-(2.26) is to treat the reservoir assuming it is able to follow adiabatically the dynamics of the condensate. This is true when the reservoir relaxes much faster than the condensate loss rate, namely $\gamma_{\mathrm{R}} \gg \gamma_{\mathrm{LP}}$. This means we can treat the reservoir density state as stationary, i.e. $n_{\mathrm{R}}(\mathbf{r},t) = n_{\mathrm{R}}(\mathbf{r})$. Such a condition has been implemented experimentally by means of extremely plain samples (Caputo *et al.*, 2017; Baboux *et al.*, 2017). Within such state-of-the-art devices, experimentalists have been able to reproduce an excitonic reservoir located far from the lower-polariton branch (Caputo *et al.*, 2017; Ballarini *et al.*, 2017). In case the reservoir rate changes proportionally to the reservoir density n_{R}, one can then simplify $R(n_R) = Rn_R$. Inserting these conditions into Eq. (2.26), and dropping the term proportional to the interaction

between reservoir polaritons g_{R} we end up with an equation for the pump term

$$P = \gamma_{\mathrm{R}} n_{\mathrm{R}} + R n_{\mathrm{R}} |\psi(\mathbf{r})|^2, \tag{2.27}$$

thus leading to an expression for the reservoir density which reads

$$n_{\mathrm{R}} = \frac{P}{\gamma_{\mathrm{R}} + R|\psi(\mathbf{r})|^2}. \tag{2.28}$$

By adding the above equation into the condensate evolution, we arrive at

$$i\hbar \frac{\partial \psi(\mathbf{r},t)}{\partial t} = \left[-\frac{\hbar^2 \nabla^2}{2m_{\mathrm{LP}}} + \frac{i\hbar}{2} \left(\frac{R}{\gamma_{\mathrm{R}}} \cdot \frac{P}{1 + \frac{R \cdot |\psi|^2}{\gamma_{\mathrm{R}}}} - \gamma_{\mathrm{LP}} \right) + g_{\mathrm{LP}} |\psi(\mathbf{r},t)|^2 \right] \psi(\mathbf{r},t), \tag{2.29}$$

where we have re-written the term $R(n_{\mathrm{R}})$, which describes the ratio of injection of polariton into the condensate, as

$$R(n_{\mathrm{R}}) = R n_{\mathrm{R}} = \frac{R \cdot P}{(\gamma_R + R|\psi(\mathbf{r})|^2)} = \frac{R}{\gamma_R} \cdot \frac{P}{(1 + \frac{R}{\gamma_R}|\psi|^2)}. \tag{2.30}$$

It is worth noting that the two models Eqs. (2.25)-(2.26) and Eq. (2.29) are equivalent under the assumption that fluctuations are small compared to the steady state solution studied (Bobrovska and Matuszewski, 2015). By defining the saturation density as the ratio between reservoir relaxation rate and amplification, i.e.

$$n_s = \frac{\gamma_R}{R}, \tag{2.31}$$

and rewriting the pump parameter $P_0 = P \cdot R/\gamma_{\mathrm{R}} = P/n_{\mathrm{s}}$, we can finally rewrite equation (2.29) and obtain the so-called *polariton GPE* (Chiocchetta and Carusotto, 2013):

$$i\hbar \frac{\partial \psi(\mathbf{r},t)}{\partial t} = \left[-\frac{\hbar^2 \nabla^2}{2m_{\mathrm{LP}}} + \frac{i\hbar}{2} \left(\frac{P_0}{1 + \frac{|\psi|^2}{n_{\mathrm{s}}}} - \gamma_{\mathrm{LP}} \right) + g_{\mathrm{LP}} |\psi(\mathbf{r},t)|^2 \right] \psi(\mathbf{r},t). \tag{2.32}$$

The *steady state* of a homogeneous system under such a description can be obtained by considering the mean-field solution $\psi(\mathbf{r},t) = \psi_0 e^{-i\omega t}$, which is translationally invariant in space. We note immediately that Eq. (2.32) has always a trivial solution $\psi = 0$ for any value of the pump P_0. At low values of the pump P_0, below the threshold $P_{\mathrm{th}} = \gamma_{\mathrm{LP}}$ the trivial solution is the only one dynamically stable. For pump intensities $P_0 > \gamma_{\mathrm{LP}}$, i.e. above threshold, the trivial solution becomes dynamically unstable and a finite density

for the steady state,

$$|\psi_0|^2 = n_s \left(\frac{P_0}{\gamma_{\mathrm{LP}}} - 1 \right), \tag{2.33}$$

appears. Plot of the density $|\psi_0|^2$ versus the pump strength P_0 for typical experimental parameters is reported as dashed blue line in Fig. (4.4).

It is straightforward to see that the polariton GPE can be mapped to Eq. (2.21) if we take

$$D^{\mathrm{pump}} = \frac{1}{2} \frac{P_0}{\left(1 + \frac{|\psi|^2}{n_{\mathrm{s}}}\right)} \psi_{\mathrm{LP}} \quad , \quad D^{\mathrm{loss}} = \frac{\gamma_{\mathrm{LP}}}{2}. \tag{2.34}$$

Such a description was used by (Keeling and Berloff, 2008) for the study of spontaneous rotating vortex lattices in a polariton condensate. A direct relation between Eq. (2.20) and Eq. (2.32) can be established with the following mapping: $A = \hbar\omega_0$, $B = \hbar^2/2m_{\mathrm{LP}}$, $C = \hbar g_{\mathrm{LP}}$, $D^{\mathrm{pump}} = P_0/2$, $D^{\mathrm{loss}} = \gamma_{\mathrm{LP}}/2$ and $E = P_0/2n_{\mathrm{s}}$. As a consequence, the coefficients in Eq. (2.20) assume the following physical interpretations: A corresponds to the energy offset, B to the dispersion coefficient, C to nonlinear interactions, $D = D^{\mathrm{pump}} - D^{\mathrm{loss}}$ to the balancing between the strength of driving and losses, and E corresponds to the nonlinear losses. Note that within this change of notation, we introduced an approximation which consists of writing the terms

$$\frac{D^{\mathrm{pump}}}{1 + \frac{E}{D^{\mathrm{pump}}}|\chi|^2} = D^{\mathrm{pump}} - E|\chi|^2, \tag{2.35}$$

which follows from the Taylor series $1 - x^2 \sim \frac{1}{1+x^2} + O(x^2)^2$, truncated at the second order.

Incoherent and frequency-dependent pumping

In the previous section we introduced the driven-dissipative polariton GPE, which has been derived based on an adiabatic approximation. The models (2.32) and (2.25) - (2.26) have been able to describe many experimental observations concerning non-equilibrium condensation, such as the onset of spontaneous coherence (Kasprzak *et al.*, 2006) and the presence of vortices (Lagoudakis *et al.*, 2008) (which is non-trivial, since vortices solved by means of the cGLE instead of the GPE, are expected to show issues, e.g. vortex splitting due to unstable quadrupole mode in attractive condensate (Saito and Ueda, 2002)). However, within these models the incoherent pump is not frequency selective, which could potentially lead to misleading results: as remarked by (Porras *et al.*, 2002), and confirmed experimentally by the observation of condensation within a harmonic confinement (Balili *et al.*, 2007), the stimulated scattering processes give rise to macroscopic population of the system lowest-energy-state showing they are in fact frequency selective.

In order to account for a frequency dependence of the amplification and dissipation reservoir in our model, as originally suggested by (Wouters and Carusotto, 2010) and confirmed in (Chiocchetta and Carusotto, 2013), we decide to include in the polariton GPE, a term proportional to the pump which has the form

$$P_0 \to P_0 \left(1 - \frac{i}{\Omega}\left(1 + \frac{|\psi_{LP}|^2}{n_s}\right)\frac{\partial}{\partial t}\right), \tag{2.36}$$

which eventually yields a generalised polariton GPE (Wouters and Carusotto, 2010):

$$i\hbar\frac{\partial\psi_{\rm LP}(\mathbf{r},t)}{\partial t} = \left[-\frac{\hbar^2\nabla^2}{2m_{LP}} + g_{\rm LP}|\psi_{LP}|^2\right]\psi_{\rm LP}(\mathbf{r},t) + \frac{i\hbar}{2}\left(\frac{P_0(\mathbf{r},t)}{1+\frac{|\psi_{\rm LP}|^2}{n_s}} - \gamma_{\rm LP}\right)\psi_{\rm LP}(\mathbf{r},t) + \frac{\hbar}{2}\frac{P_0(\mathbf{r},t)}{\Omega}\frac{\partial\psi_{\rm LP}(\mathbf{r},t)}{\partial t}, \tag{2.37}$$

where the term Ω describes the characteristic scale of the frequency dependence. The larger Ω is, the less selective is the mechanism. Such a term is also suitable for the description of energy relaxation, which was demonstrated to be relevant in the experimental setup of (Wertz *et al.*, 2010). Equivalently, within the equilibrium GPE, such a generalization is able to describe the dissipative nature of a Bose atomic gas induced by the interactions with a thermal cloud (Pitaevskii, 1959). Such a modelling has been also deeply investigated in (Wouters, 2012). This term is also considered to be important in the study of phase transitions, as it regularises the large momentum behaviour of the stochastic model obtained by the addition of a white and Gaussian noise term to Eq. (2.37). We refer to Sec. 2.3.2 for a more detailed description of such phenomenon.

Inclusion of the frequency-selective pumping term, Eq. (2.36) affects the steady state value of the condensate density, which is now dependent on the polariton-polariton interaction strength $g_{\rm LP}$, and (as expected) on the frequency cut-off Ω. The steady state now takes the form

$$n_0 = |\psi^{\rm SS}(\mathbf{r})|^2 = n_{\rm s}\left(\frac{P_0}{\frac{P_0}{\Omega}g_{\rm LP}|\psi^{\rm SS}(\mathbf{r})|^2 + \gamma_{\rm LP}} - 1\right). \tag{2.38}$$

In the limit of large cut-off values $\Omega \to \infty$, the above equation takes the form of the polariton GPE steady state solution, Eq. (2.33). However, we note that the critical point is not affected and the transition, at a mean-field level, still occurs at $P_0 = \gamma_{\rm LP}$.

In the following section, we focus on the analysis of the Bogoliubov excitation spectrum

for the different models presented, which is important for understanding the dynamical properties which can be predicted by each model.

2.2.5 Elementary excitation spectrum of driven-dissipative condensates

In Sec. 2.1.3 we have introduced the Bogoliubov theory of small excitations, by means of which one can study the behaviour of small fluctuations around the steady state. As previously discussed, the elementary excitation spectrum of a dilute Bose gas *at equilibrium* shows a two-regime dispersion, characterised by a sonic behaviour at small k, and a free-particle distribution at momenta $k = |\mathbf{k}|$ associated with wavelengths smaller than the healing length ξ (2.18).

The most interesting feature of the Bogoliubov analysis is the behaviour of the Goldstone mode, which physically corresponds to the twist of the condensate phase θ at long wavelength (small momenta), and it is characterised by the decay of its frequency dispersion $\omega_{\mathrm{G}}(k)$ in the wave-length limit to zero, namely

$$\mathfrak{R}(\omega_{\mathrm{G}}) \xrightarrow{k\to 0} 0, \quad \mathfrak{I}(\omega_{\mathrm{G}}) \xrightarrow{k\to 0} 0, \tag{2.39}$$

where $\mathfrak{R}(\omega_{\mathrm{G}})$ and $\mathfrak{I}(\omega_{\mathrm{G}})$ are the real and imaginary parts of ω_{G}, respectively (Pitaevskii and Stringari, 2003). The appearance of the Goldstone mode is an immediate consequence of the breaking of the spontaneous continuous $U(1)$ symmetry of the order parameter. It becomes thus natural to investigate its properties in order to characterise the nature of a phase transition. In the case of an equilibrium condensate, the Goldstone mode is characterised by a "soft" behaviour $\omega_{\mathrm{G}}(k) \sim c_{\mathrm{s}}k$ and a singularity at $k = 0$ (Pitaevskii and Stringari, 2003), as shown in Fig. 2.2 (a).

For driven-dissipative condensates, preliminary studies have been done under resonant (Carusotto and Ciuti, 2004) and OPO regime (Carusotto and Ciuti, 2005). The resonant case immediately shows a peculiar feature of driven-dissipative systems, namely the presence of a regime with a gapped ω_{G}, consistent with suppression of the sonic behaviour at large wavelengths. This anomaly is related to the locking of the phase condensate by means of the incident coherent beam.

In Fig. 2.2 (b) we report the dispersion of elementary excitations on top of the OPO state, which we have introduced in Sec. 2.2.3. Here, the Goldstone mode ω_{G} satisfies the conditions of Eq. (2.39). Still, it shows some differences when compared with the equilibrium case. The singularity at $\mathbf{k} = 0$ is suppressed, as well as the sonic behaviour at small momenta which is now substituted by a *diffusive* one, which can be recognised

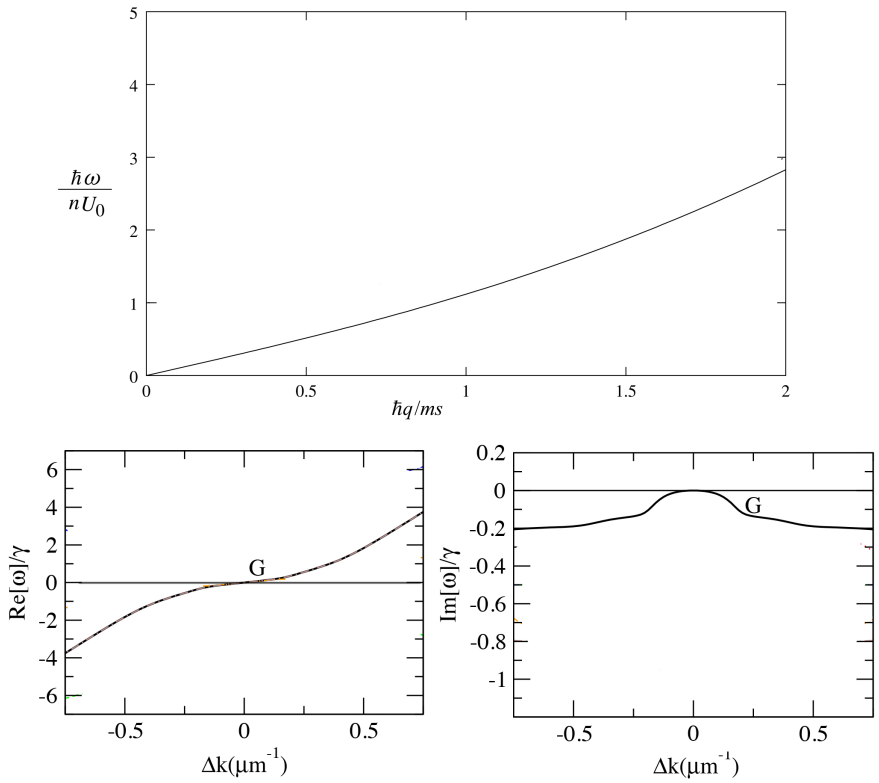

Figure 2.2: **Goldstone mode in an homogeneous Bose gas and OPO regime**. (top) Bogoliubov dispersion of collective excitations of an homogeneous Bose gas (solid line) showing a sonic behaviour at low momenta. (bottom) Real and imaginary part (left and right, respectively) of the dispesion relation of a nonequilibrium polariton condensate in the OPO regime with a vanishing Goldstone mode (black curve). Adapted from (Pitaevskii and Stringari, 2003) and (Wouters and Carusotto, 2007a), respectively.

by $\mathfrak{I}(\omega_{\mathrm{G}}) \neq 0$. Physically, the non-sonic (but non-zero) small $\mathbf{k}$ behaviour of $\mathfrak{R}(\omega_{\mathrm{G}})$ is due to the presence of the pump which builds up an injected-polariton flow with momentum $\mathbf{k}_p$ able to drag excitations, and which relaxes back to equilibrium, as one can see from the non-zero component of $\mathfrak{I}(\omega_{\mathrm{G}})$. The diffusive behaviour is a direct consequence of the $U(1)$ symmetry breaking which is now driven by the external field.

The observation of Bogoliubov excitations in exciton-polariton condensates has been reported in (Utsunomiya *et al.*, 2008).

For the incoherent pumping case, similar diffusive behaviour has been reported by (Szymańska *et al.*, 2006) and (Wouters and Carusotto, 2007b). The Bogoliubov spectrum of small excitations is obtained through the linearisation of Eqs. (2.25)-(2.26) around the stationary state. We now show the calculation for model (2.37), which is a generalisation of the incoherent pumping model without frequency-selecting term (2.9). We include

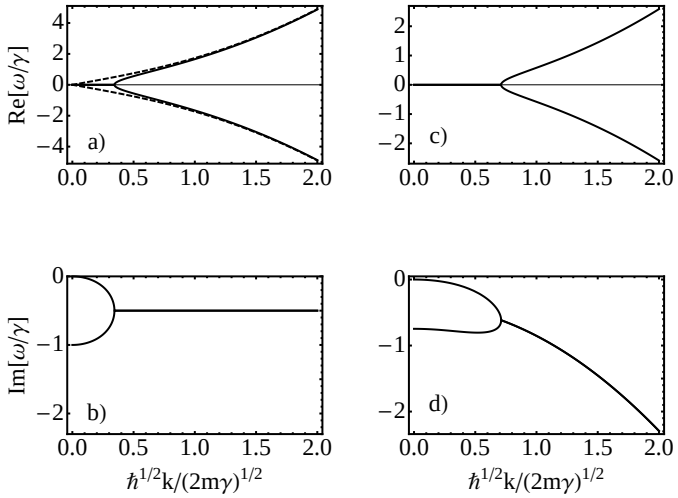

Figure 2.3: **Goldostone mode in an incoherently pumped polariton condensate**. Real part (top) and imaginary part (bottom) of the Bogoliubov dispersion of collective excitations for a nonequilibrium incoherently-pumped polariton condensate. Both frequency-independent (left) and frequency-dependent (right) cases are shown. Adapted from (Chiocchetta and Carusotto, 2013).

fluctuations on top of the homogeneous condensate such that $\psi = \psi_0 + \delta\psi$. The total field in the homogeneous case, where excitations take the form of plane waves, can be decomposed to Fourier components as

$$\psi(\mathbf{r}, t) = \psi_0 e^{-i\mu t} + \sum_{\mathbf{k}} u_{\mathbf{k}} e^{-i\mu t} e^{i(\mathbf{kr}-\omega t)} + \sum_{\mathbf{k}} v_{\mathbf{k}} e^{-i\mu t} e^{-i(\mathbf{kr}-\omega t)}. \tag{2.40}$$

Introducing this solution in Eq. (2.37) we arrive at a system of coupled equations

$$i\hbar \frac{\partial}{\partial t} \begin{pmatrix} \delta\psi(\mathbf{k}) \\ \delta\psi^*(\mathbf{k}) \end{pmatrix} = \hbar L_{\mathbf{k}} \begin{pmatrix} \delta\psi(\mathbf{k}) \\ \delta\psi^*(\mathbf{k}) \end{pmatrix}, \tag{2.41}$$

with

$$L_{\mathbf{k}} = \begin{pmatrix} \bar{\gamma}\left(\epsilon_{\mathbf{k}} + \mu - i\Gamma\right) & \bar{\gamma}\left(\mu - i\Gamma\right) \\ \bar{\gamma}^*\left(-\mu - i\Gamma\right) & \bar{\gamma}^*\left(-\epsilon_{\mathbf{k}} - \mu - i\Gamma\right) \end{pmatrix}. \tag{2.42}$$

Here,

$$\epsilon_{\mathbf{k}} = \frac{\hbar k^2}{2m}, \qquad \mu = g_{\mathrm{LP}}|\psi_0|^2, \qquad \Gamma = \frac{P_0|\psi_0|^2}{(n_s/|\psi_0|^2 + 1)} \tag{2.43}$$

and

$$\bar{\gamma} = \left(\gamma_a + i\gamma_b\right), \qquad \gamma_a = \frac{1}{(1 + (P_0/\Omega)^2)}, \qquad \gamma_b = -(P_0/\Omega)^2\gamma_a. \tag{2.44}$$

Diagonalizing Eq. (2.42) we obtain

$$\hbar\omega_{\mathbf{k}}^{\pm} = -i\hbar\tilde{\Gamma} \pm \hbar\sqrt{\tilde{E}_{\mathbf{k}}^2 - \tilde{\Gamma}^2}, \tag{2.45}$$

with $\tilde{E}_{\mathbf{k}}^2 = |\bar{\gamma}|^2\epsilon_{\mathbf{k}}\left(\epsilon_{\mathbf{k}} + 2\mu\right)$ and $\tilde{\Gamma} = \gamma_a\Gamma - \gamma_b(\epsilon_{\mathbf{k}} + \mu)$. As expected, by considering the limit $\Omega \to \infty$, the term γ_b vanishes together with the momentum-dependence of the imaginary part of the frequency branch after the transition: the new expression recovers the flat-dissipation behaviour, characteristic of a frequency-independent pumping (Wouters and Carusotto, 2007b) described by

$$\hbar\omega_{\mathbf{k}}^{\pm} = -i\hbar\Gamma \pm \hbar\sqrt{E_{\mathbf{k}}^2 - \Gamma^2}, \tag{2.46}$$

where $E_{\mathbf{k}}^2 = \epsilon_{\mathbf{k}}\left(\epsilon_{\mathbf{k}} + 2\mu\right)$.

Fig. 2.3 shows plots of the elementary excitation spectrum for the case of a frequency-independent (left) and frequency-dependent (right) pump, corresponding to Eq. 2.46 and 2.45, respectively. For the case of a pumping mechanism without frequency selection, the Goldstone mode exhibits a diffusive behaviour in the vicinity of $k = 0$. This is suggested by the real part of (2.46) which assumes zero values for $E_{\mathrm{k}}^2 > \Gamma^2$, while the imaginary part decreases quadratically. On the other hand, the inclusion of the frequency dependence of the pump (2.45) preserves the diffusive behaviour of the Goldstone mode, but modifies the dumping rate which grows rapidly at large momenta, in contrast with the flat behaviour of (2.46).

Experimental observation of the diffusive mode is still missing. Instead, the measurement of the Bogoliubov excitation spectrum showing a clear sonic behaviour at low momenta has been discussed in (Utsunomiya *et al.*, 2008) and modelled by coupling a Maxwell-Boltzmann equation to the condensate, as in (Haug *et al.*, 2014) and (Solnyshkov *et al.*, 2014).

2.3 Beyond mean field description: inclusion of fluctuations

The mean-field models described in the previous section are based on approximating the quantum polariton field by a classical complex field. This assumption explicitly excludes the presence of fluctuations: this condition is a direct consequence of the Bogoliubov replacement, Eq. (2.8), previously introduced. This "semi-classical" approach, then, is able to describe only the lowest energy modes of the Bose field, and all information on the fluctuations are thus washed away.

The physics introduced by fluctuations, however, is expected to be significant, especially in the vicinity of the critical point, where contribution from fluctuations contributions are supposed to be of the same order as, if not higher than, the order parameter. Considering a model accounting for quantum and classical fluctuations is therefore crucial for the investigation of critical phenomena, phase transitions and quench dynamics in polariton condensate; the application of such generalised model composes the essence of this thesis. The challenge is indeed linked to the need for implementing models which would be eventually suitable for implementations in classical computers. Numerous methods have been proposed, which make use of different approaches such as path integral Monte Carlo methods (Ceperley, 1995), or diagrammatic techniques (Houcke *et al.*, 2010).

In this section we focus on phase-space techniques, whose basic idea is to describe the quantum dynamics of the system through the averaging over multiple trajectories in phase space. Initially, a master equation for the density matrix which describes the lower-polariton field is derived from the nonequilibrium Hamiltonian of the system. The master equation can then be written in terms of a quasi-probability distribution function and, independent of the chosen representation, mapped to a Fokker-Planck equation. There are different ways to represent the density matrix as a probability distribution, due to its numerical versatility. Among those, the Wigner representation (Sinatra *et al.*, 2002) has been chosen over others for the modelling of polaritons under different regimes (Carusotto and Ciuti, 2013). However, within this representation, the resulting Fokker-Planck-like equation includes derivatives of the third order which make the mapping to a classical stochastic equation more complicated. In order to circumvent such difficulties, one can truncate the Fokker-Planck equation, leading to the so-called Truncated Wigner Approximation (TWA). One can finally map the truncated Fokker-Plank equation into a system of Ito stochastic differential equations (Gardiner and Collett, 1985), which can be numerically implemented throughout averaging over different realisations of the same dynamical equation.

2.3.1 The truncated Wigner method for incoherently-pumped polaritons

Here we heuristically revisit the formulation for the incoherently-pumped polariton condensate, which is reported in (Wouters and Savona, 2009). A first complication compared with the coherent (and equilibrium) cases, arises from the nature of the two level (reservoir-condensate) system. In this case, the system Hamiltonian results from the sum

of different contributions:

$$\hat{H}_{\text{system}} = \hat{H}_{\text{LP}} + \hat{H}_{\text{R}} + \hat{H}_{\text{COUP}}, \tag{2.47}$$

where the lower-polariton $\hat{H}_{\text{LP}}$ and reservoir $\hat{H}_{\text{R}}$ terms read

$$\hat{H}_{\text{LP,R}} = \int d\mathbf{r}\, \hat{\psi}^{\dagger}_{\text{LP,R}}(\mathbf{r},t)\hat{h}_{\text{LP,R}}\hat{\psi}^{\dagger}_{\text{LP,R}}(\mathbf{r},t) \tag{2.48}$$

$$+ \frac{g_{\text{LP}}}{2}\int d\mathbf{r}\, \hat{\psi}^{\dagger}_{\text{LP,R}}(\mathbf{r},t)\hat{\psi}^{\dagger}_{\text{LP,R}}(\mathbf{r},t)\hat{\psi}_{\text{LP,R}}(\mathbf{r},t)\hat{\psi}_{\text{LP,R}}(\mathbf{r},t), \tag{2.49}$$

with $\hat{h}_{\text{LP,R}} = -\hbar^2\nabla^2/2m_{\text{LP,X}}$, g_{LP} the polariton-polariton interaction and $\hat{\psi}_{\text{LP,R}}$ ($\hat{\psi}^{\dagger}_{\text{LP,R}}$) the annihilation (creation) operators for polaritons and excitons, respectively. The coupling term $\hat{H}_{\text{COUP}}$ describes the Coulomb interaction between the lower and upper branch particles.

A quantum equation for the lower-polariton field can be obtained by tracing out the incoherent excitonic particles, which reads

$$i\hbar\frac{\partial}{\partial t}\rho_{\text{LP}}(t) = \left[\hat{H}_{\text{LP}}, \rho_{\text{LP}}\right] + i\hbar K_{\text{in}}(\rho_{\text{LP}}) + i\hbar K_{\text{out}}(\rho_{\text{LP}}), \tag{2.50}$$

where the gain and loss terms, K_{in} and K_{out} respectively, arise from the in-scattering R_{in} and out-scattering R_{out} collisions among energetic excitons. Due to the large number of degrees of freedom, solving Eq. (2.50) exactly becomes a difficult challenge. The truncated Wigner method for the polariton case relies on the Wigner function representation $P(\alpha, \alpha^*, t)$, a quasi-probability distribution defined on a space for the complex variables α and α^* of the density operator ρ_{LP}. This can be written as

$$P(\alpha,\alpha^*) = \frac{1}{\pi^2}\int d^2\lambda e^{-\lambda\alpha^* + \lambda^*\alpha}\chi_{\text{P}}(\lambda,\lambda^*), \tag{2.51}$$

with $\chi_{\text{P}}(\lambda,\lambda^*)$ the Wigner characteristic function $\chi_{\text{P}}(\lambda,\lambda^*) \equiv \text{Tr}\{\rho_{\text{LP}} e^{\lambda\hat{\psi_{\text{LP}}}^{\dagger} - \lambda^*\hat{\psi}_{\text{LP}}}\}$. Generally, there exists a Wigner function P for any density operator ρ_{LP}. P can assume either positive or negative values. In the latter case, it behaves like a probability distribution for α and α^*. The moments of P correspond to those of the symmetrised operator products:

$$\left\langle \left\{ \hat{\psi}^{\text{r}}_{\text{LP}} \left(\hat{\psi}^{\dagger}_{\text{LP}}\right)^{\text{s}} \right\}_{\text{sym}} \right\rangle = \int d^2\alpha\ \ \alpha^{\text{r}}\,(\alpha^*)^{\text{s}}\,P(\alpha,\alpha^*) \equiv \langle \alpha^{\text{r}}\,(\alpha^*)^{\text{s}} \rangle_P\,. \tag{2.52}$$

From now on we subscript LP from $\hat{\psi}_{LP}$. Annihilation and creation operators can be

expressed as functional operators on the Wigner distribution function, translated as:

$$\hat{\psi}\ \rho_{\mathrm{LP}}(t) \leftrightarrow \left(\alpha + \frac{1}{2}\frac{\partial}{\partial \alpha^*}\right) P(\alpha, \alpha^*, t), \tag{2.53}$$

$$\hat{\psi}^\dagger\ \rho_{\mathrm{LP}}(t) \leftrightarrow \left(\alpha^* - \frac{1}{2}\frac{\partial}{\partial \alpha}\right) P(\alpha, \alpha^*, t), \tag{2.54}$$

$$\rho_{\mathrm{LP}}(t)\ \hat{\psi} \leftrightarrow \left(\alpha - \frac{1}{2}\frac{\partial}{\partial \alpha^*}\right) P(\alpha, \alpha^*, t), \tag{2.55}$$

$$\rho_{\mathrm{LP}}(t)\ \hat{\psi}^\dagger \leftrightarrow \left(\alpha^* + \frac{1}{2}\frac{\partial}{\partial \alpha}\right) P(\alpha, \alpha^*, t). \tag{2.56}$$

By means of these operators, the equation of motion for $P(\alpha, \alpha^*)$ can then be calculated from the master equation (2.50).

Typically, in order to numerically implement this problem, the field $\alpha(\mathbf{r}, t)$ is mapped into a d-dimensional grid. In the case of a squared grid with side $L = aN$ containing N^d points (and elementary cell volume $\Delta V = a^d$), the Fokker-Planck partial differential equation which describes the time-evolution of the field α takes the form

$$\begin{aligned}
\frac{\partial}{\partial t} P(\alpha, t) &= -\frac{\partial}{\partial \alpha}\left[F_{\mathrm{W}}(\alpha, t)\, P(\alpha, t)\right] - \frac{\partial}{\partial \alpha^*}\left[F_{\mathrm{W}}(\alpha, t)\, P(\alpha, t)\right] && (2.57)\\
&+ \left(R_{\mathrm{in}} + R_{\mathrm{out}} + \gamma_{\mathrm{LP}}\right)\frac{\partial^2}{\partial \alpha^* \partial \alpha} P(\alpha, t) && (2.58)\\
&+ i\frac{g_{\mathrm{LP}}}{2\Delta V}\frac{\partial^2}{\partial \alpha^* \partial \alpha}\left[\frac{\partial}{\partial \alpha^*}\alpha^* - \frac{\partial}{\partial \alpha}\alpha\right] P(\alpha, t), && (2.59)
\end{aligned}$$

where γ_{LP} describes cavity losses and F_{W} is the drift force term acting on the fluid of polaritons,

$$F_{\mathrm{W}} = -i\left[\omega_{\mathrm{LP}}^0 - \frac{\hbar \nabla^2}{2m_{\mathrm{LP}}} - \frac{i\left(R_{\mathrm{in}} - R_{\mathrm{out}} - \gamma_{\mathrm{LP}}\right)}{2} + g_{\mathrm{LP}}|\alpha(t)|^2\right]\alpha. \tag{2.60}$$

It is worth noting that this operation automatically introduces a cutoff for the field α.

From the numerical point of view, implementing the third order derivatives contained in Eq. (2.59) has been found very difficult. However, as discussed above, one can apply the *Truncated Wigner Approximation* and neglect these terms. As a result, the quasi-probability function P obeys a Fokker-Planck equation that corresponds to the Langevin equation

$$d\alpha(\mathbf{r}, t) = F_{\mathrm{W}}(\alpha)\, dt + dW, \tag{2.61}$$

where dW is a zero-mean, complex Gaussian white noise which satisfies the following

correlations:

$$\langle dW(\mathbf{r},t)dW(\mathbf{r}',t)\rangle = 0, \tag{2.62}$$

$$\langle dW^*(\mathbf{r},t)dW(\mathbf{r}',t)\rangle = \frac{dt}{2\Delta V}(R_{\rm in}+R_{\rm out}+\gamma_{\rm LP})\delta_{\mathbf{r},\mathbf{r}'}. \tag{2.63}$$

In order to study the validity conditions which permit the numerical implementation of the TWA method, we need to estimate the order of magnitude of the third derivative of Eq. (2.59). In the dilute gas limit, statistical fluctuations due to the noise term around the mean-field value are of the order of $\Delta\alpha \propto \Delta V^{-1/2}$. Third order derivatives are therefore expected to be of the order of $g_{\rm LP}/\Delta V$. When compared to the diffusion term $\gamma_{\rm LP}$, we can conclude that accurate result within the TWA can be obtained under the "diluteness" condition

$$\gamma_{\rm LP} \gg \frac{g_{\rm LP}}{\Delta V}. \tag{2.64}$$

As reported by (Sinatra *et al.*, 2002), when this condition is verified, the TWA becomes a suitable model for the description of dilute Bose gases.

2.3.2 A stochastic driven-dissipative GPE (SGPE) for polaritons

In the previous section we derived a stochastic model for incoherently-pumped polariton condensates from a quantum field Hamiltonian. Similar arguments can indeed be applied for the incoherently driven case with frequency dependence of the pump under adiabatic approximation, i.e. Eq. (2.37), which yields (Wouters and Carusotto, 2010)

$$i\hbar\frac{\partial\psi_{\rm LP}(\mathbf{r},t)}{\partial t} = \left[-\frac{\hbar^2\nabla^2}{2m_{\rm LP}} + g_{\rm LP}|\psi_{\rm LP}|^2_{-} + \frac{i\hbar}{2}\left(\frac{P_0(\mathbf{r},t)}{1+\frac{|\psi_{\rm LP}|^2_{-}}{n_s}} - \gamma_{\rm LP}\right) + \frac{\hbar}{2}\frac{P_0(\mathbf{r},t)}{\Omega}\frac{\partial}{\partial t}\right]\psi_{\rm LP}(\mathbf{r},t) + \sqrt{\frac{\gamma_{\rm LP}+P_0(\mathbf{r},t)}{4\Delta V}}dW(\mathbf{r},t), \tag{2.65}$$

where reduced density reads $|\psi_{LP}|^2_{-} \equiv \left(\left|\psi_{LP}(\mathbf{r},t)\right|^2 - 1/2\Delta V\right)$. In principle, the presence of a frequency-dependent term in the equation above would require a frequency-dependent (coloured) noise. However, we consider instead a white Gaussian noise term dW, namely a random variable with correlation functions

$$\langle dW(\mathbf{r},t)dW(\mathbf{r}',t)\rangle = 0, \tag{2.66}$$

$$\langle dW^*(\mathbf{r},t)dW(\mathbf{r}',t)\rangle = 2\delta_{\mathbf{r},\mathbf{r}'}dt. \tag{2.67}$$

In a typical numerical simulation of the TWA method, the initial distribution of the lower-polariton field is sampled by N_{P} different (independent) realisations. In order to have a good physical description of the system, the number of realisations has to be chosen large enough, i.e. $N_{\mathrm{R}} \gg 1$. Each initial configuration is then made to evolve according to Eq. (2.65), where both the noise and time step are different for each realisation. In a few words, the noise is chosen such that the system, at each time step, has no memory of the previous configuration: this is a characteristic of a *Wiener process*. In order to recover the "classical" dynamics of the expectation value of any observable O, one needs to average over the many different realisations. This representation makes use of the correspondence of the Wigner function with the quantum expectation values, namely (2.52). We refer to Sec. 3.1.5 where we use this rule for numerically calculating observables of interest.

By including fluctuations by means of the stochastic noise (2.67) in Eq. (2.41), we calculate the correlations at the steady state, namely the momentum distribution of particles (Chiocchetta and Carusotto, 2013)

$$n_{\mathbf{k}}^{\mathrm{SS}} = N_0\delta_{\mathbf{k}=0} + \frac{(P_0+\gamma_{LP})}{\tilde{\Gamma}+\frac{P_0}{\Omega}(\frac{\hbar^2\mathbf{k}^2}{2m_{\mathrm{LP}}}+\mu)}\left(1+\frac{\mu^2+\tilde{\Gamma}^2}{\frac{\hbar^2\mathbf{k}^2}{2m_{\mathrm{LP}}}\left(\frac{\hbar^2\mathbf{k}^2}{2m_{\mathrm{LP}}}+\mu\right)}\right), \tag{2.68}$$

which in the limit of $\Omega \to \infty$ recovers the momentum distribution for Eq. (2.37), which reads

$$n_{\mathbf{k}}^{\mathrm{SS}} = N_0\delta_{\mathbf{k}=0} + \frac{(P_0+\gamma_{LP})}{\Gamma}\left(1+\frac{\mu^2+\Gamma^2}{\frac{\hbar^2\mathbf{k}^2}{2m_{\mathrm{LP}}}\left(\frac{\hbar^2\mathbf{k}^2}{2m_{\mathrm{LP}}}+\mu\right)}\right), \tag{2.69}$$

where $N_0 = |\psi_{\mathrm{LP}}^{\mathrm{SS}}|_-^2 L^2$ is the total number of particles which populate the $\mathbf{k} = 0$ mode for a square lattice with side L.

The inclusion of a frequency dependence of the pump is able to regularise the behaviour of the momentum distribution at large k. If one calculates the momentum distribution of the steady state ψ^{SS}, it is possible to reveal the behaviour of the pump as a function of the frequency ω, namely

$$P_0(\omega) = P_0\left(1-\frac{\omega}{\Omega}\left(1+\frac{|\psi_{\mathrm{LP}}^{\mathrm{SS}}|_-^2}{n_{\mathrm{s}}}\right)\right). \tag{2.70}$$

As a consequence, while low-energy modes below the cut-off frequency

$$\omega_{\mathrm{cutoff}} = \frac{\Omega}{\left(1+\frac{|\psi_{\mathrm{LP}}^{\mathrm{SS}}|_-^2}{n_{\mathrm{s}}}\right)} \tag{2.71}$$

are amplified, being in the positive part of the pumping spectrum, modes greater than ω_{cutoff} are dumped.

A stochastic approach for the OPO regime

By making use of space-phase techniques as in the incoherent pump case, a stochastic formalism can be further derived also for the OPO model, Eq. (2.24). We note that different methods such as Keldysh field theory and Martin-Siggia-Rose (MSR) formalism (Sieberer *et al.*, 2016b), can be equivalently employed to obtain Fokker-Planck equations for the Wigner function truncated to the third-order (Carusotto and Ciuti, 2005, 2013). We then end up with a model (Dagvadorj *et al.*, 2015) which allows to solve the evolution of the coupled exciton and photon classical field $\psi_{\text{X,C}}$, in a finite grid with spacing a (and unit cell area $dV = a^2$). The generalised GPEs for the OPO regime read

$$id\begin{pmatrix}\psi_X\\ \psi_C\end{pmatrix} = \left[H_{\text{MF}}\begin{pmatrix}\psi_X\\ \psi_C\end{pmatrix} + \begin{pmatrix}0\\ F_p\end{pmatrix}\right]dt + \begin{pmatrix}\sqrt{\kappa_X}\,dW_X\\ \sqrt{\kappa_C}\,dW_C\end{pmatrix}, \tag{2.72}$$

where

$$H_{\text{MF}} = \begin{pmatrix}\frac{-\nabla^2}{2m_{\text{X}}} + g_{\text{X}}(|\psi_{\text{X}}|^2 - \frac{1}{\Delta V}) - i\kappa_{\text{X}} & \frac{\Omega_{\text{R}}}{2}\\ \frac{\Omega_{\text{R}}}{2} & \frac{-\nabla^2}{2m_{\text{C}}} - i\kappa_{\text{C}}\end{pmatrix}, \tag{2.73}$$

and dW_X and dW_C are the complex-valued zero-mean, white Wiener noise terms with

$$\langle dW_l^*(\mathbf{r},t)dW_m(\mathbf{r}',t)\rangle = 0, \tag{2.74}$$

$$\langle dW_l^*(\mathbf{r},t)dW_m(\mathbf{r}',t)\rangle = \delta_{\mathbf{r},\mathbf{r}'}\delta_{l,m}dt \tag{2.75}$$

Since $m_{\text{X}} \gg m_{\text{C}}$, the limit $m_{\text{X}} \to \infty$ is often considered and, consequently, the exciton field kinetic energy term disappears from Eq. (2.72). The TWA has been successfully used to investigate phase transition in OPO regime, thanks to the ability of these analytical models to describe strong fluctuations in the vicinity of the phase threshold (Dagvadorj *et al.*, 2015).

2.3.3 The Kardar-Parisi-Zhang (KPZ) theory for a nonequilibrium system

In order to study large phase fluctuations and their effects at long range limits, one can map the stochastic GPE for polaritons into a compact Kardar-Parisi-Zhang (KPZ) equation (Kardar *et al.*, 1986), a non-linear stochastic partial differential equation for the phase θ of the order parameter

$$\frac{\partial\theta}{\partial t} = D_{\text{x}}\frac{\partial^2\theta}{\partial x^2} + D_{\text{y}}\frac{\partial^2\theta}{\partial y^2} + \frac{\lambda_x}{2}\left(\frac{\partial\theta}{\partial x}\right)^2 + \frac{\lambda_y}{2}\left(\frac{\partial\theta}{\partial y}\right)^2 + \xi(\mathbf{r},t). \tag{2.76}$$

Here the phase θ at a time t evolves according to diffusive terms proportional to D_{i} and nonlinear terms proportional to λ_{i}, with $i = \{x, y\}$. The last term in Eq. (2.76) is a stochastic noise which satisfies the correlations $\langle \xi^*(\mathbf{r}, t)\xi(\mathbf{r}', t')\rangle = 2\sigma\delta(\mathbf{r} - \mathbf{r}')\delta(t - t')$ and $\langle \xi(\mathbf{r}, t)\xi(\mathbf{r}', t')\rangle = 0$. The KPZ equation is a nonlinear stochastic partial differential equation, which is largely used for the study of the physics of randomly growing interfaces (Whittaker, 2007), as well as growth of bacteria colonies (Wakita *et al.*, 1997) and theory of flocking (Toner and Tu, 1998). Eq. (2.76) can be considered to be an extension of the XY model, as we can see by considering the equilibrium case $\lambda_x = \lambda_y = 0$. Due to the addition of the two nonlinear terms, the KPZ equation is able to predict the decay of correlations at very long distances.

In order to determine the behaviour of the polariton system at long scales, renormalisation group analysis was employed for Eq. (2.76). It turned out that this length can be characterised by two dimensionless parameters which quantify nonlinearity,

$$g \equiv \frac{\lambda_{\mathrm{x}}^2 \Delta}{D_{\mathrm{x}}^2 \sqrt{D_{\mathrm{x}} D_{\mathrm{y}}}}, \tag{2.77}$$

and anisotropy

$$\Phi = \frac{\lambda_{\mathrm{y}} D_{\mathrm{x}}}{\lambda_{\mathrm{x}} D_{\mathrm{y}}}, \tag{2.78}$$

with Δ the noise strength of (2.76) (Altman *et al.*, 2015). One can therefore distinguish different regimes: nonlinearity dominates for $g > 1$, where stretched exponential decay occurs ("deep KPZ" phase), while diffusion dominates for $g < 1$, with algebraic decay of correlations, ("week KPZ" phase). For nonequilibrium systems, studies based on Eq. (2.76) revealed that geometrical isotropy plays a crucial role in the behaviour of correlations at large distances (Altman *et al.*, 2015).

Similar results have been worked out independently by (Gladilin *et al.*, 2014). In the case of an isotropic $2d$ system, even though the system lies deep in the superfluid phase, far from the critical point, it is able to exhibit a long-range decay of correlations characterised by two behaviours: algebraic order at short distances and exponential decay at very long scales. In these circumstances, superfluidity is therefore completely suppressed. However, the length one needs to reach for observing exponential decay is orders of magnitude higher than any reasonable experimental setup, as already proven experimentally by (Nitsche *et al.*, 2014; Caputo *et al.*, 2017), where just "pure" quasi-long range order has been observed.

2.4 Chapter summary

In this chapter we discussed the theoretical approaches for modelling nonequilibrium polariton condensates. We initially reviewed the well-known Gross-Pitaevskii equation for equilibrium Bose gases, steady state properties and the Bogoliubov theory of small excitations. Then we gave a detailed discussion of the theoretical methods developed for simulating static and dynamic properties of nonequilibrium condensates at a mean field level. We introduced the complex Ginzburg-Landau equation and derived a Gross-Pitaevskii equation for polaritons, which accounts for driving and losses of the system.

Polariton condensates can be generated by external stimulations of different nature, with each of those giving a particular characteristics to the system. Motivated by this, we described the theoretical methods for modelling the principal pumping mechanisms used in the lab. We discussed their more striking properties and compared those features of equilibrium models. Among the most important ones, the fact that a diffusive Goldstone mode characterises the nonequilibrium nature of a polariton system stands out. Following this, we introduce the description of thermal and quantum fluctuations by discussing the stochastic description. Specifically, we gave a detailed theoretical description of the model adopted in this thesis for simulating incoherently-pumped polariton condensate, and improve the physical description of such systems by the introduction of a pump with frequency dependence. Finally, we briefly introduced the KPZ theory for the study of the effects of large phase fluctuations in nonequilibrium systems.

Chapter 3

Numerical analysis of the driven-dissipative stochastic Gross-Pitaevskii equation

The stochastic GPE for polaritons, derived by means of the Truncated Wigner Approximation, Eqs. (2.65)-(2.67), describes theoretically the entire system dynamics for the lower polariton branch. The formulation and analysis of the numerical method previously introduced is illustrated in this chapter.

Initially, we present the rescaled stochastic Gross-Pitaevskii equation, and the choice of experimentally-relevant parameters. Then, we investigate boundary conditions and the pumping profile in order to define the optimum choice for studying the physics of the phase transition and dynamics of polariton condensates under realistically-implemented experimental conditions. We discuss the numerical observables of interest and illustrate a typical numerical experiment: from a nonequilibrium initial condition, we dynamically evolve to a steady state of the system.

Subsequently, we present some numerical studies based on the presented model. First, we discuss the issue of the ultraviolet (UV) divergence introduced by the numerical grid spacing. Then, we test the dynamics of the model by studying how fluid density responds when a weak perturbation is applied to the stationary state, and we compare the results with theoretical predictions of the Bogoliubov elementary excitation spectrum. In the final section we discuss the numerical technique employed for detecting topological defects. The studies undertaken in this section are important in order to define the optimal numerical conditions for the study of critical phenomena in polariton condensates.

3.1 Numerical implementation and parameter regime

3.1.1 Rescaling equations

Rescaling the model by means of the typical characteristic scales of the system is a standard procedure for its numerical implementation. The advantages are multiple: i) it reduces the number of free parameters, ii) it helps to check the consistency of model equations and iii) it reveals a smaller set of quantities that govern the dynamics of the problem investigated (Segel and Edelstein-Keshet, 2013). These characteristic scales typically correspond to the physical scales of the system considered.

Rescaling SGPE

In order to implement computationally the stochastic polariton GPE introduced in the previous chapter, we now derive a dimensionless form of the mean-field and stochastic models, Eqs. (2.32) and (2.65). In the case of polariton condensates, the timescale is normally set by the cavity polariton lifetime $\tau_{\rm pol}$, whereas the lengthscale is usually determined by the system confinement. For instance, in the case of an harmonically trapped system (Sanvitto *et al.*, 2009), the corresponding characteristic length is the harmonic oscillator length $l_{\rm trap} = \sqrt{\hbar/m\omega_{\rm trap}}$. For other types of confinement, such as periodic potentials (Ostrovskaya *et al.*, 2013), the characteristic length is chosen according to the polariton lifetime, so that $l_{\rm per} = \sqrt{\hbar/m\gamma_{\rm LP}}$. For the numerical study conducted in this work, quantities are made dimensionless by writing them in terms of the following characteristic scaling units for space, time and energy

$$l_0 = \sqrt{\frac{\hbar}{m_{\rm LP}\gamma_{\rm LP}}}, \qquad \tau_0 = \frac{1}{\gamma_{\rm LP}}, \qquad E_0 = \hbar\gamma_{\rm LP}. \tag{3.1}$$

As a consequence, rescaled dimensionless quantities are redefined according to

$$\mathbf{r} \to \frac{\mathbf{r}}{l_0}, \qquad t \to \frac{t}{\tau_0}, \qquad g_{\rm LP} \to \frac{m_{\rm LP}}{\hbar} g_{\rm LP}, \qquad P_0 \to \frac{P_0}{\gamma_{\rm LP}}, \qquad \Omega \to \frac{\Omega}{\gamma_{\rm LP}}, \tag{3.2}$$

where $\mathbf{r} = \{x, y\}$, such that the dimensionless 2d polariton SGPE reads

$$\begin{aligned} i\frac{\partial\psi_{\rm LP}(\mathbf{r},t)}{\partial t} = \left[-\frac{\nabla^2}{2} + g_{\rm LP}|\psi_{\rm LP}|^2_{-} + \frac{i}{2}\left(\frac{P_0(\mathbf{r},t)}{1+\frac{|\psi_{\rm LP}|^2_{-}}{n_s}} - 1\right) + \frac{1}{2}\frac{P_0(\mathbf{r},t)}{\Omega}\frac{\partial}{\partial t}\right]\psi_{\rm LP}(\mathbf{r},t) \\ + \sqrt{\frac{1+P_0(\mathbf{r},t)}{4\Delta V}}dW(\mathbf{r},t), \end{aligned} \tag{3.3}$$

Here $|\psi_{\rm LP}|^2_{-}$ corresponds to the physical density, determined according to standard procedures (Wouters and Savona, 2009) by $|\psi_{\rm LP}|^2_{-} = \left(\left|\psi_{\rm LP}(\mathbf{r},t)\right|^2 - 1/2\Delta V\right)$, due to the inclusion of the Wigner commutator as discussed in Sec. (3.1.5). The white Gaussian noise is correlated according to

$$\langle dW(\mathbf{r},t)dW(\mathbf{r}',t)\rangle = 0, \tag{3.4}$$

$$\langle dW^*(\mathbf{r},t)dW(\mathbf{r}',t)\rangle = 2\delta_{\mathbf{r},\mathbf{r}'}dt. \tag{3.5}$$

Rescaled mean field model (GPE)

It is straightforward to note that by simply removing the noise term dW in the stochastic model (2.65) (which physically corresponds to the removal of fluctuations from the problem investigated) we recover the mean field equation (2.32) for the wavefunction $\psi_{\rm MF}$. Hence, the stochastic polariton GPE simply corresponds to a generalisation of the mean field problem (2.32), which can therefore be rescaled by means of Eqs. (3.2). The dimensionless GPE then reads:

$$i\frac{\partial\psi_{\rm MF}(\mathbf{r},t)}{\partial t} = \left[-\frac{\nabla^2}{2} + g_{\rm LP}|\psi_{\rm MF}|^2 + \frac{i}{2}\left(\frac{P_0(\mathbf{r},t)}{1+\frac{|\psi_{\rm MF}|^2}{n_s}} - 1\right) + \frac{1}{2}\frac{P_0(\mathbf{r},t)}{\Omega}\frac{\partial}{\partial t}\right]\psi_{\rm MF}(\mathbf{r},t), \tag{3.6}$$

with $\psi_{\rm MF}$ the wavefunction of the coherent fraction of the system and where $|\psi_{\rm MF}|^2 = |\psi_{\rm MF}(\mathbf{r},t)|^2$. In a region of space with nearly constant density $|\psi_{\rm MF}|^2$, we can define a mean field characteristic length

$$\xi_{\rm MF} = \frac{\hbar}{\sqrt{2\, g_{\rm LP}\, n_0}}, \tag{3.7}$$

which corresponds to the lengthscale over which $\psi_{\rm MF}$ can change significantly. We can also think of the healing length as some kind of screening length: from the position where an obstacle is placed, it is not visible at distances larger than $\xi_{\rm MF}$.

3.1.2 Physical parameters

In order to make contact with experiments, the scaling units (3.1) are calculated using parameters close to those of the experimental setup described in (Nitsche *et al.*, 2014). The dimensional values of the parameters used in the simulations to obtain the main results shown in Part II are illustrated in Table 3.1, together with their dimensionless counterparts.

The polariton lifetime can be estimated by the cavity factor Q (which gives the photon lifetime $\tau_{\rm pol}$) and the Hopfield photon coefficient (which quantify the photon fraction

Table 3.1: Parameters

	dim	dimensionless
P_0	–	1.06
γ_{LP}	$0.22\ \mathrm{ps}^{-1}$	1
n_s	$500\mu\mathrm{m}^{-2}$	4.12×10^3
g	$6.82\ \mu eV\,\mu m^2$	5.58×10^{-3}
Ω	$11.09\ \mathrm{ps}^{-1}$	50

in each branch of the microcavity dispersion relation). From Eq. (3.1), the frequency corresponding to the polariton lifetime $\tau_{\mathrm{pol}} = 4.51$ ps, reads

$$\gamma_{\mathrm{LP}} = 0.22\ \ \mathrm{ps}^{-1}. \tag{3.8}$$

The effective mass of the lower polariton, m_{LP}, is calculated by fitting a parabola to the lower branch of the dispersion relation (see left picture of Fig. 2(a) in (Nitsche *et al.*, 2014)), which is estimated to be

$$m_{\mathrm{LP}} = 5.68 \times 10^{-35}\ \mathrm{kg}, \tag{3.9}$$

which corresponds to $m_{\mathrm{LP}} = 3.17 \times 10^4\ \mathrm{meV/c^2}$. The interaction strength depends on the characteristic of the quantum well material, which in the case of GaAs, is estimated to be approximately

$$g_{\mathrm{LP}} = 6.815\ \ \mu\mathrm{eV}\ \mu\mathrm{m}^{-2}. \tag{3.10}$$

Apart from the parameter P_0, which takes the role of the "control parameter" of the system, the parameters Ω and n_{s} are typically unknown, in principle depending on the characteristics of the pump mechanism. Unfortunately, these parameters are not possible to extract from a standard experiment (Caputo *et al.*, 2017). Hence, in order to account for their contribution, we estimate appropriate values. The cutoff energy $\hbar\Omega_{\mathrm{R}} = 7.3\ meV$ is chosen to be of the order of the Rabi-splitting energy [$\Omega_{\mathrm{R}} \approx 9.6$meV from (Nitsche *et al.*, 2014)], whereas the saturation density value is chosen as $n_{\mathrm{s}} \approx 1000\mu\mathrm{m}^{-2}$.

3.1.3 Numerical parameters

System size

Exciton polaritons are quasiparticles resulting from the strong coupling between quantum well excitons and light. Quantum wells are planar devices consisting of several thin layers of materials with different bandgap. Due to the particular geometry, the motion of excitons is thus confined to a 2d space. Experimentally, quantum wells are manufactured in planar geometries typically of the order of magnitude of $100 \times 100\mu\mathrm{m}^{-2}$. For instance,

$L \approx 30\mu$m (Nitsche *et al.*, 2014), $L \approx 160\mu$m (Amo *et al.*, 2009b), $L \approx 50\mu$m (Sun *et al.*, 2017), $L \approx 150\mu$m (Caputo *et al.*, 2017).

In order to computationally study universal phenomena in polariton condensates, one generally attempts to solve the model in a system which is as large as possible. Considering large samples has some advantageous implications. Firstly, the system can accommodate a high number of topological defects; this enables us to obtain more precise averages with smaller error bars. Secondly, larger grids facilitate long-range behaviour to be probed, which is crucial for the characterisation of the decay of spatial correlation, i.e. the type of order exhibited by the system. This becomes more clear in Sec. 4.3.2, where we use the decay of correlations to characterise the nature of the phase transition.

On the other hand, implementing large systems is computationally costly. The right choice of system size, therefore, results from a compromise among i) solving in the largest box possible, ii) minimizing computational costs, and iii) matching experimental parameters. Following such requirements, the main results of this thesis have been obtained in a square grid of side $L \sim 283.3\mu$m [98 l_0] with 289 grid points (i.e. the numerical spatial grid spacing reads $a = 0.98\mu$m [0.34 l_0]).

Choice of numerical discretisation

In this section, the numerical conditions for an accurate description of the system by the model considered, are discussed. An important role on the validity of our numerics is played by the grid spacing a.

The first condition relates to the reliability of the model from a physical point of view. In order to correctly describe the system, the spatial grid spacing a typically needs to be chosen smaller than the other system scales. There is a physical condition that the kinetic energy term has to dominate over the other energy scales. The grid spacing is directly linked to the kinetic energy as $E_{\rm kin} = \hbar^2/(2m_{\rm LP}a^2)$. This condition yields (here we consider dimensional quantities)

$$\frac{E_{\rm kin}}{\hbar\gamma_{\rm LP}} \gg 1, \qquad \frac{E_{\rm kin}}{g|\psi_0|^2} \gg 1, \tag{3.11}$$

where we implicitly consider the energy injected by the pump to be of the order of magnitude of the system losses. In order to correctly describe the physics of topological defects, the grid size is required to be smaller than the healing length, (which is usually associated with half of the size of the vortex core ξ (Pitaevskii and Stringari, 2003)); this

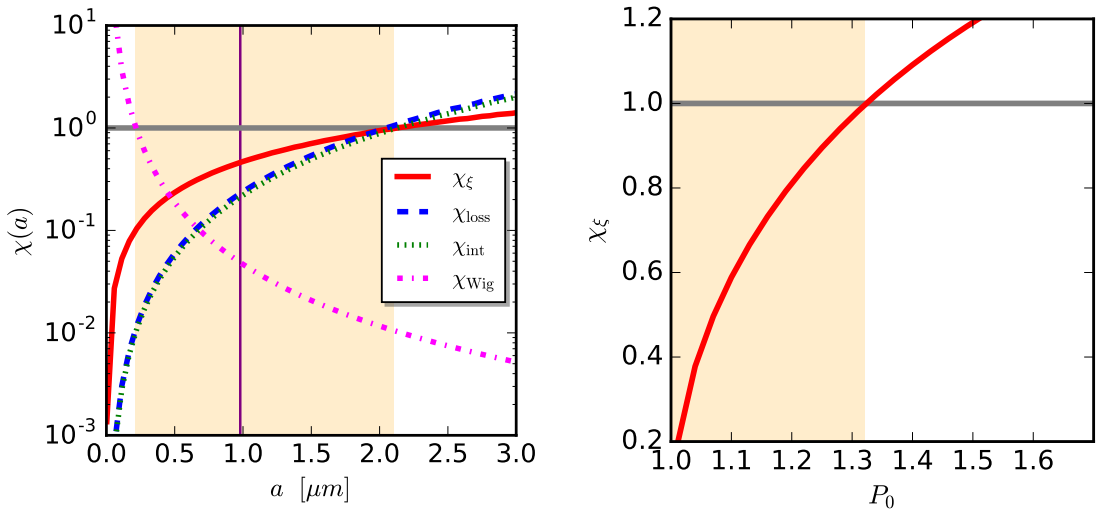

Figure 3.1: **Numerical validity conditions.** The TWA method places rigid constraints on the available range for lattice spacing. Left panel illustrates the faint orange shadowed region where dimensionless parameters $\chi_{\rm loss}$, $\chi_{\rm int}$, χ_ξ, $\chi_{\rm Wig}$ satisfy the validity condition (< 1) for $P_0 = 1.06$ (with other parameters given in Table 3.1). The vertical purple line corresponds to the grid spacing choice utilised for obtaining the main results discussed in Part II of this thesis. Right panel shows the pump power variation of the dimensionless parameter χ_ξ.

translates into the condition

$$\frac{a}{\xi} \ll 1. \tag{3.12}$$

The second condition is directly related to the validity of the method chosen, i.e. to the TWA method. In order to justify the Wigner truncation, the first order derivative terms of Eq. (2.59) need to predominate over the cubic derivatives. As discussed in Sec. 2.3.1, this condition translates into

$$a^2 \gg \frac{g_{\rm LP}}{\gamma_{\rm LP}}. \tag{3.13}$$

We note this condition sets a lower bound for the grid spacing utilised for our computations. Another issue associated with the grid spacing a is the presence of an ultraviolet divergence, which we are going to discuss in Sec. 3.3.1.

To better visualise these numerical limits, we rewrite Eqs. (3.11)-(3.13) as

$$\begin{aligned} \chi_{\rm loss} &= \frac{\gamma_{\rm LP}}{E_{\rm kin}} \ll 1, \qquad & \chi_{\rm int} &= \frac{g|\psi_0|^2}{E_{\rm kin}} \ll 1, \\ \chi_\xi &= \frac{a}{\xi} \ll 1, \qquad & \chi_{\rm Wig} &= \frac{g_{\rm LP}}{a^2\gamma_{\rm LP}} \ll 1, \end{aligned} \tag{3.14}$$

so that the conditions are all in terms of small physically-intuitive dimensionless parameters $\chi_{\rm loss}$, $\chi_{\rm int}$, χ_ξ, $\chi_{\rm Wig}$ ($\ll 1$). In Fig. 3.1 (a) we plot the grid spacing variation of the quantities above in the case of a pump strength used for the study conducted in Part II of this thesis, i.e. $P_0 = 1.06$. It is straightforward to note that, based on the combination of all above constraints, a specific validity window for the grid spacing appears (shown by the orange faint region) satisfying

$$\sqrt{\frac{g_{\rm LP}}{\gamma_{\rm LP}}} \ll a \ll \xi. \tag{3.15}$$

We note that the lower bound of the validity window, Eq. (3.15), is set by the strength of interactions and losses and does not therefore depend on the control parameter P_0. On the contrary, the upper bound is inversely proportional to the square root of the (mean-field) coherent density, see Eq. (2.18), which, in turn, increases almost proportionally to the pump strength P_0. In order to study the dependence of the orange area on the pump strength P_0, we calculate the value of a such that $\chi_\xi(P_0) = 1$. We find that for very low pump strengths compared to threshold, and above, the valid window expands according to $a[\xi(P_0 = 1.001), \chi_\xi = 1] \gg 1$. On the other side, at higher pumps we find $a(\xi(P_0 \approx 2), \chi_\xi = 1) \approx 0.8$.

We identify the optimum choice for the grid spacing $a_{\rm opt}$ —for the case illustrated in Fig. 3.1 (a)— to be $a_{\rm opt} \approx 0.5$. However, one has to consider that computational costs tend to increase rapidly if a decreases (Dennis *et al.*, 2013). To obtain the results discussed in Part II of this thesis, we find a compromise by choosing $a_{\rm sim} = 0.98$ (purple solid vertical line in Fig. 3.1 (a)). We ensure the validity of our results by testing the physically-interesting quantities against those with smaller grid spacing. The dependence of the parameter χ_ξ on the pump strength is shown in Fig. 3.1 (b), from which we can extract a "validity window" for the pump strength, for the given $a_{\rm sim}$ used for obtaining the main results of this thesis.

3.1.4 Choice of pump profiles and boundary conditions

Here we study the emerging numerical density profiles under different pumping schemes and boundary conditions, in order to determine the optimum setting for the study of phase transitions.

First, we investigate whether quench dynamics can be meaningfully studied in finite size condensates [as opposed to large (infinite) systems], under a uniform pump $P_0(\mathbf{r}, t) = P_0$. We focus on the numerical solution we obtain for the condensate profile obtained by averaging many realisations of the Wigner function once the system has reached a steady

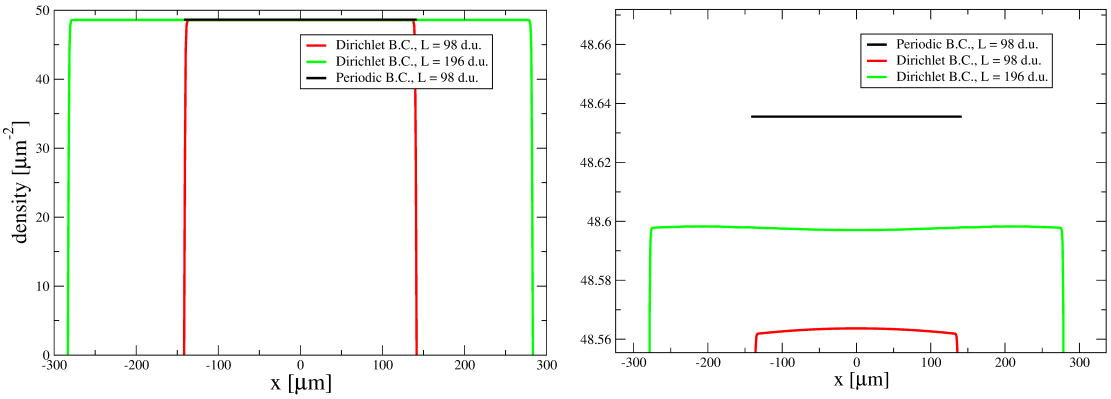

Figure 3.2: **Boundary conditions.** Density profiles at steady state $|\psi_{\rm LP}^{SS}(\mathbf{r} = (0, x))|^2$ solved with DBC for $L \sim 147\mu$m (red curve) and $L \sim 295\mu$m (green curve) versus PBC (black line), for $P_0 = 1.2$ (with other parameters given in Table 3.1). Right panel illustrates a zoom in the high density region.

state. Generally, a stationary configuration is achieved by propagating the differential equations Eq. (3.3). These need to be implemented in a computational grid based on the conditions discussed in Sec. 3.1.3. For this study, a square computational grid with sides $L_x = L_y$ is chosen such that grid spacing reads $a = L_x/n_x = L_y/n_y$, where $n_x = n_y$ is the number of points along each of the two dimensions of the system (x, y), such that the wavefunction along each direction reads $\psi_{\rm LP}(x, 0, t)$ with $x_{\rm i} \in [-L_{\rm i}/2, L_{\rm i}/2]$. The solution of ordinary or partial differential equations in the presence of a boundary, requires a choice of boundary conditions for the solution. In order to simulate a finite-size polariton condensate, a typical approach is to force the edges of the system to zero values, i.e. to set the wavefunction such that

$$\psi_{\rm i}(-L_{\rm i}/2, t) = \psi_{\rm i}(L_{\rm i}/2, t) = 0. \tag{3.16}$$

In this case, one needs to implement *Dirichlet Boundary Conditions* (DBC), which requires specifying the value of the solution at the boundaries. On the other hand, one might be interested in simulating a large (infinite) system. A typical mathematical simplification consists in solving the system with *Periodic Boundary Conditions* (PBC), which generally consists in propagating the system with the condition that the solution on the boundary on the one side of the grid is identical to the one on the other side, namely

$$\psi_i(-L_i/2, t) = \psi_i(L_i/2, t). \tag{3.17}$$

In figure 3.2 we compare the steady state density profiles $|\psi_{\rm LP}^{\rm SS}(x, 0)|^2$ as a function of x calculated with DBC and PBC by solving Eq. (3.6) with the parameters of Table 3.1. By focusing on the density profile, shown in Fig. 3.2(b), we find the profile calculated by

means of PBC to be flat; the same applies to the phase of the sample. On the contrary, due to the choice of (fixed) boundaries, the profile calculated with DBC (red solid) is slightly curved compared to the one calculated with PBC (black solid). The bending is still recognizable for double-size ($2L_x$) boxes (green solid). We attribute this bending to either a numerical artefact or to the system geometry. Thus, from here on we decide to solve our system with PBC.

We also extend our study to a spatially-dependent pumping term $P_0(x)$. In the experiments two different pump profiles have been used, namely the top-hat (Roumpos *et al.*, 2012) and Gaussian-shaped (Nitsche *et al.*, 2014) pumping beams. Unlike the case of a flat pump, the system is now always solved with DBC, which simulate the density depletion at the boundary of the laser. The top-hat-formed driving has been specifically chosen by experimentalists to recreate uniform condensate densities (Nitsche *et al.*, 2014). The top-hat pump profile $P_0(x, 0)$, flat in the centre and smooth at the edges, has the form:

$$P_0(x,0) = \begin{cases} P_0 \frac{\tanh\left(5\left(-\left(\frac{|x|-h}{L/2-h}\right)+\frac{1}{2}\right)\right)+1}{2}, & \text{if } |x| > h\frac{L}{2} \\ P_0, & \text{if } |x| < h\frac{L}{2} \end{cases} \tag{3.18}$$

where h corresponds to the ratio between the length of the central flat part of the pump to the size of the box. Alternatively, we have used a Gaussian pump profile of the form:

$$P_0(\mathbf{r}) = P_0 e^{-2\left(\frac{\log(2)}{\sigma}\right)^2 \mathbf{r}^2} \tag{3.19}$$

with σ the FWHM (full width at half maximum) of the peak. Both pumping profiles are illustrated in Fig. 3.3 (a). In Figure 3.3 (b) we show steady state density profiles for top-hat beams, for different values of h. We note that increasing h, the value in the central flat part increases as well, approaching the value obtained with a flat pump. From this analysis we conclude that, due to the presence of polariton currents in top-hat and closed-box geometries, solving the system with periodic boundary conditions and a flat pump is preferable.

3.1.5 Physical observables

Stochastic and mean-field modelling of exciton-polaritons are powerful tools which are able to reproduce numerically a vast number of experiments, e.g. (Kasprzak *et al.*, 2006; Lagoudakis *et al.*, 2008; Caputo *et al.*, 2017). Experimentally, information on physical quantities such as density of the macroscopically occupied state and its coherence are extracted from the light leaving the cavity. In our models, these quantities are directly extracted from the numerical wavefunction $\psi_{\mathrm{LP}}(\mathbf{r}, t)$, which specifies the density and

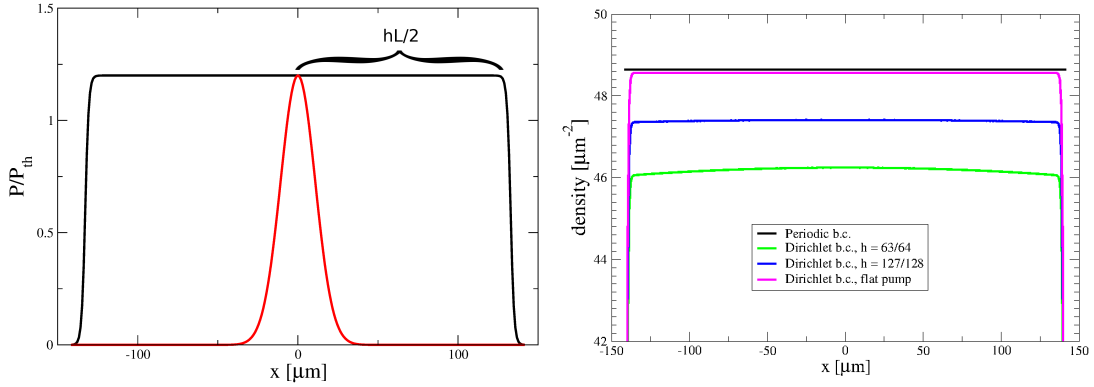

Figure 3.3: **Pumping profiles and relative steady state densities.** Left panel displys spatial profiles $P_0(\mathbf{r} = (0, x))$ for top-hat pump, corresponding to Eq. (3.18) with $h = 7/8$ (black curve), and Gaussian pump, Eq. (3.19) (red curve). Right panel shows the comparison among density profiles $|\psi^{SS}_{\rm LP}(\mathbf{r} = (0, x))|^2$ calculated with PBC (black line) and top-hat pump profiles with different values of $h = 63/64, 127/128, 1$ (colored lines), calculated with DBC. Parameters as in Fig. (3.2).

phase of the field.

In the case of a uniform system implemented on the polariton GPE, the mean field density at a time t is usually defined as the space average of the density at each point $\mathbf{r} = (x, y)$, which yields

$$n_{\rm LP}(\mathbf{r}, t) \equiv \langle n_{\rm LP}(\mathbf{r}, t)\rangle_{\mathbf{r}} = \left\langle \psi^{\dagger}_{\rm LP}(\mathbf{r}, t)\psi_{\rm LP}(\mathbf{r}, t)\right\rangle_{\mathbf{r}}. \tag{3.20}$$

If instead one considers stochastic modelling, one needs to take into account the contribution of the noise. In Sec. (2.3.1) we discussed the general rule for calculating the average expectation value of any observable within the TWA method. Using the correspondence between moments of the Wigner function and symmetrised operator products, Eq. (2.50), we find that for the field density

$$\left\langle |\psi_{\rm LP}(\mathbf{r}, t)|^2\right\rangle_W = \frac{1}{2}\left\langle \hat{\psi}^{\dagger}_{\rm LP}(\mathbf{r}, t)\hat{\psi}_{\rm LP}(\mathbf{r}, t) + \hat{\psi}_{\rm LP}(\mathbf{r}, t)\hat{\psi}^{\dagger}_{\rm LP}(\mathbf{r}, t)\right\rangle \tag{3.21}$$

$$= \left\langle \hat{\psi}^{\dagger}_{\rm LP}(\mathbf{r}, t)\hat{\psi}_{\rm LP}(\mathbf{r}, t)\right\rangle + \frac{1}{2}\left\langle \left[\hat{\psi}_{\rm LP}(\mathbf{r}, t), \hat{\psi}^{\dagger}_{\rm LP}(\mathbf{r}, t)\right]\right\rangle \tag{3.22}$$

$$= |\psi_{\rm LP}(\mathbf{r}, t)|^2_{-} + \frac{1}{2\Delta V}\delta_{\mathbf{r},\mathbf{r}}, \tag{3.23}$$

where $\langle \dots \rangle_W$ denotes the average over the Wigner quasi-distribution function. The total density of polaritons $|\psi_{\rm LP}(\mathbf{r}, t)|^2_{-} \equiv \langle \hat{n}_{\rm LP}(\mathbf{r}, t)\rangle$ calculated in a $2d$ lattice with spacing area $a^2 = \Delta V$, yields

$$|\psi_{\rm LP}(\mathbf{r}, t)|^2_{-} = \left\langle |\psi_{\rm LP}(\mathbf{r}, t)|^2\right\rangle_W - \frac{1}{2\Delta V}. \tag{3.24}$$

Concerning the first order correlation function, where translational invariance ensures

that all two-point correlators depend only on the distance $(r-u)$, we find

$$g^{(1)}(r,t)=\frac{\langle\psi^*(r+u,t)\psi(u,t)\rangle-\frac{\delta_{r+u,u}}{2\Delta V}}{\sqrt{\langle|\psi(r+u,t)|^2_-\rangle\langle|\psi(u,t)|^2_-\rangle}}\,, \tag{3.25}$$

which allows us to access information on the nature of coherence within the system. It is worth noting that both Eqs. (3.24) and (3.25) confirm the necessity of discretisation of the problem in order to avoid divergence of the physical observables, which would possibly appear in the continuous limit $\Delta V\to 0$.

3.2 Typical dynamical evolution

3.2.1 Typical generation of a non-equilibrium steady state

In this section we illustrate a typical numerical experiment, where the steady state of a uniform polariton condensate is reached from a disordered configuration. Quantum and thermal fluctuations are included within the field $\psi_{\rm LP}(\mathbf{r})$, which describes the lower polariton branch, and is numerically propagated in time by means of Eq. (3.6). The wave function $\langle\psi_{\rm LP}(\mathbf{r})\rangle$ is initialised as

$$\langle\psi_{\rm LP}(\mathbf{r},t=0)\rangle=0; \tag{3.26}$$

the growth process is introduced by the noise term proportional to dW, characteristic of either a highly nonequilibrium state, or an equilibrium disordered phase configuration. In this manner, all low-lying coherent modes, described by $\psi_{\rm LP}$, are highly occupied, as required by the classical field theory (Proukakis and Jackson, 2008; Blakie *et al.*, 2008). The initial noise, distributed uniformly over space, follows a Gaussian distribution, therefore the initial state $\psi_{\rm LP}(\mathbf{r},t=0)$ consists of a set of random variables which follow the rules of a Gaussian time-independent distribution, according to Eq. (3.5)

$$\langle\psi_{\rm LP}(\mathbf{r},t=0)\psi_{\rm LP}(\mathbf{r}',t=0)\rangle = 0, \tag{3.27}$$

$$\left\langle\psi^*_{\rm LP}(\mathbf{r},t=0)\psi_{\rm LP}(\mathbf{r}',t=0)\right\rangle = \frac{1}{2\Delta V}\delta_{\mathbf{r},\mathbf{r}'}. \tag{3.28}$$

Physically, this corresponds to include some noise in each mode of the field $\psi_{\rm LP}$, up to a momentum $k_{\rm max}=2\pi/a$, so to emulate quantum noise.

A typical dynamical growth to a nonequilibrium steady state is represented in Fig. 3.4. Here we show the computed density of the field $|\psi_{\rm LP}|^2$, according to (3.24) (red solid line), and we compare it with the mean field growth obtained by solving Eq. (3.6) for $\psi_{\rm MF}$ (blue

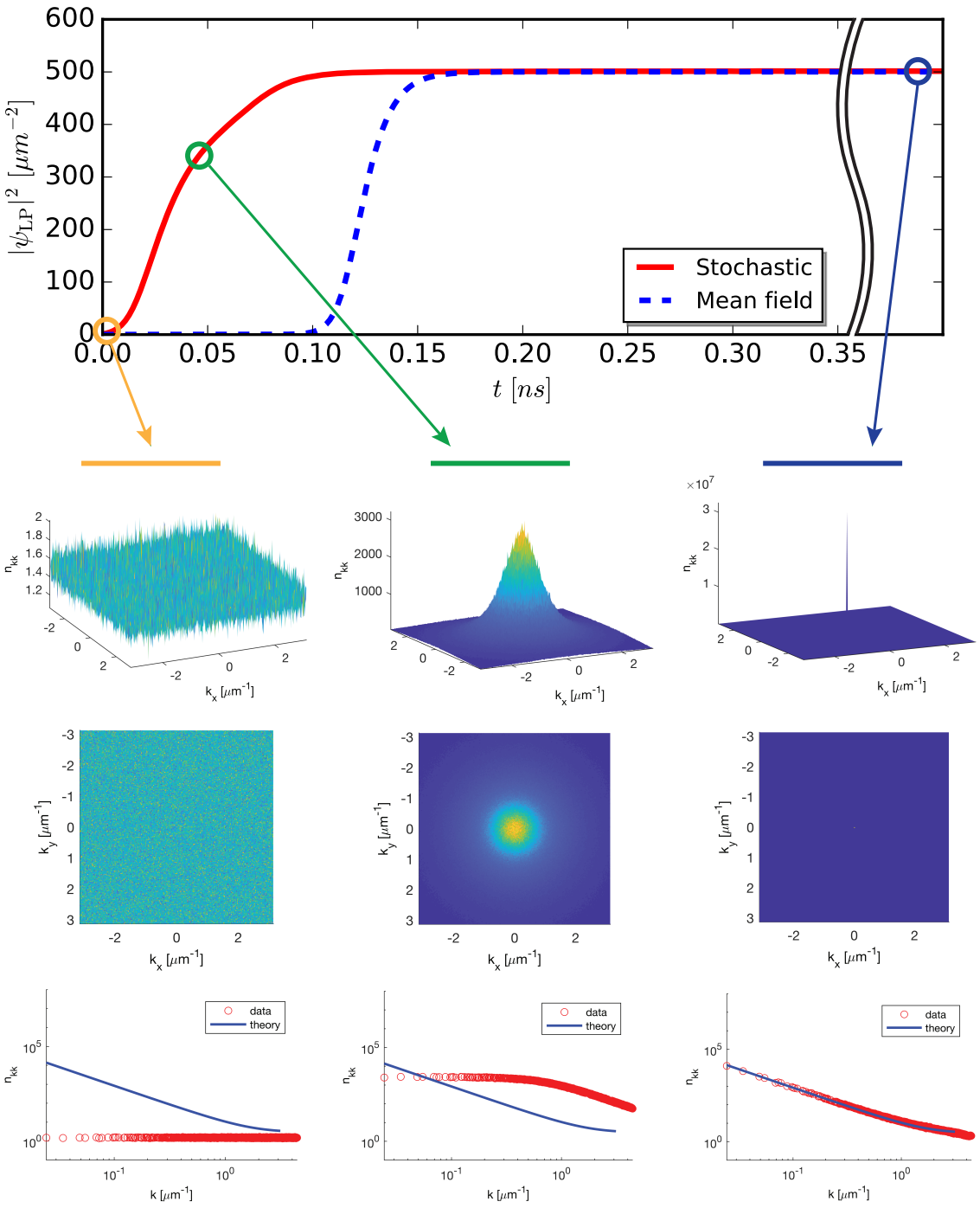

Figure 3.4: **Dynamical growth.** Time evolution of mean field (blue dashed) and average stochastic densities (red solid) are shown in top panel for $P_0 = 2$, $\Omega = \infty$ and others parameters given in Table 3.1. The time where the density starts to grow in the mean field calculation is determined on the wavefunction initial condition. We show the distribution of particles for three key snapshots of the evolution: initial configuration (orange circle), the middle of the growth (green circle) and steady state (blue circle). The latter is calculated at a time $t = 22.45ns$. For each point we show a 3d plot of the distribution of particles (first row), its projection on the plane (middle row) and the integrated momentum distribution (bottom row). In the latter, we compare computational points (red dots) with theoretical prediction calculated at steady state (blue line).

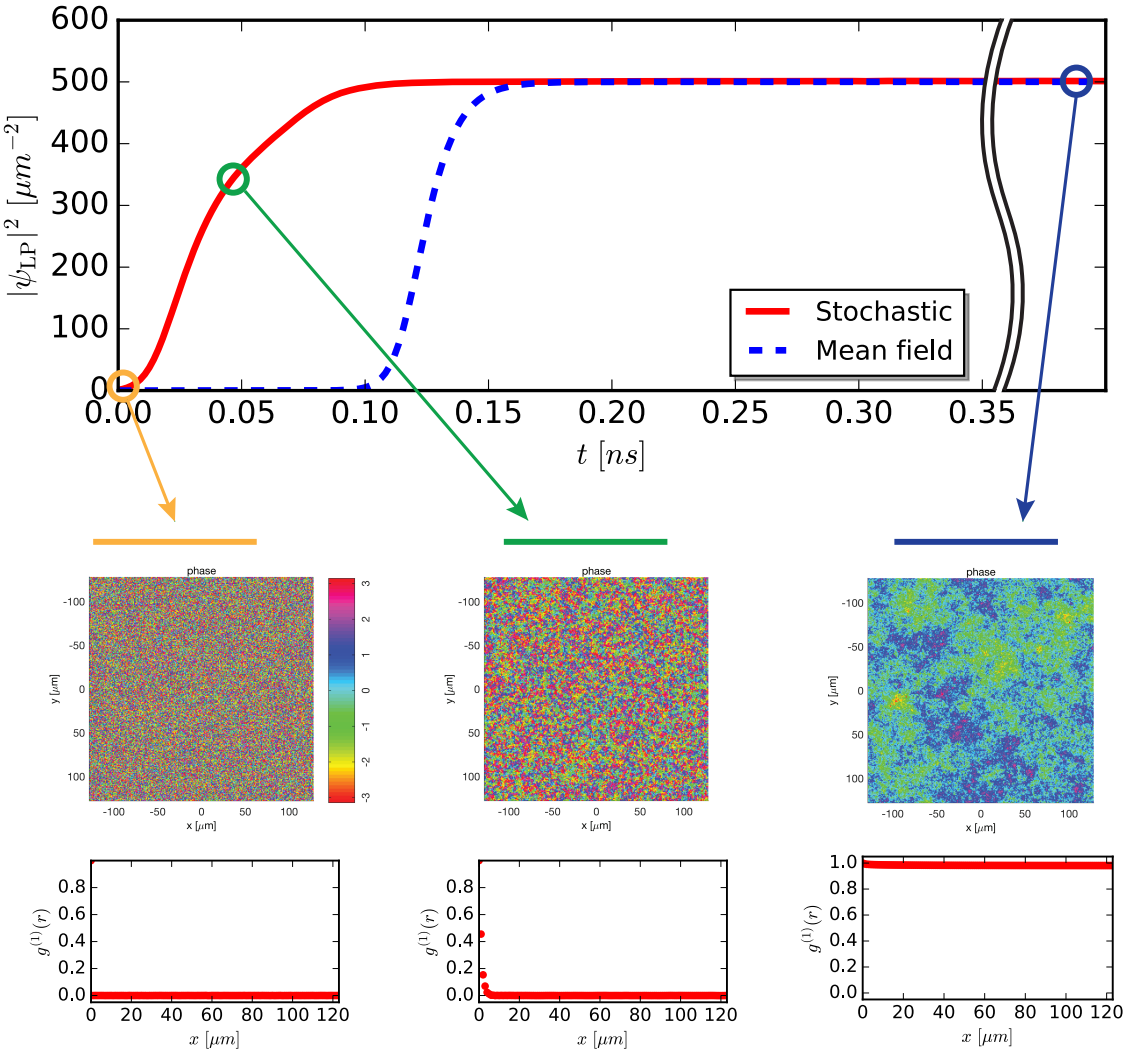

Figure 3.5: As in Fig. 3.4, but with phase depicted in the first row and spatial first order correlation function in the bottom row.

dashed line). The initial noise configuration at $t = 0$ (black circle) is driven to a steady state (green circle) as a result of the balance between driving and losses of the system. The nonequilibrium steady state is achieved when the average density reaches a constant value.

To obtain a better understanding of the system, in Fig. 3.4 we illustrate the calculated main physical quantities at different times of the growth process (solid coloured circles). Given the numerical wavefunction $\psi_{\rm LP}(\mathbf{r})$, it is straightforward to compute the momentum distribution of particle density $n_{\mathbf{k}}$, which we show in panels (a) and (b) of Fig. 3.4. Panel (a) describes a 3d plot of the distribution of particles as a function of the momentum space where a fixed momentum is identified by $\mathbf{k} = (k_x, k_y)$. Panel (b) consists of the

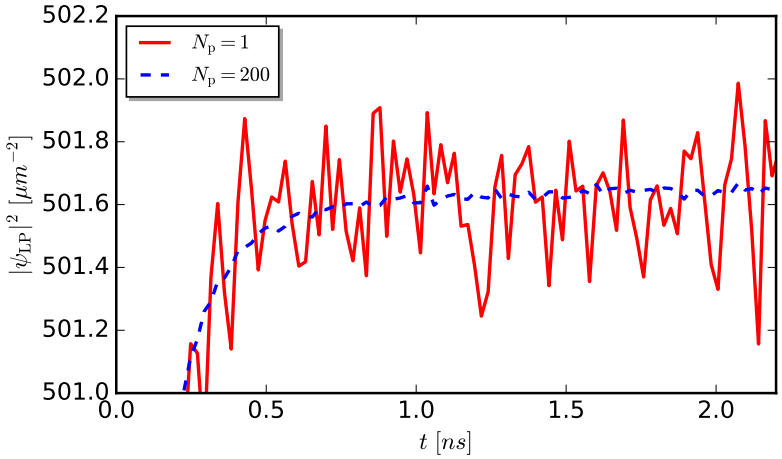

Figure 3.6: **Stochastic growth.** Average density obtained from Eq. (3.3). Comparison between single run (solid red) and averaged (dashed blue) density growth over $N_{\rm p} = 200$ stochastic paths. Parameters as in Table 3.1.

2d projection of the same in the **k**-plane. The integrated distribution is shown in figure (c); comparison with the theoretical prediction, Eq. (2.45) is given. In panel (c) and (d) we report the plots of density and phase of the polariton condensate. We can clearly distinguish topological defects, namely vortices, which gradually decay as the steady state is approached. Panel (e) shows the first order correlation function $g^{(1)}(\mathbf{r}, t)$, calculated according to Eq. (3.25). We refer to Ch. 3.3 for a detailed analysis on the steady state physics and dynamics of polariton condensates.

3.2.2 Stochastic averaging

A feature of dynamical equilibrium is that the density is characterised by fluctuations which are different from realisation to realisation. Eventually, these fluctuations are washed away by the statistical averaging over many realisations. This is clearly shown in Fig. 3.6, where we compare the density of a single run and the averaged density of $N_{\rm p} = 200$ realisations. In this vein, the numerical procedure adopted for solving Eq. (3.3) closely resembles a typical experimental procedure of Bose particles (Proukakis and Jackson, 2008; Blakie *et al.*, 2008), which consists in repeating the same experiment many times, and subsequently averaging over the different realisations, e.g. (Kasprzak *et al.*, 2006; Caputo *et al.*, 2017).

3.3 Benchmarking and testing our model

In this section, numerical studies of the models illustrated so far are discussed. Initially, equilibrium properties are studied: the cutoff introduced by the spatial grid is discussed

and the numerical momentum distribution of particles is tested by comparison to theoretical predictions. Subsequently, the dynamical properties are tested by numerical calculations of the Bogoliubov excitations spectrum.

3.3.1 Equilibrium properties: grid cutoff and momentum distribution

The inclusion of thermal and quantum fluctuations makes the stochastic GPE for polaritons a suitable tool for the study of steady state properties of systems with many degenerate modes. This is in contrast with the physical description provided by the solution of the polariton GPE, where the wavefunction ψ_{MF} only defines the single macroscopically-populated state of the system. Within the stochastic GPE, in fact, the wavefunction ψ_{LP} characterises not only the ground-state of the system, but includes a group of low-energy modes, which are assumed to be well described by a classical field (Carusotto and Ciuti, 2013). The modes which are included into the coherent field are set by the momentum cutoff k_{max}. Thus, fluctuations with momentum $k > k_{\mathrm{max}}$ are not considered into the coherent field. When computationally implemented in a numerical grid, the stochastic model is known to exhibit instabilities at high momenta, potentially leading to diverging physical observables. This is due to the momentum cutoff k_{max} being related to the numerical grid spacing a, through the relation

$$k_{\mathrm{max}} = \frac{\pi}{a}. \tag{3.29}$$

Therefore, as the continuum limit $a \to 0$ is approached, the cutoff increases and more modes are considered.

This issue is well-known in computational science (Gottlieb and Orszag, 1977) and, in order to avoid this problem, many solutions have been proposed. In the context of ultracold atom systems, a possible approach consists of estimating the particle distribution in the ideal-gas limit through a modified single-particle Hamiltonian (Sinatra *et al.*, 2007; Sinatra and Castin, 2008). An alternative method involves adjusting "by hand" the grid spacing of interacting gases simulations to match the experimentally measured occupation of the coherent fraction with those of the ideal gas at the same temperature (Brewczyk *et al.*, 2007). A detailed investigation on the cutoff dependence for an equilibrium system described by the stochastic GPE for Bose atoms has been conducted in (Cockburn and Proukakis, 2009; Blakie, 2008; Cockburn, 2010). More precisely, by solving the stochastic method implemented in a $2d$ numerical grid, the divergence of the coherent population as a function of the grid spacing a has been found to be $\propto \log(k_{\mathrm{max}}) = \log(\pi/a)$.

Concerning stochastic modelling of polaritons a detailed characterisation of the op-

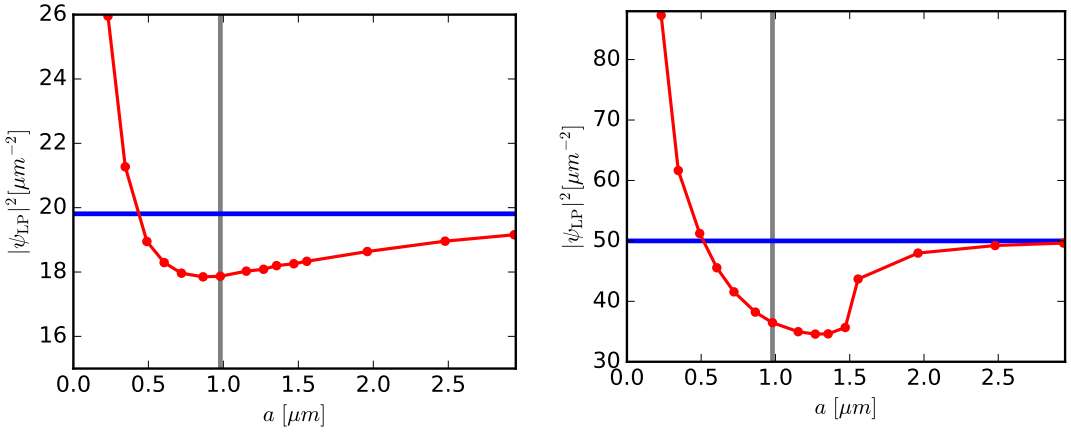

Figure 3.7: **Cutoff analysis and UV divergence.** Shown is the average density of the stochastic polariton GPE, $|\psi_{\rm LP}|^2$ (red curve), against grid spacing a for $P_0 = 1.06$, $\Omega = 50$, $n_{\rm s} = 500\mu{\rm m}^{-2}$ (left) and $P_0 = 1.1$, $\Omega = \infty$, $n_{\rm s} = 500\mu{\rm m}^{-2}$ (right), with other parameters given in Table 3.1. Computational mean field values $|\psi_{\rm MF}|^2$ (blue horizontal lines) are reported for both cases.

timal choice of $k_{\rm max}$ (or a) is still undetermined. However, it is still possible to identify some criteria which would eventually lead to a correct description of experiments by numerical methods. A detailed approach is given in Sec. 3.1.3 of this thesis. A typical ultraviolet divergence is shown in Figure (3.7), where we compare mean-field and stochastic steady state densities (dashed line and points, respectively) obtained solving Eq. (3.3) as a function of the grid spacing a. We present the same analysis for two values of P_0. The divergence at small a decreases at higher values of P_0. It is noteworthy to mention that the choice of the cutoff of numerical simulations presented in this thesis is comparable to the one of numerical measurements of spatial coherence of polariton condensates which successfully reproduced experimental results, e.g. (Caputo *et al.*, 2017).

A further approach to regularise the UV divergence behaviour at large $\mathbf{k}$ (small a) is to introduce a frequency dependence in the pump. As discussed in Sec. 2.2.4, by adding a time-derivative term in the Hamiltonian of the system, as in Eq. (2.37), the distribution of particles $n_{\mathbf{k}}$ would tend to zero instead of to a constant value. Thus, the integral of particle density $n_{\mathbf{k}}$ over space does now take a value which is finite. The dependence of particle density distribution $n_{\mathbf{k}}$ on the wavevector for the steady state has been discussed in Sec. 2.3.2 for both cases of a pump with frequency-dependence ($\Omega \neq \infty$) and without ($\Omega = \infty$). The explicit forms of the spectrum have been reported, Eq. (3.6) and Eq. (3.3), respectively. In Fig. (3.8) we plot the angular integrated momentum distribution of particles calculated averaging over 100 realisations for both cases, and we compare them with their analytical prediction, i.e. Eq. (2.68). Remarkably, we find good agreement among the analytical and numerical curves, suggesting that our model is able

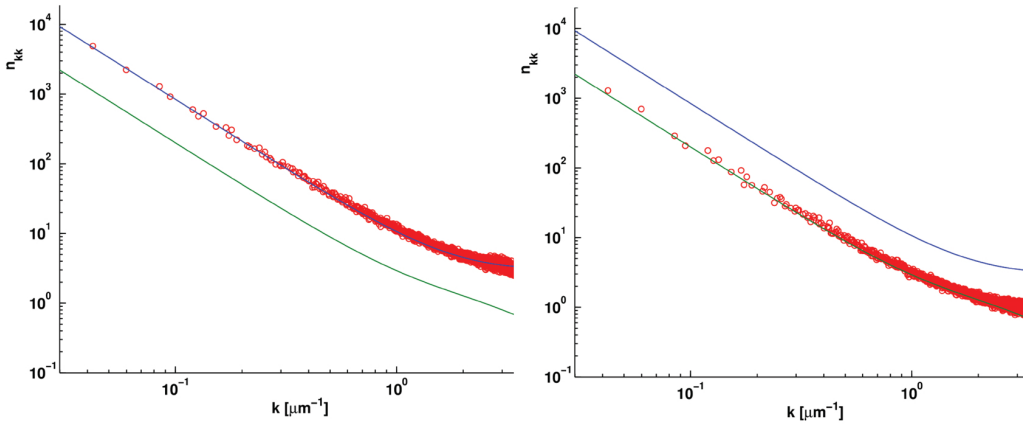

Figure 3.8: **Momentum distribution of particles.** Comparison between theoretical prediction of distribution of particle at steady state, Eq. (2.68), and computational data (red circles) obtained by solving Eq. (3.3) for a pump with frequency independence, $\Omega = \infty$ (left) and frequency dependence, $\Omega = 50$, (right). The theoretical curves calculated by means of Eq. (2.68) for $\Omega = \infty$ and $\Omega = 50$, are shown in both plots as blue and green solid lines, respectively. We average over 100 stochastic paths for $P_0 = 2$; other parameters are given in Table 3.1

.

to recover the predicted equilibrium features.

3.3.2 Dynamical properties: elementary excitation spectrum

In the previous section we discussed validity conditions and tested whether our model is able to reproduce the expected equilibrium results. In this section we concentrate on testing the dynamics. A simple way of approaching this problem is to probe the response of the mean-field fluid density, when a weak perturbation potential pulse is applied to the fluid at a given space and time, e.g.

$$V(\mathbf{r}, t) = V_0 \delta(t - t_0), \tag{3.30}$$

where t_0 is a time well after the equilibrium has been reached. By taking the space-time Fourier transform of the density in response to the potential pulse, one should be able to recover the Bologoliubov dispersion. In the case of a pump with frequency-dependence, the dispersion of small excitation corresponds to Eq. (2.45):

$$\hbar\omega_{\mathbf{k}}^{\pm} = -i\hbar\tilde{\Gamma} \pm \hbar\sqrt{\tilde{E}_{\mathbf{k}}^2 - \tilde{\Gamma}^2}, \tag{3.31}$$

which in the limit $\Omega \to \infty$ leads to the related expression $\hbar\omega_{\mathbf{k}}^{\pm} = -i\hbar\Gamma \pm \hbar\sqrt{E_{\mathbf{k}}^2 - \Gamma^2}$, as predicted in (Wouters and Carusotto, 2007a).

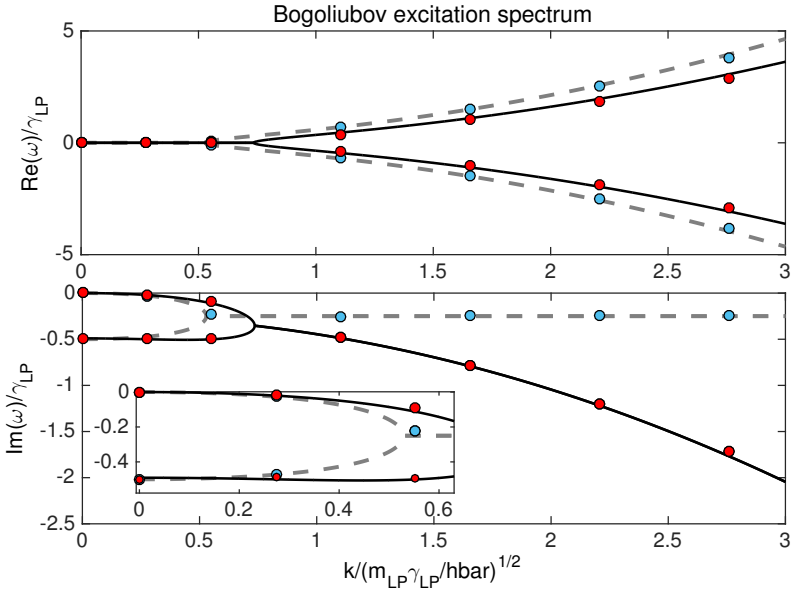

Figure 3.9: **Bogoliubov excitation spectrum for a** $2d$ **polariton condensate.** Theoretical predictions, Eq.(3.31), of the real (top) and imaginary (bottom) part of Bogoliubov modes calculated for the two cases, $\Omega = 50$ and $\Omega = \infty$, are shown as black solid and gray dashed curves, respectively. Numerical results obtained by probing the response of the homogeneaus steady state under a given perturbation are reported as red and blue points.

Computational data (red and blue points in Fig. 3.9) have been extracted by solving Eq. (3.6). In the case of no perturbation, i.e. $V_0 = 0$, the system evolves in time towards equilibrium (similarly to growth illustrated in Fig 3.4 by the blue dashed line). Transforming in $\mathbf{k}$-space the real wavefunction $\psi_{\mathrm{MF}}(\mathbf{r}, t)$, such that $\psi_{\mathrm{MF}}(\mathbf{r}, t) \rightarrow \tilde{\psi}_{\mathrm{MF}}(\mathbf{k}, t)$, we would then note a peak centred at $\mathbf{k} = 0$, corresponding to the bare condensate. On the contrary, if we excite the system by means of a particular perturbation with momentum $\mathbf{k}_{\mathrm{exc}}$, a particular Bogoliubov mode would be excited. Thus, the $\mathbf{k}$-space is now characterised by the presence of three peaks, corresponding to the trivial $\mathbf{k} = 0$ mode (which oscillates at the condensate frequency μ), and other two excited modes $\mathbf{k}_{\mathrm{exc}}$ and $-\mathbf{k}_{\mathrm{exc}}$.

Finally, by fitting the oscillation in time of these excited modes, it is straightforward to extract the information on the real and imaginary part of the Bogoliubov frequency $\omega^{\pm}_{\mathbf{k}}$, according to Eq. (3.31), a physical explanation of which is given in Sec. (2.2.5). In Fig. 3.9 we show the comparison between data and theoretical predictions, for both $\Omega = \infty$ and $\Omega \neq \infty$ cases. We conclude that our code is able to successfully capture the dynamics of the condensate at a mean-field level.

3.4 Detecting topological defects

The creation and measurement of quantum vortices stands out as one of the most attractive properties of superfluids. A quantum vortex is a topological non trivial solution of both the equilibrium, Eq. (2.9), and the nonequilibrium, Eq. (2.32), degenerate systems of bosons. These are topological excitations of the superfluid due to a 2π phase winding around the vortex core, where the phase singularity in the core at the vortex is resolved through the density tending to zero at the centre.

The standard method to create vortices in condensates is by rotation of the system (Madison *et al.*, 2000); in this case the quantised vortex line appears to be parallel to the rotation axis. Measurements of quantised circulation have been thoroughly investigated in atomic condensates. Other techniques used to create vortices include optical phase imprinting (Leanhardt *et al.*, 2002) and through motion of an obstacle in the fluid (Kwon *et al.*, 2015). They can be displayed in different arrangements such as vortex lattices (Madison *et al.*, 2000) and vortices rings (Anderson *et al.*, 2001).

Quantum vortices can also be (spontaneously) created by dynamically crossing a phase transition: in equilibrium systems, their presence decreases the free energy of the system, hence they become energetically favourable. In non-equilibrium systems, the free-energy argument cannot be applied due to the presence of dissipation. However, vortex nucleation processes have been predicted theoretically in such polariton systems (Pigeon *et al.*, 2011) and measured in many experiments as in (Lagoudakis *et al.*, 2008; Sanvitto *et al.*, 2010b; Amo *et al.*, 2011).

Superfluids can be described by a set of hydrodynamical equations (Pitaevskii and Stringari, 2003) where the macroscopic wavefunction is represented in terms of the fluid density ρ and phase θ, such that

$$\psi(\mathbf{r}, t) = \sqrt{\rho(\mathbf{r}, t)}\, e^{i\theta(\mathbf{r},t)}, \tag{3.32}$$

where the phase around any closed contour C has to be quantised, i.e.

$$\oint_C \nabla\theta \, d\mathbf{r} = 2\pi q, \tag{3.33}$$

with $q \in \mathbb{Z}$. The local velocity flow is described by the gradient of the phase $\mathbf{v} = (\hbar/m)\nabla\theta$. The fluid circulation Γ then becomes

$$\Gamma_C = \oint_C \nabla\theta \, d\mathbf{r} = \frac{2\pi\hbar}{m} q. \tag{3.34}$$

where $2\pi\hbar/m$ is the 'quantum of circulation' (Pitaevskii and Stringari, 2003). This behaviour is clearly in contrast with classical hydrodynamics where the circulation Γ_C can assume any value.

In both 3d and 2d condensates, quantum vortices are topological non-trivial solutions of the GPE, defects which carry a quantised vorticity (Pitaevskii and Stringari, 2003). For condensates of light, which are confined in $2d$, vortices play a major role, being responsible for driving the phase transition. The procedure which allows an accurate detection of the number of vortices is therefore crucial for the purpose of this work.

In the literature, many works investigated this problem, e.g. (White *et al.*, 2012; Villois *et al.*, 2016). The method we adopt (Stagg, 2016) is based on the basic property of the theorem of calculus for line integrals, which implies the integral in Eq. (3.33) to be zero only in the case no singularity of the phase is enclosed within the continuous contour C. A vortex is thus detected if

$$\Gamma_C = \oint_C \nabla\theta \, d\mathbf{r} \neq 0, \tag{3.35}$$

within the numerical accuracy. In order to detect the vortex in a square grid, the numerical routine calculates the integral above for different closed curves C_i. These curves lie on points of the grid, are square shaped with sides approximately the size of the system healing length ξ, such that $C_i/8 \approx \xi$. The phase gradient is approximated by means of finite differences, and its sign defines the polarity of the vortex. As extensively explained in (Stagg, 2016), this method can be improved further by implementing labelling of vortices and low-pass filtering with the purpose of removing all high frequency spatial waves from the vortex field. Finally, by counting the many contributions of each Γ_C within the whole sample, the numerical procedure is able to return the total number of vortices N_v and their polarity.

3.5 Chapter summary

In this chapter we initially obtained both stochastic and mean field dimensionless equations, though a rescaling of the physical models by means of relevant system scales. By showing the effects of implementing different types of pumping profiles and boundary conditions, we then identified the best condition for the study of nonequilibrium critical phenomena, discussed in Part II of this thesis. We thus showed a typical numerical growth from an incoherent configuration to an out-of-equilibrium degenerate steady state; we also displayed some examples of relevant numerical observables calculated at different steps of the evolution, such as phase, first order correlation function and particle momentum

distribution. Subsequently, numerical validity and tests on statics and dynamics of both stochastic and mean-field models were undertaken; the results obtained exhibit good agreement with theoretical predictions introduced in the previous chapter. A detailed analysis on the grid spacing variation of the steady state was given. Particularly, we focused on the UV divergence issue which arises when solving the stochastic GPE in the continuous limit $a \to 0$. Finally we discussed the numerical methods we adopted in order to extract the number of topological defects.

Part II

Steady state and quench dynamics of a driven-dissipative polariton condensate

Chapter 4

Berezinskii-Kosterlitz-Thouless (BKT) transition for incoherently-pumped polariton condensates

Dimensionality and symmetry of a system are crucial ingredients for the determination of the characteristics of the phase transition which it may undergo. In $3d$, Bose particles can exhibit ODLRO when driven by a control parameter below a specific critical point. This phenomenon is associated with the appearance of a BEC, predicted to occur in uniform systems (Pitaevskii and Stringari, 2003) and experimentally measured in trapped systems (Fletcher *et al.*, 2015).

In $2d$ systems, instead, the presence of low energetic phonons destroys ODLRO, compromising the existence of a possible phase transition to an ordered state (Mermin and Wagner, 1966; Hohenberg, 1967). Nevertheless, in 1971-73 Berezinskii, Kosterlitz and Thouless (Berezinskii, 1971; Kosterlitz and Thouless, 1973) showed that in $2d$ a *topological* phase transition to a quasi-ordered state may still occur. Their framework was formulated in terms of the defects of a system, vortices, which below a critical point change their natural configuration: from being free to proliferate at high-temperature, they bind and annihilate below the critical point.

The scenario becomes even more complicated when the conservative nature of the system is modified by introducing driving and dissipation mechanisms. A typical example of such nonequilibrium condensation has been reported for exciton-polaritons quasiparticles in semiconductors, as a result of the strong coupling between light and

matter (Kasprzak *et al.*, 2006).

The full characterisation of the type of phase transition which these systems exhibit is still being debated. Strong steps have been undertaken, both experimentally (Roumpos *et al.*, 2012; Nitsche *et al.*, 2014; Caputo *et al.*, 2017) and theoretically (Dagvadorj *et al.*, 2015), in order to establish whether $2d$ nonequilibrium systems can also be described by means of the BKT theory. This is because phase fluctuations are strongly modified by driving and dissipation, and can thus play a fundamental role in the characterisation of the transition.

Motivated by these open and fascinating questions, in this chapter we undertake a detailed analysis of the phase transition exhibited by incoherently driven polariton condensates. First, we formally describe the BKT theory by means of the $2d$ XY model (Sec. 4.1.1), and further extend it to bosonic particle systems (Sec. 4.1.2). Then, in section 4.2, the BKT transition in nonequilibrium systems is introduced. In Sec. 4.3.1 we numerically investigate the nonequilibrium phase diagram of the polariton transition. We study the dependence of the critical point on the parameters chosen in Sec. 4.3.2, then characterise in detail the critical region (Sec. 4.3.4) by means of spatial correlations and topological defects. This forms the basis of our subsequent study on critical dynamics and finite quenches presented in Chs. 5 and 6.

4.1 The BKT equilibrium phase transition

The first discussion concerning the dependence of true ODLRO —defined by means of the first correlation function in Sec. 1.2—, on dimensionality, has been made in 1934 by Peierls, who studied the effects of thermal vibrations in a $2d$ lattice at equilibrium (Peierls, 1934, 1935). Its principal result consists in claiming that at very long distances, the information on the position of atoms is lost. This was the first example of absence of ODLRO. Consequently, this concept has been formalised by Mermin and Wagner (Mermin and Wagner, 1966) in 1966 and extended to the $2d$ Bose gas by Hohenberg (Hohenberg, 1967) the following year.

In the introductory part of this thesis we heuristically demonstrated the absence of ODLRO in a $2d$ ultracold gas, by considering the diverging distribution of the number of excited particles, N_{ex} (see Eq. (4.1)). In contrast to their $3d$ counterparts, $2d$ Bose gases are demonstrated to be unstable to long wavelength (low energy) fluctuations of the order parameter, associated with the Goldstone mode of the system. In the case of interacting

atoms, those modes are usually referred as phonons, whereas in spin lattices they are termed spin-waves.

More generally, the Mermin-Wagner-Hohenberg theorem states that the destruction of ODLRO by means of low-**k** fluctuations occurs in systems which exhibit a continuous symmetry breaking (such as magnets, solid, superfluids, etc..) at some finite temperature and for dimensions $d < 2$. For the case $d = 2$, however, the divergence of the occupation of phonons for an interacting Bose gas (Hohenberg, 1967), expressed as

$$n_{\mathrm{PH}} \sim k_{\mathrm{B}} T \int dk \frac{k^{d-1}}{k^2} \tag{4.1}$$

is of logarithmic form, implying that a phase transition from a disordered state to a quasi-long-range order is still observable. We investigate this further in the context of the $2d$ XY model in the next section.

4.1.1 The $2d$ XY model

The $2d$ XY model represents an important tool for the investigation of phase transitions of systems composed of particles with spin. An example of such phase transition is the transformation of a material from ferromagnet (spins aligned in the same direction) to an antiferromagnet (random configuration of spins). In the absence of external perturbations, a $2d$ magnetic system can be approximated by a lattice of size L composed of particles with magnetic spin $\vec{S}_i$, such that $\vec{S}_i^2 = 1$. Thus, the interaction Hamiltonian for such a system reads

$$H = -J_{ij} \sum_{\langle i,j \rangle} \vec{S}_i \vec{S}_j, \tag{4.2}$$

where $\langle i, j \rangle$ denote nearest neighbours and J_{ij} the strength of the magnetic interaction. For $J < 0$, the energy is minimised for antiparallel adjacent spins (antiferromagnet configuration); when $J > 0$ spins prefer to align in a parallel configuration (ferromagnet configuration). The original Hamiltonian is simplified by introducing the angle θ of the spins into the plane as parametrisation:

$$H = -J_{ij} \sum_{\langle i,j \rangle} \cos(\theta_i - \theta_j). \tag{4.3}$$

Long range behaviour

To see whether a system is ordered, we calculate the first order correlation function, in this case defined as

$$g^{(1)}(r) = \left\langle e^{i\left(\theta(\vec{r})-\theta(\vec{0})\right)} \right\rangle, \tag{4.4}$$

where $\theta(\vec{r})$ is the value of the phase at a distance $\vec{r}$ from a fixed origin $\vec{0}$, and $r = |\vec{r} - \vec{0}|$ (Girvin, 2000).

In the case of a 3d system at zero temperature, all spins are aligned in the same direction, implying that the value of $g^{(1)}(r)$ is equal to 1 across the whole system. For an ordered system at non-zero temperature, the phase $\theta(\vec{r})$ is uniform and the correlations should remain non-zero at large distances, according to the textbook definition of ODLRO. If instead the system is disordered, spins at large distance become uncorrelated and Eq. (4.4) decays to zero after some characteristic length L_{3d}, named the correlation length. Solving Eq. (4.4) thus gives

$$g^{(1)}(r) = \begin{cases} \text{const} & T < T_c \\ c\ e^{-r/L_{3d}} & T > T_c \end{cases}. \tag{4.5}$$

It can be easily shown that for the $2d$ XY model at high temperatures, where thermal fluctuations dominate the spin interactions, i.e. $J/k_B T \ll 1$, the correlations (4.4) take the form $g^{(1)}(r) \sim \left(\beta J/2\right)^r$, with $\beta = 1/k_B T$, which can be eventually approximated by

$$g^{(1)}(r) \sim e^{-r/L_{2d}}, \tag{4.6}$$

where L is the $2d$ correlation length. Thus, at high temperatures, first order correlations decay exponentially to zero and ODLRO is suppressed.

On the other side, for an ordered phase characterised by spin interactions, spin interactions dominate over thermal fluctuation, i.e. $J/k_B T \gg 1$. Under this assumption, fluctuations between adjacent spins are negligible, and the Hamiltonian (4.3) is approximated to

$$H = -\frac{J}{2} \sum_{\langle i,j \rangle} (\theta_i - \theta_j)^2. \tag{4.7}$$

We note that by assuming very low temperature, the condition $L \gg a$ (where a is the lattice spacing and L the system size) allows one to move in the continuum limit and rewrite the lattice theory as a field theory for the effective Hamiltonian

$$H_{XY} = \frac{J}{2} \int d^2\mathbf{r} |\nabla\theta|^2, \tag{4.8}$$

where the phase field $\theta(\mathbf{r})$ replaces θ_i. Since the Hamiltonian is Gaussian, we can calculate the first order correlation function by means of

$$g^{(1)}(r) = e^{-\frac{1}{2}\left\langle\left(\theta(\vec{r})-\theta(\vec{0})\right)^2\right\rangle}. \tag{4.9}$$

To calculate the argument of the exponential, one can expand $\theta(\mathbf{r})$ in term of Fourier components; after these substitutions and some algebra, the final expression reads

$$\left\langle\left(\theta(\vec{r}) - \theta(\vec{0})\right)^2\right\rangle = \frac{k_B T}{J\pi}\int_{1/r}^{1/a} dk \frac{1}{k}, \tag{4.10}$$

$$= \frac{k_B T}{J\pi}\log\left(\frac{r}{a}\right), \tag{4.11}$$

where an ultraviolet cutoff a^{-1} has been introduced by hand in order to regularise the integral. The logarithmic divergence, instead, is truncated at $1/r \ll 1/a$. In the limit $r \gg a$ we obtain

$$g^{(1)}(r) \sim r^{-\alpha(T)}, \tag{4.12}$$

with

$$\alpha(T) = \frac{T k_B}{2\pi J}. \tag{4.13}$$

This demonstrates that for any $T > 0$, ODLRO is forbidden, which is in agreement with the Mermin-Wagner-Hohenberg theorem cited above. However, the important result is that the decay is slower than the behaviour measured in a disordered system; this slower decay of first order correlation is named *quasi-long-range* order, or *topological* order.

Topological defects

An important feature of the $2d$ XY model Hamiltonian, Eq. (4.3), lies in the invariance property

$$\theta(\vec{r}) \to \theta(\vec{r}) + 2\pi n, \qquad n \in Z. \tag{4.14}$$

This approximation guarantees that the energy is invariant under the continuous global $U(1)$ transformation. A further symmetry is also included in the problem, once we introduce the parametrisation as in Eq. (4.3), which consists in treating the field θ as *locally* invariant. This feature is crucial because it allows for the existence of topological defects, e.g. quantum vortices in superfluid systems. A quantum vortex, as discussed in detail in Sec. 3.4 of this thesis, is physically speaking a depletion in the superfluid density in which the phase winds by $\pm 2\pi$, as described by Eq. (3.34).

The role of topological defects in the characterisation of the phase transition is in-

vestigated by calculating the energy cost for introducing a vortex in our system. In the continuum limit, the energy of a vortex centred on the origin with charge q reads

$$E_{\mathrm{v}} = \frac{q^2 J}{2} \int_a^L \frac{d^2\mathbf{r}}{r^2} \sim \pi q^2 J \log\left(\frac{L}{a_{\mathrm{c}}}\right), \tag{4.15}$$

with a_{c} the size of the vortex core. It is worth mentioning that in Eq. (4.15) we subtracted the core energy E_{c}. The free energy, F_{v}, of a single vortex reads

$$F_{\mathrm{v}} = E_{\mathrm{v}} - S_{\mathrm{v}} T \tag{4.16}$$

where S_{v} is the entropy of the vortex. Such relation can be used to determine the temperature at which isolated vortices become favourable. In a lattice with size L, one can place at most $N_{\mathrm{v}} = L^2/a^2$ vortices. Therefore, the free energy cost to introduce a single vortex reads

$$\begin{aligned} F_{\mathrm{v}} &= (\pi J - 2k_{\mathrm{B}}T)\log\left(\frac{L}{a}\right) && (4.17)\\ &= 2k_{\mathrm{B}}\left(T_{\mathrm{BKT}} - T\right)\log\left(\frac{L}{a}\right). && (4.18) \end{aligned}$$

Applying the principle of minimisation of the free energy, it is thus clear that topological defects are responsible for driving the BKT phase transition. On the one side, for $T > T_{\mathrm{BKT}}$, the free energy is large and negative, thus able to support spontaneous creation of new free vortices. On the other side, for $T < T_{\mathrm{BKT}}$, the free energy is large and positive, thus it exhibits instability on the creation of a free vortex. Free vortices then have the power to destroy topological order above T_{BKT}. At the critical temperature $T = T_{\mathrm{BKT}} = \pi J/2k_{\mathrm{B}}$, Eq. (4.12) imposes that $\alpha = 1/4$.

4.1.2 Relation to the $2d$ equilibrium Bose gas

Following the discussion in the previous section, the BKT theory for the $2d$ XY model provides an explanation for the absence of ODLRO in $2d$ systems, predicted by the Mermin-Wagner-Hohenberg theorem; it provides a description of the phase transition based on the topological nature of the system.

The XY model is a very simple model which can be applied to a distinct range of physical systems, in particular the uniform $2d$ equilibrium Bose gas (Hadzibabic and Dalibard, 2011). Both models belong to the same universality class, meaning they exhibit similar fundamental properties in the infinite size limit. Both the $2d$ XY model and the $2d$ Bose gas system present a continuous symmetry breaking, short-range interacting particles, presence of Goldstone modes which prevent ODLRO and appearance of topological

defects.

The direct link between these two models relies on the similar scaling of the energy with respect to the spin angle θ for the $2d$ spin lattice H_{XY}, Eq. (4.8), and with respect to the superfluid phase ϑ for the $2d$ uniform Bose gas Hamiltonian, H_{SF}. The latter is defined by

$$H_{\mathrm{SF}} \sim \frac{\hbar^2}{2m} n_{\mathrm{SF}} \int d^2\mathbf{r} |\nabla \vartheta|^2. \tag{4.19}$$

where m is the mass of the Bose particle and n_{SF} the superfluid density. Similar links can be established between the spin magnitude and the superfluid density. As a consequence, the power-law exponent and the BKT threshold can be rewritten as

$$\alpha = \frac{T k_{\mathrm{B}}}{2\pi J} = \frac{1}{n_{\mathrm{SF}} \lambda_{\mathrm{dB}}^2}, \tag{4.20}$$

$$T_{\mathrm{BKT}} = \frac{\pi J}{2 k_{\mathrm{B}}} \to \frac{n_{\mathrm{SF}} \lambda_{\mathrm{dB}}^2 T}{4} \tag{4.21}$$

with λ_{dB} the de-Broglie wavelength associated to the Bose particle. Thus, the exponent α is dependent on both superfluid density and de-Broglie wavelength. We then expect that for $T > T_{\mathrm{BKT}}$ correlations decay exponentially and free vortices proliferate, whereas for $T = T_{\mathrm{BKT}}$ the system reaches a critical phase space density

$$n_{\mathrm{SF}} \lambda_{\mathrm{dB}}^2 = 4. \tag{4.22}$$

As the temperature is further lowered, vortices start to pair, corresponding to a discontinuous jump of the superfluid density, and spatial correlations exhibit algebraic decay with exponent

$$\alpha = \frac{1}{n_{\mathrm{SF}} \lambda_{\mathrm{dB}}^2} = \frac{1}{4}. \tag{4.23}$$

Below T_{BKT} the system is expected to show algebraic decay with $\alpha < 1/4$ and bound vortex-antivortex pairs. A sketch of the BKT phase transition is shown in Fig. 4.1.

It is very important to note that while in spin models (like the $2d$ XY model) the magnitude of the spin variation is fixed, $2d$ Bose gases exhibit a fluctuating superfluid density, especially in the vicinity of the critical region. In order to account for this feature, the equation of motion for the field ϑ can be improved by including a stochastic noise term, which mimics density and phase fluctuations on top of the superfluid (Jelić and Cugliandolo, 2011). In addition, phase fluctuations can be also be considered at higher order, as applied for instance within the framework of the KPZ theory (Altman *et al.*, 2015).

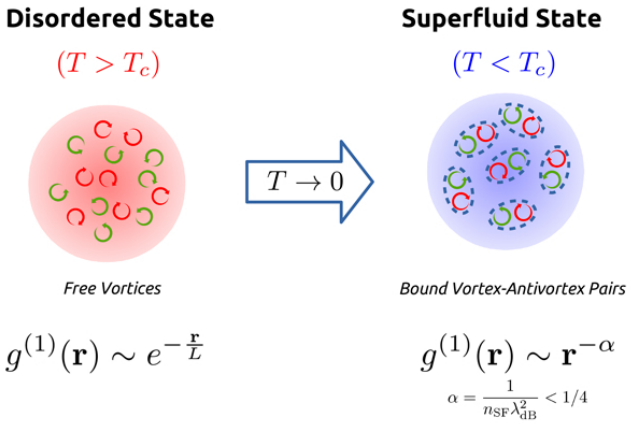

Figure 4.1: **The BKT transition.** Schematics showing the phase transition from a disordered (normal) phase at high temperatures to a quasi-ordered (superfluid) phase at low temperatures. The threshold is set at $T = T_{\mathrm{BKT}}$. In the high-temperature regime, free vortices proliferate and correlations decay exponentially, whereas in the low-temperature regime the vortex-antivortex pairs are bounded, and correlations decay algebraically, which is a signature of topological order.

4.2 The BKT transition in nonequilibrium systems

The BKT theory successfully describes a plethora of experiments conducted in different physical systems. Typical examples concerning the investigation of 2*d* superfluidity in Helium thin films (Bishop and Reppy, 1978; Anikin *et al.*, 1980) and trapped 2*d* Bose gases (Stock *et al.*, 2005; Hadzibabic *et al.*, 2006; Cladé *et al.*, 2009; Fletcher *et al.*, 2015).

The XY model reviewed in the previous section is the ideal tool for investigating the physical properties linked to the onset of topological order. Within this picture, the binding-unbinding crossover of quantum vortices responsible for driving the transition, is based on the principle of minimum energy. According to the second law of thermodynamics, for a closed system with constant external parameter and entropy, approaching equilibrium corresponds to a minimisation of its free energy.

This principle indeed applies to many experiments where the system is considered closed and in thermal equilibrium. This is not the case for polariton condensates, which are strongly-driven systems, where emergence of a nonequilibrium steady state is dependent on the pumping strength, which should dominate over the losses of the optical cavity. Here the free energy minimisation principle cannot be applied (Dagvadorj *et al.*, 2015), so the relevance of the BKT picture is far from obvious in open-dissipative systems.

However, a transition from a disordered to an ordered superfluid phase has been experimentally observed in polariton systems (Kasprzak *et al.*, 2006) and their superfluid

properties have been investigated in detail, see e.g. early work by (Amo *et al.*, 2009a,b). Nevertheless, the study of the extent to which the BKT theory can apply to the phase transition exhibited by nonequilibrium condensates has been challenging both from the experimental and the theoretical points of view.

First experimental attempts in this direction have been conducted by Yamamoto's group (Roumpos *et al.*, 2012), who observed the crossover from power-law to exponential decay of correlations for an incoherently-driven polariton condensate. Interestingly, the algebraic exponent measured as soon as the system entered the ordered regime was found to exceed the equilibrium value of $\alpha = 1/4$ (see Fig. 4.2); specifically they found $0.9 < \alpha < 1.2$. Few years later further measurements from the same group observed an exponent $\alpha < 1/4$ consistent with "equilibrium" BKT predictions (Nitsche *et al.*, 2014). The contrasting outcomes of these experiments suggests that driving and dissipation could somehow alter equilibrium BKT predictions.

Numerical simulations within the OPO regime have confirmed the possibility of a nonequilibrium condensate to exhibit $\alpha > 1/4$ (Dagvadorj *et al.*, 2015). In Fig. 4.3 we report the crossover from exponential to algebraic decay of spatial correlations showing an exponent $0 \lesssim \alpha < 1.4$.

Theoretically, the actual nonequilibrium phase transition is described by the KPZ theory (Altman *et al.*, 2015), which accounts for phase fluctuations to second-order and predicts the existence of stretched-exponential correlations for isotropic systems, as discussed in Sec. 2.3.3. However, these effects are predicted to appear at very large scales compared to those achievable both experimentally and numerically.

A recent detailed work by (Caputo *et al.*, 2017) thoroughly investigated this issue by measuring correlations in a high quality sample. They concluded that, in order to fully characterise the nature of the BKT phase transition, one needs to investigate both spatial and temporal correlations.

Specifically, the crossover from a "classical equilibrium" to a "nonequilibrium" regime is supposed to depend on whether the algebraic exponents of spatial (α_s) and temporal (α_t) correlations match. On the one hand, for high polariton lifetimes ($\tau_{pol} \sim 100ps$), the system shows "classical" equilibrium where $\alpha_t = \alpha_s \leq 1/4$. Here, the dispersion of small excitations is then expected to show a sonic behaviour at low momenta. On the other hand, for shorter lifetimes the transition departs from the equilibrium condition if the two exponents do not match, i.e. $\alpha_t \neq \alpha_s$ and the system is then expected to show

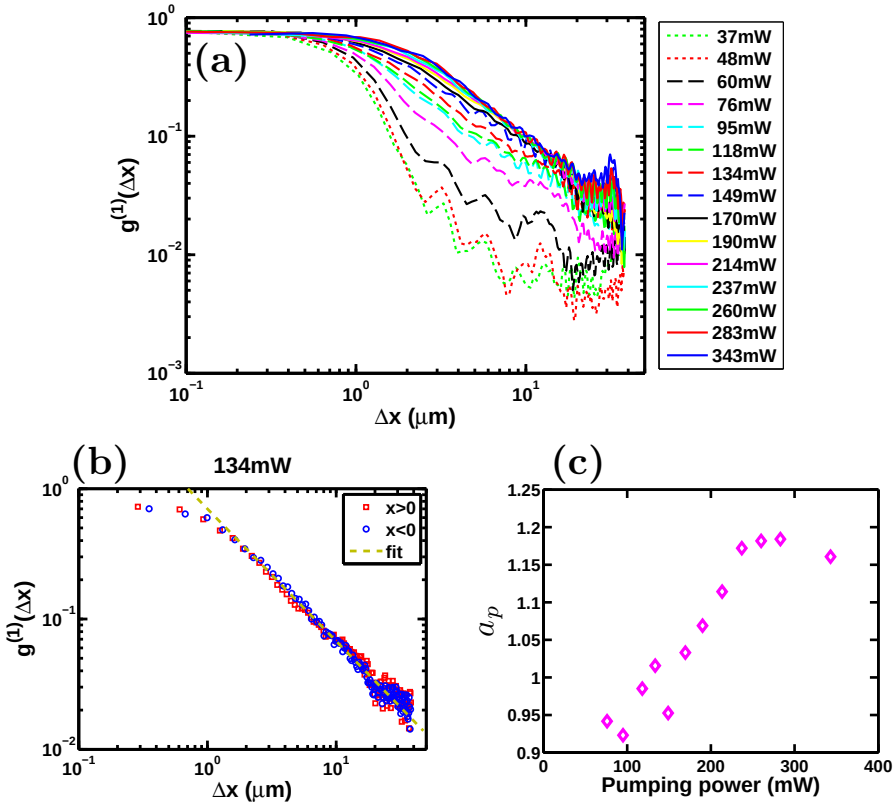

Figure 4.2: **Experimental results showing $\alpha > 1/4$.** (a) Spatial correlations measured for an incoherently-pumped polariton condensate generated by a laser spot with radius $r = 19\mu m$ and threshold power $P_{\text{th}} = 55mW$. (b) Typical spatial correlation for one particular laser power and for both positive (blue circles) and negative (red squares) values of the spatial extent. Dashed line is a power law fit. (c) Algebraic exponent α_{p} of the power law decay as a function of pump power. Adapted from (Roumpos *et al.*, 2012).

"nonequilibrium" features, such as $\alpha_{\text{s}} > 1/4$, and presence of diffusive behaviour at low momenta of the excitation spectrum.

Motivated by the open physical question regarding the type of transition that polariton condensates should exhibit, and inspired by the results reported in (Roumpos *et al.*, 2012), this chapter undertakes a detailed numerical study of the phase transition of an incoherently-pumped polariton condensate. Following the BKT literature, we find $\alpha > 1/4$, but an interesting arising question is the extent to which this argument on its own is sufficient to state that the polariton phase transition is a "nonequilibrium" one. This is of particular relevance in light of recent works highlighting the potential importance of a stretched exponential in the transition region.

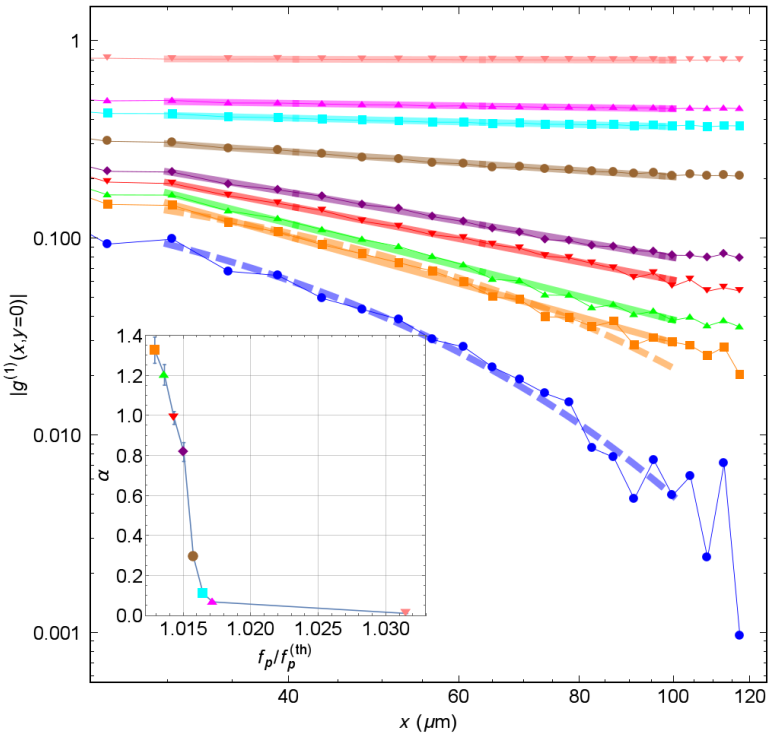

Figure 4.3: **BKT transition for the OPO regime.** Numerical results of algebraic and exponential decay of the first-order correlation function. Main panel: Long-range spatial dependence for different pump powers $f_p/f_p^{(th)}$ close to the mean field pump threshold $f_p^{(th)}$. Thick solid (thick dashed) lines are power-law (exponential) fitting, from which values of the exponent α are derived. The $f_p/f_p^{(th)} = 1.0129$ case (orange squares) is a marginal case where both algebraic and exponential fits apply almost equally well, signaling the BKT transition region. Inset: Power-law algebraic decay exponent α for different pump powers. Adapted from (Dagvadorj *et al.*, 2015).

4.3 Numerical study of the polariton phase transition

In the present section we solve computationally the steady state physics of polariton condensates. The purpose of this study is to characterise the type of transition which nonequilibrium systems undergo. More specifically, we probe polariton densities, spatial correlations and topological defects. We focus our attention on the dependence of the location of the critical point on the parameter choice. The characterisation of the threshold point is crucial for the study of quench dynamics in polariton condensates, which we conduct in Chs. 5-6. It is worth noting that the results of our analysis shown in this thesis are consistent with those presented for the OPO regime (Dagvadorj *et al.*, 2015).

4.3.1 Phase diagram

In Fig. 4.4 we show a typical BKT phase transition diagram of a polariton condensate, in which all relevant observables are shown as a function of the order parameter P_0.

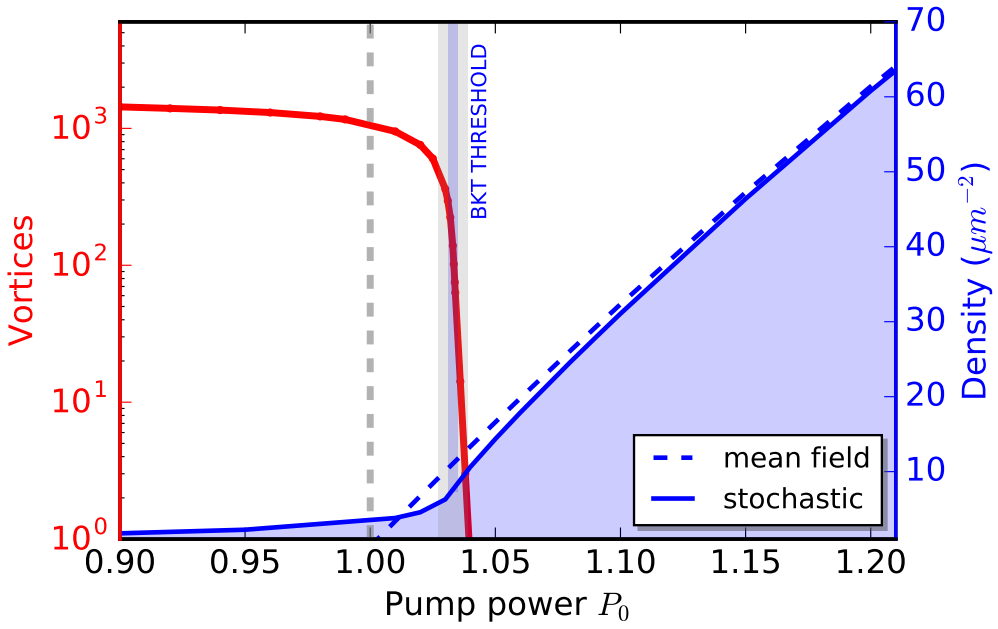

Figure 4.4: **The BKT transition of a polariton condensate.** Steady state phase diagram showing mean field and stochastic density (dashed and solid blue lines, respectively) and vortex number (red solid line) calculated for an incoherently-pumped system crossing the BKT transition. Mean field and stochastic thresholds are highlighted with dashed and solid vertical lines, respectively. Parameters as in Table 3.1.

We calculate the mean field density $|\psi_{\rm MF}(t)|^2 = (\int |\psi_{\rm MF}(\mathbf{r},t)|^2 d\mathbf{r})/L^2$, with L^2 the system surface, by evolving Eq. (3.6) from a very small initial value of the density, thereby simulating all cases starting from a state without a condensate, to a steady state with a non-zero coherent density. The parameters used are those appearing in Table 3.1. This procedure is iterated for many values of the order parameter P_0, both below and above threshold.

The mean field density is shown as a thick dashed blue line in Fig. 4.4: the threshold for the onset at a non-zero superfluid density is set of $P_{\rm th} = 1$ (thick dashed vertical grey line), below which the density assumes zero value, as expected by the polariton GPE discussed in Secs. 2.2.4-2.2.4. In this case, the threshold corresponds to a sudden appearance of the condensate mean field density. Generally, for values of a frequency-independent pump ($\Omega = \infty$) higher than threshold, i.e. $P_0 > P_{\rm th}$, a condensate appears according to the steady state analytical solution Eq. (2.33). In this case, the steady state density is expected to grow linearly with the pump strength, with the slope of the curve matching the saturation density $n_{\rm s}$. At very large values of the pump, far from the transition, the density eventually saturates at a value corresponding to $n_{\rm s}$. On the other hand, for a pump which is frequency-selective ($\Omega = 50$), as the one illustrated in Fig. 4.4,

the behaviour of the steady state growth now depends on a combination of the values of the principal physical quantities (such as those described by the terms Ω, g_{LP}, n_{s}), as described by Eq. (2.38).

We also show the stochastic steady state average density $\left\langle |\psi_{\mathrm{LP}}(t)|^2 \right\rangle$, where $\langle \dots \rangle$ indicates the average over N_{p} realisations ($N_{\mathrm{p}} = 200$ for the case investigated). With the introduction of thermal and quantum fluctuations, by means of the noise term Eq. (3.3), the field is always non-zero, independently of the value of the pump P_0. This behaviour is particularly noticeable especially in the disordered phase, where, in contrast to the mean field description, fluctuations are responsible for building up a small but not negligible density. The small fluctuations are also responsible for a shift in the threshold point P_{BKT}, which is identified by the solid faint vertical blue line in Fig. 4.4. Contrary to the mean field treatment, in the stochastic model the density increases continuously with the order parameter; thus, one needs to define a new procedure to identify the threshold point. For the incoherent pumping case, this procedure, discussed in detail in Section 4.3.4, involves the estimation of the decay of correlations and behaviour of vortices in the vicinity of criticality. Also, it is worth noting that the BKT threshold is found to occur always at larger values, i.e. $P_{\mathrm{BKT}} > P_{\mathrm{th}}$, with its exact location depending on the choice of parameters: we are going to discuss in detail this dependence in the following section.

The behaviour of topological defects is crucial for the description of the BKT phase transition. Similarly to the procedure adopted to obtain the steady state polariton density, the average total number of topological defects is evaluated for different values of the pump power and plotted in Fig. 4.4 as a thick red line. In order to detect and count the vortices, we make use of the methods explained in Sec. 3.4.

Here, two different phases are easily distinguishable. At low pump powers, the vortices are higher in number than for higher pump powers, corresponding to a phase characterised by the proliferation of free vortices. Due to the high density of topological defects d_{V} at this stage, we shall ensure that its value is always smaller that the average polariton field density $\left\langle |\psi_{\mathrm{LP}}(t)|^2 \right\rangle$, in order to have a correct physical description of the problem. We find that $d_{\mathrm{v}} \approx 0.01 \mu\mathrm{m}^{-2}$ and $d_{\mathrm{v}} / \left\langle |\psi_{\mathrm{LP}}(t)|^2 \right\rangle \approx 0.01$, for $P_0 \sim 0.9$.

By increasing the pump power, the number of vortices decreases and we observe a steep drop in the vicinity of the actual critical point. This behaviour is linked to the divergence of the correlation length, a detailed study of which is presented in Chapter (6) of this thesis. At the critical point, which corresponds to the point where pairing of vortices and antivortices start to take place, the average number of vortices is non-zero

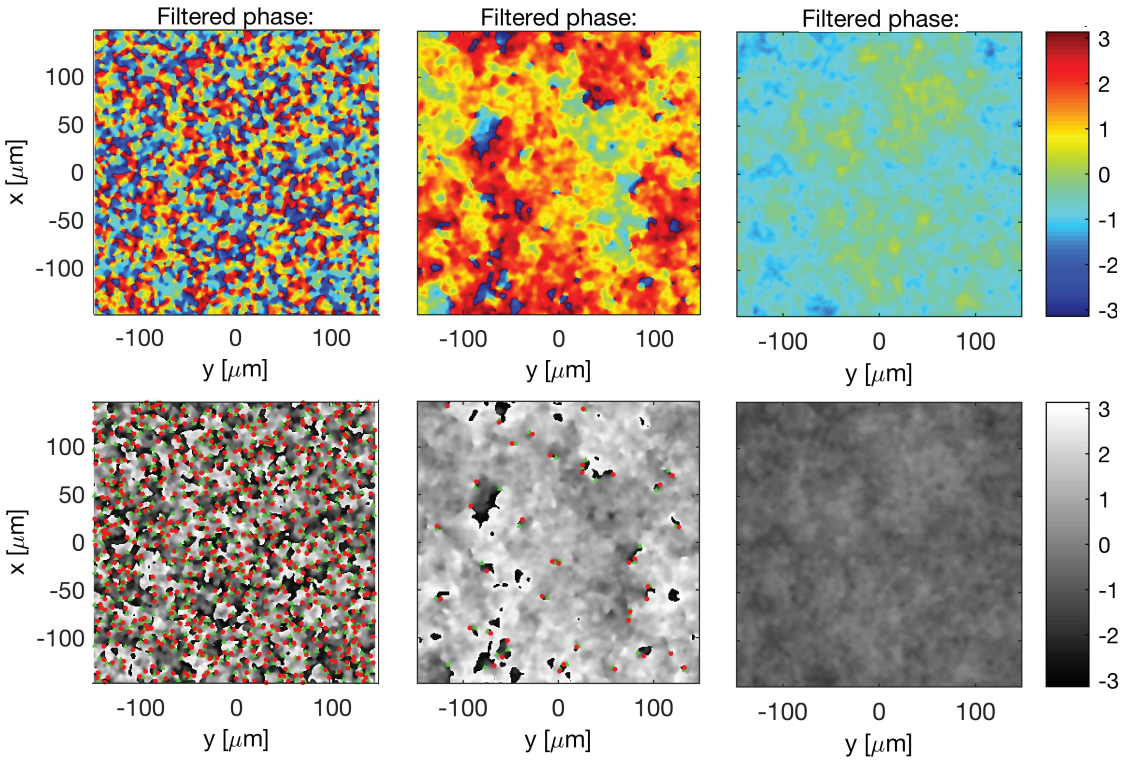

Figure 4.5: **Binding/unbinding crossover of topological defects.** Top panel depicts the phase of the system in three different configurations of the phase diagram shown in Fig. 4.4: $P_0 = 0.95$ (left), $P_0 = 1.034$ (middle) and $P_0 = 1.06$ (right). Parameter as in Fig. 4.4. Bottom panel show the same in black and white so as to facilitate the reader to identify vortices (red dots) and antivortices (green dots). It is worth noting that the phase illustrated in middle panels corresponds to the configuration immediately after the system has entered the ordered phase, which presents only vortex-antivortex pairs.

($n_v \sim 139$). Immediately after the critical point the drop is severe and the average number of topological defects decreases rapidly to zero, due to vortices and antivortices which are binding, and eventually annihilating one another, as expected for a BKT transition. Finally, the ordered phase, i.e. $P_0 \gg P_{BKT}$ is characterised by the absence of vortices, which gradually disappear due to binding with each other. This coincides with the growth of the stochastic density. The proliferation of vortices below the BKT threshold, followed by a decrease of their density due to the onset of annihilation processes, is illustrated in Fig. 4.5.

These results suggest that, for the parameters taken into consideration, the incoherently-pumped polariton system undergoes a phase transition driven by topological defects, in analogy with the classical BKT transition.

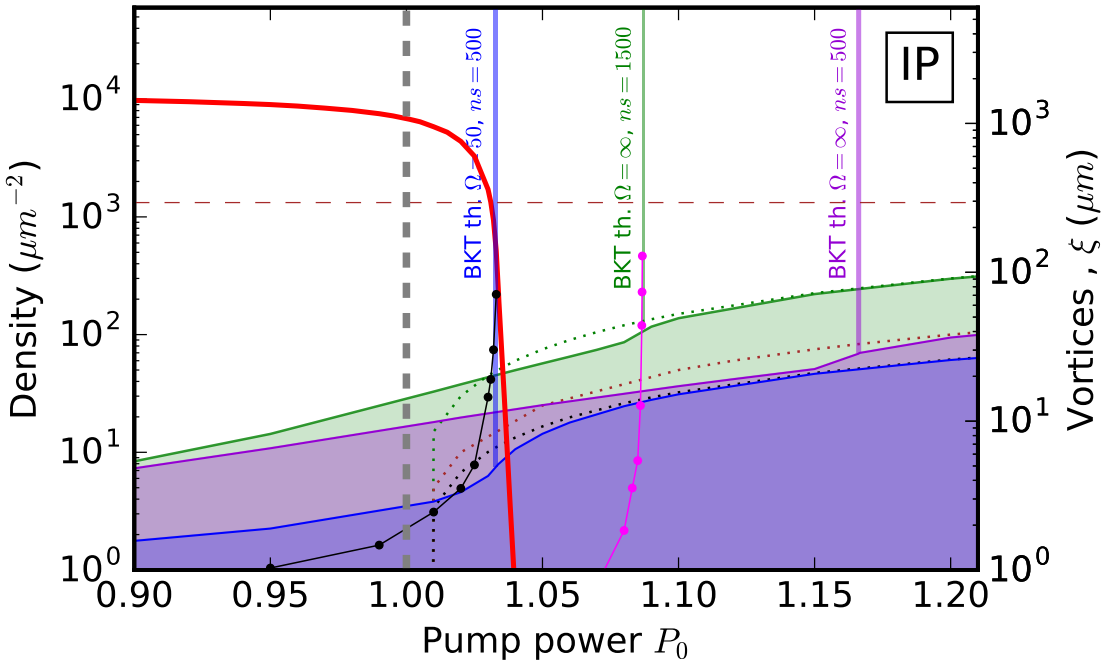

Figure 4.6: **Phase diagram for different parameter sets.** As in Fig. 4.4, we show the average density (colored curves). For each set of parameters, we associate a color: blue (labelled as $\mathrm{IP}_{\Omega=50}$): $\Omega = 50\gamma_{LP} = 11.09ps^{-1}$ and $n_s = 500\mu\mathrm{m}^{-2}$, green (labelled as $\mathrm{IP}_{\Omega=\infty}$): $\Omega = \infty$ and $n_s = 1500\mu\mathrm{m}^{-2}$, violet (labelled as $\mathrm{IP}_{\Omega=\infty}$): $\Omega = \infty$ and $n_s = 500\mu\mathrm{m}^{-2}$. Dashed horizontal curve corresponds to the system size. The average number of vortices (corresponding to the $\mathrm{IP}_{\Omega=50}$ case) are depicted as a red curve. For completeness, we plot the correlation length ξ for both $\mathrm{IP}_{\Omega=50}$ (black circles and solid curve) and $\mathrm{IP}_{\Omega=\infty}$ (magenta circles and solid curve) cases. The brown horizontal line correspond to the box size.

4.3.2 Dependence of the threshold point on input parameters n_s and Ω

Fig. 4.6 shows the phase diagram for three different choices of parameters, listed in the caption of the figure. For each case analysed, the transition points are highlighted with a vertical colored thick line. It is worth noting that stronger fluctuations at higher modes ($\Omega \to \infty$) and smaller saturation density ($n_s \to 0$) lead to a larger shift of the pump power of the BKT transition with respect to the mean field onset of macroscopic population growth.

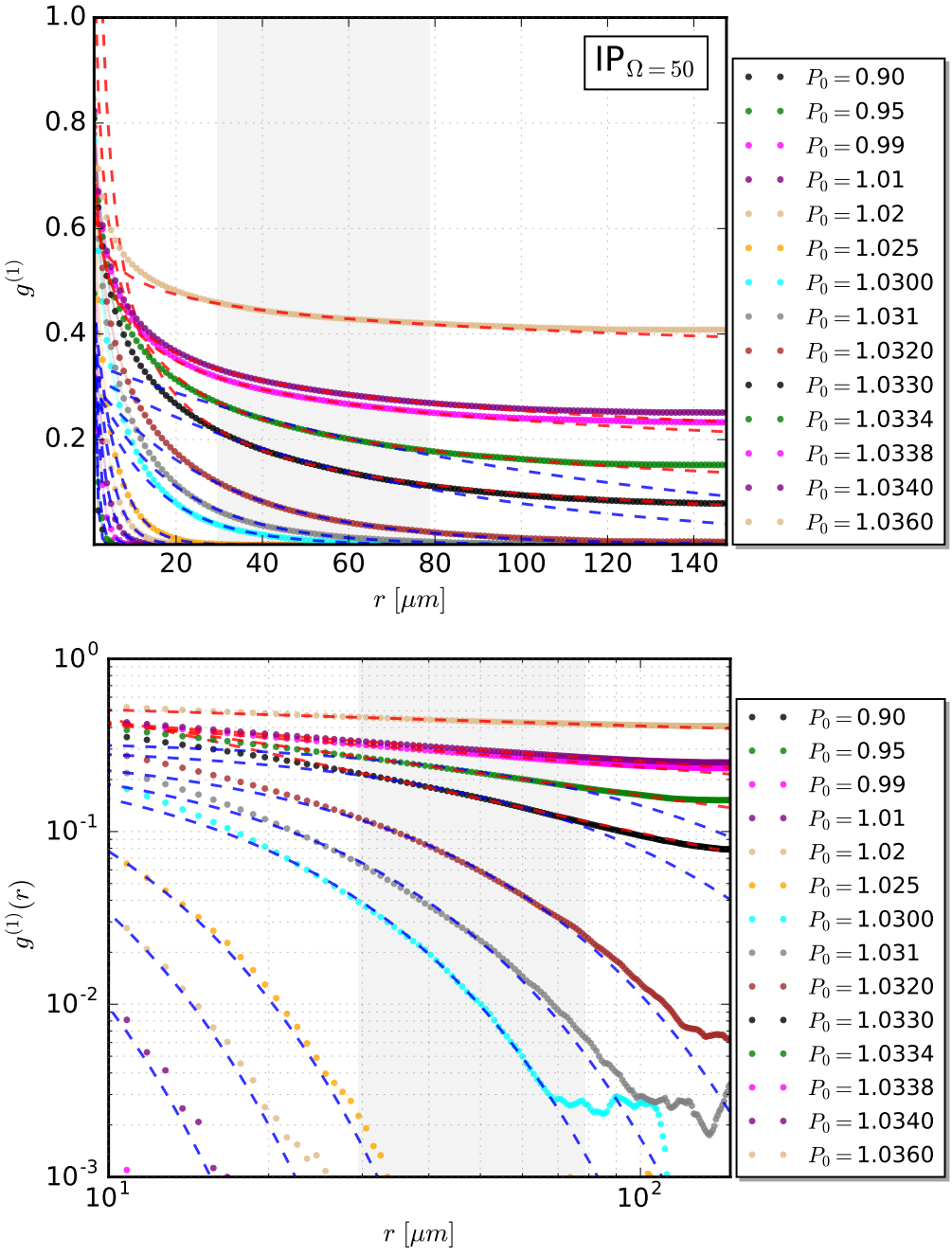

Figure 4.7: **Exponential and algebraic decay crossover of spatial correlations for IP$_{\Omega=50}$.** Long-range decay of first order correlation function $g^{(1)}(r)$ for different values of the pump P_0. Thick dashed blue (red) curves correspond to exponential (power-law) fitting, from which values of correlation length ξ and power-law exponent α are extracted and plotted in Fig. 4.9. For each curve, we superimpose only the relative fit; we show both fits for curves which lie in the critical region (see Sec. 4.3.4 for a detailed discussion).

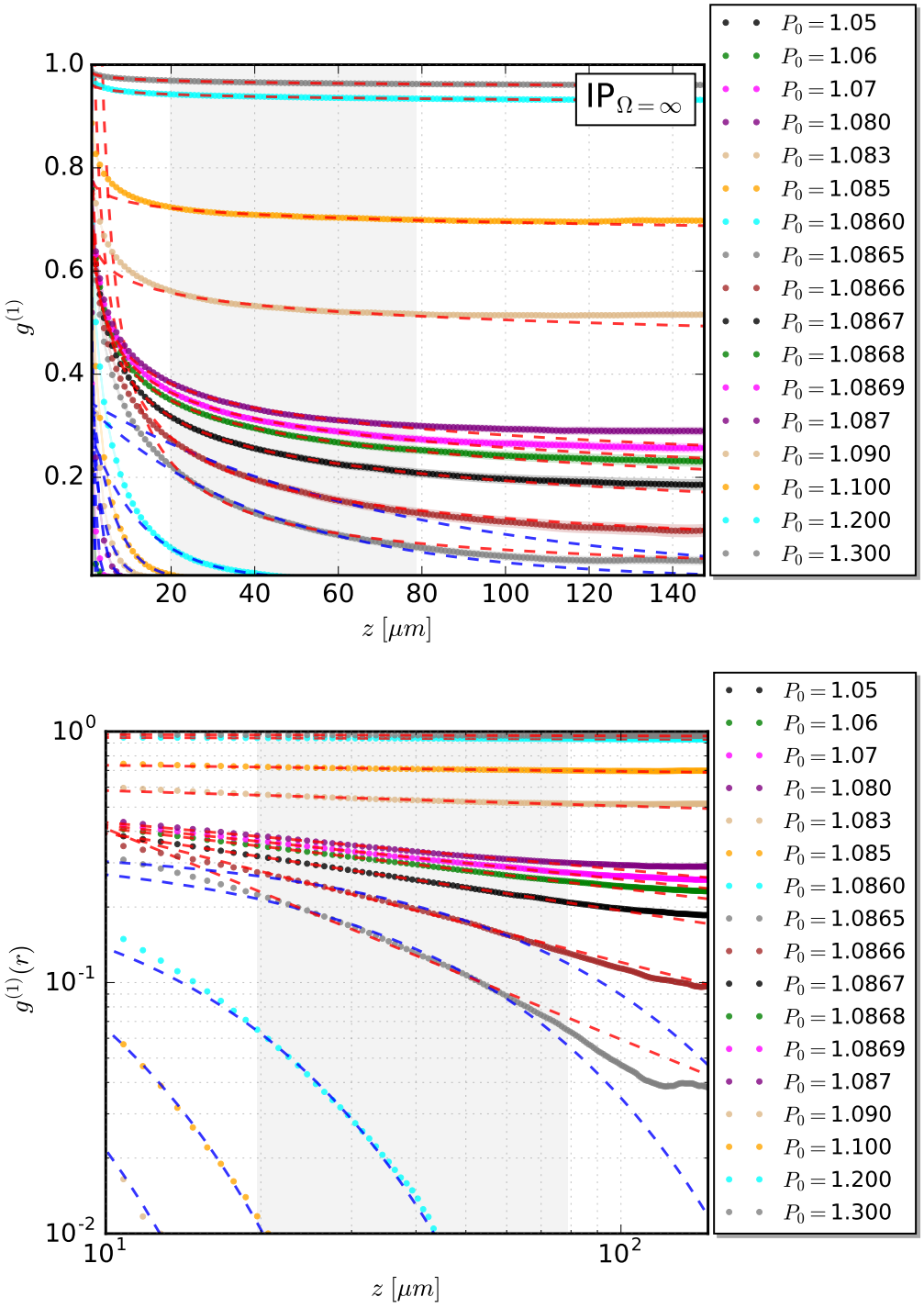

Figure 4.8: **Exponential and algebraic decay crossover of spatial correlations for IP$_{\Omega=\infty}$.** As Fig. 4.7, but for the case IP$_{\Omega=\infty}$.

This feature can be understood by fixing one of the two parameters and focusing on the other. In the case of $\Omega \to \infty$ fixed (green and red cases), we note that by increasing n_s the BKT threshold P_{BKT} shifts closer to P_{th}. This is due to the fact that increasing the saturation density, one increases the slope of the total density, moving the BKT threshold at value of pump power closer to mean field threshold.

On the other hand, if one fixes the saturation density to be $n_s = 500\mu m^{-2}$ (blue and red curves), one can study the effect of introducing a frequency-dependence to the pump. From the physical point of view, increasing the cutoff ($\Omega \to \infty$) leads to the inclusion of more modes, and reaching condensation of many modes requires higher particle density.

4.3.3 Decay of first-order correlation function

In this section we investigate the decay of the first-order correlation function $g^{(1)}$ for an incoherently-pumped polariton condensate. We study two different cases, namely a condensate with frequency-selective ($IP_{\Omega=50}$) and one without frequency-selective ($IP_{\Omega=\infty}$) pump.

In both cases, the procedure we apply is the following. We evaluate the first order correlation function in a $2d$ system according to Eq. (3.25), namely:

$$g^{(1)}(r,t) = \frac{\langle \psi^*(r+u,t)\psi(u,t)\rangle - \frac{\delta_{r+u,u}}{2\Delta V}}{\sqrt{\langle |\psi(r+u,t)|^2_-\rangle \langle |\psi(u,t)|^2_-\rangle}}\,, \tag{4.24}$$

which gives a function of the auxiliary position r. The extracted curves are illustrated in Fig 4.7 ($P_{\Omega=50}$) and Fig 4.8 ($P_{\Omega=\infty}$), both in linear (top) and log-log (bottom) scales. From this, we characterise the behaviour of the correlation length at long distances. We pay particular attention to ensure that all computational results are converged and independent from size and short range interaction effects. A list of tests conducted is given in Appendix A.1.

We study the transition from an exponential decay $g^{(1)} \sim e^{r/\xi}$ in the disordered phase, to a power-law decay $g^{(1)} \sim r^{-\alpha}$ in the ordered phase. In order to identify whether it is characterised by either exponential or power-law decay, we fit each curve with both functions. A detailed analysis is conducted in order to identify whether a specific curve is better fitted by one or the other. In both cases we apply the numerical fitting with the exponential law:

$$y = A_0 e^{-r/\xi}, \tag{4.25}$$

and the power-law

$$y = B_0 r^{-\alpha}, \tag{4.26}$$

according to the expected forms of the two-point correlator for an equilibrium BKT transition, as discussed in Sec. 4.1.1. Here A_0, B_0, ξ and α are treated as free parameters. In Figs. 4.7 and 4.8 we have superimposed on top of each correlation function $g^{(1)}$, the "appropriate" fitting curve, represented by blue or red dashed lines, corresponding to Eq. (4.25) and Eq. (4.26), respectively. In order to distinguish whether one correlator belongs to either a power-law or an exponential form, we compare the different "goodness of fits", calculated by means of the RMS of residuals.

We observe that a crossover between a power-law decay and an exponential decay takes place for both $\mathrm{IP}_{\Omega=50}$ and $\mathrm{IP}_{\Omega=\infty}$ cases. A narrow critical region can be identified, whose upper (lower) limits are delineated by the last curves exhibiting a well-defined algebraic (exponential) decay. In the next section we are going to discuss the procedure we adopt in order to identify the critical region.

4.3.4 Determination of critical pump, $P_{\mathbf{BKT}}$

In the previous section we explained the procedure adopted to characterise the transition from a disordered to an ordered phase in a polariton condensate. The procedure we employ to characterise an actual transition point (or region) is based on the analysis of the form of the steady state correlation functions at different pump strengths. In this section we define the critical region and show that it coincides with the crossover exhibited by the decay in the number of vortices.

In order to characterise the long-range behaviour of the steady state correlation function, as introduced in the previous section, we fit the tails of such functions with both Eqs. (4.25) and (4.26). From the fits, we can extrapolate parameters which are linked to the physical nature of the problem; the parameter ξ represents the correlation length of the system, whereas the exponent α is related to the superfluid density as in Eq. (4.20). For the cases considered, the correlation length $\xi(P_0)$ and the exponent $\alpha(P_0)$ are extracted from the fits, and shown in Fig. 4.9, represented with black and red dashed thick lines, respectively. The dots are colored such to match those of Figs. 4.7 and 4.8.

In order to quantify whether the numerical data are better fitted with either Eq. (4.25) or Eq. (4.26), we calculate the Root Mean Square (RMS) of the residuals of the fits (within

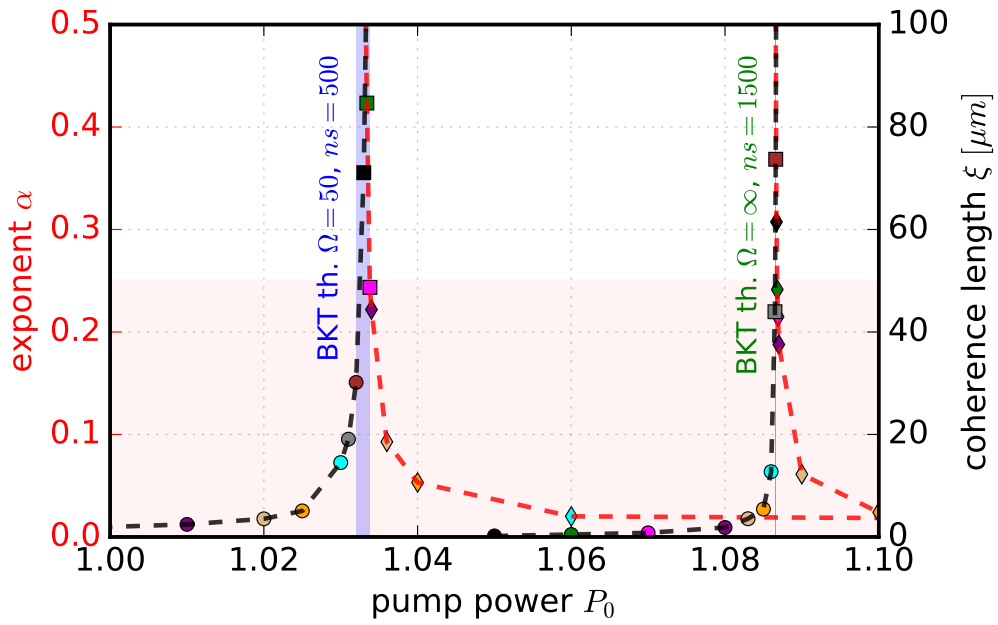

Figure 4.9: **Algebraic exponent and correlation length.** Power-law exponent α (diamonds and red dashed curve) and correlation length ξ (circles and black dashed curve) close to the corresponding critical threshold are shown for the cases $\mathrm{IP}_{\Omega=50}$ and $\mathrm{IP}_{\Omega=\infty}$. Square points correspond to values of α and ξ which fall in the critical region. Solid blue (green) vertical shadows identify the critical region for $\mathrm{IP}_{\Omega=50}$ ($\mathrm{IP}_{\Omega=\infty}$).

the fitting window selected) defined as

$$\mathrm{RMS} = \sqrt{\frac{1}{n}\sum_{n}\left(d_i - f_i\right)^2}, \tag{4.27}$$

where d_i and f_i are the data points and the fit points at a position j in space within the fitting window, with $j = 1, \ldots, n$. These values are plotted in Figs. 4.10 (top) and 4.11, for the $\mathrm{IP}_{\Omega=50}$ and $\mathrm{IP}_{\Omega=\infty}$ cases, respectively.

Fig. 4.10 shows how we characterise the critical region for the $\mathrm{IP}_{\Omega=50}$ case, by means of the RMS of the fits. At first glance, by simply comparing the residuals of the exponential and power-law fits, illustrated in Fig. 4.10 (top), one could infer a threshold location at the point where the two curves intersect. In fact, the lowest the residual, the better the fit. However, by comparing Fig. 4.10 (top) and Fig. 4.7, one can also identify an intermediate regime, where the curves are neither exactly fitted by a power-law or an exponential form.

Following this discussion, we refer to the critical region as the portion of the phase diagram which is defined by the last correlator showing "clear" exponential decay (lower

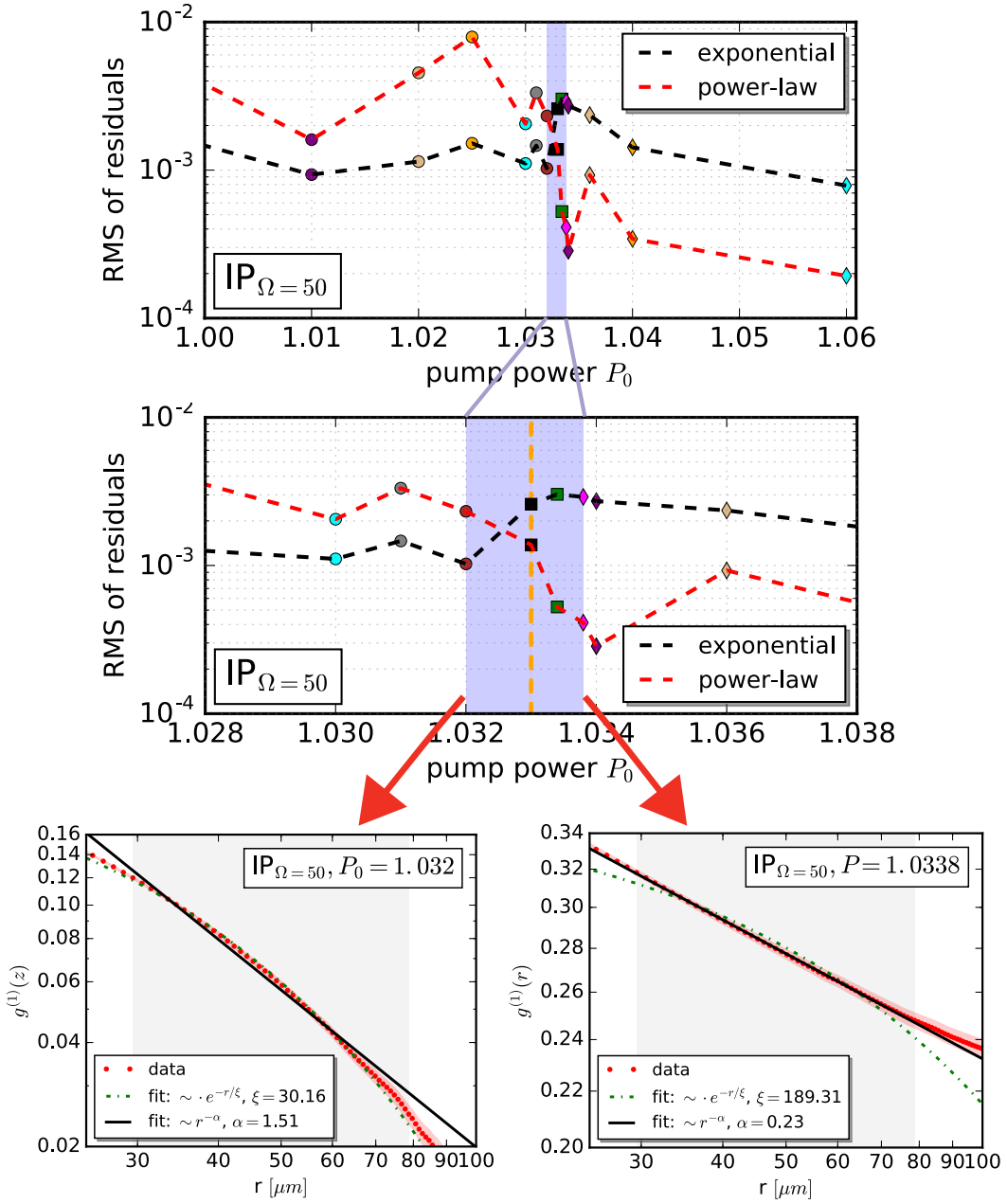

Figure 4.10: **BKT critical region.** Top: the Root Mean Square (RMS) of residuals for both power-law (red dashed) and exponential (black dashed) fits of Fig. 4.7 are shown as a function of the pump power. Points are colored corresponding to the correlation functions in Fig. 4.7 and points in Fig. 4.9. The critical region (blue shaded region) is identified as $1.032 < P_0 < 1.0338$. Due to the the choice of different fitting region for different pump values, we note that the behaviour of the RMS between is not "clear" as expected. Still, we are able to identify the best fit for each pump. Middle: as top panel but for a narrower window around the critical region, showing our heuristic identification of $P_0 = 1.033$ as our threshold "point". Bottom: $g^{(1)}$ as a function of the distance r together with fitting curves are shown for the lower (left) and upper (right) bounds of the critical region.

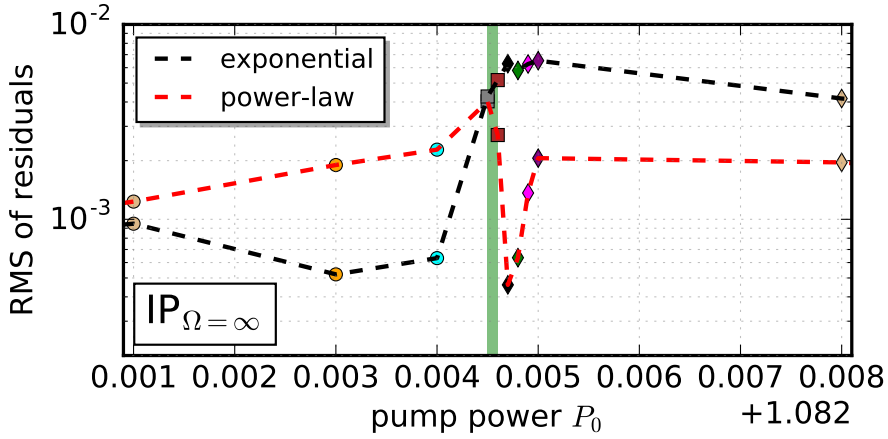

Figure 4.11: **RMS of residual.** For completeness, we report same plot as Fig. 4.10 (top panel), but for $\mathrm{IP}_{\Omega=\infty}$.

bound) and the first exhibiting "clear" power-law decay (upper bound). In both top and middle panels of Fig. 4.10, we identify the critical region with a blue shaded region. For our specific parameters considered here, lower and upper bound of the critical region coincide with $P_0 = 1.032$ and $P_0 = 1.0338$, respectively. For the sake of clarity, corresponding correlation functions are given in Fig. 4.10 (bottom), in both left (lower bound) and right (upper bound) panels. Data are also fitted with exponential and power-law functions, according to Eqs. (4.25) and (4.26).

For all subsequent analysis we need to identify a "characteristic" threshold point: we heuristically chose this as $P_{\mathrm{BKT}} \sim 1.033$ [orange dashed vertical line in Fig. 4.10 (bottom)]. This is used in the following analysis to rescale the pump strength such that the parameter characterising deviation from criticality reads

$$\epsilon = \frac{P_0 - P_{\mathrm{BKT}}}{P_{\mathrm{BKT}}}. \tag{4.28}$$

Concerning $\mathrm{IP}_{\Omega=\infty}$, from our calculations we obtain the corresponding values of $P_0 = 1.0865$ and $P_0 = 1.0866$ (see Fig. 4.11), for lower and upper bounds of the critical region, respectively.

It is worth noting that the critical point could also be inferred from change of behaviour of the static configuration of average number of topological defects. Fig. 4.12 displays in fact the behaviour of averaged vortices at steady state, calculated as

$$n_{\mathrm{v}}^{\mathrm{SS}} \equiv \langle n_{\mathrm{v}} \rangle_{\mathrm{p}} \,, \tag{4.29}$$

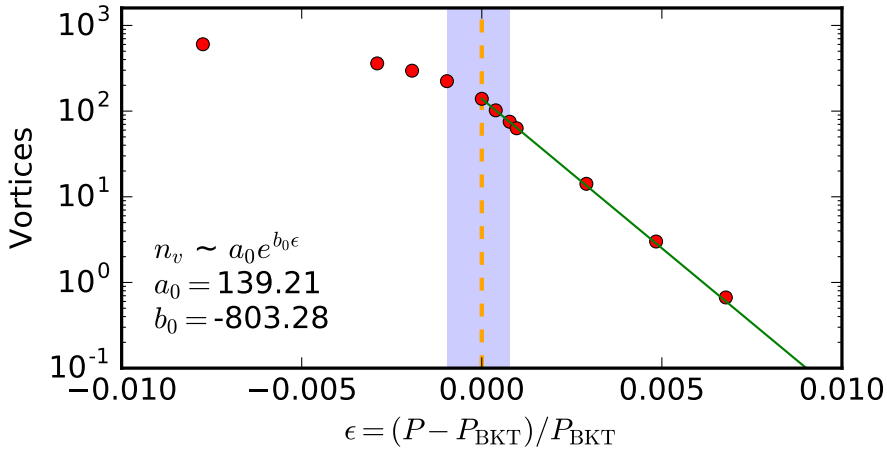

Figure 4.12: **steady state number of vortices.** Number of vortices at steady state $n_{\mathrm{v}}^{\mathrm{SS}}$ calculated in the vicinity of the threshold $\epsilon = 0$, corresponding to $P_0 = 1.033$. Below this point, the number of vortices exhibits critical slowing down (related analysis shown in Fig. 6.3). Above this point, the number of average topological defects is tentatively fitted with a negative exponential curve $n_{\mathrm{v}}(\epsilon) \sim L_{\mathrm{v}}(\epsilon)^{-2} = a_0 e^{b_0 \epsilon}$, from which we extract $a_0 \sim 139.2$ and $b_0 \sim -803.28$.

where $\langle \cdots \rangle_{\mathrm{p}}$ is the average over stochastic paths, for $\mathrm{IP}_{\Omega=50}$. The vertical blue shadowed area, corresponding to the critical region, divides the phase diagram into regions of disordered (left) and quasi-ordered (right) phases. On the disordered side ($\epsilon < 0$), topological defects decrease according to the equilibrium critical slow down of the system, as shown in Fig. 6.3. On the ordered side, once the system crosses the threshold ($\epsilon > 0$), we find the number of vortices n_{v} to decay exponentially, in accordance with OPO results (Dagvadorj *et al.*, 2015).

After having determined the critical region through the independent measurements of spatial coherence (see Fig. 4.10) and topological defects (see Fig. 4.12) for the set of parameters taken in consideration, we can now focus on the characterisation of the nature of the phase transition. In an attempt to further investigate the "correct" value of the power-law exponent α for such a system for IP parameters, we enlarge the box size. We find $\alpha > 1/4$ suggesting the system is of the "nonequilibrium" type. In the following section we investigate further this subtle point.

4.3.5 Long-range behaviour at the critical point

The results presented in the previous section show that a phase transition between a disordered phase, in which correlations decay exponentially, and a quasi-long range ordered phase, characterised by algebraic decay and bound vortex-antivortex pairs, can appear in an incoherently-pumped polariton condensate.

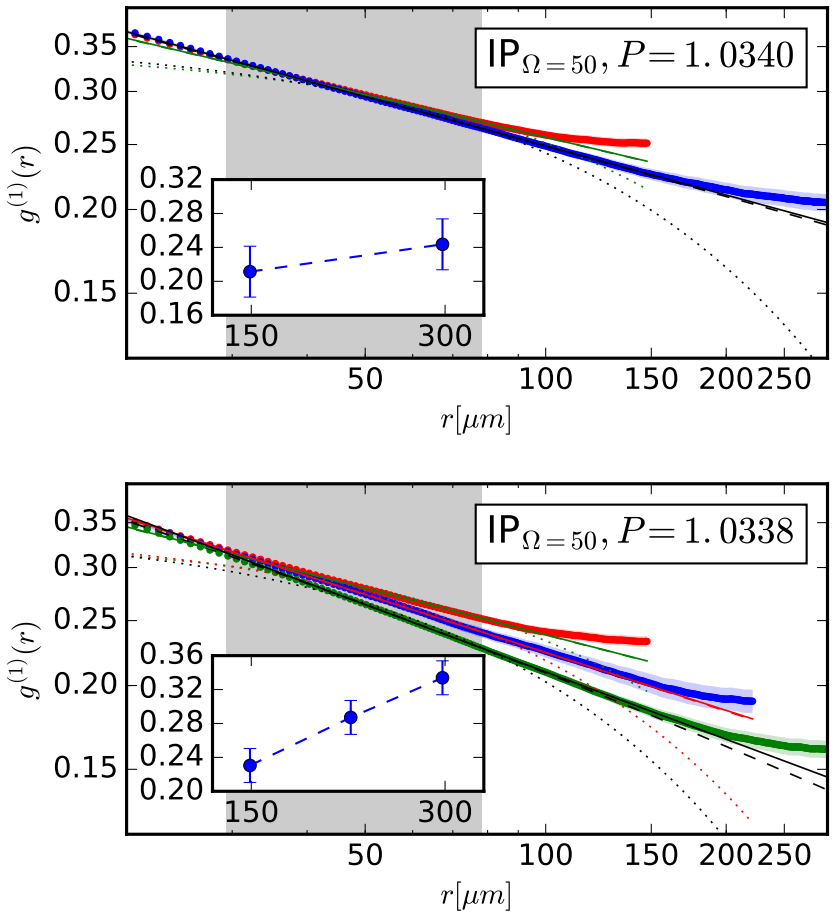

Figure 4.13: **Spatial correlations for larger system sizes.** Top panel: spatial correlations for P_0 = 1.0340, immediately outside the critical region in the quasi-ordered phase, calculated for different lattice size L = 295.11μm (red points) and L = 444.42μm (blue points), for the case IP$_{\Omega=50}$. Bottom panel: as top panel but for P_0 = 1.0338 (middle), borderline case of the critical region, calculated for different lattice size L = 295.11μm (red points), L = 444.42μm (blue points) and L = 590.22μm (green points). Red points correspond to the spatial correlation for the "standard" box size, employed throughout the analysis of this chapter. In both panels power-law (solid line), stretched-exponential (dashed line) and exponential (dotted line) fits are reported. The exponent α as a function of the system size L is reported in the insets of each panel.

Motivated by the experimental observation of values of the power-law exponent close to criticality exceeding the classical limit α = 1/4 (Roumpos *et al.*, 2012), we investigate the properties of the correlation function in the vicinity of the incoherently-pumped polariton critical region. Such a study should essentially allow us to investigate possible finite-size effects and the critical value of the algebraic exponent around the BKT threshold.

In the previous section, we tentatively identified the critical region for IP$_{\Omega=50}$ to lie in the window 1.032 < P_0 < 1.0338. Fig. 4.13 shows comparison of spatial correlation

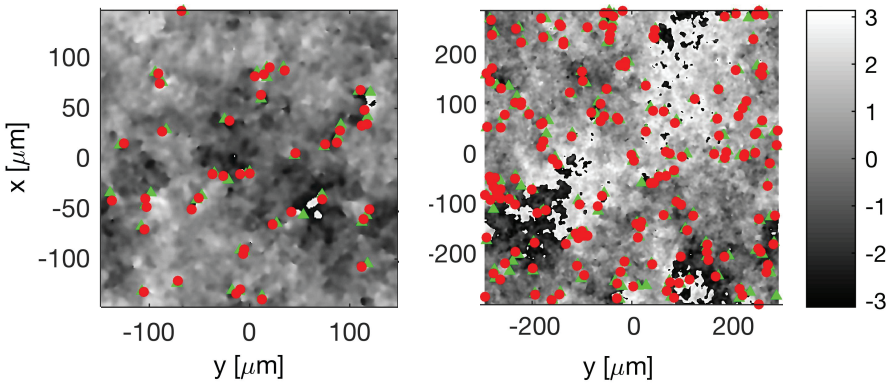

Figure 4.14: **Vortex-antivortex pairs for the borderline case.** Filtered phase with detected vortices (red dots) and antivortices (green dots) are displayed for the case $P_0 = 1.0338$, for $L = 295.11\mu$m (left) and $L = 444.42\mu$m (right), for the case $\mathrm{IP}_{\Omega=50}$. We note that only vortex-antivortex pairs are present in both configurations, suggesting the system is in a quasi-ordered phase. Colorbar shows the value of the phase.

functions calculated for different box sizes, for $P_0 = 1.0340$ (top), outside the critical region, and in the borderline case of the ordered regime $P_0 = 1.0338$ (bottom). Spatial correlations for different box sizes are compared. Red points correspond to the correlations computed with a lattice size $L = 295.11\mu m$ and $N = 301$ points (which corresponds to the size of the lattice used for obtaining the results discussed in the previous section). Blue and green points (when shown) correspond to $L = 444.42\mu m$ and $L = 590.22\mu m$, i.e. to a box size enlarged by 50% and 100%, respectively.

The different curves are then fitted with exponential and power-law functions, as in Fig. 4.7. We also tentatively fit the curves with a stretched-exponential function, of the form

$$y = C_0 e^{-(r/b)^c}, \tag{4.30}$$

with C_0, b and c free parameters. The exponential, stretched-exponential and power-law fits are shown, respectively, as dotted lines, solid lines and dashed lines in Fig. 4.13.

We note that while for the case $P_0 = 1.0340$, the curves are converged within the fitting area (grey faint region), confirming the power-law decay for larger boxes, the case $P_0 = 1.0338$ exhibits a further decrease of the slope as the system size increases. Larger boxes, in fact, are expected to show smaller coherence. As one moves away from the critical region, the fluctuation strength decreases and this effect become less evident. It is worth noting that similar effects have been observed by stochastic simulations for the OPO case (Dagvadorj *et al.*, 2015).

Let us focus on the exponent α extracted from the power-law fit for the case $P_0 = 1.0338$; this is of particular interest because it corresponds to the case $\alpha \sim 1/4$. In the inset of Fig. 4.13 (bottom), we plot the exponent α as a function of the box size. Here we find that the larger the box, the higher the exponent. Specifically, the"standard" box size shows $\alpha = 0.23$ (just below the equilibrium threshold) while, for larger boxes, α exceeds the limit of $1/4$, with $\alpha = 0.28$ and $\alpha = 0.33$ for $L = 444.42\mu m$ and $L = 590.22\mu m$, respectively. Thus, we apparently find $\alpha > 1/4$, implying that the nature of the system should be of the "nonequilibrium" type, a conclusion which is also suggested by the presence of only vortex pairs in one of the many system realisations, as illustrated in 4.14.

Nevertheless, Fig. 4.13 (bottom) which displays the various fits for a larger box, appears to show a slightly better fit of the stretched exponential to such curve, suggesting a value $\alpha < 1/4$ at equilibrium.

On the one hand, the presence of a stretched-exponential curve could indicate the features of KPZ theory (Altman *et al.*, 2015). However, this possibility is automatically ruled out by calculations of the length L_* (associated with the onset of stretched-exponential decay) for the parameters taken in consideration here, which confirm this length to be orders of magnitude larger than the system size L (see Appendix B.1 for a detailed discussion). Hence, one would not expect to find such behaviour on the range of scales we probed here.

On the other hand, a plausible cause may be the presence of finite size effects, which could be responsible for altering the decay of the spatial correlation function in the vicinity of the critical region; further investigation with larger boxes is indeed suggested. It is worth noting that similar effects at the boundaries of the system have also been observed theoretically in (Caputo *et al.*, 2017).

In order to remove any doubt regarding the nonequilibrium nature of the phase transition, one should investigate further the borderline case ($P_0 = 1.0338$) by ensuring all single realisations show evidence of only vortex-antivortex pairs, and more importantly, to check whether the exponent of the algebraic decay of the spatial correlations differs from the exponent of the time correlations (Caputo *et al.*, 2017).

Notwithstanding these interesting open questions, our work clearly defines a very narrow critical region for the BKT phase transition, although we cannot precisely ascertain the exact location of the critical point, or the nature of the phase transition occurring at that point with certainty.

In the following chapters, we study quenches about that critical region, and ensure that due to the region being narrow, our results are not affected by such small potential shift of the critical point (within the identified critical region).

4.4 Chapter summary

In this chapter we have described the theory of $2d$ phase transitions by means of the basic spin lattice model and shown the correspondence to a $2d$ Bose gas. We also discussed recent findings concerning the nature of the BKT transition of nonequilibrium systems, and undertook a detailed numerical study of the phase transition of an incoherently-pumped exciton polariton condensate. We reproduced successfully the phase diagram for the steady state density with both mean field and stochastic models. The average number of vortices exhibits a binding/unbinding crossover similar to the one exhibited by equilibrium systems. Particular attention was given to the critical region: the study on how it depends on the choice of pump-related parameters reveals that stronger fluctuations at higher modes ($\Omega \to \infty$) and smaller saturation density ($n_s \to 0$) lead to a larger shift of the pump power of the BKT transition with respect to the mean-field onset of macroscopic population growth.

Investigations of the decaying form of spatial correlations at the crossover between binding/unbinding of vortices, for the parameters taken into consideration, allowed us to identify a narrow critical region in which the decay of correlations changes from exponential to power-law. In the very vicinity of the transition, the algebraic exponent seems to show values higher than the equilibrium limit of $1/4$, indicating a nonequilibrium nature of the phase transition. However, the observed dependence of the precise value of α in large boxes, and the potential better fit of such decay with a stretched exponential function, suggest the need for further investigation.

Chapter 5

Dynamic scaling of driven-dissipative systems

In this work we address the open question of the dynamic scaling for a strong quantum dissipative system, focusing on $2d$ strongly-interacting quantum light-matter systems. Due to an unprecedented experimental and theoretical progress in recent years supported by an excellent degree of control and tunability of the system, strongly interacting light-matter platforms, particularly exciton-polaritons in microcavities, form one of the most exciting and promising group of driven-dissipative quantum-systems (Carusotto and Ciuti, 2013; Keeling and Berloff, 2011; Proukakis *et al.*, 2013; Deng *et al.*, 2010). Particularly appealing are the recent studies regarding critical properties of these system at steady state, revealing universal aspects and scaling properties, some with no counterpart for equilibrium systems (Altman *et al.*, 2015; Zamora *et al.*, 2017).

In the present study we show that these quantum fluids of light display a self-similar behaviour for the domain patterns during the coarsening process after an infinite rapid quench across a critical point, verifying the dynamic scaling hypothesis. This work was carried out in collaboration with Galbadrakh Dagvadorj (Department of Physics and Astronomy, University College London, United Kingdom), Alex Zamora (Department of Physics and Astronomy, University College London, United Kingdom), Iacopo Carusotto (INO-CNR BEC Center and Università di Trento, Italy), Marzena Szymańska (Department of Physics and Astronomy, University College London, United Kingdom), as detailed in Ch. 1. In particular, we stress that all numerical calculations, analysis and results concerning the OPO mechanism shown in this chapter, have been carried exclusively by the UCL group.

5.1 Theoretical background

One of the most attractive topics in statistical physics is the study of scaling phenomena. Complex systems at criticality display a self-similar patterns, since the system is statistically equivalent after a global and arbitrary change of scale (Binney *et al.*, 1992). The scaling phenomenon reveals the existence of critical exponents, which characterize the statistical magnitudes of the system at critical points and permit to identify universality classes for the classification of complex systems. Rapidly cooling (quenching) the system across the critical point from a disordered to an ordered phase leads to the creation of topological defects, such as vortices, which eventually decay in time. This process occurs concurrently to the growth of order through domain coarsening. At late enough times (compared to the time of crossing the critical point) the system is then expected to undergo "phase ordering dynamics": the system exhibits *universality* characterized by a single length scale $L(t)$ that governs the temporal evolution of all relevant quantities of the system.

The extension of the study of critical phenomena to out of equilibrium systems is a relatively new field. Particularly interesting is the study of out of equilibrium dynamics of systems which are quenched from the disordered to the ordered (or quasi-ordered) phase, across a critical point (Hohenberg and Halperin, 1977). This out of equilibrium dynamics is characterized by the formation and evolution of domains with different values of the order parameter (different broken phases). Depending on the symmetries, the system may present topological defects (domain walls, vortices, strings, monopoles), which are *surfaces* with a vanishing order parameter, which separates domains of different order parameters (Bray, 2002). The dynamics of these topological defects may play an important role since their densities can reveal universal aspects of the system in finite rate quench protocols, as pointed out by Kibble and later by Zurek (Kibble, 1976; Zurek, 1985). During the dynamical phase-ordering after the quench, a typical length scale $L(t)$ of the domains grows in time, reflecting the competition between the different orders.

We now recall the time dependence of this characteristic length for the $2d$ XY model (Jelić and Cugliandolo, 2011), where the coarsening process reveals a scaling and universal phenomenon at late-time dynamics. Comparison of the patterns of the domains at different times shows that they are statistically equivalent after a rescaling of the lengths by $L(t)$. This length turns out to be the single relevant length scale of the system at late-time dynamics. This is the so-called *dynamic scaling hypothesis* (Bray, 2002), which assumes that the non-steady state two-point correlator for the polariton field that fulfils

the form (Jelić and Cugliandolo, 2011; Bray *et al.*, 2000; Rutenberg and Bray, 1995):

$$g^{(1)}(r,t) \sim g^{(1)}_{\mathrm{SS}}(r,t) \cdot F\left(\frac{r}{L(t)}\right). \tag{5.1}$$

Here, according to the $2d$ XY model theory discussed in Sec. 4.1.1 of this thesis, the steady state correlation function decays algebraically at long distances, as

$$g^{(1)}_{\mathrm{SS}}(r) \sim r^{-\alpha}. \tag{5.2}$$

The scaling function F tends to 1 when $r \ll L(t)$, indicating that the critical correlations have been established at distances much smaller than $L(t)$ at time t, which defines the characteristic length-scale of the system $L(t)$.

The dynamic scaling hypothesis has been tested in many different complex physical systems. Of particular interest is the planar XY model in $2d$, since it has provided theoretical studies supported by strong numerical simulations of the dynamic scaling behaviour (Pargellis *et al.*, 1994; Fisher and Huse, 1988; Langer and Godrèche, 1992) and has been tested in different physical systems, as smetic liquid crystals (Pargellis *et al.*, 1994), magnetic ultra-thin films (Heinrich and Bland, 1994) and structure factors (Binder and Stauffer, 1974; Furukawa, 1978). The classical paradigm of phase ordering has been extended to quantum systems, particularly to systems subjected to a unitary (energy-conserving) evolution, such as Bose-Einstein condensates of atomic gases, both for spinless and spinor components (Damle *et al.*, 1996; Williamson and Blakie, 2016).

The inspection of the phase ordering shows that $L(t)$ typically follows a power law in time for a system free of topological defects: $L^z \sim t$, where the dynamical critical exponent z can present different values, depending on the particular system (as for example, $z = 2, 3$ for non-conserved and conserved fields respectively, or model A and B (Hohenberg and Halperin, 1977)). However, the dynamics of topological defects during the phase ordering can introduce modifications in this power law. As an example in a $2d$ equilibrium condensate, the vortices introduce a logarithmic term to the diffusive equation for $L(t)$ in non-conserved fields (Pargellis *et al.*, 1992; Yurke *et al.*, 1993):

$$L(t) \sim \left(\frac{t}{\log(t)}\right)^{1/z}. \tag{5.3}$$

This expression can be inferred by calculating the typical velocity of the vortex speed for the XY-model (which estimates $z = 2$) as shown in (Bray, 2000). The basic idea is to

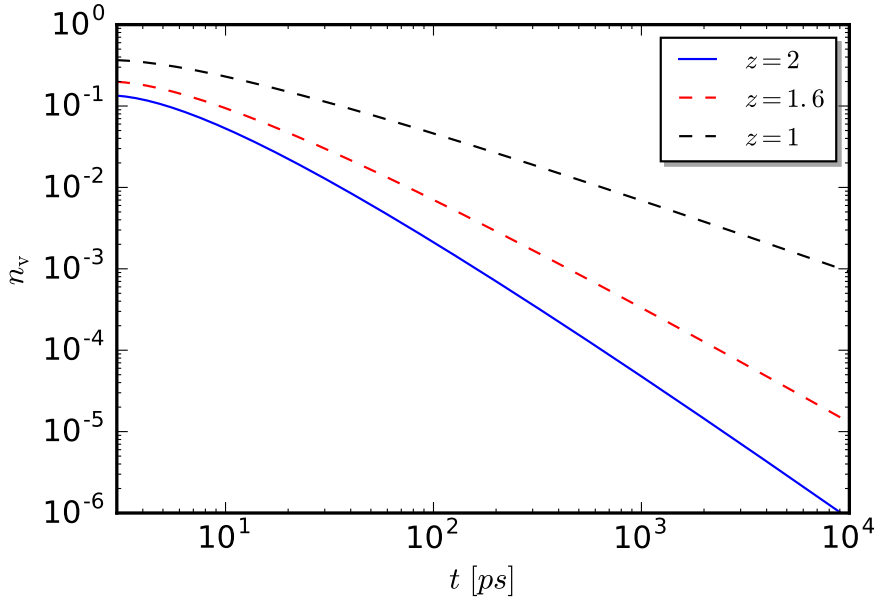

Figure 5.1: **Decay of topological defects in time**. We plot the time variance of the number of topological defects, Eq. (5.3), for different critical exponents, e.g. $z = 2$ XY-model (Model A) (Pargellis *et al.*, 1992; Yurke *et al.*, 1993), $z = 1.61$ (KPZ model) (Pagnani and Parisi, 2015), and $z = 1$ for conservative Bose systems Damle *et al.* (1996). We stress that the shape of the curves changes significantly at very long times.

consider the energy E_p of a single vortex-antivortex pair, i.e.

$$E_v \sim \log\left(\frac{r}{a}\right) \tag{5.4}$$

where r is the distance between the two vortex cores, and calculate the force between them, $F = -dE_p/dr \sim 1/r$. The same force can be deduced by the relation between the velocity of the vortex pair and the vortex mobility μ, by means of $\mu = v/F$, where μ is found to depend logarithmically on the distance r (Yurke *et al.*, 1993). By equating these two forces, we arrive at an equation for r which, once integrated, gives Eq. (5.3). A schematic plot which illustrates the behaviour of Eq. (5.3) is reported in Fig. (5.1), for different values of the dynamical critical exponents.

5.2 Motivation for this work

Critical exponents which characterise the phase ordering process for driven-dissipative microcavity polaritons have not been measured to date, while theoretical predictions are subject to debate. Specifically, $2d$ driven-dissipative systems described by KPZ-like phase dynamics are expected to show the dynamical critical exponent $z \approx 1.61$ (Pagnani and

Parisi, 2015; Canet *et al.*, 2010; Halpin-Healy and Palasantzas, 2014) while in the equilibrium limit, where the KPZ nonlinearity ceases to be important, we expect $z = 2$. Moreover, it has been suggested that the dynamical critical exponent z for microcavity polaritons coupled to a reservoir takes values of either 1 or 2, depending on system parameters (Kulczykowski and Matuszewski, 2017), casting doubt upon the universality of the phase ordering in this system.

Motivated by these considerations, we explore the critical properties of $2d$-microcavity polaritons, and in particular the characteristic length and density of topological defects (vortices), by studying the phase ordering (scaling) dynamics after an infinitely rapid quench from the disordered to deep in the (quasi)ordered (Hohenberg and Halperin, 1977; Bray, 2002) phase.

It is worth noting that although the polariton system and the planar XY-model are paradigmatic examples of extremely different critical systems (since the first is a genuine nonequilibrium system and the second is a canonical case of an equilibrium system) we assume that driven-dissipative systems should follow the scaling assumption (5.1). This is based on the analogies between both systems, since

- both systems present a disordered phase with exponential decay of correlation, and an algebraically quasi-ordered phase, separated by a critical point,
- both systems undergo a BKT-type of phase transition when crossing the critical point due to the binding/unbinding process of topological defects,
- the nature of the vortices comes from isomorphic symmetry groups, which are the SO(2) for the planar XY-model and U(1) for the polariton system.

5.3 Numerical results

In this section we report strong numerical evidence of the universal scaling dynamics during the phase ordering of the microcavity-polariton system, both in the parametric and incoherent pump schemes, since the system shows a self-similar patter of the domains after a rescaling of the lengths with a characteristic length $L(t)$ at late-time dynamics. We observe that this length-scale takes the form given by Eq. (5.3), exhibiting the characteristic logarithmic correction due to the role of the topological defects (vortices) during the coarsening process. The dynamic scaling exponent takes the value $z \approx 2$, which coincides with the one of the classical model A (no-conserved) fields, i.e. the classical planar XY-model.

5.3.1 System parameters

We address the phase ordering kinetics of $2d$ polariton field in a microcavity by considering the two different schemes for the external drive which have been considered traditionally by the community, namely the parametric and incoherent pump regimes.

Motivated by the study on the BKT transition for the incoherently-pumped condensate, discussed in Chapter 4, we solve the model (3.3) by making use of the same sets of parameters, which we recount as follows. We use typical experimental parameters (Nitsche *et al.*, 2014): $\gamma_{\rm LP} = 1/\tau_{\rm LP}$ with the polariton lifetime $\tau_{\rm LP} = 4.5ps$, polariton mass $m_{\rm LP} = 6.2\ 10^{-5}\ m_{\rm e}$, polariton-polariton interaction strength $g_{LP} = 6.82\ 10^{-3}\ meV\mu m^2$. We use here $P/P_{\rm th} = 1.06$, where $P_{\rm th} = \gamma_{\rm LP}$ is the mean field critical pump, $\Omega = 50\gamma_{\rm LP} = 11.09ps^{-1}$ and $n_{\rm s} = 500\mu m^{-2}$ (labelled as $\mathrm{IP}_{\Omega=50}$), for the frequency-dependent pumping, and $P/P_{\rm th} = 1.1$, $\Omega = \infty$ and $n_{\rm s} = 1500\mu m^{-2}$ for the frequency-independent driving (labelled $\mathrm{IP}_{\Omega=\infty}$). We solve Eq. (3.3) in a square lattice of 301^2 points, lengths $L_x = L_y = 295.11\mu m$ and periodic boundary condition and average over a sufficiently-large number (400) of realisations in all schemes.

Since we are interested in the universal properties of driven-dissipative systems, we also consider the alternative typical set-up of parametric driving. For the parametric pump polariton system, whose numerical implementation is discussed in Sec. 2.3.2, we specifically focus our study on a particular configuration extensively studied both theoretically and experimentally. The cavity for this configuration is characterized by a large value for the loss-rate of the cavity-photons, which leads to a particularly small cavity-photon mean lifetime: $\tau_{pol} \approx 7ps$, as the most promising for observation of the different phases. However, current state-of-the-art inorganic microcavities are characterised by much longer polariton lifetime, since these values may run from standard values $\tau_{pol} \approx 30ps$ up to very long life times, as for example $\tau_{pol} \approx 150ps$ in extremelly good inorganic samples. The other parameters characterizing the system are chosen to be close to current experiment values (Sanvitto *et al.*, 2010b; Dagvadorj *et al.*, 2015). Thus, the Rabi frequency for the oscillation between the photons and the excitons in our system takes the value $\Omega_R \approx 4.4meV$ and the exciton-exciton strength interaction $g_x \approx 0.002meV\mu m^2$ (Carusotto and Ciuti, 2013). We consider a zero-detuning between the cavity-photons and the excitons. The parametric external drive is set to act with a momentum $\mathbf{k}_p = (1.6, 0)\mu m$ and resonantly with the lower polariton dispersion relation ω_{LP}, since the external drive frequency is given by $\omega_p = \omega_{LP}(\mathbf{k}_p)$. Hence, we present the results for a polariton system solved by means of Eq. (2.72) implemented on a square lattice of total length $444.416\mu m$, computed on a grid of 512^2 lattice points with lattice spacing $a = 0.868\mu m$. It is worth noting that the healing lengths (here approximated by the mean-field equivalent, since

they are probed in a regime where fluctuations are very low)

$$\xi = \frac{1}{\sqrt{2m_{\mathrm{C,LP}}\, g_{\mathrm{C,LP}}\, \left|\psi_{\mathrm{C,LP}}\right|^2_-}} \tag{5.5}$$

at the end of the evolution are respectively $\xi^{\mathrm{IP}}_{\Omega=50} \simeq 2.2\mu m$, $\xi^{\mathrm{IP}}_{\Omega=\infty} \simeq 0.8\mu m$ and $\xi^{\mathrm{OPO}} \simeq 1.84\mu m$, with the condition $L(t) \gg \xi$ fulfilled in all cases.

5.3.2 Universal dynamic scaling

In both models a non-equilibrium steady state with finite particle density $|\psi_{\mathrm{X,C,LP}}|^2$ is established once the pumping strength overcomes the cavity losses. Also by tuning the strength of the pump power both the OPO and the IP system (with/without frequency-dependent pumping mechanism) undergo a BKT-type of phase transition between a disordered phase with exponential and an ordered phase with power-law decay of spatial coherence, governed by the binding/unbinding of vortex-antivortex pairs (see Fig. 5.2). For the parametric pumping, the BKT transition in the steady-state is analysed in detail in (Dagvadorj *et al.*, 2015).

The following quench protocols are implemented. Specifically, for the parametrically pumped case (see Fig. 5.2 top), we quench through the upper critical threshold f_p^{up}. The system is prepared in the steady-state of a deeply disordered phase at a given pump power $f_p^i > f_p^{\mathrm{up}}$ where bound and unbound vortices proliferate (see the inset), and is instantaneously quenched to a deep quasi-ordered regime by adjusting the external drive to f_p^f, with $f_p^f < f_p^{up}$. For the incoherently-pumped case (see Fig. 5.2 bottom), we consider a sudden quench from the random initial configuration of the system deep in the disordered phase (i.e. steady-state for $P^i = 0$), to a quasi-ordered regime by setting the external drive to $P^f > P_{\mathrm{th}}$ at $t = 0$ and letting the system evolve.

Immediatelly after the quench, both in the parametric and incoherent scenarios, the different domains present at the initial time, due to the disorder characterizing the initial state, start to compete between them and the typical size of those domains, given by $L(t)$, starts to grow monotonically in time, leading to the phase ordering process.

As a consequence, the density of the vortices decreases in time through annihilation processes between vortices and antivortices, as displayed in Fig. 5.3 for 3 different snapshots at different times during the dynamics of the incoherently-pumped system. In equilibrium system (modelled by standard GPE equation) the vortex motion is directly determined by the interaction potential. In the case of a vortex anti-vortex pair, they

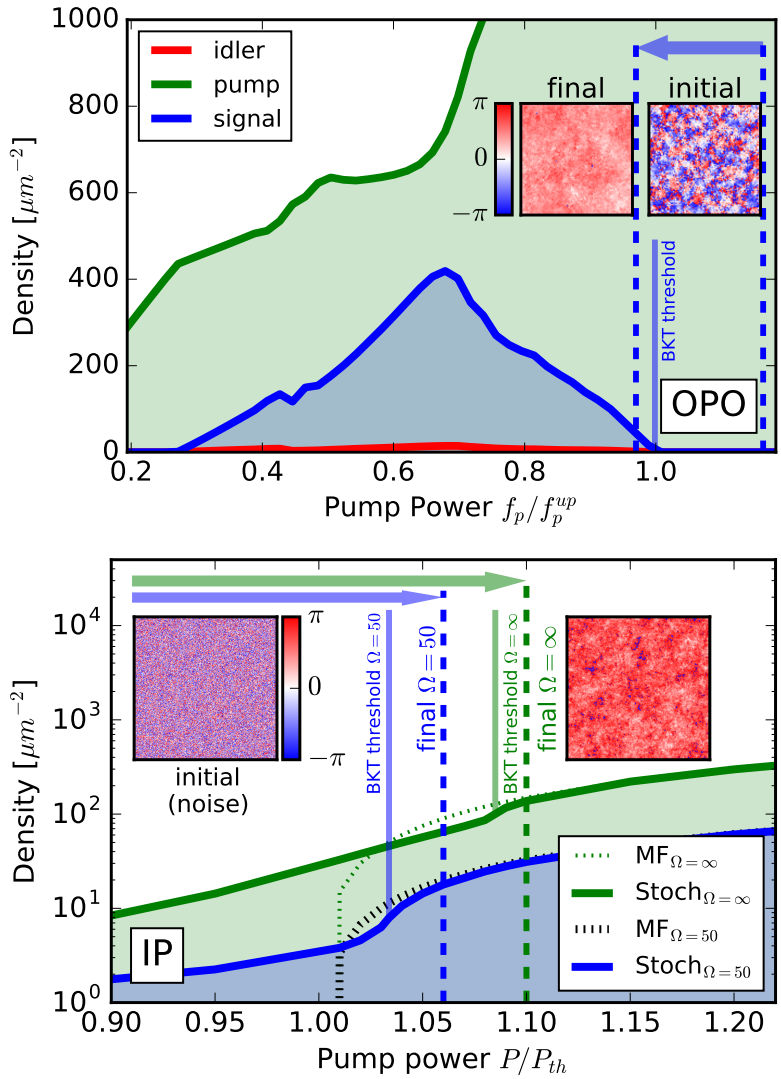

Figure 5.2: **BKT transition with parametric and incoherent pumping.** Top panel: noise-averaged density from stochastic equations of the signal (blue), idler (red) and pump (green) as a function of pump power f_p for parametrically driven polaritons across OPO. Bottom panel: mean-field (dotted lines) and noise-averaged (solid lines) densities for frequency-independent (green) and frequency-dependent (blue) incoherent pumping. In both panels arrows indicate the infinitely rapid quench protocol across the critical region and pump powers are scaled to their corresponding mean-field threshold values. The insets show typical snapshots of the real space phase profile for the initial and late-time states.

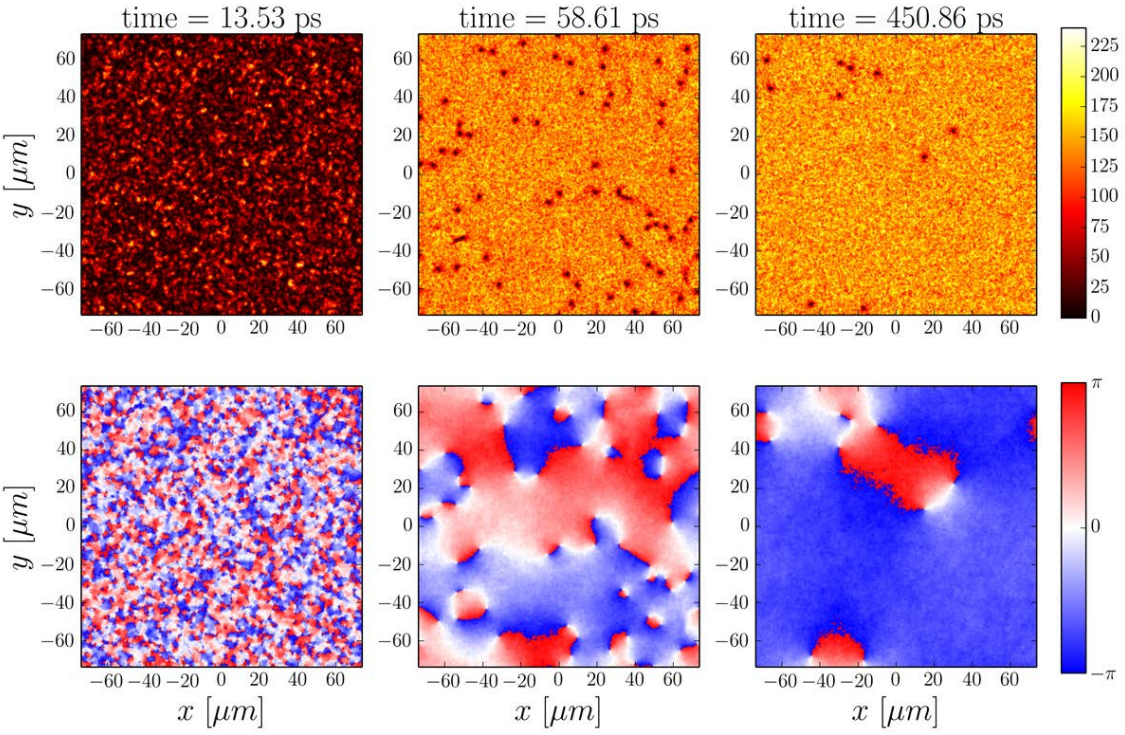

Figure 5.3: **Phase ordering dynamics of an IP system.** Snapshots capturing the phase ordering process for condensate density in μm^{-2} (top) and phase (bottom) of an incoherently-pumped system. The initially noisy configuration of the system (left) becomes gradually ordered through the annihilation of vortex pairs (centre and right) according to the scaling law of Eq. (5.15). Parameters as in Fig. A.4.

move in parallel. The interaction energy, as well as the vortex trajectories, are strongly modified by driving and dissipation; in particular, self-acceleration of the single vortex takes place under strongly nonequilibrium conditions (Gladilin and Wouters, 2017). The recombination and decay process of vortex and antivortex pairs, which is similar to the one described through Kibble-Zurek mechanism for finite quenches protocols, has been also observed in other different polariton systems (Kulczykowski and Matuszewski, 2017; Matuszewski and Witkowska, 2014b; Liew *et al.*, 2015).

We explore the dynamic scaling properties of the system during the phase ordering process by considering the first order two-point correlation function:

$$g^{(1)}(r,t) = \frac{\langle \psi^*(r+u,t)\psi(u,t)\rangle - \frac{\delta_{r+u,u}}{2\Delta V}}{\sqrt{\langle |\psi(r+u,t)|^2_-\rangle \langle |\psi(u,t)|^2_-\rangle}}\,, \tag{5.6}$$

where $\langle \dots \rangle$ denotes averaging over both noise realisations and the auxiliary position $\mathbf{u}$,

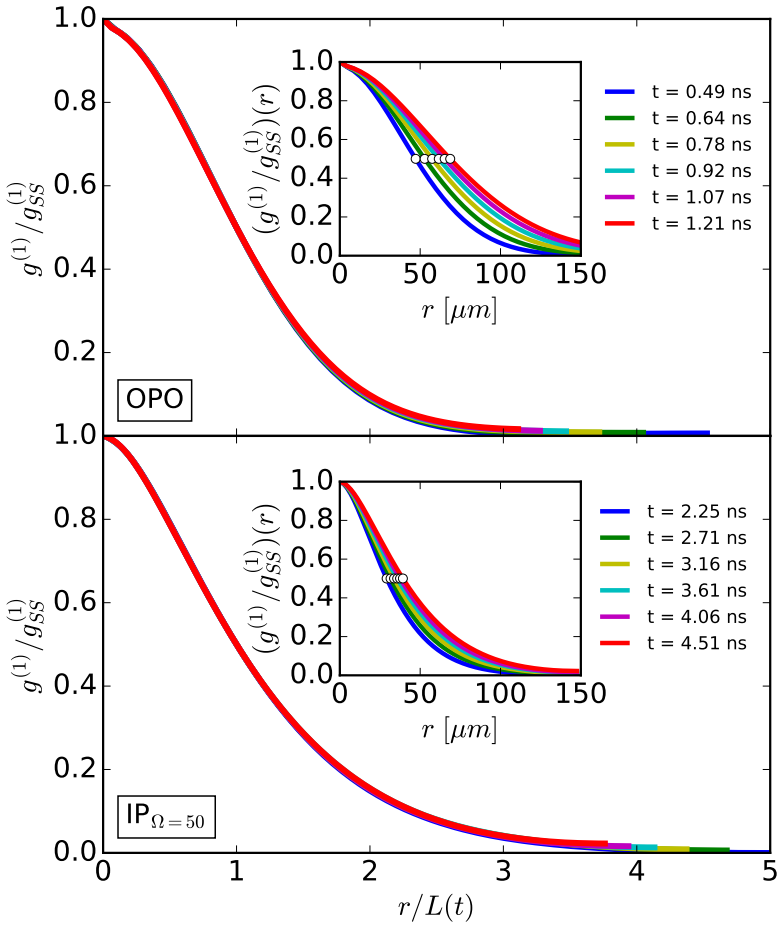

Figure 5.4: **Scaling of the two-point correlation function.** First-order correlation function $g^{(1)}$ (normalised by the corresponding steady state correlator $g^{(1)}_{\rm SS}$) for the parametrically-pumped (top) and incoherently-pumped polaritons with (bottom) frequency-dependent pumping as a function of the rescaled distance $r/L(t)$ at different times during the phase-ordering process. The apparent collapse of the curves confirms the dynamic scaling hypothesis. Insets show $g^{(1)}/g^{(1)}_{\rm SS}$ at different times, from which the characteristic length-scale $L(t)$ is obtained by considering $(g^{(1)}/g^{(1)}_{\rm SS})(L(t),t) = 0.5$ (white dots).

and t is the time after the quench. For the parametrically pumped scheme, ψ in Eq. (5.6) corresponds to the signal, which is obtained by filtering the cavity-photon field ψ_C from Eq. (2.72) around the signal momentum $\mathbf{k}_s$. For incoherently-pumped system, ψ is the polariton field ψ_{LP}. From the calcutions of first order correlation functions at different times, we are now able to test whether, and in which temporal window, universal dynamic scaling holds for the different pumping schemes considered.

We note that the configurations of the microcavity-polaritons considered in this study has been predicted to display a faster decay of correlations after a very long scale L_*.

According to the KPZ theory (see Sec. 2.3.3), after this scale non-equilibrium effects become relevant (Altman *et al.*, 2015; Zamora *et al.*, 2017). However, since this scale is much bigger than the scales considered in this work, as discussed in App. B.1, we expect the polariton system to fulfil the scaling form appearing at Eq. (5.1).

We observe that the system holds the dynamic scaling hypothesis during the phase-ordering kinectics since we obtain a perfect collapse when plotting the function $g^{(1)}/g^{(1)}_{\mathrm{SS}}$ as a function of the rescaled length $r/L(t)$ at different times of the late dynamics. These results are displayed at Fig. 5.4 for the parametric and incoherent scenarios respectively. Thus, the system fulfils the scaling expression given at Eq. (5.1) and, consequently, shows a self-similar pattern for the domains during the coarsening process after the infinitely rapid quench. For consistency, we extract the length-scale $L(t)$ when

$$(g^{(1)}/g^{(1)}_{\mathrm{SS}})(L(t), t) = 0.5 \tag{5.7}$$

(white dots in insets of Fig. 5.4), with the independence of our conclusions on the intersection value verified in Section (5.4.4) of this thesis.

5.3.3 Evolution of the characteristic length and number of defects

Since our polariton system fulfils the scaling hypothesis, as revealed by the collapse of the two-point correlation function, we can access the universal dynamical critical exponent z of our driven-dissipative system by analysing the growth of the characteristic length $L(t)$ and the decay of the number of topological defects (vortices) at late times after a sudden quench. Note that an equilibrium analogue of the phase degree of freedom for polariton system is the planar XY-model, where free vortices and bound vortex-antivortex pairs exist even in the steady-state below and above the BKT phase transition respectively.

The existence of the steady-state vortices plays a fundamental role in the phase ordering process and introduces the characteristic logarithmic correction into the late-time dynamics both of $L(t)$ and number of vortices n_{v} following a sudden quench (Yurke *et al.*, 1993; Jelić and Cugliandolo, 2011), such that

$$L(t) \sim \left(\frac{t/t_0}{\log(t/t_0)}\right)^{1/z} \tag{5.8}$$

and

$$n_{\mathrm{v}}(t) \sim \left(\frac{t/t_0}{\log(t/t_0)}\right)^{-2/z} \tag{5.9}$$

where t_0 is a nonuniversal microscopic system timescale. The two relations follow from

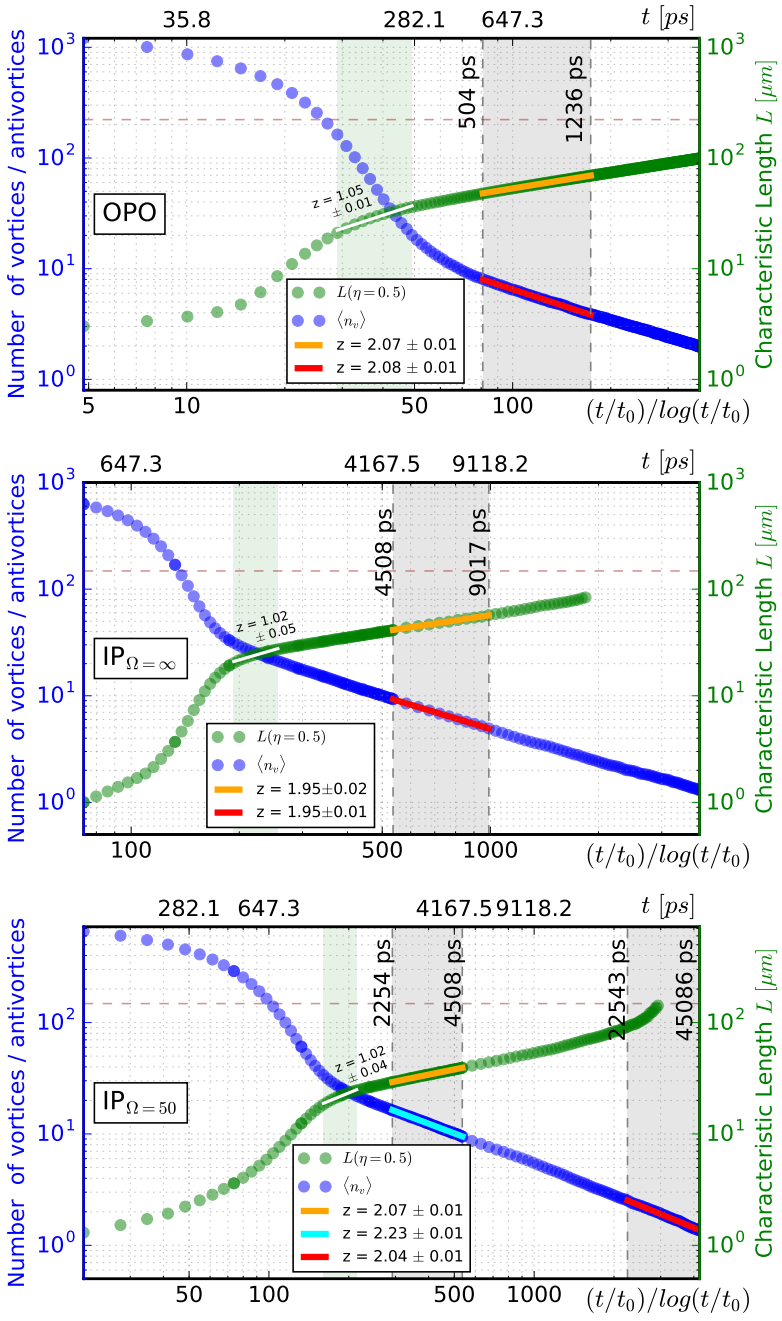

Figure 5.5: **Topological defects and $L(t)$ during phase ordering**. Density of vortices (blue) and the characteristic length-scale $L(t)$ (green) as a function of time after an infinite rapid quench for parametric (top panel), frequency-independent (central panel) and frequency-dependent (bottom panel) incoherently-pumped polaritons. The size of the numerical grid is marked by the horizontal (brown) dashed lines. Late-time dynamics show characteristic diffusive behaviour described by logarithmic corrections $(t/t_0)/\log(t/t_0)$ to the dominant power-law scaling due to the presence of the topological defects. For all configurations, we obtain a non-equilibrium dynamical critical exponent $z \approx 2$ within the grey-shaded regions.

the fact that

$$n_{\mathrm{v}}(t) \sim \frac{1}{L(t)^2} \tag{5.10}$$

when there is a *unique* length-scale in the system, which is true at late times in the dynamics. We check this condition in Sec. 5.4.3 of this thesis. Here we take $t_0 = 1ps$, which is in agreement with previous theoretical investigations (Jelić and Cugliandolo, 2011). However, we present a detailed study on the role of this parameter on the dynamical exponent z in Sec. 5.4.5 (see Fig. 5.12 where we investigate the relation between the two quantities, in time, for different pumping schemes).

To demonstrate the emergence of this universal scaling from our numerical data, Fig. 5.5 plots the characteristic length $L(t)$ and number of vortices $n_{\mathrm{v}}(t)$ for the three different pumping schemes considered. OPO (top) and $\mathrm{IP}_{\Omega=\infty}$ (centre) cases are found to be qualitatively similar, in the sense that $g^{(1)}$ collapses in the same time window as that in which the respective vortex dynamics reaches the converged $z \approx 2$ value. We are careful to fit $L(t)$ and n_{v} late enough in the quench so the dynamics becomes universal (indeed both reveal $z \approx 2$) but before size effects, power-law correlations or very small vortex numbers affect our analysis. However, in the case of $\mathrm{IP}_{\Omega=50}$ (bottom), strong damping of collective fluctuations, introduced by the explicitly frequency-dependent nature of the pump, is responsible for the collective modes to reach $z \approx 2$ at a much earlier time than the topological modes. Nevertheless, both channels show the dynamical critical exponents to be $z \approx 2$ in their appropriate late time windows. A more detailed discussion about the fitting criteria can be found in Sec. 5.4.2.

We note our results are also in agreement with the late-time decay of a dissipative $2d$ homogeneous quantum system, characterised by a two-vortex annihilation process resulting in a scaling $n_{\mathrm{v}} \sim t^{-1}$. This is intrinsically different from the non-dissipative case, where $n_{\mathrm{v}} \sim t^{-0.3}$ (Baggaley and Barenghi, 2018). However, we stress that in the driven-dissipative case, solved with the set of parameters considered in this work, the (slower) three-vortex annihilation process $n_{\mathrm{v}} \sim t^{-1/2}$, expected to take place in a non-dissipative system before the two-vortex annihilation process, is not seen within our simulations.

We stress that the sufficiently late-time analysis is essential to allow all channels to equilibrate properly, and fulfil the scaling hypothesis, whereas fitting early in the phase-ordering process, and before the dynamics becomes universal (light green regions in Fig. 5.5), can lead to the incorrect conclusion of $z \approx 1$. Note that for the experimentally realistic parameters considered in our simulations, the phase-ordering takes place on timescales similar to the polariton population growth, as discussed in Sec. 5.4.1 which is the case for

which Ref. (Kulczykowski and Matuszewski, 2017) predicted $z \approx 1$.

5.4 Identification of dynamical critical exponent z

In this section we present technical details related to our numerical procedure and analysis, offering convincing proof that $z \approx 2$ with logarithmic corrections is the correct dynamical exponent for exciton-polariton systems across all experimentally-relevant regimes. After discussing the different physical regimes probed in terms of the interplay of density-growth and vortex-decay dynamics, we demonstrate the clear emergence of $z \approx 2$ in the presence of logarithmic corrections at sufficiently late evolution times. We refer to Sec. A.1.2 for a detailed discussion on the numerical convergence of our computational results. We also show the direct relation between vortex number and the obtained characteristic length scale, demonstrating the effective independence of our conclusions on the choice of intersection point for the correlation function collapse and show that careful consideration of the conventionally-ignored intrinsic nonuniversal timescale t_0 does not affect our findings.

5.4.1 Vortex number dynamics

A previous study (Kulczykowski and Matuszewski, 2017) of incoherently-pumped exciton-polariton systems (which however also includes simple modelling of the reservoir dynamics by a rate equation) has observed the dynamical critical exponent to be dependent on the quality of the sample, through the polariton lifetime, thus arguing for different types of non-universal dynamics for the driven-dissipative exciton-polariton system. Contrary to such a statement, our work, based on two rather distinct models, demonstrates unequivocally that the universality class of the phase transition in polariton systems of experimentally realistic sizes falls, as anticipated, within the $2d$ XY-model universality class provided that exponents are extracted at the appropriate late times.

Fig. 5.6 displays time evolutions of the averaged particle density and average number of vortices for the OPO (top) and IP (middle/bottom) systems. During the growth of the density of the degenerate exciton-polariton system, the vortex pairs decay monotonically in time, eventually reaching the long-time limit where universal phase-ordering kinetics features should set in.

By including a simple rate-equation model for the reservoir, Ref. (Kulczykowski and Matuszewski, 2017) effectively argued that the value of the dynamical critical exponent

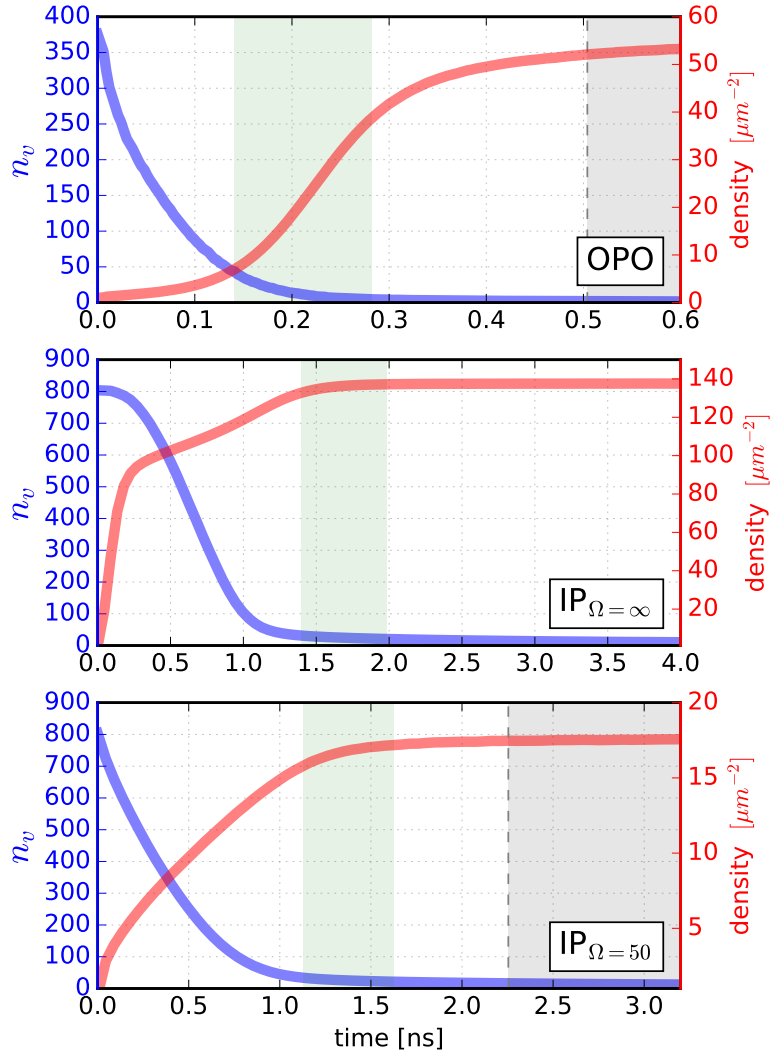

Figure 5.6: **Evolution of averaged density and number of vortices.** Density growth and pair annihilation for parametric (top), frequency-dependent (central) and frequency-independent incoherent pumping systems (bottom). We report regions where vortex dynamics follows Eq. (5.13) with critical exponent $z \approx 1$ (faint green region) and $z \approx 2$ (grey region) as reported in Fig. 5.5.

depends on the interplay between timescales for density saturation and vortex pair annihilation. Specifically, it has been suggested that in cases where the two processes occur effectively in parallel (i.e. on similar timescales) one would expect the critical exponent $z = 1$, characteristic of conservative superfluids (Damle *et al.*, 1996; Williamson and Blakie, 2016), whereas in the case where the majority of vortex pair annihilation occurs after the density has effectively saturated, one would expect $z = 2$, as in the $2d$ XY model (Bray *et al.*, 2000; Jelić and Cugliandolo, 2011).

Fig. 5.6 shows the three cases considered within our numerics, based on experimentally-

relevant parameters (Kasprzak *et al.*, 2006; Nitsche *et al.*, 2014). Specifically we consider cases in which the two processes occur in parallel (bottom), where the density growth is initially much faster than vortex annihilation (middle), and where the density grows after most vortex annihilation has taken place (top). As reported in the main text (Fig. 5.5), when fitting all such cases with the applicable scaling law with logarithmic corrections

$$n_{\mathrm{v}}(t) \sim \left(\frac{(t/t_0)}{\log(t/t_0)} \right)^{-2/z}, \tag{5.11}$$

we find clearly that $z \approx 1$ at early evolution times (highlighted in Fig. 5.6 by the faint green regions), and that the dynamical critical exponent always converges to $z \approx 2$ at later times (grey regions in same plots), as shown convincingly in next section.

5.4.2 Logarithmic corrections and dynamical exponent

We now discuss the fitting criteria and the determination of errors in the late-time dynamics (grey regions in Fig. 5.5) of the coarsening process. Each data point has a statistical error arising from averaging over many realisations. We fit such data with the appropriate power law curve (Eqs. (2)-(8)) and extract the optimum exponent with an error bar arising from the fitting procedure, specifically from the estimated variance. The large number of data points with small error bars combined with the fact that all points lie convincingly on a given straight line in log-log scale, lead to a very small fitting error (of the order of 1%-2%) in the determination of z.

Specifically for vortex dynamics, the time evolution of the average number of vortices during the annealing process is fitted with (Jelić and Cugliandolo, 2011)

- A power law formula for a diffusive system

$$n_{\mathrm{v}}(t) = A_0 \cdot (t/t_0)^{-2/\bar{z}}, \tag{5.12}$$

  or,

- a function with logarithmic corrections to account for the dynamics of pairs of topological defects:

$$n_{\mathrm{v}}(t) = A_0 \cdot \left(\frac{(t/t_0)}{\log(t/t_0)} \right)^{-2/z}, \tag{5.13}$$

where A_0, $\bar{z}$ and z are free parameters of the fit, and $\bar{z}$, z correspond to the extracted dynamical critical exponents in the presence, or absence, of logarithmic corrections.

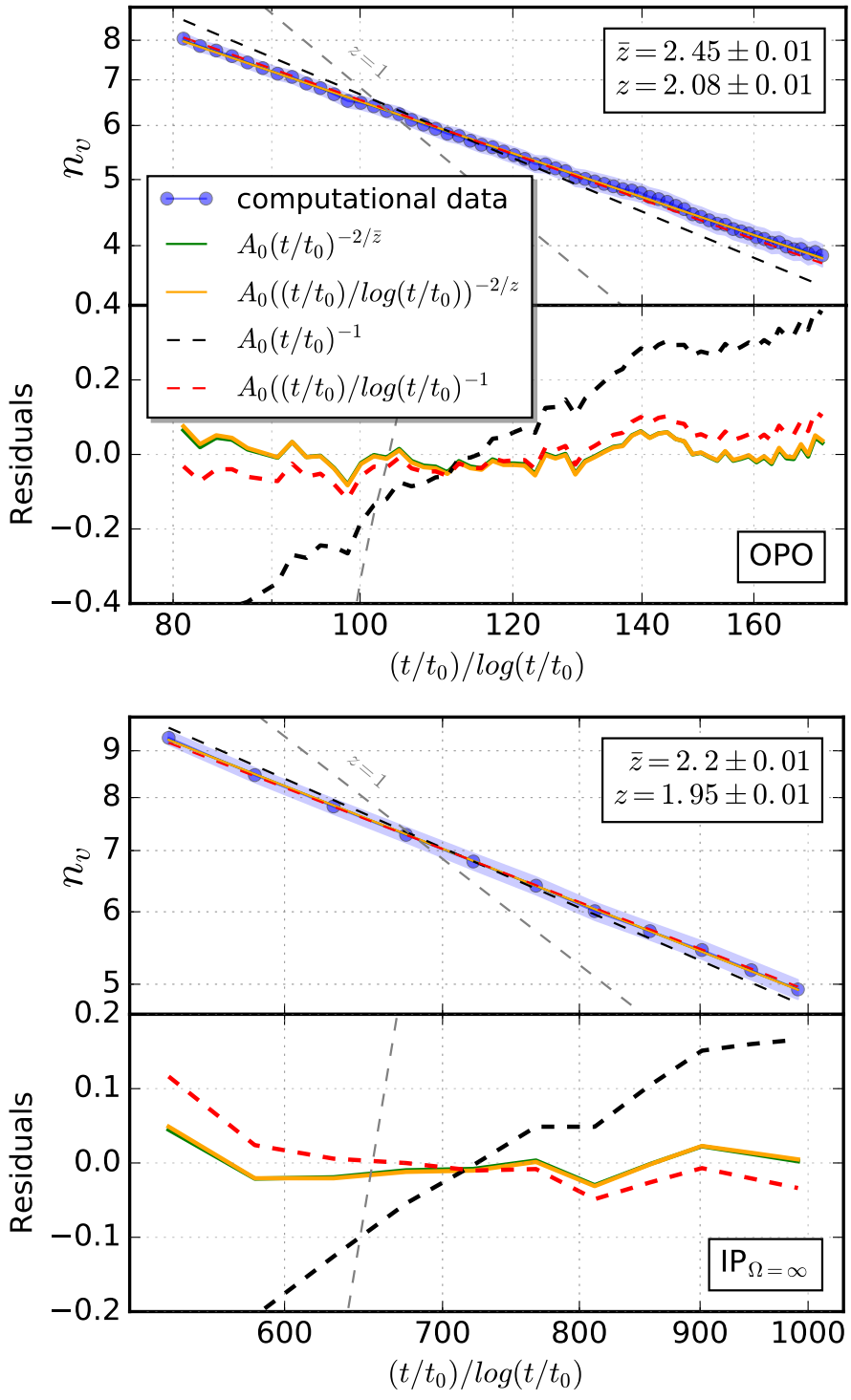

Figure 5.7: **Analysis of logarithmic corrections**. Different fitting curves are used to capture the role of the logarithmic corrections appearing in the vortex number evolution at late times for the cases of OPO (top) and IP$_{\Omega=\infty}$ (bottom). Extracted exponents with (z) or without ($\bar{z}$) logarithmic corrections are reported in the text boxes. Dashed grey lines show the corresponding results for value of z = 1. In each case we also show the residuals of the fits. Parameters as in Fig. 5.5.

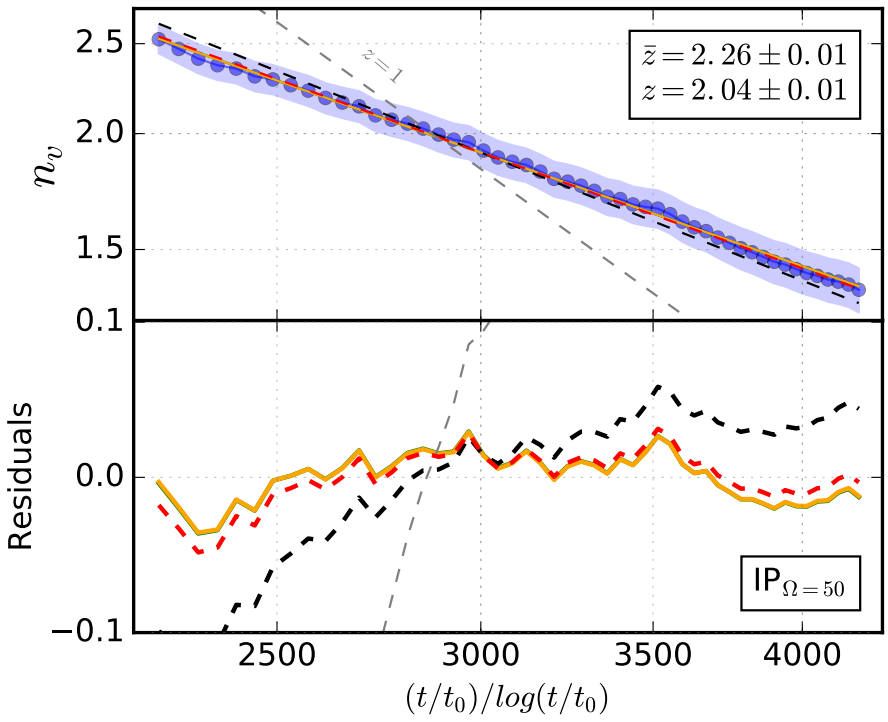

Figure 5.8: **Analysis of logarithmic corrections**. As in Fig. 5.7, but for the IP$_{\Omega=50}$ case.

Constraining the dynamical exponent to the theoretically anticipated $z = 2$ value, we also show fits to defects dynamics with

$$n_{\rm v}(t) = A_0 \cdot (t/t_0)^{-1}, \tag{5.14}$$

$$n_{\rm v}(t) = A_0 \cdot \left(\frac{(t/t_0)}{\log(t/t_0)}\right)^{-1} . \tag{5.15}$$

Comparison of different fitting curves are shown in Fig. 5.7 for IP$_{\Omega=\infty}$ (top) and IP$_{\Omega=50}$ (bottom) cases, and in Fig. 5.8 for OPO, within our region of convergence (grey band), from which we can infer numerous conclusions.

Firstly, while all fits of Eqs. (5.12)-(5.13) provide a reasonable description, careful consideration rules out the value $z = 2$ in the absence of logarithmic corrections (black dashed lines). Moreover, although fits of Eqs. (5.12) and (5.13) (solid green and yellow lines respectively) are practically indistinguishable in these figures (even in terms of their residuals), we stress that the exponent z, extracted by fitting Eq. (5.13) [with logarithmic corrections], is always closer to the anticipated theoretical value for the dynamical exponent ($z = 2$) than the extracted exponent $\bar{z}$ obtained from the fit based on Eq. (5.12). This suggests that, to the extent that the dynamical exponent should be consistent with

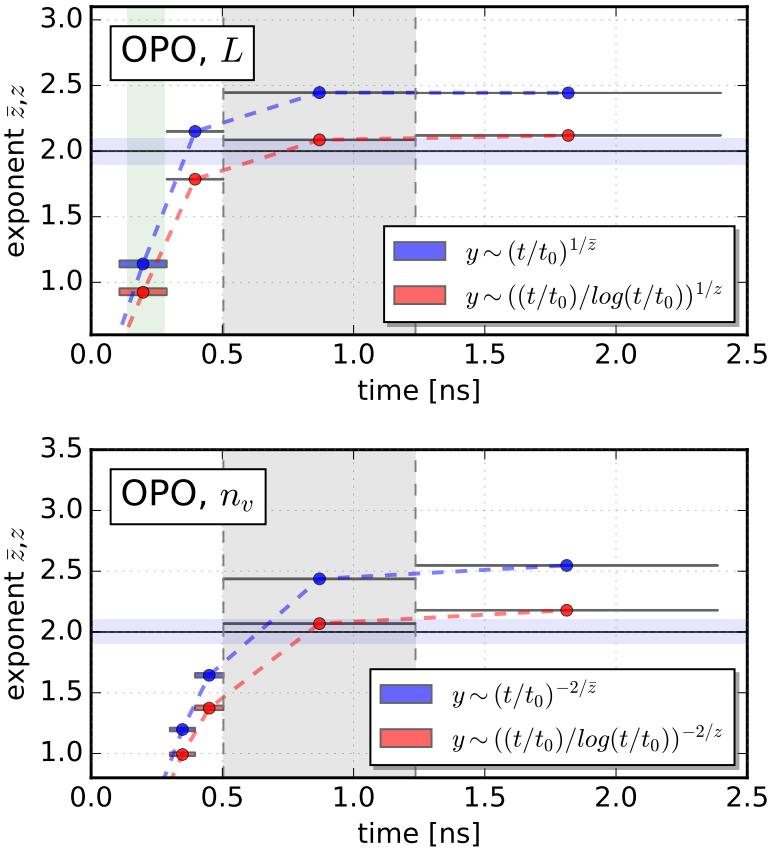

Figure 5.9: **Time evolution of the exponent z for OPO-regime.** Exponents z (circles) are extracted as a function of different temporal windows, for both characteristic length (top) and number of vortices (bottom). Results in absence (blue) and presence (red) of logarithmic corrections are compared. Temporal averaging intervals and numerical-fit errors are reported for completeness by the bands around the points. The vertical green and grey bands indicate corresponding regions shown in Figs. 5.5 and 5.6.

a value of 2, logarithmic corrections have to be present in the system, thus confirming the theoretically-anticipated description (Bray *et al.*, 2000; Jelić and Cugliandolo, 2011). A detailed analysis on the evolution of these exponents on the chosen evolution time window is given below.

Specifically, fitting our data with the "conservative superfluid" prediction of $z = 1$ (Kulczykowski and Matuszewski, 2017; Damle *et al.*, 1996; Williamson and Blakie, 2016) based on

$$n_{\mathrm{v}}(t) = A_0 \cdot \left(\frac{(t/t_0)}{\log(t/t_0)} \right)^{-2}, \tag{5.16}$$

reveals strong disagreement for all three cases (as shown by dashed grey lines in Figs. 5.7 and 5.8), thus ruling out such a value (in our chosen late-time windows). Above curves

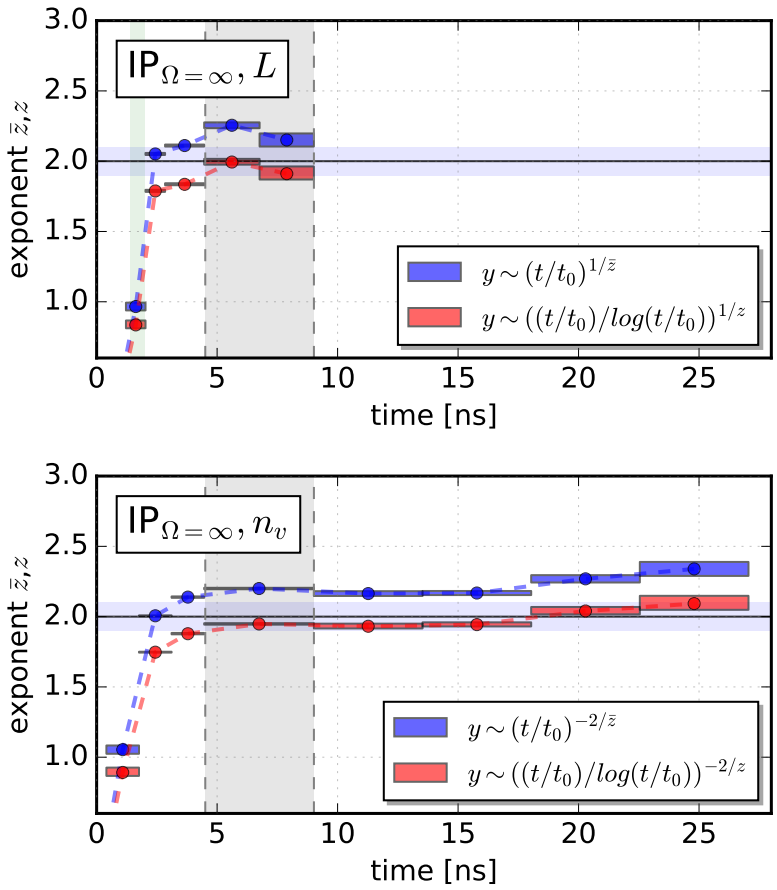

Figure 5.10: Same as Fig. 5.9 but for frequency-independent pumping scheme.

also display with shaded regions the numerically extracted error bars in the fits; such errors arise from standard deviation of a sample of $N_{\rm p}$ = 400 independent realisations of the number of vortices at each time.

To further highlight the importance of logarithmic corrections and the unequivocal observation of the correct universal dynamics at appropriately late-time evolution, we next analyse the temporal evolution of the numerically-extracted dynamical exponent z obtained both from the characteristic length $L(t)$ (through analysis of the collapse in correlation function $g^{(1)}/g^{(1)}_{\rm SS}$) and from the average number of vortices $n_{\rm v}(t)$.

The dynamical exponents are extracted from the number of vortices by fitting our data with Eqs. (5.12) and (5.13) as above. For the corresponding determination based on the characteristic length, $L(t)$, we first obtain $L(t)$ from our simulations by intersecting the graph of $g^{(1)}/g^{(1)}_{\rm SS}(L(t))$ at a value of η = 0.5, ensuring we are insensitive to both short-range and finite-size effects. We then fit the extracted $L(t)$ by the corresponding relations

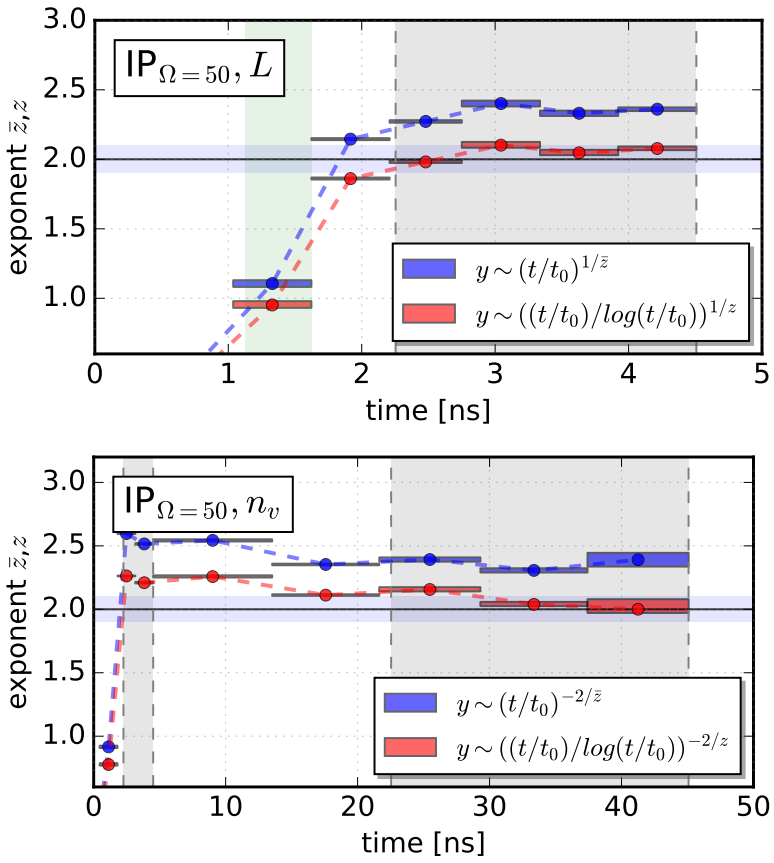

Figure 5.11: Same as Fig. 5.9 but for frequency-dependent pumping scheme. Note the different time axis in this case associated with the disparity in timescales for collective and topological channel equilibration. See Fig. 3 (bottom) in main text.

(Bray *et al.*, 2000; Jelić and Cugliandolo, 2011)

$$L(t) = B_0 \cdot (t/t_0)^{1/\bar{z}}, \tag{5.17}$$

$$L(t) = B_0 \cdot \left(\frac{(t/t_0)}{\log(t/t_0)} \right)^{1/z}, \tag{5.18}$$

where B_0, $\bar{z}$ and z are free parameters. The time evolution of the numerically-extracted dynamical exponents are shown in Figs. 5.9-5.11 for both cases of vortex (top) and length scale (bottom) determination, with extracted average exponents in the probed temporal regions indicated by circles; the widths and heights of the "bands" around such points correspond respectively to the temporal averaging intervals and the error bars from the numerical fits. The vertical green and grey bands indicate corresponding regions shown in Figs. 5.5.

From such plots, corresponding to different parameter space and pumping schemes,

we can infer the following general conclusions about the evolution of the exponent z:

- **Early time dynamics with** $z \approx 1 \ll 2$: At early times, the system is rapidly approaching (and eventually crossing) the critical region. The dynamical exponents from both characteristic length L and vortex number n_{v} agree, but scaling hypothesis does not hold in this regime (i.e. the correlation function does not collapse onto each other). Within this early-stage evolution, it is possible to identify a precise time-window where $z \sim 1$ (shown only for L by the vertical light green bands in Figs. 5.9-5.11).

- **Intermediate dynamics with** $z \approx 2$ **but no discernible logarithmic corrections:** During this stage, the system has crossed the transition but not relaxed enough for logarithmic corrections to become visible. Both functions are well-fitted by Eqs. (5.12) and (5.17), yielding a dynamical exponent $z \sim 2$ which does not include logarithmic correction.

- **Late-time dynamics with** $z \approx 2$ **with evident presence of logarithmic corrections:** After sufficient evolution, the system enters the regime where the scaling hypothesis holds: in this regime the logarithmic corrections are measurable and the dynamical exponent $z \sim 2$ is consistent with fitting curves with Eqs. (5.13) and (5.18). At such times, the vortex decay has slowed down, with the system left with vortex-antivortex pairs only.

We stress that in all cases, the exponents extracted at late times by fittings curves with logarithmic corrections are much closer to the expected value of $z = 2$ than corresponding fits without logarithmic corrections. As a guide to the eye, Figs. 5.9-5.11 highlight the interval $1.9 < z < 2.1$ by a horizontal light-blue shaded region.

Summarising, we note that our detailed analysis demonstrates that late-time dynamics of parametrically and incoherently-pumped exciton-polariton systems follow a unique scaling law, consistent with that theoretically predicted for two-dimensional geometries in the context of the $2d$ XY model (Bray *et al.*, 2000; Jelić and Cugliandolo, 2011). We also stress that achieving the correct dynamical exponent $z = 2$ requires very extensive numerical simulations featuring long-time evolution (such that the system fully enters the correlation-function collapse window where the scaling hypothesis holds), a very high temporal resolution during all dynamics and a large number of independent numerical realisations.

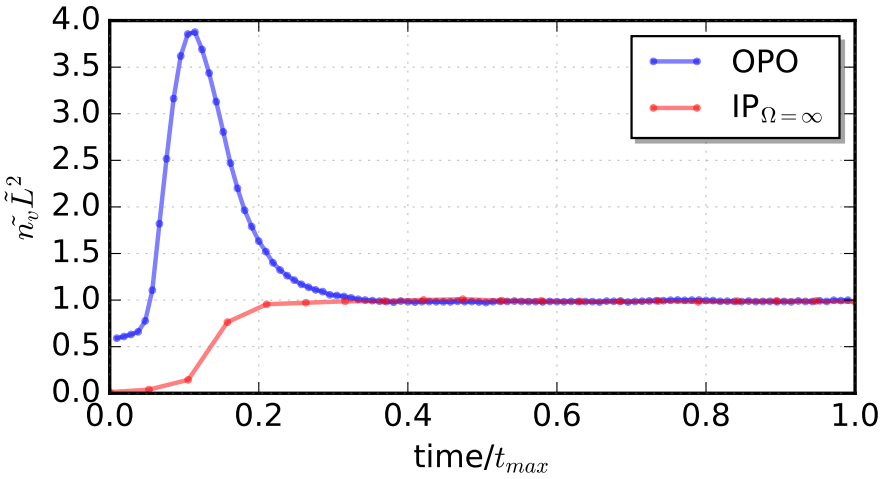

Figure 5.12: **Comparison of the number of vortices with the characteristic length scale of the system**. Scaled number of topological defects $\tilde{n}_\mathrm{v} = n_\mathrm{v}(t)/n_\mathrm{v}(t_{max})$ multiplied by the square of the scaled characteristic length $\tilde{L} = L(t)/L(t_{max})$ as a function of time for the parametrically (blue) and incoherently-pumped (red) system. We show results from the start of the quench ($t = 0$) to the end of the collapse region ($t = t_{max}$). We observe that at late-time dynamics the system fulfils $\tilde{n}_\mathrm{v}\tilde{L}^2 \sim 1$, indicating that during dynamic scaling the mean domain size $L_\mathrm{v} \sim n_\mathrm{v}^{-1/2}$ is proportional to the length scale $L(t)$.

5.4.3 Self-consistency of characteristic length-scale

The scaling hypothesis implies the existence of a unique length scale $L(t)$. This length scale, extracted from the collapsing correlation functions, should agree with the corresponding length scale $L_\mathrm{v}(t)$ obtained from the vortex density through $L_\mathrm{v}(t) \sim n_\mathrm{v}(t)^{-1/2}$ which coincides with the mean distance between vortices. Such a correspondence should happen at sufficiently late times in the system evolution.

Fig. 5.12 demonstrates clearly that, at appropriately late times the scaled quantity $\tilde{n}_\mathrm{v}\tilde{L}^2$, where $\tilde{n}_\mathrm{v} = n_\mathrm{v}(t)/n_\mathrm{v}(t_\mathrm{max})$ and $\tilde{L} = L(t)/L(t_\mathrm{max})$, converges to a constant value of 1. Convergence is well established at a time t/t_max which corresponds to the real time $t \sim 0.3$ns and $t \sim 3.6$ns for OPO and IP$_{\Omega=\infty}$, respectively. Both times are below the respective onset of the universal temporal region, namely at $t \sim 0.5$ps and $t \sim 4.5$ns), confirming that the mean distance between vortices $L_\mathrm{v}(t)$ is always proportional to the growing length scale $L(t)$ during the dynamic scaling.

5.4.4 Dependence of z_L on the intersection point η

In order to obtain the characteristic length-scale from the correlation function essential for demonstrating dynamic scaling, we have used the condition $(g^{(1)}/g^{(1)}_{\mathrm{SS}})(L) = \eta$, with the value of η chosen as 0.5 for all three cases corresponding to OPO, IP$_{\Omega=50}$ and IP$_{\Omega=\infty}$.

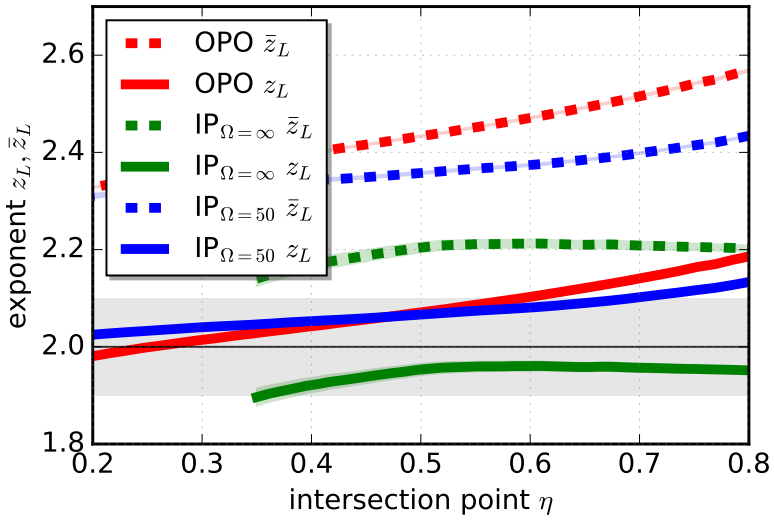

Figure 5.13: **Analysis on the dependence of z_L on the intersection point η.** We study the dependence of exponents z extracted from the characteristic length scale $L(t)$ on intersection condition $(g^{(1)}/g^{(1)}_{\rm SS})(L) = \eta$ within the collapse region for the three systems analysed: OPO (red), IP$_{\Omega=50}$ (blue) and IP$_{\Omega=\infty}$ (green). Values of exponents z_L (solid lines) are always closer to 2 (grey band) than exponents $\bar{z}_L$ (dashed lines).

Here we confirm the validity of our results, by a detailed consideration of the behaviour of the exponents z_L and $\bar{z}_L$ extracted by fitting $L(t)$ (with Eqs. (5.17) and (5.18) respectively) over the entire time window for which the scaling hypothesis holds (corresponding to the grey regions of Fig. 5.5) as a function of the intersection point η. Such a dependence is shown in Fig. 5.13, which confirms our key point that the exponent z_L obtained in the presence of logarithmic corrections is closer to the predicted value of 2, than the numerically-extracted exponent, $\bar{z}_L$, obtained in the absence of logarithmic corrections.

Moreover, we stress that the exponent z_L lies within the range $1.9 < z_L < 2.1$ for a wide range of η values, including values of η used in previous works to extract the growing length scale $L(t)$, such as $\eta = 0.25$ in Ref. (Kulczykowski and Matuszewski, 2017) and $\eta = 0.3$ in Ref. (Jelić and Cugliandolo, 2011). Deviations only occur at quite extreme values of η, where finite-size and short-range effects come into play.

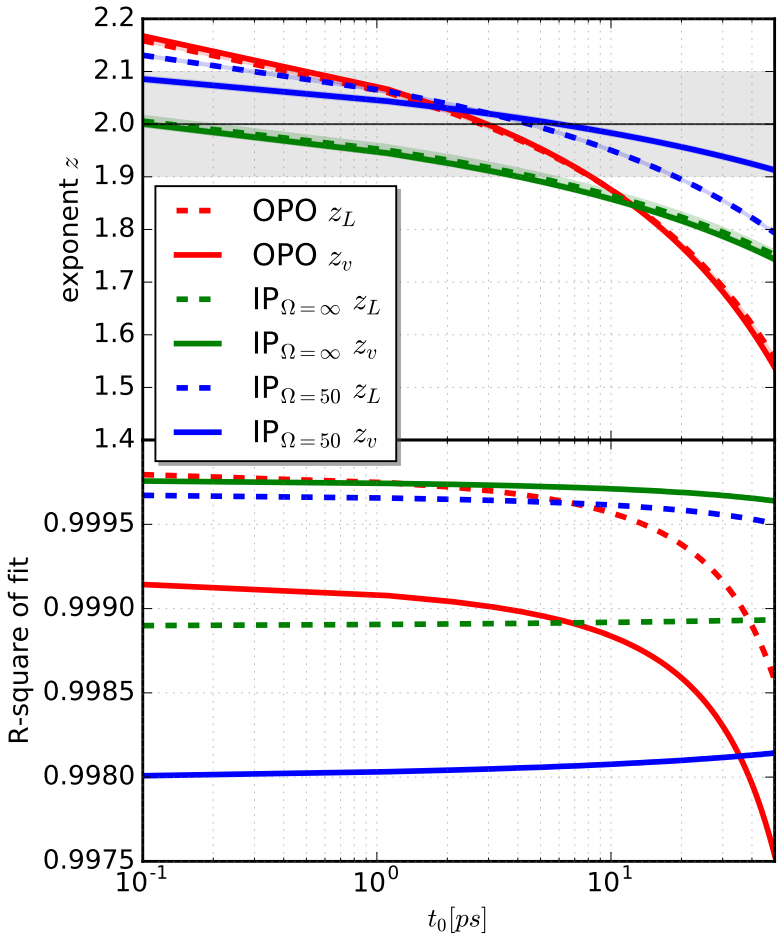

Figure 5.14: **Dependence of z on the timescale t_0.** Dependence of exponent z obtained by fitting both number of vortices and characteristic length within the collapse region for the three cases.

5.4.5 Role of nonuniversal microscopic system timescale t_0 on the dynamical exponent z

The introduction of the anticipated logarithmic corrections through the related formulas

$$\begin{aligned} n_{\mathrm{v}}(t) &= A_0 \cdot \left(\frac{(t/t_0)}{\log(t/t_0)} \right)^{-2/z} \\ L(t) &= B_0 \cdot \left(\frac{(t/t_0)}{\log(t/t_0)} \right)^{1/z} \end{aligned} \tag{5.19}$$

introduces a nonuniversal microscopic system timescale, t_0. The presence of t_0 is typically ignored, on the grounds that it should not affect universal features, but its detailed consideration is nonetheless relevant for the precise slope of the corresponding curves for n_{v} and L. Following common practice (Bray *et al.*, 2000; Jelić and Cugliandolo, 2011),

	OPO		**IP**$_{\Omega=50}$	**IP**$_{\Omega=\infty}$
$\tau_{\rm ph} = \tau_{\rm ex}$	3.29	$\tau_{\rm LP}$	4.51	4.51
$\tau_{\rm Rabi}$	0.15	τ_{γ}	4.51	4.51
$\tau_{\rm P}$	$(-)0.71$	$\tau_{\rm P}$	4.78	4.96
$\tau_{g\cdot n_0}$	5.98	$\tau_{g\cdot n_0}$	5.98	0.77

Table 5.1: Timescales for parametrically and incoherently-pumped systems. We report photon, exciton and lower-branch polariton lifetimes ($\tau_{\rm ph}$, $\tau_{\rm ex}$ and $\tau_{\rm LP}$ respectively), timescales for Rabi oscillations ($\tau_{\rm Rabi}$), losses (τ_{γ}), pumping ($\tau_{\rm P}$) and interactions ($\tau_{g\cdot n_0}$); all timescales are quoted here in picoseconds.

we have effectively chosen t_0 such that it "drops out" of the corresponding equations. By considering the dependence of the universal dynamical exponent z on this nonuniversal parameter, we effectively shed more light onto why such an approach is acceptable.

Since t_0 is a typical system timescale, it should be of broadly the same order of magnitude as other relevant system timescales. All such plausible timescales are listed, for both OPO and IP schemes in Table I, demonstrating that they all lie well within the range 10^{-1} ps $< \tau_{\rm system} < 10^{1}$ps. This already suggests that the conventional choice of t_0 taking the value of 1 in the system units is acceptable, which for our current purposes would imply the already-chosen value of $t_0 = 1$ps. However, in order to be certain that our results do not critically depend on our choice of t_0, Fig. 5.14 displays the dependence of the dynamical exponent z (in the presence of logarithmic corrections) on t_0 within the anticipated relevant time window 10^{-1}ps $< t_0 < 10^{1}$ps. From this figure it is evident that, within this range, all our numerically-extracted values for z take a value $1.9 < z < 2.1$ (depicted by the horizontal light grey area in Fig. 5.14).

We thus conclude that our extensive numerical analysis confirms that all three physical cases considered (OPO, IP with and without frequency-dependent pumping) are consistent with the presence of logarithmic corrections and a dynamical critical exponent of $z = 2$, as expected for the system to be in the same universality class as the $2d$ XY model.

5.5 Chapter summary

In this chapter we have shown that the critical properties of driven-dissipative quantum systems can be extended to dynamic scenarios, particularly to the phase ordering

kinetics after an infinitely rapid quench across a critical point, from the disordered to the quasi-long ordered phases. Focussing on exciton-polariton gases in semiconductor microcavities under different pumping configurations, our work reveals clearly that universal physics emerges in the late-time, long-distance dynamics of both the topological defects and smooth phase fluctuations, whereas the non-universal early dynamics can give misleading information about the critical exponents.

The required system size in the 100 μm range needed to access this physics appears reachable in the new generation of samples (Caputo *et al.*, 2017; Baboux *et al.*, 2017). In particular, our $z \approx 2$ prediction for the dynamical critical exponent of realistic size systems is different from the ones of conservative Bose systems (Damle *et al.*, 1996; Williamson and Blakie, 2016; Kudo and Kawaguchi, 2013; Hofmann *et al.*, 2014) and of non-equilibrium KPZ systems, and rather recovers diffusive dynamics in the planar XY-model (Jelić and Cugliandolo, 2011; Bray *et al.*, 2000; Rutenberg and Bray, 1995).

A natural extension of the presented work is to study the Kibble-Zurek mechanism in such driven-dissipative quantum systems, by considering finite rate quenches across the critical point: this is interesting because the behaviour of the topological densities in this quench protocol also contains information about universal properties of the system. Preliminary results on this are presented in the following chapter.

Chapter 6

Universal scaling after finite-duration quenches: the Kibble-Zurek mechanism in polariton condensates

6.1 Introduction

The idea that the dynamics of a system can lead to a spontaneous organisation, when undergoing a transformation of its state, is common to many scientific contests. The process of spontaneous emergence of ordered patterns is generally ascribed to the symmetry breaking of an order parameter during a phase transition, and is often combined with the formation of topological defects. In cosmology, the study of such phenomena dates back to 1976 when Kibble proposed a description of the early stages of the universe based on self-organisation dynamics of the system (Kibble, 1976).

This theory attracted a consistent scientific interest when Zurek proposed to apply Kibble's idea to condensed matter systems that show similar symmetry breaking. Zurek also suggested scaling laws for the number of topological defects involving equilibrium critical exponents which are characterised by the universality class of the phase transition. For a $3d$ Bose system, when the order parameter is approaching the critical point, the correlation length and the relaxation time diverge polynomially, regulated by the static and dynamic critical exponents, ν and z respectively. In $2d$, the scenario changes and the introduction of logarithmic corrections is essential (Jonsson and Minnhagen, 1997).

In the original framework, the problem was discussed for classical systems. Recently, boosted by the development of technologies able to investigate ultracold systems, several attempts have been made to prove the validity of this picture in isolated quantum systems.

Zurek first applied Kibble's idea to superfluid ^{4}He (Zurek, 1985). The Kibble-Zurek theory has been investigated in system of different nature, e.g. superconducting loops (Monaco *et al.*, 2009) and liquid crystals (Chuang *et al.*, 1991; Griffin *et al.*, 2012), and has been confirmed by numerous numerical studies, e.g. (Laguna and Zurek, 1998; Dziarmaga *et al.*, 1999; Antunes *et al.*, 1999; Kobayashi and Cugliandolo, 2016; Shimizu *et al.*, 2018). It is worth noting that the Kibble-Zurek theory has been also considered for $2d$ systems characterised by a second-ordered phase transition (Yates and Zurek, 1998; Ducci *et al.*, 1999; Miranda *et al.*, 2013). In fact, A. del Campo *et al.* have investigated vortex filaments in inhomogeneous systems (del Campo *et al.*, 2011) and quench dynamics in quantum phase transitions has been investigated in (Dziarmaga and Zurek, 2014). More recently Lamporesi (Lamporesi *et al.*, 2013) and Chomaz (Chomaz *et al.*, 2015) experimentally observed scaling of topological defects in atomic cigar-shaped and $2d$ box confinements, respectively. Critical phenomena have been probed in homogeneous Bose Gases (Navon *et al.*, 2015). Finally, growth dynamics of an elongated $3d$ quenched condensate was investigated in (Liu *et al.*, 2017).

The Kibble-Zurek mechanism (KZM) has been studied extensively in systems exhibiting equilibrium BEC or BKT phase transitions (such as ultracold atoms and superfluids), however, it is not clear if KZM can be extended to nonequilibrium systems such as exciton-polariton condensates. This issue is nowadays under intense debate. Motivated by this open question, after a preliminary investigation on the critical slowing down properties of the system, in this chapter we numerically investigate the quench dynamics of a nonequilibrium system. In order to determine whether the KZ hypothesis holds in polariton condensates, we compare the scaling laws of the freeze time (time after which the dynamically-evolving system is supposed to depart from equilibrium) with the quench duration, inferred independently from numerical and theoretical analysis.

This work was carried out in collaboration with Galbadrakh Dagvadorj (Department of Physics and Astronomy, University College London, United Kingdom), Alex Zamora (Department of Physics and Astronomy, University College London, United Kingdom), Marzena Szymańska (Department of Physics and Astronomy, University College London, United Kingdom) and Iacopo Carusotto (INO-CNR BEC Center and Università di Trento, Italy).

6.2 The "standard" Kibble-Zurek mechanism

Let us consider a quantum many-body system whose phase transition is of the second order, occurring at the critical point T_c. Below such temperature, $T < T_c$, the system

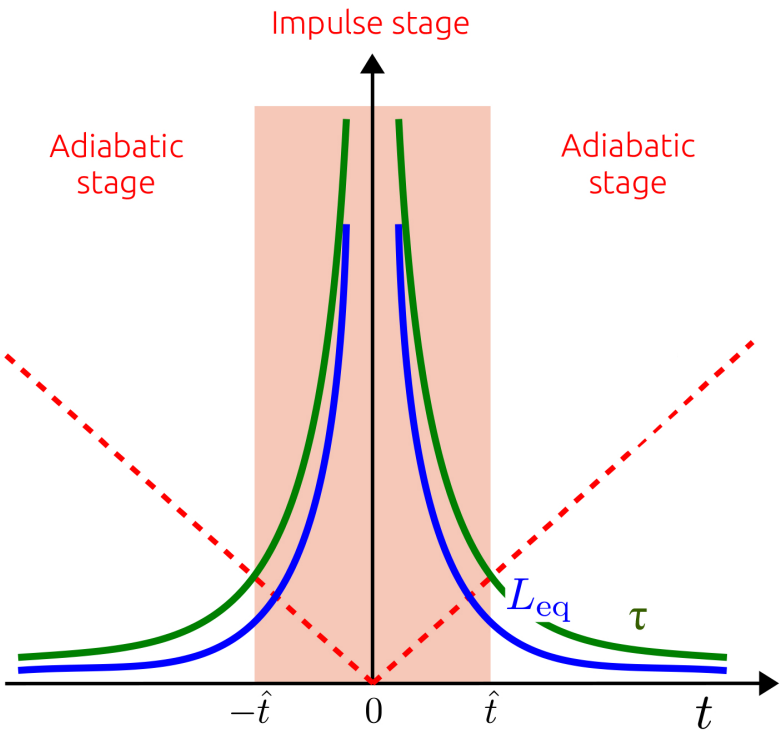

Figure 6.1: **Schematics of the Kibble-Zurek mechanism.** This plot portrays the physics of a finite rate quench across a second order phase transition in a very simple way: it divides the whole evolution of the system in three stages, namely adiabatic (below threshold, $t < -\hat{t}$), impulse (shaded red region), and adiabatic (above threshold, $t > \hat{t}$). Divergence of the equilibrium length L_{eq} and τ are sketched with solid green and blue curves, respectively. The timescale of the quench $\epsilon/\dot{\epsilon}$ is reported as a dashed red line.

exhibits an ordered phase, which is characterised by the symmetry breaking of the order parameter; here a BEC appears. As the system approaches the critical point from above, the most relevant physical quantities, such as the correlation length L_{eq} and the relaxation time τ, are known to diverge as (Hohenberg and Halperin, 1977)

$$L_{eq}(\epsilon) \sim |\epsilon|^{-\nu}, \tag{6.1}$$

and

$$\tau(\epsilon) \sim \left(L_{eq}\right)^{z} \sim |\epsilon|^{-\nu z}, \tag{6.2}$$

where, for simplicity, we have introduced the parameter $\epsilon = 1 - T/T_c$, which defines the relative distance of the temperature T at each instant of the quench (REMOVE: of a given configuration) from the critical point T_c. Here, the exponents ν and z are the (positive) static and dynamic critical exponents, which are known to define the universality class of the phase transition. In the case of mean field theory, $\nu_{MF} = 1/2$ and $z = 2$ (Hohenberg and Halperin, 1977). From these two quantities, it is possible to calculate the velocity of

propagation for the system phase, i.e. $v = L_{\rm eq}/\tau \sim |\epsilon|^{(z-1)\nu}$ (del Campo and Zurek, 2014), which decreases to zero as the system approaches the critical point.

Let us now suppose that the system is quenched linearly in time from a disordered state at $T > T_{\rm c}$ (where the system is initially at equilibrium) to an ordered state at $T < T_{\rm c}$, such that we can rewrite ϵ as follows

$$\epsilon(t) = \frac{t}{2\tau_{\rm Q}}, \tag{6.3}$$

with $t \in [-\tau_{\rm Q}, \tau_{\rm Q}]$. At $t = -\tau_{\rm Q}$, the system lies in a highly disorder phase, and evolves adiabatically towards the phase transition. The adiabatic stage is characterised by the relaxation time $\tau(\epsilon)$ to be always smaller than the quench timescale t (which can be rewritten as $\epsilon(t)/\dot{\epsilon}(t)$), i.e.

$$\tau\left(\epsilon(t)\right) < \left(\frac{\epsilon(t)}{\dot{\epsilon}(t)}\right). \tag{6.4}$$

The evolution continues until the system approaches very closely the threshold, as illustrated in Fig. 6.1, where a schematic representation of the KZM is given. The closer to the threshold, the smaller the gap between the two competing timescales. When approaching the phase transition, the system is characterised by a "slowing down" of its dynamics, related to the drastic increase of all its significant equilibrium physical quantities. In other words, transmitting the information of the order-parameter phase, from one point of the system to the other, requires more time. There is a characteristic timescale, denoted by $-\hat{t}$, at which

$$\tau(\epsilon(-\hat{t})) = -\hat{t}, \tag{6.5}$$

for which the evolution ceases to be adiabatic. At the time $-\hat{t}$, often referred as the "freeze" time, the system enter the so-called "impulse" regime where the correlation length is assumed to remain fixed at a value $\hat{L}_{\rm eq} = L_{\rm eq}(\hat{t})$. This thus leads to the formation of patterns with similar average size (imposed by the frozen correlation length $\hat{L}_{\rm eq}$), characterised by a (local) symmetry-broken phase. Under this assumption, the typical size of these domains eventually determines the average number of topological defects in the low-temperature phase. After having crossed the impulse region, at a time $\hat{t}$ the order parameter is supposed to enter again an adiabatic regime, whose dynamics is characterised by coarsening process. Considering the above arguments, the KZM predicts that freeze time and characteristic length scale with the quench duration as

$$\hat{t} \sim \tau_{\rm Q}^{\frac{z\nu}{1+z\nu}}, \tag{6.6}$$

and

$$\hat{L}_{\mathrm{eq}}(t) \sim \tau_{\mathrm{Q}}^{\frac{\nu}{1+z\nu}}, \tag{6.7}$$

respectively (Zurek, 1985).

6.3 The Kibble-Zurek mechanism in the BKT transition

In this section, we review the principal aspects of the theory of quenched dynamics in $2d$ for an equilibrium system.

The static properties of a system in the vicinity of the BKT phase transition are described by scaling laws which are substantially different from Eq. (6.1) and (6.2). As discussed in Sec. 4.1.1, the equilibrium properties of the (infinite-order) $2d$ XY model are characterised by an exponential decay of correlations in the disordered phase whereas the ordered phase coherence is described by an algebraic decay.

In the disordered phase, and close to criticality, the correlation length has been predicted to diverge more rapidly than the polynomial behaviour of a second-order phase transition (Jelić and Cugliandolo, 2011; Dziarmaga and Zurek, 2014), namely

$$L_{\mathrm{eq}}(\epsilon) \sim a_L e^{b_L |\epsilon|^{-\nu}}, \tag{6.8}$$

with ν the critical static exponent, a_L a microscopic scale and $b_L \sim 1$ (Berezinskii, 1971; Kosterlitz and Thouless, 1973), a non-universal constant. In this case, since Eq. (6.8) loses its polynomial form, the parameter ν, strictly speaking, does not refer to the static exponent any more. The exponential divergence of L_{eq} can be naively explained by forcing the "true" static exponent of Eq. (6.1) to be $\nu = \infty$ (Girvin, 2000).

An exponential divergence of the relaxation time of the system τ can be also derived (Jonsson and Minnhagen, 1997). Here we recount the method shown by (Jelić and Cugliandolo, 2011), assuming that the typical speed of a topological defect approaching the relative antivortex, placed at a distance λ, holds in the disordered phase (Gupta *et al.*, 1988; Bray *et al.*, 2000). This speed can be calculated by means of the $2d$ XY model (see Sec. 4.1.1), and reads

$$v_\lambda(t) \sim \frac{\lambda^{-1}}{\log\left(\frac{\lambda(t)}{a}\right)}, \tag{6.9}$$

where a is the minimum distance between any two spins in the $2d$ lattice. By matching this equation with the equilibrium law, i.e. $v_\lambda(t) = L_{\mathrm{eq}}/\tau$, one finds the relation between

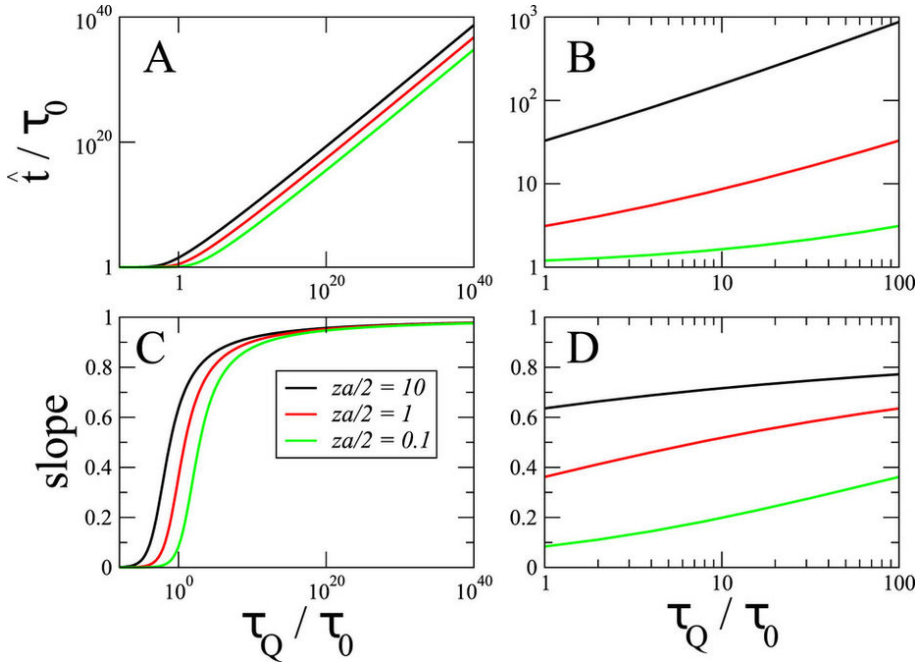

Figure 6.2: **Analysis on the relation between $\hat{t}$ and τ_Q.** We include here Fig. 1 of (Dziarmaga and Zurek, 2014), which plots in (A) and (B) the scaling of the freeze time over different ranges of the quench duration. The analytical expression plotted is $\hat{t} \sim \tau_Q \left((za/2)/\mathcal{L}\left[(za/2)\sqrt{\tau_Q/\tau_0}\right]\right)^{1/\nu}$, similar to Eq. (6.13), where $\mathcal{L}$ is the Lambert function, $\tau_0 = a_\tau$ and $a = b_L$. The slope of the panel (A) is plotted for a vast range (C) and a "realistic" range (D) of the duration quench τ_Q. While the unitary solution ($\nu \to \infty$) is matched asymptotically at "astronomical" τ_Q, for realistic timescales of the quench the exponent is found to be always below unity.

the equilibrium length and the relaxation time for the XY model to be

$$\tau \sim L_{\text{eq}}^z \log\left(\frac{L_{\text{eq}}}{a}\right), \tag{6.10}$$

from which one obtains the exponential dependence in the form

$$\tau \sim L_{\text{eq}}^z \, |\epsilon|^{-\nu} \sim a_L e^{(b_L z |\epsilon|^{-\nu})} |\epsilon|^{-\nu}. \tag{6.11}$$

Knowing the behaviour of the length and timescales in the vicinity of the critical point allows one to attempt the calculations for the freeze time $\hat{t}$ for the $2d$ XY model. Let us consider a linear ramp as in Eq. (6.3). If we assume that the system departs from the equilibrium condition in the vicinity of the critical point, we can use Eq. (6.5) to obtain an expression for the freeze time $\hat{t}$, i.e.

$$\hat{t} \sim e^{b_L z \left(\frac{t}{\tau_Q}\right)^{-\nu}} \left(\frac{t}{\tau_Q}\right)^{-\nu}. \tag{6.12}$$

A solution of this transcendental equation is

$$\hat{t} \sim \tau_{\mathrm{Q}} \left(\frac{b_L z}{\log\left((\tau_{\mathrm{Q}}/a_\tau) \left(\frac{b_L z}{\log\left(\tau_{\mathrm{Q}}/a_\tau\right)^{(1+\nu)/\nu}} \right) \right)} \right)^{1/\nu}, \tag{6.13}$$

from which we can infer the expression of the correlation length at the freeze time, i.e.

$$\hat{L}_{\mathrm{eq}} \sim a_L \left\{ \frac{\tau_{\mathrm{Q}}}{a_\tau} \left[\frac{1}{\log(\frac{\tau_{\mathrm{Q}}}{a_\tau})} \right]^{(1+\nu)/\nu} \right\}^{1/z}. \tag{6.14}$$

A similar relation has been derived in (Dziarmaga and Zurek, 2014) which consider the slowing down of the relaxation time to scale as

$$\tau = L_{\mathrm{eq}}^z \sim e^{(b_L z \epsilon^{-\nu})}. \tag{6.15}$$

The asymptotic behaviour of Eqs. (6.13) and (6.14) have been studied in detail (Dziarmaga and Zurek, 2014). The equilibrium length and timescales are found to asymptotically approach

$$\hat{t} \sim \tau_{\mathrm{Q}}^1, \quad \hat{L}_{\mathrm{eq}} \sim (\tau_{\mathrm{Q}})^{\frac{1}{z}}, \tag{6.16}$$

for $\tau_{\mathrm{Q}} \to \infty$, as one can find by heuristically setting $\nu \to \infty$ in Eqs. (6.6) and (6.7). In Fig. 6.2, the freeze time $\hat{t}$ is plotted over many decades of τ_{Q}, according to Eq. (6.13). The relation becomes linear only for "astronomical" (compared with standard numerical and experimental scales) durations of the finite quench.

Although it has been shown that polariton condensates may differ substantially from equilibrium system, as discussed in (Zamora *et al.*, 2017), our findings reported in Chs. 4-5, concerning the BKT phase transition and universal dynamic physics of polariton condensates —also supported by recent works, e.g. (Dagvadorj *et al.*, 2015)— suggest that nonequilibrium systems may fall in the universality class of the $2d$ XY model. Motivated by this open question, in the next section we will present some preliminary results on the critical slowing down of the system characteristic length. Subsequently, we discuss universal behaviour in terms of finite quench dynamics.

6.4 Numerical analysis of critical slowing down

In this section we focus on the preliminary study of the critical slowing down of a incoherently-pumped polariton system. Specifically, we will attempt to tentatively extract

values of the static exponent ν from two independent physical quantities: the steady state *correlation length* $L_{\mathrm{v}}(\epsilon)$ and the equilibrium *relaxation time* $\tau(\epsilon)$.

The procedure which we adopt in this section is based on fitting these quantities with the theoretical predictions discussed in the previous sections, namely the critical growth of correlation length and relaxation time for a second-order phase transition and an infinite-order phase transition. In order to tentatively characterise the phase transition from the diverging length and time scales, we extract the static exponents (treated as free parameters) from these fits, independently, and subsequently we compare them with the expected value ν_{MF} predicted by means field calculations (Hohenberg and Halperin, 1977). In doing so, we assume the dynamical exponent $z = 2$, according to the study conducted in Ch. 5.

We find useful to define $\epsilon = P_0/P_{\mathrm{BKT}} - 1$ as the distance-from-criticality parameter (from now on termed as "control" parameter), such that $\epsilon_{\mathrm{BKT}} = 0$. Both $L_{\mathrm{v}}(\epsilon)$ and $\tau(\epsilon)$ are extracted by means of the steady state and dynamical properties of the number of topological defects, whose density is directly related to the growing length by

$$\rho_{\mathrm{v}} \sim L_{\mathrm{v}}^{-d}, \tag{6.17}$$

where d is the dimensionality of the system (in our case, $d = 2$).

First, we discuss how we extract the correlation length $L_{\mathrm{v}}(\epsilon)$ from the average number of defects at steady state. In the previous sections we introduced the theoretical expressions for the correlation length approaching threshold from the disordered side, i.e. Eqs. (6.1) and (6.8), respectively for a second-order and infinite-order phase transition. Following the relation (6.17), these can be rewritten as

$$n_{\mathrm{v}}(\epsilon) \sim n_{\mathrm{v}}^{\epsilon=0} + a_{n_{\mathrm{v}}} \epsilon^{2\nu_L^{\shortparallel}}, \tag{6.18}$$

and

$$n_{\mathrm{v}}(\epsilon) \sim n_{\mathrm{v}}^{\epsilon=0} + b_{n_{\mathrm{v}}} e^{-2 \cdot b_L \epsilon^{-\nu_L^{\infty}}}, \tag{6.19}$$

respectively. Here, $n_{\mathrm{v}}^{\epsilon=0}$ corresponds to the average number of vortices calculated at the critical point, $\nu_L^{\shortparallel}$ and ν_L^{∞} the corresponding static critical exponents and $a_{n_{\mathrm{v}}}, b_{n_{\mathrm{v}}} \sim a_L^{-2}$ (Jelić and Cugliandolo, 2011).

The critical slowing down is considered a useful tool for identifying the universality class to which a particular system belongs. In this light, data are tentatively fitted with

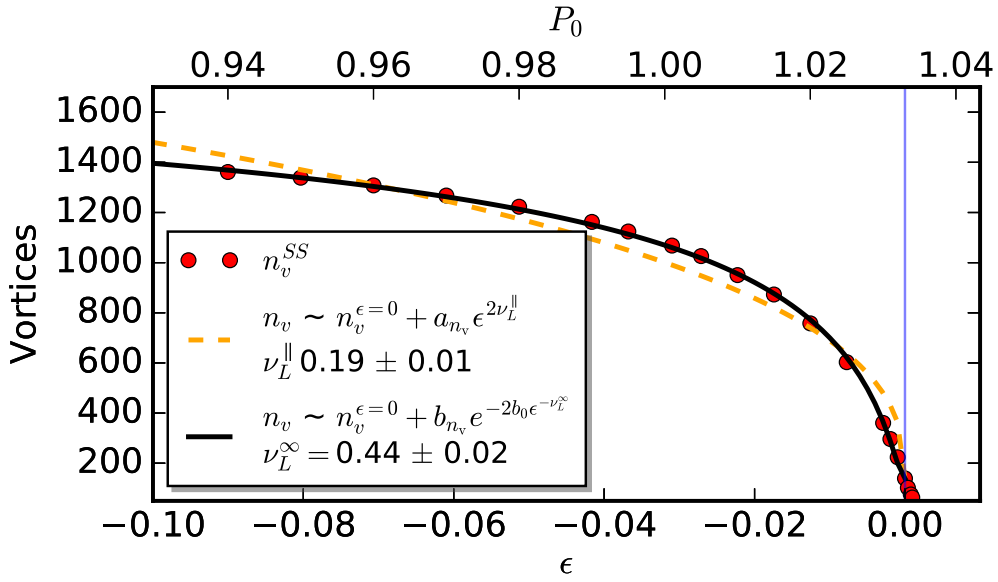

Figure 6.3: **Steady state number of vortices.** Number of vortices at steady state n_v^{SS} (red dots) in the disorder phase $\epsilon < 0$. The number of vortices exhibits critical slowing down. Computational data are fitted with Eq. (6.18) (yellow dashed curve) and Eq. (6.19) (black solid curve), from which we tentatively infer the value of the static exponent ν. a_{n_v}, b_{n_v} and $\nu_L^{\parallel}, \nu_L^{\infty}$ are treated as free parameters; here $n_v^{\epsilon=0} = 139$ corresponds to the number of vortices at threshold.

the corresponding theoretical models and critical exponents $\nu_L^{\parallel}$ and ν_L^{∞} are extracted.

We study critical phenomena in the vicinity of the narrow critical region extracted in Ch. 4. We choose the critical point to lie at the value $P_{\mathrm{BKT}} = 1.033$, according to the critical region study presented in Sec. 4.3.4. We check that by varying the critical point within the critical region $1.032 < P_{\mathrm{BKT}} < 1.0338$, our final results are consistent within the error bars computed. Subsequently, we probe the region which is in the vicinity of the phase transition, i.e. $-0.1 < \epsilon < 0$.

The procedure adopted for extracting the static exponents $\nu_L^{\parallel}$ and ν_L^{∞} from the steady state number of vortices resembles the analysis shown in (Jelić and Cugliandolo, 2011), and it consists of a sudden quench of the system from a random configuration to a configuration with $\epsilon < 0$. Similarly to the method used to study the BKT phase transition in Ch. 4, the system is allowed to evolve until a steady state is reached. The resulting number of vortices at steady state is the same as the one reported in Fig. 4.4.

The dynamics of the system are evolved by computationally solving Eq. (3.3) in a square lattice of 301^2 points, lengths $L_x = L_y = 295.11\mu$m. We average over a sufficiently-large number ($N_{\mathrm{p}} = 200$) of realisations, with other parameters given in Table 3.1.

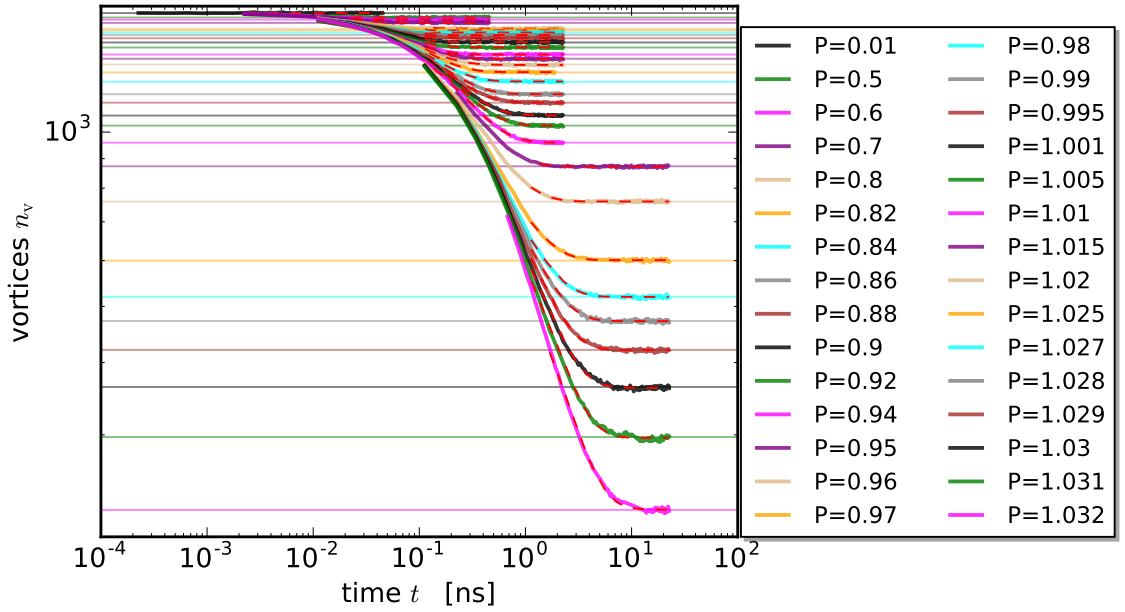

Figure 6.4: **Numerical extraction of the relaxation timescale τ.** The figure shows the decay of vortices to a steady state after a sudden quench into the disordered phase. The system is quenched infinitely rapidly from a noisy configuration to different values of the control parameter $\epsilon < 0$, and allowed to relax to the steady state value $n_v^{SS}(\epsilon)$ (horizontal lines). Relaxation times as a function of ϵ are extracted by fitting each curve with Eq. (6.20) (red dashed curves). Values of τ as a function of the control parameter in the disordered phase are shown in Fig. 6.5.

The static exponents $\nu_L^{\shortparallel}$ and ν_L^{∞} are extracted by fitting the steady state number of vortices $n_v^{SS}(\epsilon)$ with the theoretical predictions Eqs. (6.18)-(6.19), i.e. for a second-order and infinite-order phase transition, respectively. Fig. 6.3 shows the number of topological defects obtained at different values of the control parameter ϵ. Solid black and dashed orange lines correspond to the fitting curves obtained. The respective extracted exponent are reported in the legend of Fig. 6.3.

A second method for the estimation of the static exponent ν from numerical calculation concerns the dynamical evolution of the defects. Specifically, we are interested in the characteristic time associated with the relaxation of the system towards the steady state configuration. As discussed in Sec. 6.3, the relaxation time τ is expected to diverge at criticality, according to Eq. (6.11). Fig. 6.4 shows the different evolutions of the number of defects $n_v(t, \epsilon)$ (for different final values of ϵ) after a sudden quench into the disordered phase. In order to extract the relaxation time $\tau(\epsilon)$, one can operate in two different ways.

A first approach consists of numerically estimating the time spent by the defects to reach the steady state. This is easily obtained by probing the average difference between

Table 6.1: Static exponent

	ν_L	ν_τ	ν_{τ_*}
second-order (ν^{II})	0.19 ± 0.01	0.2 ± 0.05	0.19 ± 0.01
infinite-order (ν^{∞})	0.44 ± 0.02	0.49 ± 0.05	0.64 ± 0.04

each temporal point $n_{\text{v}}(t_{\text{j}})$ and their corresponding values of adjacent timesteps, $n_{\text{v}}(t_{\text{j-1}})$ and $n_{\text{v}}(t_{\text{j+1}})$, where t_j is the time a the $j-$th step of the temporal evolution. When this difference is lower than the fluctuation strength of a curve $\sigma = \sqrt{(N_{\text{p}})}$, the average density of points $n_{\text{v}}(t)$ is considered to be at steady state, and the relaxation time of the quench, τ_*, to be t. Such times are plotted in Fig. 6.5 as orange points.

The second approach consists of fitting the curves with the following expression

$$n_{\text{v}}(t, \epsilon) \sim n_{\text{v}}^{\text{SS}}(\epsilon) + a_\tau e^{-\frac{t}{\kappa(\epsilon)}}, \tag{6.20}$$

where a_τ and $\kappa(\epsilon)$ are free parameters and $n_{\text{v}}^{\text{SS}}(\epsilon)$ the extracted average vortex number at steady state. For each value of ϵ, $\kappa(\epsilon)$ results to be proportional to $\tau_*(\epsilon)$ (determined from the first method), i.e. $\kappa(\epsilon) = \tau_*(\epsilon)/A$. By linear regression of all $\big(\kappa(\epsilon_j), \tau_*(\epsilon_j)\big)$ we find A, deriving hence the relaxation time associated with the second method, $\tau(\epsilon) = A\kappa(\epsilon)$. The relaxation times τ_* and τ, corresponding to the first and second method, are reported in Fig. 6.5 as orange and blue points, respectively. Finally, for both cases we plot $\tau(\epsilon)$, and tentatively fit the curves with the theoretical scaling laws, Eqs. (6.2) and (6.11), predicted by the $2d$ XY model.

From the analysis discussed in this section, we have been able to tentatively extract the critical static exponent from both the divergent behaviour of the correlation length L_{v} (extracted by the vortex density ρ_{v}) and the relaxation time τ calculated in two different ways. We show these exponents in Table 6.1. The value of the exponents obtained by the tentative fits with predictions for infinite-order phase transitions seems to be more compatible with the expected value $\nu_{\text{MF}} = 0.5$ than those obtained by fitting with the theoretical prediction for a second-order phase transitions. However, we stress that further analysis is needed.

After having tentatively investigated the critical behaviours of nonequilibrium systems, in the following section we will discuss results on finite quench dynamics.

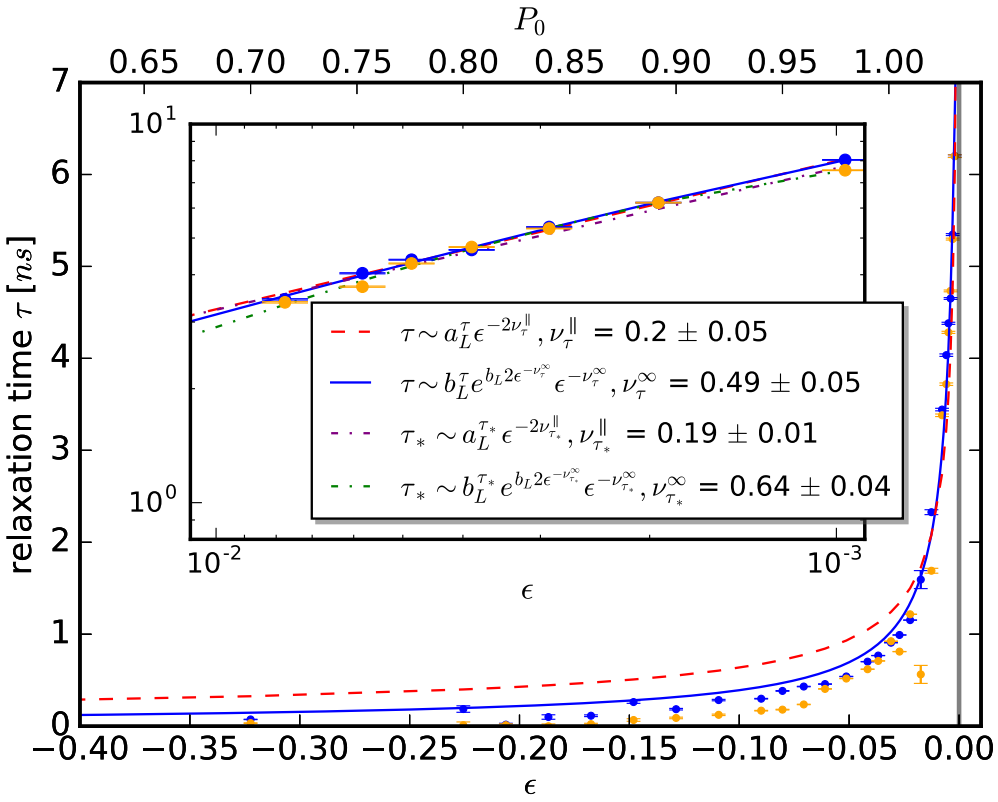

Figure 6.5: **Relaxation time τ in the vicinity of the transition.** The relaxation time τ (blue points) and τ_* (orange points) are plotted as a function of the control parameter ϵ approaching the critical point $\epsilon = 0$ from the disordered phase. Inset: (tentative) fits of τ and τ_* with different laws corresponding to Eq.(6.2) and Eq. (6.11), for second-order and infinite-order phase transitions, respectively. $a_L^{\tau}, b_L^{\tau}, a_L^{\tau_*}, b_L^{\tau_*}, b_L, \nu_{\tau}^{\infty}, \nu_{\tau}^{\parallel}, \nu_{\tau_*}^{\infty}, \nu_{\tau_*}^{\parallel}$ are treated as free parameters. Corresponding extracted exponents are shown in legend. Blue solid and red dashed lines correspond to the fit to the relaxation times τ (also plotted in main panel); green and purple dashed dotted lines correspond to the fit to τ_*.

6.5 Dynamics after a slow linear quench

According to the KZM, the system follows the variation of the control parameter (ϵ) adiabatically, adjusting its correlation length to the equilibrium one up to a time $-\hat{t}$, after which the dynamical evolution is frozen until $\hat{t}$. The purpose of this section is to probe this condition in polariton systems, by calculating $-\hat{t}$ from our simulations and comparing to theoretical predictions. First, we explain the quench protocol, then we focus on the method adopted for extracting $\hat{t}$ as predicted by the theory, by means of the numerical relaxation times calculated for the analysis of the critical slowing down. Subsequently, we extract $\hat{t}$ from our numerical simulations. Finally, we discuss the late-time dynamics by means of the number of defects.

6.5.1 The quench protocol

In this section the quenching procedure of the system is discussed.

First, the system is suddenly quenched from a random initial condition and it is let to evolve until it reaches a steady state at a pump value P^{in}, which we will eventually treat as the initial condition of our symmetric and linear quench protocol. We ensure this final steady state to be always below the threshold, calculated as in Sec. 6.4, so that $P^{\text{in}} < P_{\text{BKT}}$. Secondly, a linear quench with duration $2\tau_{\text{Q}}$ is initiated at $t = 0$. The steady state configuration, reached for P^{in}, is eventually let to evolve to a final pump value $P^{\text{fin}} > P_{\text{BKT}}$. The final pump can be expressed as a function of $P(t)$ as

$$P(t) = P^{\text{in}} + (P^{\text{fin}} - P^{\text{in}})\frac{t}{2\tau_{\text{Q}}}. \tag{6.21}$$

Generally, the quench protocol can be implemented either symmetrically with respect to the critical point (Jelić and Cugliandolo, 2011) or not. In this study we adopt a symmetric quench, and thus it can be helpful to rewrite the quench variables such that they assume zero value at the threshold point. From this point forward, we change notation and refer to the "real" time as $\bar{t} \in [0, 2\tau_{\text{Q}}]$, thus we can introduce the rescaled time

$$t = \bar{t} - \bar{t}_{\text{BKT}}, \tag{6.22}$$

which corresponds to the time left to reach the threshold. Thus, $t_{\text{BKT}} = 0$ and $t \in [-\tau_{\text{Q}}, \tau_{\text{Q}}]$. Here the time $\bar{t}_{\text{BKT}}$ corresponds to the time at which the threshold is crossed by the system, and reads (cfr. Eq. (6.21) substituting t with $\bar{t}$)

$$\bar{t}_{\text{BKT}} = \bar{t}(P_{\text{BKT}}) = \left(\frac{P_{\text{BKT}} - P^{\text{in}}}{P^{\text{fin}} - P^{\text{in}}}\right) 2\tau_{\text{Q}}. \tag{6.23}$$

In terms of the parameter $\epsilon = P/P_{\text{BKT}} - 1$, the rescaled quench protocol reads

$$\epsilon(t) = \zeta\frac{t}{2\tau_{\text{Q}}}. \tag{6.24}$$

Here we have introduced ζ as a parameter which quantifies the velocity of the quench according to the initial condition ϵ_i.

In the analysis presented in this chapter, the evolution of the system is initiated at $\epsilon_{\text{in}} = -0.1$, which implies $\zeta = 0.2$. A graphical representation of the procedure is provided in Fig. 6.6 (a). Once the system is prepared in the initial configuration ϵ_{in}, quenches with different durations τ_{Q} are applied. Values of τ_{Q} are reported in the legend of Fig. 6.6. The resulting density of the field ψ_{LP} and vortices n_{v} are plotted as a function of time t in

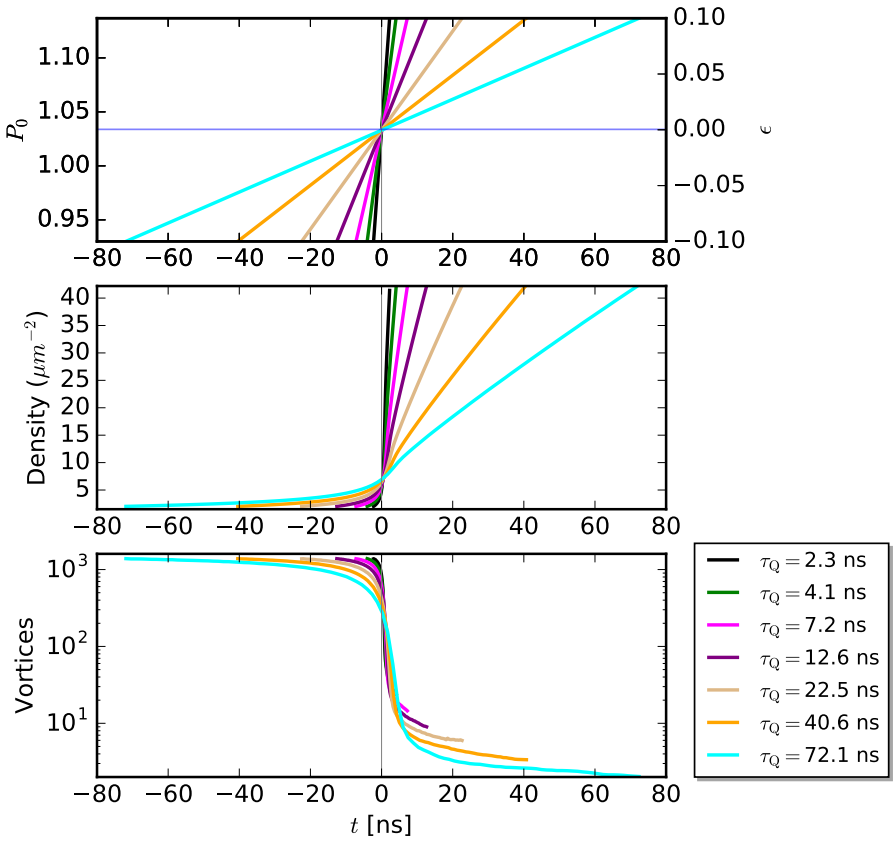

Figure 6.6: **Quench protocol.** Top panel: the control parameter $\epsilon = (P - P_{\rm BKT})/P_{\rm BKT}$ grows linearly from -0.1 ($P^{\rm in} \simeq 0.93$) to 0.1 ($P^{\rm fin} \simeq 1.14$) from $t^{\rm in} = -\tau_{\rm Q}$ to $t^{\rm fin} = \tau_{\rm Q}$ over a quench duration $2\tau_{\rm Q}$, such that $\epsilon(t) = \zeta \cdot t/2\tau_{\rm Q}$, with $\zeta = 0.2$. The symmetric quench crosses threshold at $\epsilon_{\rm BKT} = 0$ ($P_{\rm BKT} = 1.033$) (blue horizontal line) at a time $t = 0$ (grey vertical line). Density and vortex evolutions during the quench are shown in middle and bottom panels, respectively.

Fig. 6.6 (bottom) and Fig. 6.6 (middle), respectively. In Fig. 6.7 we plot same quantities as in Fig. 6.6, but as a function of the "real" time $\bar{t}$.

For completeness, an illustration of the number of vortices $n_{\rm v}$ as a function of time $\bar{t}$ is reported in Fig. 6.8. The colored curve starts from the same initial condition at $\bar{t} = 0$ and evolve according to Eq. (6.21) until the end of the quench $\bar{t} = 2\tau_{\rm Q}$. All curves present two regions where the behaviour of $n_{\rm v}$ changes drastically, one where the concavity is negative, the other when it is positive. It is worth noting that after the second kink the system enters the adiabatic stage characterised by a power-law decay. As shown by the comparison with the scaling t^{-1} (solid blue line), the decay at long times remarkably agree with the universal dynamic scaling results presented in Ch. 5. Specifically, the decay t^{-1} is consistent with our findings for the dynamical exponent $z = 2$ (although logarithmic corrections are not investigated in the present figure, but eventually discussed in Sec. 6.8).

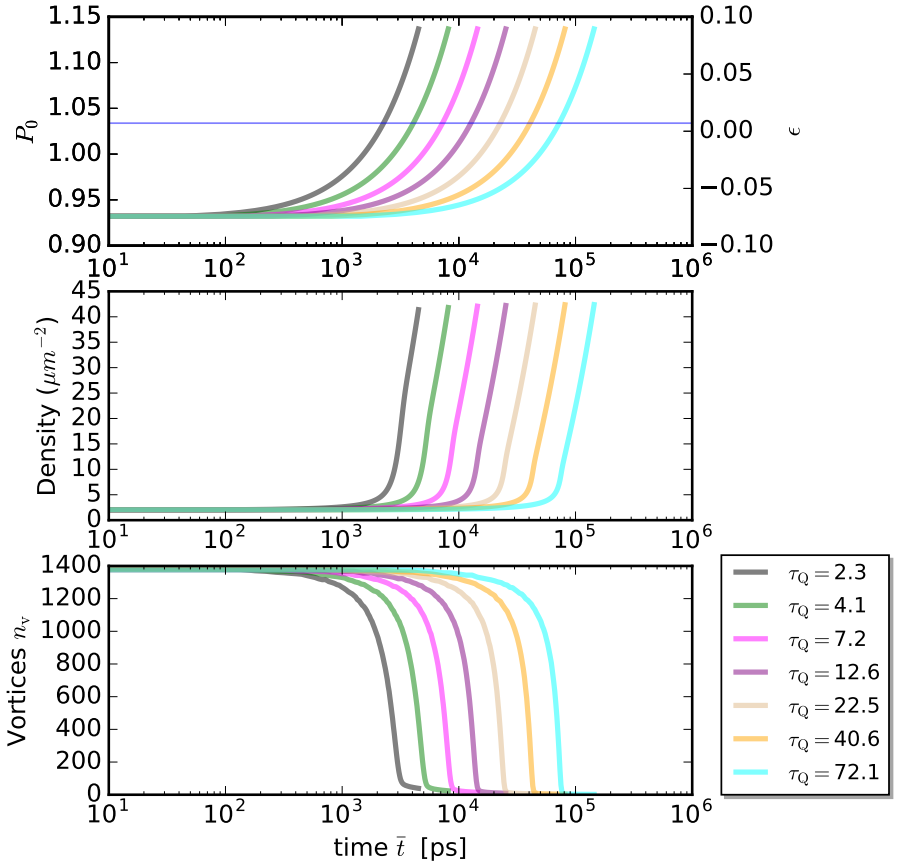

Figure 6.7: **Quench protocol.** As in Fig. 6.6, but as a function of "real" $\bar{t}$ instead of rescaled time t.

6.6 Numerical extraction of the freeze time

In the following section, we will present preliminary results on the universal features of nonequilibrium condensates. In order to determine whether the KZM predictions hold for polariton condensates, we compare the scaling of the freeze time $-\hat{t}$ as a function of the quench rate τ_Q independently from our numerical data and from the theoretical predictions.

In Sec. 6.6.1 we use the condition (6.5) to infer the freeze time $-\hat{t}_{\text{pred}}$ (henceforth termed "predicted" freeze time in this thesis) which we numerically extract by assuming *a priori* that the condition (6.5) holds in the case considered. In the following section we show how we calculate $-\hat{t}_{\text{pred}}$, for different quench rates τ_Q, from the relaxation time τ and τ_* previously obtained, see Sec. 6.4. Subsequently, these two values will be compared with the freeze time $-\hat{t}_{\text{num}}$ (termed "numerical" freeze time), which we obtain exclusively from our calculations. This is extracted as the time at which the dynamically-evolving average number of defects deviates from the distribution of number of defects in equilibrium (see

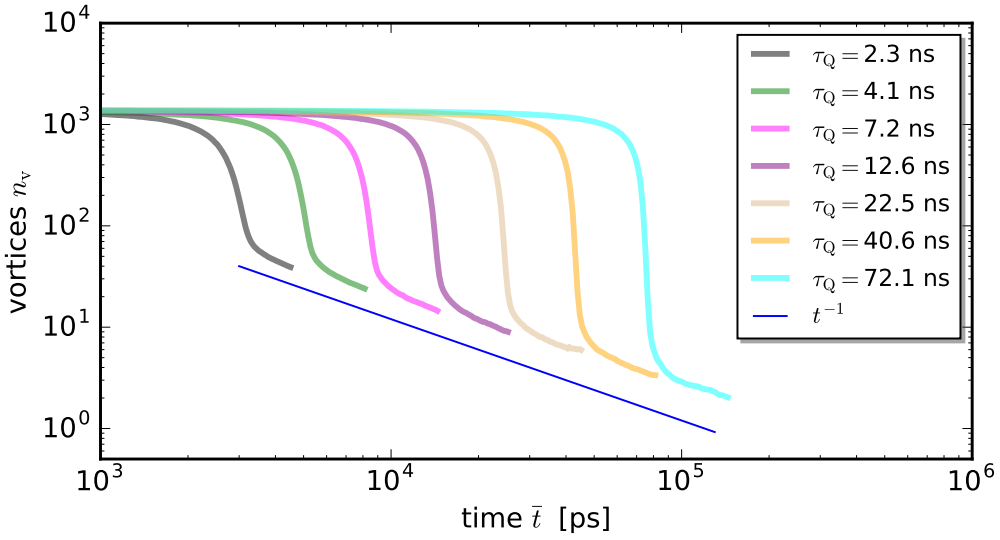

Figure 6.8: **Temporal evolution of defect numbers for different quench rates τ_Q.** In all cases, the late time evolution shows phase ordering with a dynamical exponent consistent with $z \approx 2$ (solid blue line).

Sec. 6.6.2). Results are finally discussed in Sec. 6.7.

6.6.1 Numerical extraction of the "predicted" freeze time

In order to numerically obtain the freeze point $-\hat{t}_{\text{pred}}$, as predicted by the KZM, the procedure we adopt is the following: for each τ_Q we plot the implicit dependence of relaxation time τ on t in the disordered phase ($t < 0$) through

$$\tau\left(\epsilon(t)\right) \rightarrow \tau(t). \tag{6.25}$$

Fig. 6.9 shows the relaxation time (colored solid curves), corresponding to the relaxation time τ (blue points in Fig. 6.5), plotted as a function of the absolute value of time relative to the quench, calculated as $|t| = |\epsilon \cdot \zeta^{-1} \cdot 2\tau_Q|$. Here ϵ is the control parameter which ranges from $\epsilon = \epsilon_{\text{in}}$ (initial condition) to $\epsilon = 0$ (threshold), according to the quench protocol adopted, i.e. Eq. (6.24). It is worth noting that the slower the quench, the more stretched the curves are. This eventually results in higher values of $|-\hat{t}|$, as expected for slower quenches falling out of equilibrium earlier than faster ones. Similar features has been observed in computational studies probing system of different nature (Kobayashi and Cugliandolo, 2016; Shimizu *et al.*, 2018).

Subsequently, we make use of the "fundamental" assumed condition of KZ

$$\tau(t) = t(t), \tag{6.26}$$

to evaluate $|-\hat{t}_{\rm pred}|$ for different quench rates. These are obtained as the intersection point between $\tau(t)$, colored curve in Fig. 6.9, and the linear time $t(t)$, depicted with a blue dashed line in Fig. 6.9. We reiterate this procedure, initially adopted for τ, for the case of the relaxation time τ_*, previously evaluated. This allow us to collect two different measurements of the freeze time as a function of the quench duration.

Having extracted the "predicted" values of the freeze time for the case considered, in order to check whether this condition is verified also computationally, we now discuss how we extract the freeze time from our numerical simulations.

6.6.2 Numerical extraction of the "numerical" freeze time

In order to extract the numerical value of the $-\hat{t}_{\rm num}$ we evolve in time our system according to the quench protocol discussed in Sec. 6.5.1, and calculate the average number of vortices during the quench. We make use of the relation

$$\hat{t}_{\rm num}(\tau_{\rm Q}) = \zeta^{-1} \cdot 2\tau_{\rm Q}\hat{\epsilon}_{\rm num}(\tau_{\rm Q}), \tag{6.27}$$

in which $\hat{\epsilon}_{\rm num}(\tau_{\rm Q})$ specifies, for each quench of duration $\tau_{\rm Q}$, the point where the dynamical vortex number deviates from that of an adiabatic quench (steady state curve $n_{\rm v}^{\rm SS}$). In Fig. 6.10 we show the decay of number of vortices as a function of the pump power $P_0(t)$, for different quench durations $\tau_{\rm Q}$, computed according to the quench protocol (6.24). The equilibrium values of $n_{\rm v}$ which form the adiabatic curve $n_{\rm v}^{\rm SS}(\epsilon)$ (red points and solid line in Fig. 6.10) correspond to the steady state number of vortices shown in Fig. 6.3 (red circles) and 4.4 (thick red curve).

In order to numerically determine $\hat{\epsilon}_{\rm num}$, we look for the point at which each curve $n_{\rm v}(\epsilon, \tau_{\rm Q})$ departs from the adiabatic curve $n_{\rm v}^{\rm SS}(\epsilon)$. It is worth noting that similar investigation has been originally adopted for studying linear quench dynamics in the $2d$ XY model (Jelić and Cugliandolo, 2011). We now illustrate the method implemented in this thesis for extracting $\hat{\epsilon}_{\rm num}(\tau_{\rm Q})$.

The procedure adopted is the following: initially, we compute the difference, Δ,

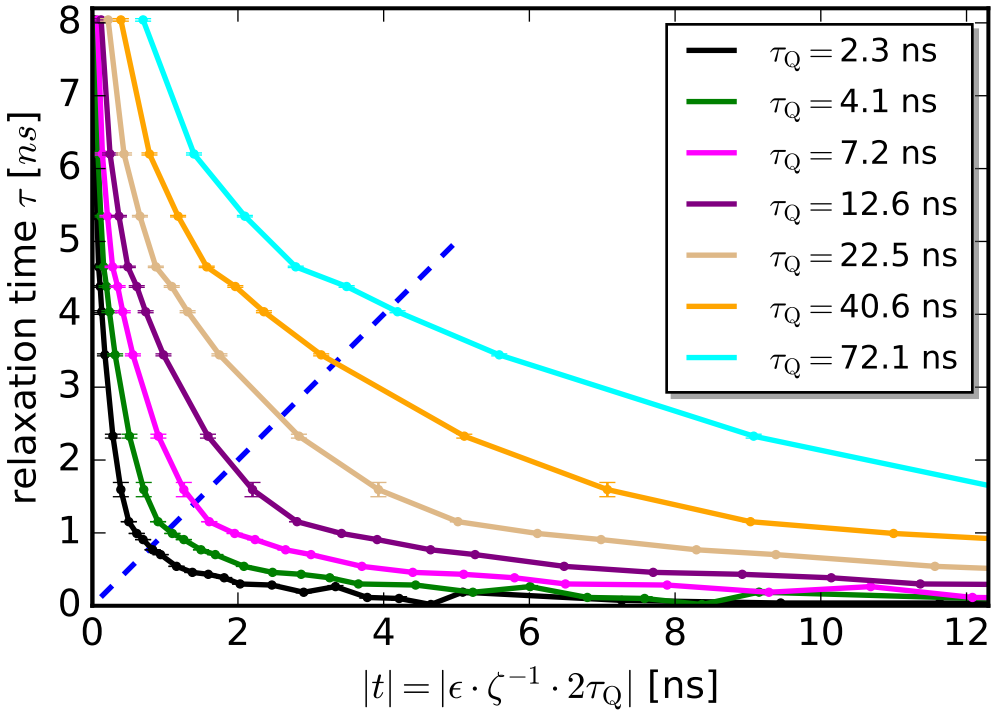

Figure 6.9: **Numerical extraction of predicted $-\hat{t}$, labelled $-\hat{t}_{\text{pred}}$.** For each τ_Q (solid lines, colours as Fig. (6.6)) we plot the implicit dependence of relaxation time τ on t (through $\tau(\epsilon(t)) \to \tau(t)$) and use the condition $\tau(t) = t(t)$ to obtain the expected value of $t = |-\hat{t}_{\text{pred}}|$ at the intersection point. Relaxation times are extracted from the fitting of the dynamical growth of the vortex number after an infinite quench (procedure illustrated in Fig. (6.4)).

between the adiabatic curve n_v^{SS} and the finite quenches $n_v(\tau_Q)$, defined as

$$\Delta(\tau_Q) = \frac{\left|n_v(\tau_Q) - n_v^{SS}\right|}{n_v^{SS}}. \tag{6.28}$$

Let us consider the ideal case of a system where the defects evolution is completely smoothed from fluctuations. Far from the critical region, at the beginning of its evolution, $\Delta = 0$ and this condition would hold as long as the system lies in the adiabatic region. At the freeze time $-\hat{t}$, a sudden increase of Δ would appear, suggesting the system has entered the non-adiabatic regime. Thus, for identifying the freeze point it would be sufficient to compute the position at which $\Delta \neq 0$.

Because of the presence of fluctuations, such a neat approach cannot be applied to the dynamics of stochastic quantities. In order to circumvent this issue, we decide to introduce a threshold $\eta \ll 1$ such that the system is considered to lie in the adiabatic regime for $\Delta < \eta$, and behave non-adiabatically for $\Delta > \eta$. The freezing point $\hat{\epsilon}_{\text{num}}$ is

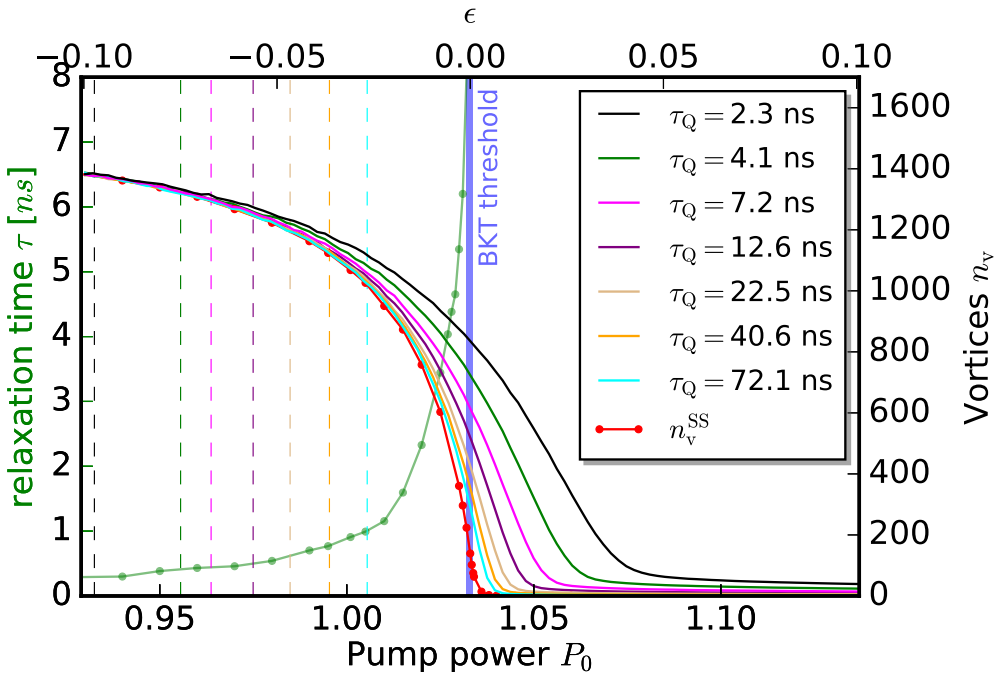

Figure 6.10: **Numerical extraction of $\hat{\epsilon}_{\text{num}}$.** The point $\hat{\epsilon}_{\text{num}}$ at which the dynamically-evolving vortex number deviates from the steady state curve n_v^{SS} (red points and solid line) is calculated for each linear quench with duration τ_Q (colored solid lines). For completeness, Vertical dashed lines show the extracted points $\hat{\epsilon}_{\text{num}}(\tau_Q)$ (colours as Fig. 6.6) for $\eta = 0.005$ (see Fig. 6.11). Green solid lines correspond to the relaxation time τ.

thus taken at the intersection point $\Delta = \eta$. In order to improve further this procedure, an interpolation method is applied to each curve.

Fig. 6.11 shows the variation $\Delta(\tau_q)$ on the control parameter ϵ and pump P_0. The points $\hat{\epsilon}_{\text{num}}(\tau_Q)$ extracted at $\eta = 0.005$ are shown in Fig. 6.11 (top) and Fig. 6.10 by means of vertical colored dashed lines. Subsequently, the freeze times $|-\hat{t}_{\text{num}}|$ are inferred from the relation (6.27). Each set of points, corresponding to a given η, is fitted with a power-law $y = a\tau_Q^b$. In Fig. 6.11 (bottom) we show the scaling of the freeze times calculated for different values of the threshold parameter η.

In the following section we discuss the comparison between the scaling of the extracted "numerical" freeze time $\hat{t}_{\text{num}}(\tau_Q)$ and the "predicted" freeze time $\hat{t}_{\text{pred}}(\tau_Q)$ with the quench duration.

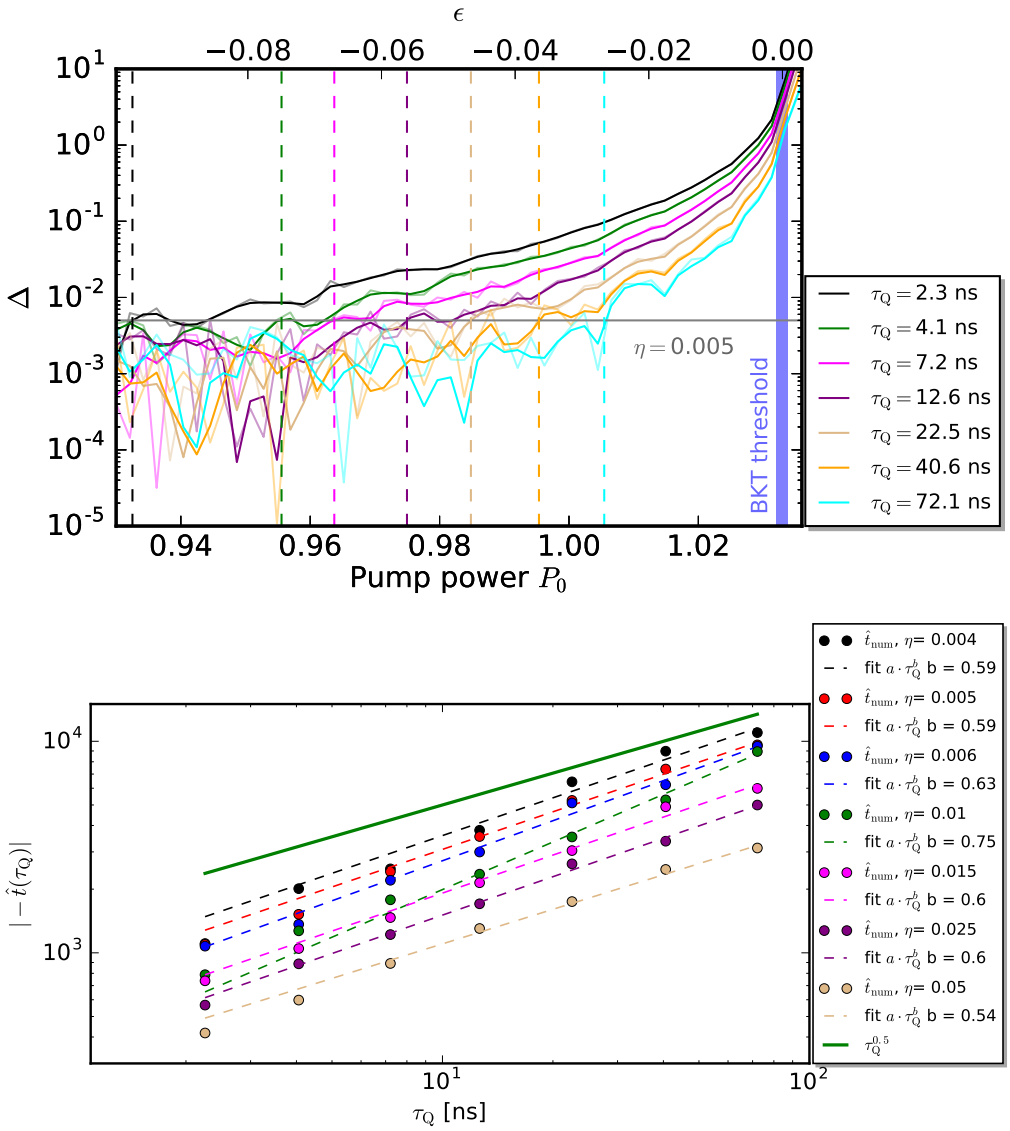

Figure 6.11: **Numerical extraction of $\hat{t}_{num}$.** (top) Fractional difference between equilibrium number of vortices n_v^{SS} and time-dependent number of vortices $n_v(\tau_Q)$ for different cooling rates. For each quench (colored solid curves) we show the numerical interpolation (bold lines) from the actual noisy numerical data (faint curve). From the numerical interpolation curve, we extract the freeze pump $\hat{\epsilon}_{num}(\tau_Q)$ (dashed vertical lines), taken as the point which satisfy $\Delta = \left|n_v(\tau_Q) - n_v^{SS}\right| / n_v^{SS} = \eta$ with η an arbitrary threshold value chose here as $\eta = 0.005$ (grey horizontal line). (bottom) The extracted values of $|-\hat{t}_{num}|$ are plotted as a function of the quench rate τ_Q, for different values of η, (reported in legends) together with the slopes b obtained by fitting with the power-law function $y = a\tau_Q^b$, with a, b free parameters.

6.7 Discussion

In Fig. 6.12 we compare and show computational estimation of the absolute value of freeze time $\hat{t}_{\rm num}(\tau_{\rm Q})$, extracted at $\eta = 0.005$, (blue circles) with the theoretical prediction $\hat{t}_{\rm pred}(\tau_{\rm Q})$ (red squares). The "predicted" freeze times obtained by means of the relaxation time τ and τ_*, are plotted in top and bottom panels, respectively. We tentatively fit the data with a power-law $y = a\tau_{\rm Q}^b$, from which we can infer an algebraic exponent b, evaluated for each set. Such exponents are then reported in the corresponding legend. In both top and bottom panels, we also show the scaling $\tau_{\rm Q}^1$ and $\tau_{\rm Q}^{0.5}$ to guide the eye.

We note that the "predicted" freeze times calculated for the two curves, τ and τ_*, show preliminary values of the exponent b comparable with $b \sim 0.5$ ($b = 0.46$ and $b = 0.52$, for τ and τ_*, respectively). Remarkably, we find that both exponents also are comparable with the value of b extracted from the growth of $\hat{t}_{\rm num}(\tau_{\rm Q})$, $b = 0.59$.

While our analysis is not sufficient to infer the nature of the phase transition, i.e. whether it is of the second-order or infinite-order, our results show good agreement between theoretical prediction and numerical results, suggesting that the KZM condition (6.5) holds for nonequilibrium systems. It is worth noting that the exponent extracted by fitting the number of vortices is found to be consistent with early studies of quenches across a second order phase transition (cfr. Eq. (6.6)) in $2d$ (Yates and Zurek, 1998; Ducci *et al.*, 1999; Miranda *et al.*, 2013).

6.8 Scaling of defects at long times

At the freeze time $-\hat{t}$, the system enters the impulse stage, where the dynamics ceases to be adiabatic. After this time, the system continues to evolve according to the rules of the phase ordering process discussed in Ch. 5. The long time dynamics after a slow quench has been investigated in the context of the $2d$ XY model by Jelic *et al.* in (Jelić and Cugliandolo, 2011). In Fig. 6.13 we show the number of vortices, (normalised by their maximum value $n_{\rm v}^{\rm max}$), calculated at the end of the linear and symmetric quench, at $\epsilon_{\rm fin} = 0.1$, as a function of the quench duration $\tau_{\rm Q}$. Data are fitted with the analytical prediction for the XY model (Jelić and Cugliandolo, 2011),

$$n_{\rm v} \sim \left\{ \frac{\tau_{\rm Q} + \hat{t}}{\log\left(\tau_{\rm Q} + \hat{t}\right)} \right\}^{-1}, \tag{6.29}$$

where we use $\hat{t} = |-\hat{t}_{\rm num}|$. We stress good agreement between computational data and theoretical predictions. A further confirmation of this behaviour is given in Fig. 6.8,

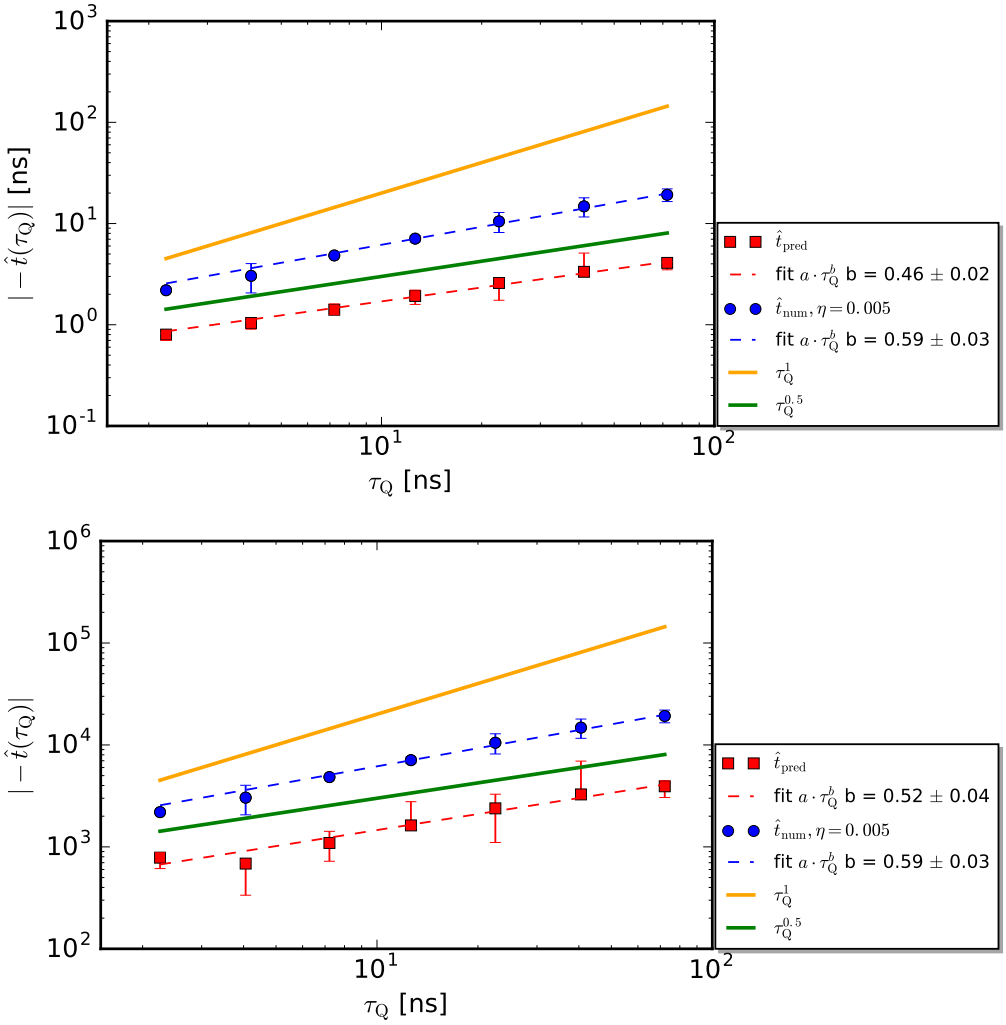

Figure 6.12: **Comparison between $\hat{t}_{\mathbf{pred}}(\tau_Q)$ and $\hat{t}_{\mathbf{num}}(\tau_Q)$.** (top) Comparison between scaling laws of $|-\hat{t}_{\mathrm{pred}}(\tau_Q)|$ calculated by means of the relaxation time τ (red squares) as in Fig. 6.9, and $|-\hat{t}_{\mathrm{num}}(\tau_Q)|$ (blue circles) calculated as in Fig. 6.10, for $\eta = 0.005$. Dashed lines show a tentative power-law fitting to both data sets with relative extracted exponents b shown in legend. $\hat{t}_{\mathrm{num}}(\tau_Q)$: for each quench τ_Q, we plot tentative error bars (blue) whose upper and lower bound are taken intersecting Δ with, correspondingly, $\eta + 0.001$ and $\eta - 0.001$. $\hat{t}_{\mathrm{pred}}(\tau_Q)$: we plot tentative errorbars (red), calculated from the abscissa points $t(\tau)$ before and after the intersection point extracted as described in Fig. 6.9. (bottom) As above, but for τ_*.

showing the decay of number of vortices after a slow and linear quench which is consistent with $n_v \sim t^{-1}$, as theoretically predicted by numerical investigation of the $2d$ XY model (Jelić and Cugliandolo, 2011) and investigate extensively in Ch. 5 of this thesis for nonequilibrium condensates.

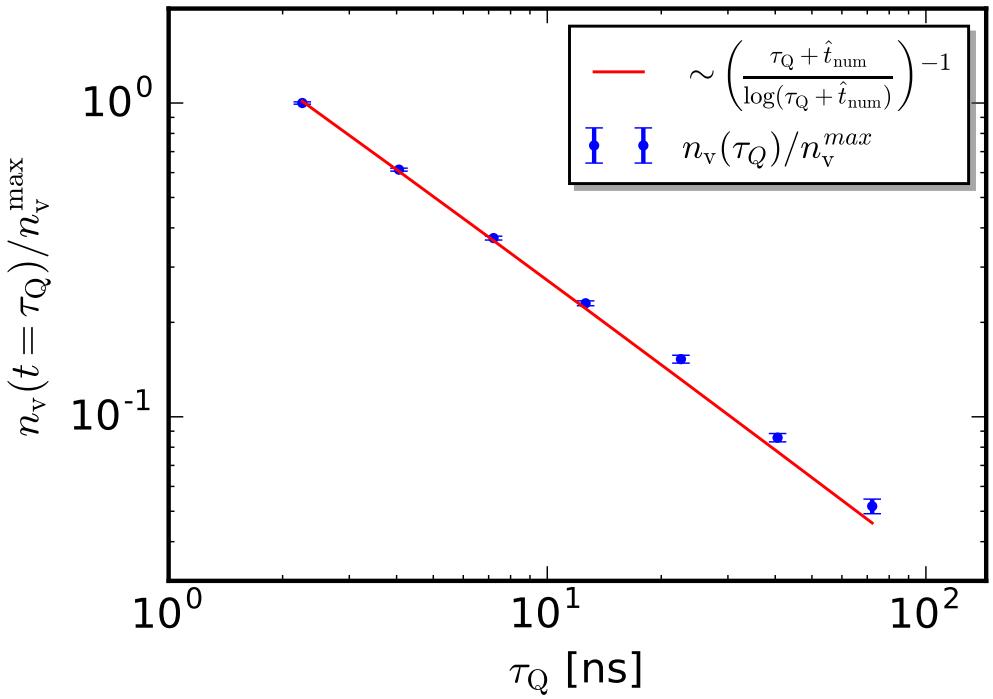

Figure 6.13: **Decay of number of vortices at the end of the quench as a function of the quench duration τ_Q.** We evaluate the dependence of vortex number at the end of the quench as a function of the quench duration τ_Q. Numerical fit of data using Eq. (6.29) is represented by red solid line.

6.9 Conclusions

In this chapter we presented a preliminary analysis on the critical slowing down and the Kibble Zurek mechanism in nonequilibrium systems.

After having theoretically introduced the Kibble-Zurek mechanism in Secs. 6.1, we revisited the theory of finite quench dynamics in second-order and infinite-order phase transitions, in Sec. 6.2 and Sec. 6.3, respectively. Results on the critical slowing down of the system obtained by investigating the divergence behaviour of equilibrium characteristic length and relaxation time when approaching criticality were presented in Sec. 6.4. Numerical data were fitted with theoretical predictions for both a second-order and a infinite-order phase transition. The preliminary results obtained suggest that values of critical exponents extracted by fitting with theoretical predictions for the 2*d* XY model (infinite-order phase transition) were more compatible with those extracted by fitting with the theoretical predictions for a second-order phase transition. This infinite-order-like behaviour is supported by the scaling of the average number of vortices at the end of the quench with the quench rate. In order to clarify this interesting open question, further analysis is needed.

Subsequently, in Sec. 6.5 we investigated quench dynamics of an incoherently driven polariton condensate. A quenched system is known to respond adiabatically to the change of the control parameter until a time $-\hat{t}$; at this time the equilibrium relaxation time is supposed to match the time left to the dynamically-evolving system to reach the critical point. In order to determine whether the KZ mechanism hypothesis is valid for driven-dissipative condensates, we directly probed this condition.

First, in Sec. 6.6.2 we inferred the freeze time computationally, by calculating the point where each quench deviated from that of an adiabatic one. From the scaling of the values of the freeze time as a function of the quench duration, we tentatively extracted an algebraic exponent which was compared with that obtained from theoretical predictions, Sec. 6.6.1. The preliminary analysis showed very good agreement between theoretical prediction and numerical results. This confirms the initial hypothesis and is also clear evidence of the validity of KZ framework in nonequilibrium condensates. Interestingly, the exponents extracted from the scaling of the freeze time with the duration quench was found to be consistent with early studies of quenches across a second order phase transition in $2d$ (Yates and Zurek, 1998; Ducci *et al.*, 1999; Miranda *et al.*, 2013). However, our analysis is not sufficient to determine whether the phase transition is of the second-order or infinite-order, suggesting the need for further investigation.

Chapter 7

Conclusions and future work

In this chapter, we summarise the important results shown throughout the thesis, and outline possible future work related to the open questions that have arisen.

7.1 Summary of obtained results

In this thesis we have theoretically studied the phase transition and the universal critical properties of $2d$ driven-dissipative Bose systems. This analysis has been undertaken by solving the stochastic polariton GPE, which corresponds to a stochastic nonlinear Langevin equation for the lower polariton branch. In contrast to the "standard" polariton Gross-Pitaevskii equation (GPE), in which the wavefunction only describes the bare coherent part of the system, in the polariton SGPE the wavefunction includes quantum and thermal fluctuations, which can be thought of as the effect of the continuous flow of particles which enter the condensate in the presence of pumping and leave the condensate due to microcavity losses.

In order to include such effects, phase space techniques were employed. The truncated Wigner approximation, adopted here, proved to be an efficient method to include these fluctuations by means of the inclusion of a Gaussian white noise in the equation of motion for the wavefunction. While the mean field model is able to successfully simulate equilibrium properties of the coherent field, it dramatically fails to describe the relevant physics in the vicinity of the phase transition. Such a description, essential for the study of dynamical properties of the system across the phase transition, is instead correctly captured by the stochastic method employed in this work.

In Ch. 3 we presented a detailed numerical analysis of both mean field and stochastic models. We compared results obtained by implementing different pumping profiles and

boundary conditions of the numerical grid. We successfully identified the best conditions for studying phase transitions and quench dynamics avoiding numerical errors in our implementation of the model. Such "optimum"conditions were found to correspond to a system driven by a homogeneous pump and simulated in a numerical grid with periodic boundary conditions. We described a typical dynamical growth of the polariton stochastic GPE and showed key physical observables calculated at several dynamical stages in the evolution, based on the model introduced in Ch. 2. Subsequently, numerical tests for the static and dynamic properties of this system were performed. The obtained results showed good agreement with theoretical predictions. The three key physical outputs based on this model that were presented in this thesis are summarised below.

7.1.1 BKT transition in driven-dissipative systems

In Ch. 4 we investigated the phase transition of a driven-dissipative condensate. We successfully reproduced the phase diagram for the steady state density calculated with both mean field and stochastic models. We undertook a detailed numerical study of the relevant physical quantities such as spatial correlations, number of topological defects and average density. Our calculations demonstrated that a BKT phase transition between a disordered phase, where correlations decay exponentially, to a quasi-long-range ordered phase characterised by algebraic decay and bound vortex-antivortex pairs, can appear in an incoherently pumped system. Our results also revealed that stronger fluctuations at higher modes ($\Omega \to \infty$) and smaller saturation density ($n_s \to 0$) led to a larger shift of the critical pump power of the BKT transition with respect to the mean-field onset of macroscopic population growth.

Particular attention was given to the critical region, identified as the threshold between the binding/unbinding of vortices, at which the decaying spatial correlation function was observed to crossover from exponential to power-law forms. Importantly, we saw that the exponent of the algebraic decay can exceed (at least for some parameters choices) the limit of 1/4, arising in the equilibrium BKT transition. This suggests that, for the parameters taken into consideration, the nature of the transition could be characterised as being a "nonequilibrium BKT" phase transition.

The discussion on whether a driven-dissipative system, like the one considered in this work, could be classified as an equilibrium or nonequilibrium transition, is actually an ongoing debate. Following the outcomes of recent experimental and theoretical studies (Caputo *et al.*, 2017), the extent of the nonequilibrium nature of the BKT phase transition could potentially be associated with the difference between the spatial and temporal

correlation exponents calculated in the ordered phase. It has been predicted that an important role is played by phase fluctuations which are responsible for a slower decay (consistent with a stretched exponential form) of spatial correlations at very large scales compared with ordinary system sizes (Altman *et al.*, 2015).

Concerning the system considered in this thesis, our calculations were able to identify a narrow critical region where the crossover takes place. Nonetheless, we were not able to conclusively resolve this delicate issue regarding the precise nature of the phase transition and exact location of the critical point. A potential future systematic work on this should also undertake a parallel investigation of spatial and temporal correlations for a broad range of parameters. This could be useful in regard to future endeavours (see Sec. 7.2).

7.1.2 Phase ordering kinetics after an infinitely rapid quench

Although recent theoretical works have highlighted equilibrium systems to be predominantly of the BKT type (Dagvadorj *et al.*, 2015; Caputo *et al.*, 2017), a conclusion supported by the results shown in Ch. 4, there has previously been no detailed study investigating whether this should also hold when the phase transition is crossed dynamically.

In Ch. 5 we presented strong numerical evidence of the universal scaling dynamics of a driven-dissipative condensate. We undertook a full characterisation of the late time dynamics of a polariton condensate after an infinitely rapid quench across the BKT phase transition from a disordered configuration to a configuration deep in the ordered phase. In order to preserve the universal features of our results, the same study was performed for both incoherently-pumped (with and without frequency-selective pump) and parametrically-driven systems (the latter done by our UCL collaborators).

This study was based on the extraction of the characteristic length from both spatial correlation functions and topological defects. Such a length scale was extracted when the system was at sufficiently late times, so that the scaling hypothesis could be applied. From the growth of such a characteristic length, we found the scaling exponent $z \approx 2$ in all cases considered. Our finding ruled out the possibility that polaritons exhibit physics of conservative Bose (Damle *et al.*, 1996) and non-equilibrium KPZ systems (Altman *et al.*, 2015). Remarkably, through our results we were able to confirm that the long-time dynamics are characterised by a logarithmic correction (a direct consequence of the topological order characteristic of $2d$ systems) in perfect agreement with the predicted case of the canonical $2d$ XY model.

In support of these significant results, we provided a detailed technical analysis of the

numerical procedures adopted. We discussed extensively the extraction of the dynamical exponent from both the characteristic length and topological defects, the presence of logarithmic corrections, the evolution of the exponent for different temporal windows, the direct relation between density of vortices and the characteristic length scale, and the role of the microscopic time scale on the exponent evolution.

Thus, the study undertaken in Ch. 5 demonstrated conclusively that the universal properties of the system are dominated by BKT-type of physics for dynamical crossing of the phase transition. Our work also clearly revealed that early dynamics can give misleading results, e.g. that the value of the dynamical critical exponent may depend on the interplay between pumping and loss (Kulczykowski and Matuszewski, 2017), which would in fact negate the precise concept of universality, a concept which has proven so useful in characterizing many different physical systems.

7.1.3 Kibble-Zurek mechanism in driven-dissipative condensates

In Ch. 6, we further investigated the critical behaviour of driven-dissipative systems. First, we undertook a preliminary analysis of the critical slowing down of the correlation length and relaxation times at the vicinity of the narrow critical region extracted in Ch. 4. We extracted the correlation length by means of the average number of topological defects in the steady state. Then, we calculated the relaxation time from the dynamical equilibration of the number of defects to the steady state. The preliminary fits of both characteristic length and relaxation time with the analytical expressions predicted by the $2d$ XY model suggested a static exponent close to the one predicted by the mean field theory, namely $\nu = 1/2$.

By analysing finite-duration quench dynamics across the phase transition, we explicitly verified universal behaviour in the form of the Kibble-Zurek mechanism, a universal scaling law relating the number of spontaneously-generated defects (vortices) to the quench duration. The analysis consisted in the comparison between the freeze time (time after which the dynamically-evolved system is supposed to fall out of equilibrium) calculated numerically and theoretically, independently. The protocol used in our analysis was based on linear quenches which were implemented symmetrically across the critical region. In so doing, we ensured that the results obtained were independent of the value of the critical point chosen within the critical region.

Remarkably, the preliminary results obtained qualitatively suggest that the freeze times extracted by our numerical data were consistent with the theoretical KZM predictions. Moreover, the scaling of the freeze time with the quench duration was found to

be consistent with early studies of quenches across a second order phase transition in $2d$ (Yates and Zurek, 1998; Ducci *et al.*, 1999; Miranda *et al.*, 2013). Having reviewed our key finding, we now briefly discuss what further work could be done to shed more light on the above partly-open questions.

7.2 Future work

In Ch. 4 we demonstrated that even for a system characterised by strong nonequilibrium features (in the sense that the polariton lifetimes considered —taken from the earlier experiments on nonequilibrium BKT (Roumpos *et al.*, 2012)— is orders of magnitudes lower than the lifetimes of new generations samples (Caputo *et al.*, 2017; Sun *et al.*, 2017)), the phase transition is still mediated by the presence of quantum vortices which drive the transition to a superfluid state. Consistent with recent findings on nonequilibrium phase transitions (Roumpos *et al.*, 2012; Dagvadorj *et al.*, 2015), the system considered in this thesis appears to exhibit a value of the exponent α exceeding the equilibrium threshold value of 1/4. However, we have argued (Sec. 7.1) that this condition is not sufficient to characterise the nonequilibrium nature of the system. It would be an extremely interesting direction for future work to investigate these issues, by computationally calculating the temporal correlations, and testing whether the algebraic exponent α_t (if correlations would be found to be algebraic) corresponds to the spatial exponent α.

Furthermore, it would be interesting to approach the same questions by varying the set of parameters used in this work, for the purpose of investigating the possible emergence of a value of $\alpha > 1/4$ at the edge of the ordered phase, and their possible relations with the pump parameters. This could lead to the identification of a possible "tunable" threshold for the equilibrium-nonequilibrium nature of the condensate. Similar physics can be also probed by looking at the sonic behaviour of the excitation spectrum (Caputo *et al.*, 2017).

In Ch. 5 we have studied and fully characterised the universal dynamical scaling for the incoherently (and parametrically) pumped polariton condensate. For the incoherently pumped case, we adopted a model which assumes the reservoir of high-energy excitons adiabatically follows the condensate (Carusotto and Ciuti, 2013). An interesting direction for future work would be to consider the effect of dynamical coupling of the reservoir to the condensate dynamics thus shedding more light on the perplexing, in our view, findings presented in (Kulczykowski and Matuszewski, 2017) where it was argued that the dynamical critical exponent, z, varied from 1 to 2 depending on the interplay of pumping and dissipation rates. Given that the required system size in the 100 μm range needed to access such physics appears achievable in the new generation of samples (Caputo *et al.*,

2017; Baboux *et al.*, 2017), experiments could also investigate such features and shed more light on these questions.

Finally, concerning the preliminary results described in Ch. 6, it would be interesting to investigate (as currently underway at UCL) whether the exponent obtained by fitting the freeze time as a function of the quench duration in OPO would lead to similar results as those found for the incoherently pumped mechanism.

We believe the next few years will lead to a range of interesting developments on the precise details of the polariton phase transition which could prove useful in providing a more in-depth understanding of phase transitions in general while also in this case leading to advances in potential future quantum-technological devices.

Appendix A

Numerical convergence

A.1 Convergence tests

In the following section, we show examples of convergence tests and debate validity conditions which endorse the results shown in Part II.

A.1.1 Convergence to a steady state

It is worth noting that each test discussed below has been conducted for each point of the phase diagram illustrated in Fig. 4.4. These concern spatial first order correlation functions, average vortex number and average density. Here we decide to show only a few key examples among the vast plethora of tests performed.

Number of realizations

The expectation value of a specific symmetrized operator is given by the corresponding stochastic average over a certain amount of different paths. Concerning spatial fist order correlation function and polariton density, these are given by Eqs. 3.24 and 3.25, respectively. In Fig. A.1 we compare the spatial first order correlation function calculated over many stochastic realizations $N_{\mathrm{p}} = 50, 100, 200, 400$ for $P_0 = 1.5$. We note that all the curves lie inside the error bars appertaining to the curve obtained with $N_{\mathrm{p}} = 400$. In principle, the analysis suggests that 50 realizations are sufficient to give a reliable converged result. However, in order to have smother curves and decrease the RMS of the fit residuals in the analysis discussed in Sec. 4.3.2, we calculate each curve by averaging over $N_{\mathrm{p}} = 200$ realisations.

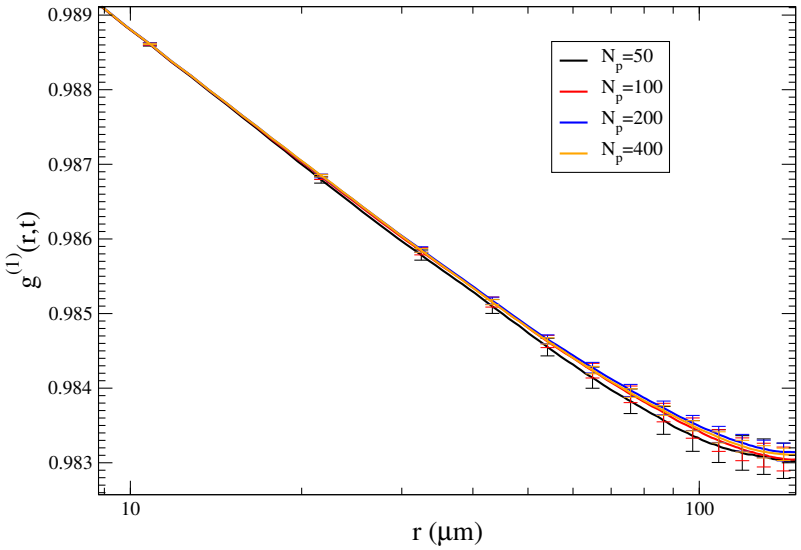

Figure A.1: **Convergence in the number of stochastic path.** First order correlation function calculated averaging over different numbers of stochastic paths: N_p = 50 (black), N_p = 100 (red), N_p = 200 (blue) and N_p = 400 (orange), for P_0 = 1.5, other parameters as in Table 3.1.

Convergence in time and dependence on different initial conditions

In order to achieve the steady state for a given pump power, we quench infinitely rapidly from a given initial condition and let the system evolve to a static configuration. To evaluate when the steady state has been reached, we evolve our system from different initial configurations, namely from either a white Gaussian noise (which mimic a highly disordered state) or the corresponding mean field steady state. We iterate this procedure for all physical quantities investigated. In Figs. A.2-A.3 we plot the temporal evolution of density and vortex number, respectively, for the cases P_0 = 0.99, P_0 = 1.0338 and P = 1.06.

A.1.2 Convergence tests for the system dynamics

Convergence in lattice size. Fig. A.4 provides conclusive evidence of the independence of our results on lattice size for both OPO and IP regimes, based on which the analysis Ch. 5 is conducted for grid spacings $a = 0.87\mu m$ (OPO), $a = 0.98\mu m$ (IP) and grid sizes 444.42 μm (OPO) and $l = 295.11\mu m$ (IP). Specifically, the top (middle) panel shows a comparison of the time-evolution of the vortex density for the OPO (IP) case upon increasing the total grid size, while keeping discretisation fixed. Fig. A.4 (bottom) shows corresponding IP results (for $\Omega = 50\gamma_{\mathrm{LP}}$) for the correlation function, with the coloured bands indicating the error bars; this demonstrates that our numerics is sufficient to avoid the correlation function being affected by boundary effects even as the system approaches the critical region.

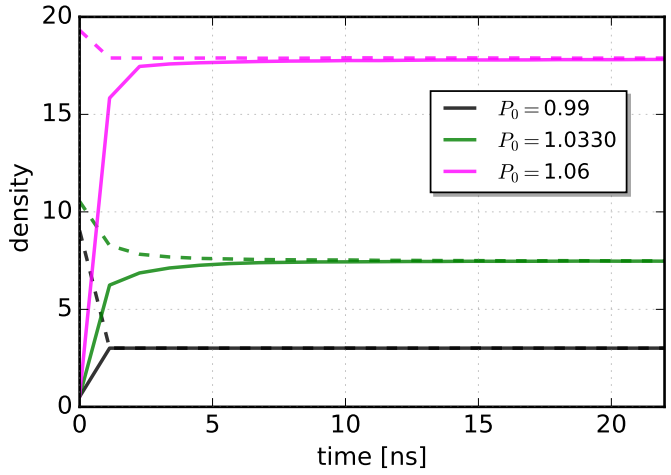

Figure A.2: **Convergence in time for the number of vortices.** Here we show the average density $\left\langle |\psi_{\mathrm{LP}}|^2 \right\rangle$ over $N_{\mathrm{p}} = 200$ realisations. We analyse different pump strengths according to configurations far below threshold ($P_0 = 0.99$), about threshold ($P_0 = 1.033$) and above threshold ($P_0 = 1.06$). Interestingly, the curves below and about threshold spend more time to reach a steady state, due to the strong fluctuations. Also, the evolution is shown to be converged for different initial conditions, i.e. white noise (solid lines) and mean field steady state (dashed lines).

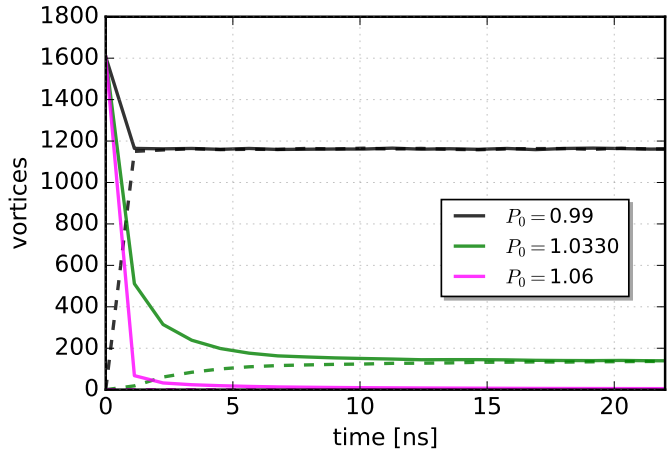

Figure A.3: **Convergence in time for the number of vortices.** As Fig. A.2, but for the average number of vortices $\langle n_{\mathrm{v}} \rangle$.

Convergence in stochastic numerical realisations. Having fixed the grid spacing and size, we next investigate the dependence of results on the number of different numerical trajectory realisations (done in addition to averaging over the entire grid in single realisations). Although Fig. A.5 shows that on first inspection a number of ≈ 100 (OPO) or 50 (IP) realisations may be enough for sufficient convergence in the overall dynamics, we nonetheless stress that averaging over a high number of realisations is essential for correlation functions which are smooth over the entire spatial grid, thus allowing for an

accurate determination of the long-time dynamical critical exponent for L and n_{v}. We have therefore chose to use $N_p = 400$ realisations for both OPO and IP cases, for both $g^{(1)}$ and n_{v}.

Convergence in computational method (Incoherently pumped system). To ensure independence of our numerical results on computational method, we have implemented two distinct schemes for the incoherently-pumped case, based on finite differences method for the Laplacian implemented in Fortran and based on spectral methods and the publicly-available XMDS2 code (Dennis *et al.*, 2013). Fig. A.6 (top) shows consistency between the two cases already at the level of only 50 numerical realisations. We have chosen to report results based on the XMDS2 spectral method, as this has exponential convergence, i.e. the error scales as $\propto a^N$ with increasing resolution (where N is the number of grid points) - as opposed to the algebraic scaling $\propto a^2$ of finite difference schemes.

Convergence in cut-off choice (Incoherently pumped system). Within the stochastic Gross-Pitaevskii equation, the grid spacing a sets a maximum momentum cut-off $\propto a^{-1}$ in the numerical representation of the quantum field, restricting the maximum number of evolving modes. A detailed discussion is reported in Sec. 3.1.3 of this thesis. We check that our results do not depend on the chosen cut-off value. Fig. A.6 (bottom) demonstrates that for two different grid spacings $a = 0.49\ \mu m$ and $a = 0.98 \mu m$ (while keeping the total box size fixed to $l = 295.11 \mu m$ by varying the number of grid points) the evolution of n_{v} is practically identical.

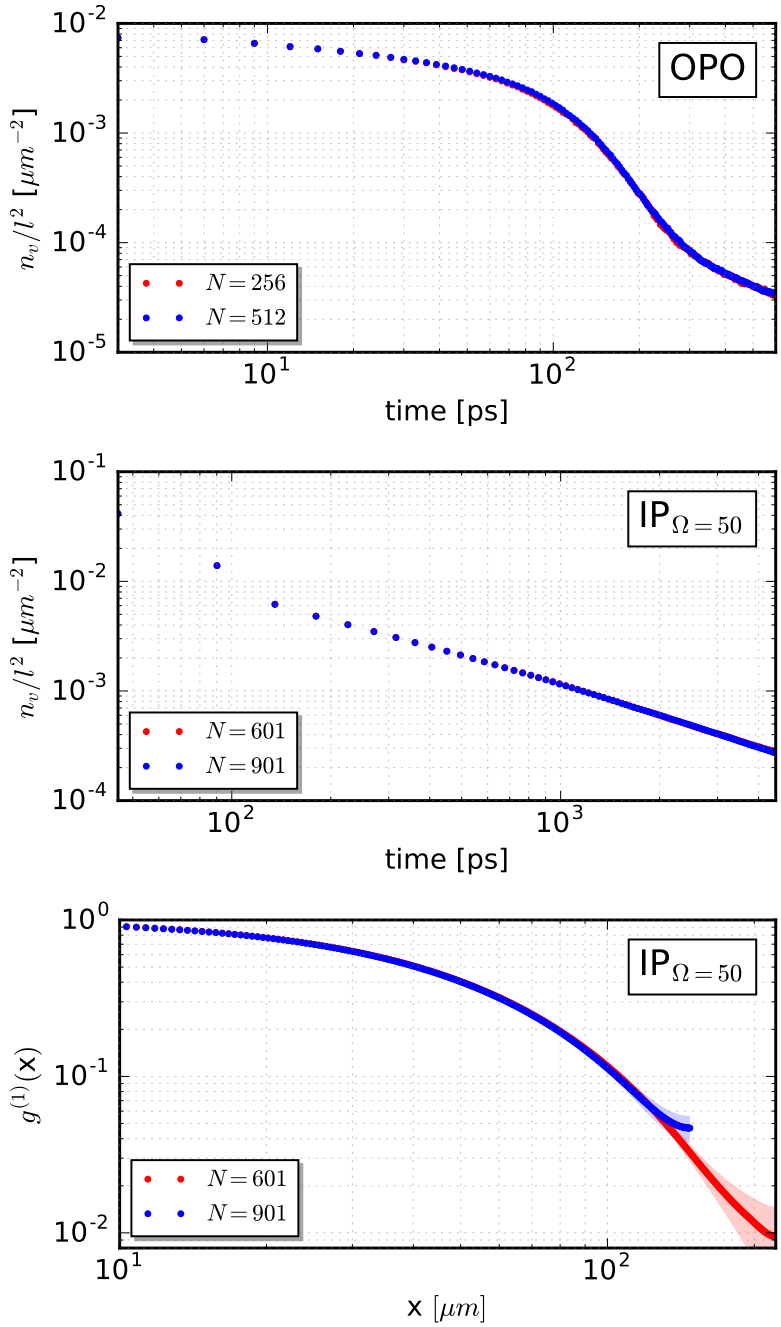

Figure A.4: **Convergence in lattice size.** Top panel: convergence in time of vortex density for OPO system with $f_p/f_p^{up} = 0.97$, for two different box of size $l = 222.208\ \mu m$ and $l = 444.42\ \mu m$ with respectively $N = 256$ and $N = 512$ number of points and grid spacing $a = 0.87\ \mu m$. Central panel: convergence in time of vortex density for IP system with $P/P_{\text{th}} = 1.5$, $\Omega = 11.09\ ps^{-1}$ and $n_s = 500\ \mu m^{-2}$, for two different box of size $l = 295.11 \mu m$, $l = 444.42\ \mu m$ with respectively $N = 601$ and $N = 901$ number of points. Bottom panel: spatial convergence of first order correlation function for IP system before it enters the power-law stage at $t = 4.5\ ns$ for the two different boxes.

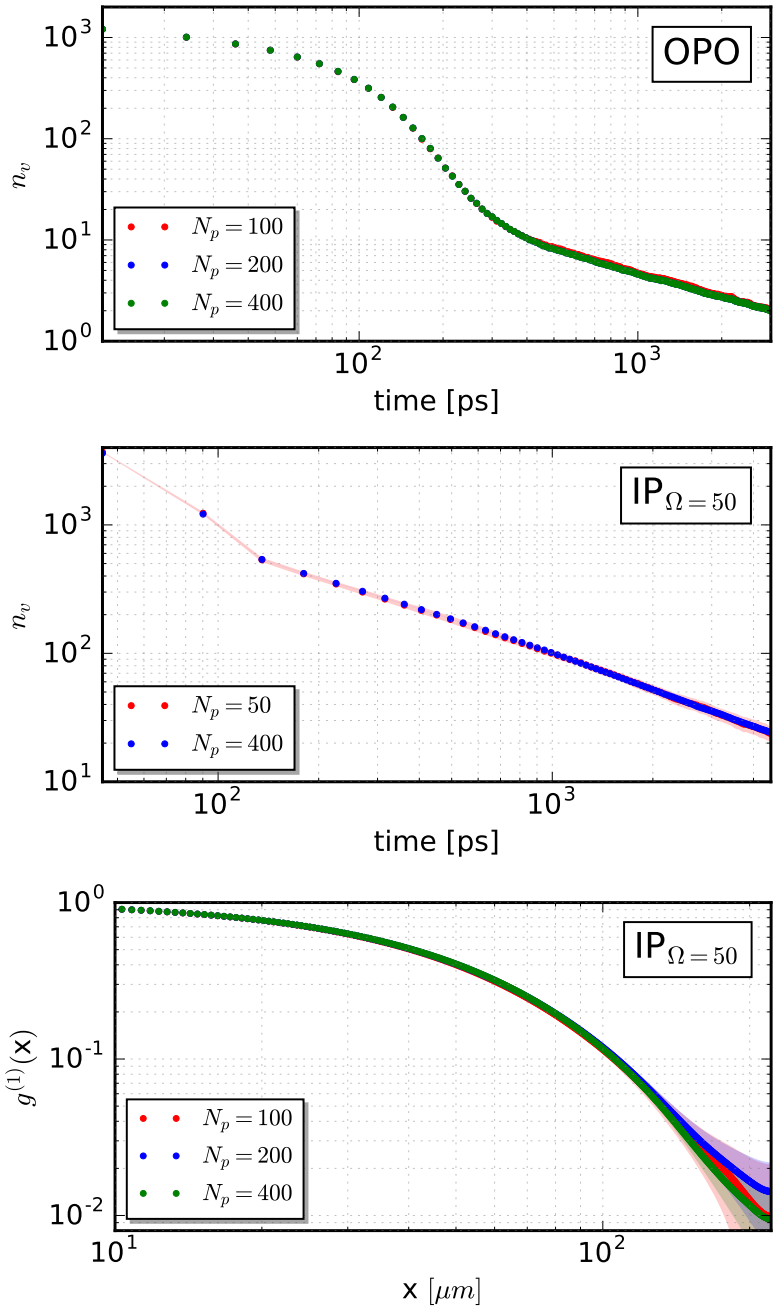

Figure A.5: **Convergence in number of stochastic paths.** Top panel: convergence in time of number of vortices for OPO system averaged over $N_p = 100, 200, 400$ stochastic paths. Central panel: convergence in time of number of vortices for IP system averaged over $N_p = 50, 400$ noise realizations. Bottom panel: spatial convergence of first order correlation function for IP system before it enters the power-law stage at $t = 4.5\ ns$ over $N_p = 100, 200, 400$ stochastic paths. Parameters as in Fig. A.4.

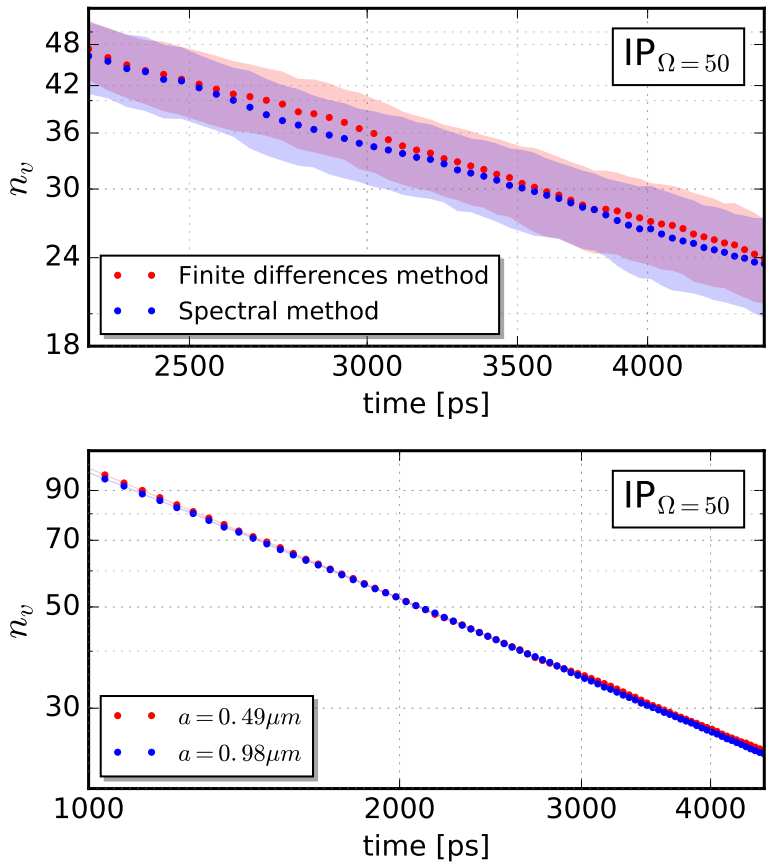

Figure A.6: **Convergence in methods and cut-off choice for the incoherently pumped system.** Top panel: evolution of number of vortices for two different computational schemes: spectral methods (red points) and finite differences methods (blue points). Bottom panel: time evolution of number of vortices for two different lattice spacings, i.e. cut-off choice, $a = 0.49\mu m$ (red points) and $a = 0.98\mu m$ (blue points). Parameters as in Fig. A.4.

Appendix B

The characteristic KPZ length scale

B.1 Calculations for the incoherently-pumped condensate

In this section we calculate the KPZ length, L_*, for the case considered in this thesis. For lengths $L > L_*$, a nonequilibrium condensate has been predicted to show a stretched exponential decay of the spatial correlation function (Altman *et al.*, 2015). As discussed in Sec. 4.1 the nonequilibrium nature of a system modelled by the KPZ equation, Eq. 2.76, is characterised by the dimensionless nonlinearity g, Eq. (2.77), and the anisotropy parameter Φ, Eq. (2.78). Nonlinearity and appearance of a stretched exponential decay of spatial correlation functions appear for values of $g > 1$, whereas diffusion and algebraic decay of spatial correlations dominate for $g < 1$. By mapping the polariton SGPE coupled with reservoir, Eqs. 2.25-2.26 to the KPZ equation, as shown in (Altman *et al.*, 2015), the bare nonlinearity term g_0 reads

$$g_0 = 2\bar{g}\bar{\gamma}^2\left(\frac{\bar{\gamma}^2 + (1+x)^2}{x\,(1+x)^3}\right), \tag{B.1}$$

where $\bar{g}$, $\bar{\gamma}$ and x correspond to the dimensionless interaction constant, dimensionless loss rate and dimensionless tuning parameter, respectively. In the case of $g_0 \ll 1$, the renormalised value $g = 1$ is reached at very large distances

$$L_* = \xi_{\mathrm{LP}} e^{8\pi/g_0}. \tag{B.2}$$

Let us consider the case of an incoherently-pumped polariton condensate whose dynamics is described by Eq. (3.3). In this case the dimensionless terms $\bar{g}$, $\bar{\gamma}$ and x can be

written as

$$\bar{g} = \frac{2m_{\mathrm{LP}}g_{\mathrm{LP}}}{\hbar^2}, \tag{B.3}$$

$$\bar{\gamma} = \frac{\gamma_{\mathrm{LP}}}{n_{\mathrm{s}}g_{\mathrm{LP}}}, \tag{B.4}$$

$$x = P_0 - 1. \tag{B.5}$$

Thus, the bare nonlinearity term (B.1) reads

$$g_0 = 2\bar{g}\bar{\gamma}^2\left(\frac{\bar{\gamma}^2 + P_0^2}{(P_0-1)\,P_0^3}\right). \tag{B.6}$$

We calculate Eq. (B.2) for the set of parameters shown in Table 3.1, by means of Eq. (B.6) and the mean field healing length, i.e. Eq. (3.7). We find that for values of the pump very close to the mean field threshold ($1.00004 < P_0 < 1.00008$), where the characteristic KPZ length is expected to decrease drastically, the corresponding characteristic KPZ length results to be $2.910^3\mathrm{km} < L_* < 8.910^{10}\mathrm{km}$.

Bibliography

E. Fermi, *Thermodynamics*, Dover books in physics and mathematical physics (Dover Publications, 1956), ISBN 9780486603612, URL https://books.google.co.uk/books?id=AuHcCgAAQBAJ.

K. Huang, *Statistical Mechanics* (John Wiley and Sons, 2000), ISBN 9789971512958, URL https://books.google.co.uk/books?id=jbNTewAACAAJ.

A. Dragulescu and V. Yakovenko, The European Physical Journal B - Condensed Matter and Complex Systems **17**, 723 (2000), ISSN 1434-6036, URL https://doi.org/10.1007/s100510070114.

H. E. Stanley, Rev. Mod. Phys. **71**, S358 (1999), URL https://link.aps.org/doi/10.1103/RevModPhys.71.S358.

C. Castellano, S. Fortunato, and V. Loreto, Rev. Mod. Phys. **81**, 591 (2009), URL https://link.aps.org/doi/10.1103/RevModPhys.81.591.

M. J. Spivey, S. E. Anderson, and R. Dale, New Mathematics and Natural Computation (NMNC) **5**, 197 (2009), URL https://ideas.repec.org/a/wsi/nmncxx/v05y2009i01ns1793005709001234.html.

T. Sauer, The European Physical Journal Special Topics **226**, 539 (2017), ISSN 1951-6401, URL https://doi.org/10.1140/epjst/e2016-60344-y.

G. Jaeger, Archive for History of Exact Sciences **53**, 51 (1998), ISSN 1432-0657, URL https://doi.org/10.1007/s004070050021.

W. Heisenberg, Zeitschrift für Physik **43**, 172 (1927), ISSN 0044-3328, URL https://doi.org/10.1007/BF01397280.

L. V. P. R. de Broglie, Annals Phys. **2**, 22 (1925).

Bose, Zeitschrift für Physik **26**, 178 (1924), ISSN 0044-3328, URL https://doi.org/10.1007/BF01327326.

A. Einstein, Sitzungsberichte der Preussischen Akademie der Wissenschaften, Physikalisch-mathematische Klasse pp. 261–267 (1924).

C. J. Pethick and H. Smith, *Bose-Einstein Condensation in Dilute Gases* (Cambridge University Press, 2008), 2nd ed.

W. Pauli, Zeitschrift für Physik **31**, 765 (1925), ISSN 0044-3328, URL https://doi.org/10.1007/BF02980631.

D. S. Petrov and G. V. Shlyapnikov, Phys. Rev. A **64**, 012706 (2001), URL https://link.aps.org/doi/10.1103/PhysRevA.64.012706.

Z. Hadzibabic and J. Dalibard, Rivista del Nuovo Cimento **34**, 389 (2011), URL https://www.sif.it/riviste/sif/ncr/econtents/2011/034/06/article/0.

W. Keesom, *Helium* (Elsevier, Amsterdam, 1942).

P. Kapitza, Nature **141**, 74 EP (1938), URL http://dx.doi.org/10.1038/141074a0.

J. F. Allen and A. D. Misener, Nature **141**, 75 EP (1938), URL http://dx.doi.org/10.1038/141075a0.

F. London, Nature **141**, 643 EP (1938), URL http://dx.doi.org/10.1038/141643a0.

K. H. Onnes, Kamerlingh Onnes Archive, Boerhaave Museum, Leiden, the Netherlands. pp. 56, 57 (1911).

L. Tisza, Nature **141**, 913 EP (1938), URL http://dx.doi.org/10.1038/141913a0.

L. Landau, Phys. Rev. **60**, 356 (1941), URL https://link.aps.org/doi/10.1103/PhysRev.60.356.

C. E. Hecht, Physica **25**, 1159 (1959), ISSN 0031-8914, URL http://www.sciencedirect.com/science/article/pii/0031891459900357.

W. C. Stwalley and L. H. Nosanow, Phys. Rev. Lett. **36**, 910 (1976), URL https://link.aps.org/doi/10.1103/PhysRevLett.36.910.

M. H. Anderson, J. R. Ensher, M. R. Matthews, C. E. Wieman, and E. A. Cornell, Science **269**, 198 (1995), ISSN 0036-8075, http://science.sciencemag.org/content/269/5221/198.full.pdf, URL http://science.sciencemag.org/content/269/5221/198.

K. B. Davis, M. O. Mewes, M. R. Andrews, N. J. van Druten, D. S. Durfee, D. M. Kurn, and W. Ketterle, Phys. Rev. Lett. **75**, 3969 (1995), URL https://link.aps.org/doi/10.1103/PhysRevLett.75.3969.

C. C. Bradley, C. A. Sackett, J. J. Tollett, and R. G. Hulet, Phys. Rev. Lett. **75**, 1687 (1995), URL https://link.aps.org/doi/10.1103/PhysRevLett.75.1687.

C. C. Bradley, C. A. Sackett, J. J. Tollett, and R. G. Hulet, Phys. Rev. Lett. **79**, 1170 (1997), URL https://link.aps.org/doi/10.1103/PhysRevLett.79.1170.

S. L. Cornish, N. R. Claussen, J. L. Roberts, E. A. Cornell, and C. E. Wieman, Phys. Rev. Lett. **85**, 1795 (2000), URL https://link.aps.org/doi/10.1103/PhysRevLett.85.1795.

G. Modugno, G. Ferrari, G. Roati, R. J. Brecha, A. Simoni, and M. Inguscio, Science **294**, 1320 (2001), ISSN 0036-8075, http://science.sciencemag.org/content/294/5545/1320.full.pdf, URL http://science.sciencemag.org/content/294/5545/1320.

A. Robert, O. Sirjean, A. Browaeys, J. Poupard, S. Nowak, D. Boiron, C. I. Westbrook, and A. Aspect, Science **292**, 461 (2001), ISSN 0036-8075, http://science.sciencemag.org/content/292/5516/461.full.pdf, URL http://science.sciencemag.org/content/292/5516/461.

Y. Takasu, K. Maki, K. Komori, T. Takano, K. Honda, M. Kumakura, T. Yabuzaki, and Y. Takahashi, Phys. Rev. Lett. **91**, 040404 (2003), URL https://link.aps.org/doi/10.1103/PhysRevLett.91.040404.

T. Weber, J. Herbig, M. Mark, H.-C. Nägerl, and R. Grimm, Science **299**, 232 (2003), ISSN 0036-8075, http://science.sciencemag.org/content/299/5604/232.full.pdf, URL http://science.sciencemag.org/content/299/5604/232.

A. Griesmaier, J. Werner, S. Hensler, J. Stuhler, and T. Pfau, Phys. Rev. Lett. **94**, 160401 (2005), URL https://link.aps.org/doi/10.1103/PhysRevLett.94.160401.

S. Stellmer, M. K. Tey, B. Huang, R. Grimm, and F. Schreck, Phys. Rev. Lett. **103**, 200401 (2009), URL https://link.aps.org/doi/10.1103/PhysRevLett.103.200401.

S. Stellmer, M. K. Tey, R. Grimm, and F. Schreck, Phys. Rev. A **82**, 041602 (2010), URL https://link.aps.org/doi/10.1103/PhysRevA.82.041602.

P. G. Mickelson, Y. N. Martinez de Escobar, M. Yan, B. J. DeSalvo, and T. C. Killian, Phys. Rev. A **81**, 051601 (2010), URL https://link.aps.org/doi/10.1103/PhysRevA.81.051601.

S. Kraft, F. Vogt, O. Appel, F. Riehle, and U. Sterr, Phys. Rev. Lett. **103**, 130401 (2009), URL https://link.aps.org/doi/10.1103/PhysRevLett.103.130401.

M. Lu, N. Q. Burdick, S. H. Youn, and B. L. Lev, Phys. Rev. Lett. **107**, 190401 (2011), URL https://link.aps.org/doi/10.1103/PhysRevLett.107.190401.

J. M. Blatt, K. W. Böer, and W. Brandt, Phys. Rev. **126**, 1691 (1962), URL https://link.aps.org/doi/10.1103/PhysRev.126.1691.

L. V. Butov, C. W. Lai, A. L. Ivanov, A. C. Gossard, and D. S. Chemla, Nature **417**, 47 EP (2002), URL http://dx.doi.org/10.1038/417047a.

A. A. High, J. R. Leonard, M. Remeika, L. V. Butov, M. Hanson, and A. C. Gossard, Nano Letters **12**, 2605 (2012), URL https://doi.org/10.1021/nl300983n.

S. O. Demokritov, V. E. Demidov, O. Dzyapko, G. A. Melkov, A. A. Serga, B. Hillebrands, and A. N. Slavin, Nature **443**, 430 EP (2006), URL http://dx.doi.org/10.1038/nature05117.

A. A. Aczel, Y. Kohama, C. Marcenat, F. Weickert, M. Jaime, O. E. Ayala-Valenzuela, R. D. McDonald, S. D. Selesnic, H. A. Dabkowska, and G. M. Luke, Phys. Rev. Lett. **103**, 207203 (2009), URL https://link.aps.org/doi/10.1103/PhysRevLett.103.207203.

V. Berestetskii, L. Landau, E. Lifshitz, L. Pitaevskii, and J. Sykes, *Quantum Electrodynamics*, Course of theoretical physics (Butterworth-Heinemann, 1982), ISBN 9780750633710, URL https://books.google.co.uk/books?id=URL5NKX8vbAC.

M. Combescot, R. Combescot, and F. Dubin, Reports on Progress in Physics **80**, 066501 (2017), URL http://stacks.iop.org/0034-4885/80/i=6/a=066501.

J. Klaers, J. Schmitt, F. Vewinger, and M. Weitz, Nature **468**, 545 EP (2010), URL http://dx.doi.org/10.1038/nature09567.

P. B. Littlewood and A. Edelman, *Introduction to Polariton Condensation* (Cambridge University Press, 2017), p. 57âĂŞ74.

C. Weisbuch, M. Nishioka, A. Ishikawa, and Y. Arakawa, Phys. Rev. Lett. **69**, 3314 (1992), URL https://link.aps.org/doi/10.1103/PhysRevLett.69.3314.

J. P. Reithmaier, G. Sęk, A. Löffler, C. Hofmann, S. Kuhn, S. Reitzenstein, L. V. Keldysh, V. D. Kulakovskii, T. L. Reinecke, and A. Forchel, Nature **432**, 197 EP (2004), URL http://dx.doi.org/10.1038/nature02969.

M. Benyoucef, J. Shim, J. Wiersig, and O. G. Schmidt, physica status solidi (b) **249**, 925 (2011), https://onlinelibrary.wiley.com/doi/pdf/10.1002/pssb.201100062, URL https://onlinelibrary.wiley.com/doi/abs/10.1002/pssb.201100062.

H. Hattermann, D. Bothner, L. Y. Ley, B. Ferdinand, D. Wiedmaier, L. Sárkány, R. Kleiner, D. Koelle, and J. Fortágh, Nature Communications **8**, 2254 (2017), URL https://doi.org/10.1038/s41467-017-02439-7.

J. Keeling, F. M. Marchetti, M. H. SzymaÅĎska, and P. B. Littlewood, Semiconductor Science and Technology **22**, R1 (2007), URL http://stacks.iop.org/0268-1242/22/i=5/a=R01.

J. Kasprzak, M. Richard, S. Kundermann, A. Baas, P. Jeambrun, J. Keeling, F. Marchetti, M. Szymańska, R. Andre, J. Staehli, *et al.*, Nature **443**, 409 (2006).

I. Carusotto and C. Ciuti, Reviews of Modern Physics **85**, 299 (2013).

L. M. Sieberer, M. Buchhold, and S. Diehl, Reports on Progress in Physics **79**, 096001 (2016a), URL http://stacks.iop.org/0034-4885/79/i=9/a=096001.

N. P. Proukakis, D. W. Snoke, and P. B. Littlewood, *Universal Themes of Bose-Einstein Condensation* (Cambridge University Press, 2017).

D. Snoke, *Polariton Condensation and Lasing* (Springer Berlin Heidelberg, Berlin, Heidelberg, 2012), pp. 307–327, ISBN 978-3-642-24186-4, URL https://doi.org/10.1007/978-3-642-24186-4_12.

T. Byrnes, N. Y. Kim, and Y. Yamamoto, Nature Physics **10**, 803 EP (2014), URL http://dx.doi.org/10.1038/nphys3143.

Y. Sun, P. Wen, Y. Yoon, G. Liu, M. Steger, L. N. Pfeiffer, K. West, D. W. Snoke, and K. A. Nelson, Phys. Rev. Lett. **118**, 016602 (2017), URL https://link.aps.org/doi/10.1103/PhysRevLett.118.016602.

H. Haken, in *Quantum Optics*, edited by S. M. Kay and A. Maitland (1970), p. 201.

P. Eastham and P. Littlewood, Solid State Communications **116**, 357 (2000), ISSN 0038-1098, URL http://www.sciencedirect.com/science/article/pii/S0038109800003501.

J. Keeling, P. R. Eastham, M. H. Szymanska, and P. B. Littlewood, Phys. Rev. Lett. **93**, 226403 (2004), URL https://link.aps.org/doi/10.1103/PhysRevLett.93.226403.

M. H. Szymańska, J. Keeling, and P. B. Littlewood, Phys. Rev. Lett. **96**, 230602 (2006), URL https://link.aps.org/doi/10.1103/PhysRevLett.96.230602.

M. Wouters and I. Carusotto, Phys. Rev. A **76**, 043807 (2007a), URL https://link.aps.org/doi/10.1103/PhysRevA.76.043807.

M. Wouters and I. Carusotto, Phys. Rev. Lett. **99**, 140402 (2007b), URL https://link.aps.org/doi/10.1103/PhysRevLett.99.140402.

D. Porras, C. Ciuti, J. J. Baumberg, and C. Tejedor, Phys. Rev. B **66**, 085304 (2002), URL https://link.aps.org/doi/10.1103/PhysRevB.66.085304.

E. Wertz, L. Ferrier, D. D. Solnyshkov, R. Johne, D. Sanvitto, A. Lemaître, I. Sagnes, R. Grousson, A. V. Kavokin, P. Senellart, *et al.*, Nature Physics **6**, 860 EP (2010), URL http://dx.doi.org/10.1038/nphys1750.

D. Caputo, D. Ballarini, G. Dagvadorj, C. Sánchez Muñoz, M. De Giorgi, L. Dominici, K. West, L. N. Pfeiffer, G. Gigli, F. P. Laussy, *et al.*, Nature Materials **17**, 145 EP (2017), URL http://dx.doi.org/10.1038/nmat5039.

J. J. Baumberg, P. G. Savvidis, R. M. Stevenson, A. I. Tartakovskii, M. S. Skolnick, D. M. Whittaker, and J. S. Roberts, Phys. Rev. B **62**, R16247 (2000), URL https://link.aps.org/doi/10.1103/PhysRevB.62.R16247.

R. M. Stevenson, V. N. Astratov, M. S. Skolnick, D. M. Whittaker, M. Emam-Ismail, A. I. Tartakovskii, P. G. Savvidis, J. J. Baumberg, and J. S. Roberts, Phys. Rev. Lett. **85**, 3680 (2000), URL https://link.aps.org/doi/10.1103/PhysRevLett.85.3680.

I. Carusotto and C. Ciuti, Physical Review B **72**, 125335 (2005).

C. Ciuti, P. Schwendimann, B. Deveaud, and A. Quattropani, Phys. Rev. B **62**, R4825 (2000), URL https://link.aps.org/doi/10.1103/PhysRevB.62.R4825.

D. M. Whittaker, Phys. Rev. B **63**, 193305 (2001), URL https://link.aps.org/doi/10.1103/PhysRevB.63.193305.

L. S. Dang, D. Heger, R. André, F. Bœuf, and R. Romestain, Phys. Rev. Lett. **81**, 3920 (1998), URL https://link.aps.org/doi/10.1103/PhysRevLett.81.3920.

M. Richard, J. Kasprzak, R. Romestain, R. André, and L. S. Dang, Phys. Rev. Lett. **94**, 187401 (2005), URL https://link.aps.org/doi/10.1103/PhysRevLett.94.187401.

J. Keeling and N. G. Berloff, Phys. Rev. Lett. **100**, 250401 (2008), URL https://link.aps.org/doi/10.1103/PhysRevLett.100.250401.

M. Wouters and I. Carusotto, Phys. Rev. Lett. **105**, 020602 (2010), URL https://link.aps.org/doi/10.1103/PhysRevLett.105.020602.

M. Wouters and V. Savona, Phys. Rev. B **79**, 165302 (2009), URL https://link.aps.org/doi/10.1103/PhysRevB.79.165302.

R. Balili, V. Hartwell, D. Snoke, L. Pfeiffer, and K. West, Science **316**, 1007 (2007), ISSN 0036-8075, http://science.sciencemag.org/content/316/5827/1007.full.pdf, URL http://science.sciencemag.org/content/316/5827/1007.

S. Kéna-Cohen and S. R. Forrest, Nature Photonics **4**, 371 EP (2010), URL http://dx.doi.org/10.1038/nphoton.2010.86.

K. S. Daskalakis, S. A. Maier, R. Murray, and S. Kéna-Cohen, Nature Materials **13**, 271 EP (2014), URL http://dx.doi.org/10.1038/nmat3874.

G. Lerario, D. Ballarini, A. Fieramosca, A. Cannavale, A. Genco, F. Mangione, S. Gambino, L. Dominici, M. De Giorgi, G. Gigli, *et al.*, Light: Science &Amp; Applications **6**, e16212 EP (2017), URL http://dx.doi.org/10.1038/lsa.2016.212.

D. Sanvitto and S. Kéna-Cohen, Nature Materials **15**, 1061 EP (2016), URL http://dx.doi.org/10.1038/nmat4668.

A. Chiocchetta, A. Gambassi, and I. Carusotto, *Laser Operation and Bose-Einstein Condensation: Analogies and Differences* (Cambridge University Press, 2017), p. 409âĂŞ423.

H. Deng, D. Press, S. Götzinger, G. S. Solomon, R. Hey, K. H. Ploog, and Y. Yamamoto, Phys. Rev. Lett. **97**, 146402 (2006), URL https://link.aps.org/doi/10.1103/PhysRevLett.97.146402.

G. Roumpos, M. Lohse, W. H. Nitsche, J. Keeling, M. H. Szymańska, P. B. Littlewood, A. Löffler, S. Höfling, L. Worschech, A. Forchel, *et al.*, Proceedings of the National Academy of Sciences **109**, 6467 (2012), ISSN 0027-8424, http://www.pnas.org/content/109/17/6467.full.pdf, URL http://www.pnas.org/content/109/17/6467.

W. H. Nitsche, N. Y. Kim, G. Roumpos, C. Schneider, M. Kamp, S. Höfling, A. Forchel, and Y. Yamamoto, Phys. Rev. B **90**, 205430 (2014), URL https://link.aps.org/doi/10.1103/PhysRevB.90.205430.

D. Ballarini, D. Caputo, C. S. Muñoz, M. De Giorgi, L. Dominici, M. H. Szymańska, K. West, L. N. Pfeiffer, G. Gigli, F. P. Laussy, *et al.*, Phys. Rev. Lett. **118**, 215301 (2017), URL https://link.aps.org/doi/10.1103/PhysRevLett.118.215301.

L. Pitaevskii and S. Stringari, *Bose-Einstein Condensation*, International Series of Monographs on Physics (Clarendon Press, 2003), ISBN 9780198507192, URL https://books.google.co.uk/books?id=rIobbOxC4j4C.

D. R. Nelson and J. M. Kosterlitz, Phys. Rev. Lett. **39**, 1201 (1977), URL https://link.aps.org/doi/10.1103/PhysRevLett.39.1201.

M. Holzmann, G. Baym, J.-P. Blaizot, and F. Laloë, Proceedings of the National Academy of Sciences **104**, 1476 (2007), ISSN 0027-8424, http://www.pnas.org/content/104/5/1476.full.pdf, URL http://www.pnas.org/content/104/5/1476.

O. L. Berman, Y. E. Lozovik, and D. W. Snoke, Phys. Rev. B **77**, 155317 (2008), URL https://link.aps.org/doi/10.1103/PhysRevB.77.155317.

A. Amo, D. Sanvitto, F. P. Laussy, D. Ballarini, E. d. Valle, M. D. Martin, A. Lemaître, J. Bloch, D. N. Krizhanovskii, M. S. Skolnick, *et al.*, Nature **457**, 291 EP (2009a), URL http://dx.doi.org/10.1038/nature07640.

G. E. Astrakharchik and L. P. Pitaevskii, Phys. Rev. A **70**, 013608 (2004), URL https://link.aps.org/doi/10.1103/PhysRevA.70.013608.

A. Amo, J. Lefrère, S. Pigeon, C. Adrados, C. Ciuti, I. Carusotto, R. Houdré, E. Giacobino, and A. Bramati, Nature Physics **5**, 805 EP (2009b), URL http://dx.doi.org/10.1038/nphys1364.

A. Chiocchetta and I. Carusotto, EPL (Europhysics Letters) **102**, 67007 (2013), URL http://stacks.iop.org/0295-5075/102/i=6/a=67007.

E. Altman, L. M. Sieberer, L. Chen, S. Diehl, and J. Toner, Phys. Rev. X **5**, 011017 (2015), URL http://link.aps.org/doi/10.1103/PhysRevX.5.011017.

V. N. Gladilin, K. Ji, and M. Wouters, Phys. Rev. A **90**, 023615 (2014), URL https://link.aps.org/doi/10.1103/PhysRevA.90.023615.

G. Dagvadorj, J. Fellows, S. Matyjaśkiewicz, F. Marchetti, I. Carusotto, and M. Szymańska, Physical Review X **5**, 041028 (2015).

C. Domb, *Phase Transitions and Critical Phenomena*, no. v. 19 in Phase Transitions and Critical Phenomena (Elsevier Science, 2000), ISBN 9780080538761, URL https://books.google.co.uk/books?id=a9Xe1SGXEYYC.

J. Zinn-Justin, *Quantum Field Theory and Critical Phenomena*, International series of monographs on physics (Clarendon Press, 2002), ISBN 9780198509233, URL https://books.google.co.uk/books?id=N8DBpTzBCJYC.

A. P. Gottlob and M. Hasenbusch, Physica A: Statistical Mechanics and its Applications **201**, 593 (1993), ISSN 0378-4371, URL http://www.sciencedirect.com/science/article/pii/037843719390131M.

H. Kleinert, *VORTEX LINES IN THE GINZBURG-LANDAU THEORY AND THEIR DISORDER FIELD THEORY* (1989), pp. 716–742.

A. J. Bray, Advances in Physics **51**, 481 (2002).

A. del Campo and W. H. Zurek, International Journal of Modern Physics A **29**, 1430018 (2014), http://www.worldscientific.com/doi/pdf/10.1142/S0217751X1430018X, URL http://www.worldscientific.com/doi/abs/10.1142/S0217751X1430018X.

T. W. B. Kibble, Journal of Physics A: Mathematical and General **9**, 1387 (1976), URL http://stacks.iop.org/0305-4470/9/i=8/a=029.

W. Zurek, Nature **317**, 505 (1985).

M. Kulczykowski and M. Matuszewski, Phys. Rev. B **95**, 075306 (2017), URL https://link.aps.org/doi/10.1103/PhysRevB.95.075306.

T. Liew, O. Egorov, M. Matuszewski, O. Kyriienko, X. Ma, and E. Ostrovskaya, Physical Review B **91**, 085413 (2015).

M. Matuszewski and E. Witkowska, Phys. Rev. B **89**, 155318 (2014a), URL https://link.aps.org/doi/10.1103/PhysRevB.89.155318.

S. Utsunomiya, L. Tian, G. Roumpos, C. W. Lai, N. Kumada, T. Fujisawa, M. Kuwata-Gonokami, A. Löffler, S. Höfling, A. Forchel, *et al.*, Nature Physics **4**, 700 EP (2008), URL http://dx.doi.org/10.1038/nphys1034.

A. Amo, S. Pigeon, D. Sanvitto, V. G. Sala, R. Hivet, I. Carusotto, F. Pisanello, G. Leménager, R. Houdré, E. Giacobino, *et al.*, Science **332**, 1167 (2011), ISSN 0036-8075, http://science.sciencemag.org/content/332/6034/1167.full.pdf, URL http://science.sciencemag.org/content/332/6034/1167.

K. G. Lagoudakis, M. Wouters, M. Richard, A. Baas, I. Carusotto, R. André, L. S. Dang, and B. Deveaud-Plédran, Nature Physics **4**, 706 EP (2008), URL http://dx.doi.org/10.1038/nphys1051.

D. Sanvitto, F. M. Marchetti, M. H. Szymańska, G. Tosi, M. Baudisch, F. P. Laussy, D. N. Krizhanovskii, M. S. Skolnick, L. Marrucci, A. Lemaître, *et al.*, Nature Physics **6**, 527 EP (2010a), URL http://dx.doi.org/10.1038/nphys1668.

G. Roumpos, M. D. Fraser, A. Löffler, S. Höfling, A. Forchel, and Y. Yamamoto, Nature Physics **7**, 129 EP (2010), URL http://dx.doi.org/10.1038/nphys1841.

J. Keeling, L. M. Sieberer, E. Altman, L. Chen, S. Diehl, and J. Toner, *Superfluidity and Phase Correlations of Driven Dissipative Condensates* (Cambridge University Press, 2017), p. 205âĂŞ230.

N. P. Proukakis and B. Jackson, Journal of Physics B: Atomic, Molecular and Optical Physics **41**, 203002 (2008), URL http://stacks.iop.org/0953-4075/41/i=20/a=203002.

A. L. Fetter, Annals of Physics **70**, 67 (1972), ISSN 0003-4916, URL http://www.sciencedirect.com/science/article/pii/0003491672903302.

N. Bogoliubov, J. Phys. (Moscow) **11**, 23 (1947), ISSN 0003-4916.

E. P. Gross, Phys. Rev. **106**, 161 (1957), URL https://link.aps.org/doi/10.1103/PhysRev.106.161.

V. L. Ginzburg and L. P. Pitaevskii, Sov. Phys. JETP **7**, 858 (1958), URL http://www.jetp.ac.ru/cgi-bin/e/index/e/7/5/p858?a=list.

W. van Saarloos and P. Hohenberg, Physica D: Nonlinear Phenomena **56**, 303 (1992), ISSN 0167-2789, URL http://www.sciencedirect.com/science/article/pii/016727899290175M.

I. S. Aranson and L. Kramer, Rev. Mod. Phys. **74**, 99 (2002), URL https://link.aps.org/doi/10.1103/RevModPhys.74.99.

N. Bobrovska and M. Matuszewski, Phys. Rev. B **92**, 035311 (2015), URL https://link.aps.org/doi/10.1103/PhysRevB.92.035311.

M. Wouters and I. Carusotto, Phys. Rev. B **75**, 075332 (2007c), URL https://link.aps.org/doi/10.1103/PhysRevB.75.075332.

P. G. Savvidis, J. J. Baumberg, R. M. Stevenson, M. S. Skolnick, D. M. Whittaker, and J. S. Roberts, Phys. Rev. Lett. **84**, 1547 (2000), URL https://link.aps.org/doi/10.1103/PhysRevLett.84.1547.

C. Ciuti, P. Schwendimann, and A. Quattropani, Semiconductor Science and Technology **18**, S279 (2003), URL http://stacks.iop.org/0268-1242/18/i=10/a=301.

M. Szymańska, J. Keeling, and P. Littlewood, Physical Review B **75**, 195331 (2007).

M. Wouters and I. Carusotto, Physical Review B **75**, 075332 (2007d).

M. Wouters and I. Carusotto, Phys. Rev. B **74**, 245316 (2006), URL https://link.aps.org/doi/10.1103/PhysRevB.74.245316.

M. Wouters and I. Carusotto, Phys. Rev. A **76**, 043807 (2007e), URL https://link.aps.org/doi/10.1103/PhysRevA.76.043807.

G. Franchetti (2013).

F. Baboux, D. B. D., V. Goblot, V. Gladilin, C. Gomez, E. Galopin, L. Le Gratiet, A. LemaÃőtre, I. Sagnes, I. Carusotto, *et al.*, arXiv:1707.05798 (2017), URL https://link.aps.org/doi/10.1103/PhysRevE.78.026704.

H. Saito and M. Ueda, Phys. Rev. Lett. **89**, 190402 (2002), URL https://link.aps.org/doi/10.1103/PhysRevLett.89.190402.

L. P. Pitaevskii, Sov. Phys. JETP **8**, 282 (1959).

M. Wouters, New Journal of Physics **14**, 075020 (2012), URL http://stacks.iop.org/1367-2630/14/i=7/a=075020.

I. Carusotto and C. Ciuti, Phys. Rev. Lett. **93**, 166401 (2004), URL https://link.aps.org/doi/10.1103/PhysRevLett.93.166401.

M. Szymańska, J. Keeling, and P. Littlewood, Physical review letters **96**, 230602 (2006).

H. Haug, T. D. Doan, and D. B. Tran Thoai, Phys. Rev. B **89**, 155302 (2014), URL https://link.aps.org/doi/10.1103/PhysRevB.89.155302.

D. D. Solnyshkov, H. Terças, K. Dini, and G. Malpuech, Phys. Rev. A **89**, 033626 (2014), URL https://link.aps.org/doi/10.1103/PhysRevA.89.033626.

D. M. Ceperley, Rev. Mod. Phys. **67**, 279 (1995), URL https://link.aps.org/doi/10.1103/RevModPhys.67.279.

K. V. Houcke, E. Kozik, N. ProkofâĂŹev, and B. Svistunov, Physics Procedia **6**, 95 (2010), ISSN 1875-3892, computer Simulations Studies in Condensed Matter Physics XXI, URL http://www.sciencedirect.com/science/article/pii/S1875389210006498.

A. Sinatra, C. Lobo, and Y. Castin, Journal of Physics B: Atomic, Molecular and Optical Physics **35**, 3599 (2002), URL http://stacks.iop.org/0953-4075/35/i=17/a=301.

C. W. Gardiner and M. J. Collett, Phys. Rev. A **31**, 3761 (1985), URL https://link.aps.org/doi/10.1103/PhysRevA.31.3761.

L. M. Sieberer, M. Buchhold, and S. Diehl, Reports on Progress in Physics **79**, 096001 (2016b), URL http://stacks.iop.org/0034-4885/79/i=9/a=096001.

M. Kardar, G. Parisi, and Y.-C. Zhang, Phys. Rev. Lett. **56**, 889 (1986), URL https://link.aps.org/doi/10.1103/PhysRevLett.56.889.

D. Whittaker, Superlattices and Microstructures **41**, 297 (2007), ISSN 0749-6036, proceedings of the 6th International Conference on Physics of Light-Matter Coupling in Nanostructures, URL http://www.sciencedirect.com/science/article/pii/S0749603607000225.

J.-i. Wakita, H. Itoh, T. Matsuyama, and M. Matsushita, Journal of the Physical Society of Japan **66**, 67 (1997), URL https://doi.org/10.1143/JPSJ.66.67.

J. Toner and Y. Tu, Phys. Rev. E **58**, 4828 (1998), URL https://link.aps.org/doi/10.1103/PhysRevE.58.4828.

L. A. Segel and L. Edelstein-Keshet, *Chapter 4: Introduction to nondimensionalization and scaling* (Society for Industrial and Applied Mathematics, 2013), pp. 67–82, ISBN 978-1-61197-249-8, URL https://doi.org/10.1137/1.9781611972504.ch4.

D. Sanvitto, A. Amo, L. Viña, R. André, D. Solnyshkov, and G. Malpuech, Phys. Rev. B **80**, 045301 (2009), URL https://link.aps.org/doi/10.1103/PhysRevB.80.045301.

E. A. Ostrovskaya, J. Abdullaev, M. D. Fraser, A. S. Desyatnikov, and Y. S. Kivshar, Phys. Rev. Lett. **110**, 170407 (2013), URL https://link.aps.org/doi/10.1103/PhysRevLett.110.170407.

G. R. Dennis, J. J. Hope, and M. T. Johnsson, Computer Physics Communications **184**, 201 (2013), ISSN 0010-4655, URL http://www.sciencedirect.com/science/article/pii/S0010465512002822.

P. Blakie, A. Bradley, M. Davis, R. Ballagh, and C. Gardiner, Advances in Physics **57**, 363 (2008), https://doi.org/10.1080/00018730802564254, URL https://doi.org/10.1080/00018730802564254.

D. Gottlieb and S. Orszag, *Numerical Analysis of Spectral Methods* (Society for Industrial and Applied Mathematics, 1977), https://epubs.siam.org/doi/pdf/10.1137/1.9781611970425, URL https://epubs.siam.org/doi/abs/10.1137/1.9781611970425.

A. Sinatra, Y. Castin, and E. Witkowska, Phys. Rev. A **75**, 033616 (2007), URL https://link.aps.org/doi/10.1103/PhysRevA.75.033616.

A. Sinatra and Y. Castin, Phys. Rev. A **78**, 053615 (2008), URL https://link.aps.org/doi/10.1103/PhysRevA.78.053615.

M. Brewczyk, M. Gajda, and K. RzaÃĚÅŠewski, Journal of Physics B: Atomic, Molecular and Optical Physics **40**, R1 (2007), URL http://stacks.iop.org/0953-4075/40/i=2/a=R01.

S. P. Cockburn and N. P. Proukakis, Laser Physics **19**, 558 (2009), ISSN 1555-6611, URL https://doi.org/10.1134/S1054660X09040057.

P. B. Blakie, Phys. Rev. E **78**, 026704 (2008), URL https://link.aps.org/doi/10.1103/PhysRevE.78.026704.

S. P. Cockburn (2010).

K. W. Madison, F. Chevy, W. Wohlleben, and J. Dalibard, Phys. Rev. Lett. **84**, 806 (2000), URL https://link.aps.org/doi/10.1103/PhysRevLett.84.806.

A. E. Leanhardt, A. Görlitz, A. P. Chikkatur, D. Kielpinski, Y. Shin, D. E. Pritchard, and W. Ketterle, Phys. Rev. Lett. **89**, 190403 (2002), URL https://link.aps.org/doi/10.1103/PhysRevLett.89.190403.

W. J. Kwon, S. W. Seo, and Y.-i. Shin, Phys. Rev. A **92**, 033613 (2015), URL https://link.aps.org/doi/10.1103/PhysRevA.92.033613.

B. P. Anderson, P. C. Haljan, C. A. Regal, D. L. Feder, L. A. Collins, C. W. Clark, and E. A. Cornell, Phys. Rev. Lett. **86**, 2926 (2001), URL https://link.aps.org/doi/10.1103/PhysRevLett.86.2926.

S. Pigeon, I. Carusotto, and C. Ciuti, Phys. Rev. B **83**, 144513 (2011), URL https://link.aps.org/doi/10.1103/PhysRevB.83.144513.

D. Sanvitto, F. Marchetti, M. Szymańska, G. Tosi, M. Baudisch, F. Laussy, D. Krizhanovskii, M. Skolnick, L. Marrucci, A. Lemaitre, *et al.*, Nature Physics **6**, 527 (2010b).

A. C. White, C. F. Barenghi, and N. P. Proukakis, Phys. Rev. A **86**, 013635 (2012), URL https://link.aps.org/doi/10.1103/PhysRevA.86.013635.

A. Villois, G. Krstulovic, D. Proment, and H. Salman, Journal of Physics A: Mathematical and Theoretical **49**, 415502 (2016), URL http://stacks.iop.org/1751-8121/49/i=41/a=415502.

G. W. Stagg (2016).

R. J. Fletcher, M. Robert-de Saint-Vincent, J. Man, N. Navon, R. P. Smith, K. G. H. Viebahn, and Z. Hadzibabic, Phys. Rev. Lett. **114**, 255302 (2015), URL https://link.aps.org/doi/10.1103/PhysRevLett.114.255302.

N. D. Mermin and H. Wagner, Phys. Rev. Lett. **17**, 1133 (1966), URL https://link.aps.org/doi/10.1103/PhysRevLett.17.1133.

P. C. Hohenberg, Phys. Rev. **158**, 383 (1967), URL https://link.aps.org/doi/10.1103/PhysRev.158.383.

V. L. Berezinskii, Sov. Phys. JETP **32**, 493 (1971).

J. M. Kosterlitz and D. J. Thouless, Journal of Physics C: Solid State Physics **6**, 1181 (1973), URL http://stacks.iop.org/0022-3719/6/i=7/a=010.

R. E. Peierls, Helv. Phys. Acta **7**, 81 (1934).

R. E. Peierls, Ann. Inst. Henri Poincaré **5**, 177 (1935).

S. M. Girvin, Boulder (2000).

A. Jelić and L. F. Cugliandolo, Journal of Statistical Mechanics: Theory and Experiment **2011**, P02032 (2011).

D. J. Bishop and J. D. Reppy, Phys. Rev. Lett. **40**, 1727 (1978), URL https://link.aps.org/doi/10.1103/PhysRevLett.40.1727.

S. A. Anikin, O. I. Zavialov, and N. I. Kartchev, Theor. Math. Phys. **44**, 291 (1980).

S. Stock, Z. Hadzibabic, B. Battelier, M. Cheneau, and J. Dalibard, Phys. Rev. Lett. **95**, 190403 (2005), URL https://link.aps.org/doi/10.1103/PhysRevLett.95.190403.

Z. Hadzibabic, P. Krüger, M. Cheneau, B. Battelier, and J. Dalibard, Nature **441**, 1118 EP (2006), URL http://dx.doi.org/10.1038/nature04851.

P. Cladé, C. Ryu, A. Ramanathan, K. Helmerson, and W. D. Phillips, Phys. Rev. Lett. **102**, 170401 (2009), URL https://link.aps.org/doi/10.1103/PhysRevLett.102.170401.

J. Keeling and N. G. Berloff, Contemporary Physics **52**, 131 (2011).

N. Proukakis, S. Gardiner, M. Davis, and M. Szymańska, *Quantum Gases: Finite Temperature and Non-Equilibrium Dynamics*, vol. 1 (World Scientific, 2013).

H. Deng, H. Haug, and Y. Yamamoto, Reviews of modern physics **82**, 1489 (2010).

A. Zamora, L. M. Sieberer, K. Dunnett, S. Diehl, and M. H. Szymańska, Phys. Rev. X **7**, 041006 (2017), URL https://link.aps.org/doi/10.1103/PhysRevX.7.041006.

J. J. Binney, N. J. Dowrick, A. J. Fisher, and M. Newman, *The theory of critical phenomena: an introduction to the renormalization group* (Oxford University Press, Inc., 1992).

P. C. Hohenberg and B. I. Halperin, Reviews of Modern Physics **49**, 435 (1977).

A. Bray, A. Briant, and D. Jervis, Physical review letters **84**, 1503 (2000).

A. Rutenberg and A. Bray, Physical Review E **51**, R1641 (1995).

A. N. Pargellis, S. Green, and B. Yurke, Physical Review E **49**, 4250 (1994).

D. S. Fisher and D. A. Huse, Physical Review B **38**, 373 (1988).

J. Langer and C. Godrèche, edited by C. Godreche p. 297 (1992).

B. Heinrich and J. A. C. Bland, *Ultrathin Magnetic Structures II*, vol. 1 (Springer, 1994).

K. Binder and D. Stauffer, Physical Review Letters **33**, 1006 (1974).

H. Furukawa, Progress of Theoretical Physics **59**, 1072 (1978).

K. Damle, S. N. Majumdar, and S. Sachdev, Physical Review A **54**, 5037 (1996).

L. A. Williamson and P. Blakie, Physical review letters **116**, 025301 (2016).

A. Pargellis, P. Finn, J. Goodby, P. Panizza, B. Yurke, and P. Cladis, Physical Review A **46**, 7765 (1992).

B. Yurke, A. Pargellis, T. Kovacs, and D. Huse, Physical Review E **47**, 1525 (1993).

A. J. Bray, Phys. Rev. E **62**, 103 (2000), URL https://link.aps.org/doi/10.1103/PhysRevE.62.103.

A. Pagnani and G. Parisi, Phys. Rev. E **92**, 010101 (2015), URL https://link.aps.org/doi/10.1103/PhysRevE.92.010101.

L. Canet, H. Chaté, B. Delamotte, and N. Wschebor, Phys. Rev. Lett. **104**, 150601 (2010), URL https://link.aps.org/doi/10.1103/PhysRevLett.104.150601.

T. Halpin-Healy and G. Palasantzas, EPL (Europhysics Letters) **105**, 50001 (2014), URL http://stacks.iop.org/0295-5075/105/i=5/a=50001.

V. N. Gladilin and M. Wouters, New Journal of Physics **19**, 105005 (2017), URL http://stacks.iop.org/1367-2630/19/i=10/a=105005.

M. Matuszewski and E. Witkowska, Physical Review B **89**, 155318 (2014b).

A. W. Baggaley and C. F. Barenghi, Phys. Rev. A **97**, 033601 (2018), URL https://link.aps.org/doi/10.1103/PhysRevA.97.033601.

K. Kudo and Y. Kawaguchi, Physical Review A **88**, 013630 (2013).

J. Hofmann, S. S. Natu, and S. D. Sarma, Physical review letters **113**, 095702 (2014).

A. Jonsson and P. Minnhagen, Phys. Rev. B **55**, 9035 (1997), URL https://link.aps.org/doi/10.1103/PhysRevB.55.9035.

R. Monaco, J. Mygind, R. J. Rivers, and V. P. Koshelets, Phys. Rev. B **80**, 180501 (2009), URL https://link.aps.org/doi/10.1103/PhysRevB.80.180501.

I. Chuang, R. DURRER, N. TUROK, and B. YURKE, Science **251**, 1336 (1991), ISSN 0036-8075, http://science.sciencemag.org/content/251/4999/1336.full.pdf, URL http://science.sciencemag.org/content/251/4999/1336.

S. M. Griffin, M. Lilienblum, K. T. Delaney, Y. Kumagai, M. Fiebig, and N. A. Spaldin, Phys. Rev. X **2**, 041022 (2012), URL https://link.aps.org/doi/10.1103/PhysRevX.2.041022.

P. Laguna and W. H. Zurek, Phys. Rev. D **58**, 085021 (1998), URL https://link.aps.org/doi/10.1103/PhysRevD.58.085021.

J. Dziarmaga, P. Laguna, and W. H. Zurek, Phys. Rev. Lett. **82**, 4749 (1999), URL https://link.aps.org/doi/10.1103/PhysRevLett.82.4749.

N. D. Antunes, L. M. A. Bettencourt, and W. H. Zurek, Phys. Rev. Lett. **82**, 2824 (1999), URL https://link.aps.org/doi/10.1103/PhysRevLett.82.2824.

M. Kobayashi and L. F. Cugliandolo, Phys. Rev. E **94**, 062146 (2016), URL https://link.aps.org/doi/10.1103/PhysRevE.94.062146.

K. Shimizu, Y. Kuno, T. Hirano, and I. Ichinose, Phys. Rev. A **97**, 033626 (2018), URL https://link.aps.org/doi/10.1103/PhysRevA.97.033626.

A. Yates and W. H. Zurek, Phys. Rev. Lett. **80**, 5477 (1998), URL https://link.aps.org/doi/10.1103/PhysRevLett.80.5477.

S. Ducci, P. L. Ramazza, W. González-Viñas, and F. T. Arecchi, Phys. Rev. Lett. **83**, 5210 (1999), URL https://link.aps.org/doi/10.1103/PhysRevLett.83.5210.

M. A. Miranda, D. Laroze, and D. González-Viñas, Journal of Physics: Condensed Matter **25**, 404208 (2013), URL http://stacks.iop.org/0953-8984/25/i=40/a=404208.

A. del Campo, A. Retzker, and M. B. Plenio, New Journal of Physics **13**, 083022 (2011), URL http://stacks.iop.org/1367-2630/13/i=8/a=083022.

J. Dziarmaga and W. H. Zurek, Scientific Reports **4**, 5950 EP (2014), URL http://dx.doi.org/10.1038/srep05950.

G. Lamporesi, S. Donadello, S. Serafini, F. Dalfovo, and G. Ferrari, Nature Physics **9**, 656 EP (2013), URL http://dx.doi.org/10.1038/nphys2734.

L. Chomaz, L. Corman, T. Bienaimé, R. Desbuquois, C. Weitenberg, S. Nascimbène, J. Beugnon, and J. Dalibard, Nature Communications **6**, 6162 EP (2015), URL http://dx.doi.org/10.1038/ncomms7162.

N. Navon, A. L. Gaunt, R. P. Smith, and Z. Hadzibabic, Science **347**, 167 (2015), ISSN 0036-8075, http://science.sciencemag.org/content/347/6218/167.full.pdf, URL http://science.sciencemag.org/content/347/6218/167.

I.-K. Liu, S. Donadello, G. Lamporesi, G. Ferrari, S.-C. Gou, F. Dalfovo, and N. Proukakis (2017), URL http://arxiv.org/abs/1712.08074.

R. Gupta, J. DeLapp, G. G. Batrouni, G. C. Fox, C. F. Baillie, and J. Apostolakis, Phys. Rev. Lett. **61**, 1996 (1988), URL https://link.aps.org/doi/10.1103/PhysRevLett.61.1996.